UNIVERSITY OF OKLAHOMA

GRADUATE COLLEGE

FROM PRIMORDIAL BLACK HOLES TO CEPHEIDS, A FOCUS ON THE EARLY AND LATE UNIVERSE

A DISSERTATION

SUBMITTED TO THE GRADUATE FACULTY

in partial fulfillment of the requirements for the

degree of

Doctor of Philosophy

By

THOMAS C. GEHRMAN JR.
Norman, Oklahoma
2025

Downloaded from SHAREOK. Persistent Handle URL: https://hdl.handle.net/11244/341727

FROM PRIMORDIAL BLACK HOLES TO CEPHEIDS, A FOCUS ON THE EARLY AND LATE UNIVERSE

A DISSERTATION APPROVED FOR THE
HOMER L. DODGE DEPARTMENT OF PHYSICS AND ASTRONOMY

BY THE COMMITTEE CONSISTING OF

Dr.Kuver Sinha (Chair)

Dr. John Stupak

Dr. Howard Baer

Dr. Xinyu Dia

Dr. Keri Kornelson

© Copyright by THOMAS C. GEHRMAN JR. 2025
All Rights Reserved.

This work is dedicated to my parents, Thomas M. Gehrman, Jenny Morrisey, Ingrid Westin, and Vaclav Vyvoda. To my many brothers and sisters, Melissa Gehrman, Samantha Gehrman, Stephanie Westin, Daniel Westin, Annika Westin, Tim Ofenbeck, and Persephony Ofenbeck. I also dedicate this work to all my friends. I will always be forever grateful for the love and support you have provided throughout my life.

Acknowledgments

I would like to thank my advisor, Dr. Kuver Sinha, for the support and guidance he has provided throughout my career. He was the first person to teach me physics, and that an idea can be transformed into a beautiful story. I am thankful that you introduced me to the world of high energy phenomenology, primordial black holes, and BSM physics. I truly appreciate how patient and understanding you are, considering I started initially way outside the field of high-energy physics. Dr. Tao Xu has provided me with many insightful discussions and guided me to the necessary tools to succeed in this field; I am grateful for your support. Science today is typically accomplished in a group and built upon the work of others. The work presented in this dissertation wouldn't have been possible without the contributions of my collaborators, Dr. Tao Xu, Dr. Kuver Sinha, Dr. Barmak Shams Es Haghi, Dr. Pearl Sandick, Edward Walsh, and Kaleb Anderson. Both Dakotah Martinez and Henri LeMieux have been instrumental in assisting me through my Master's and PhD. Their words of encourgment and ability to guide me to the finish line I was able to finish this work. Finally, I would not have been able to achieve this milestone without the encouragement of my previous mentors, Dr. Paul Eskridge, Dr. Barton Pritzl, and Dr. Nadia Kaltcheva.

Table of Contents

Acknowledgments v

List Of Tables x

List Of Figures xi

Abstract xxi

1 Introduction to Primordial Black Holes 1
- 1.1 Motivation . . . 1
- 1.2 Introduction . . . 2
- 1.3 PBH Evaporation . . . 4
- 1.4 PBH Formation . . . 7
  - 1.4.1 Scalar Perturbations . . . 8
    - 1.4.1.1 Gravitational Waves from Scalar Perturbations . . . 11
  - 1.4.2 First Order Phase Transitions . . . 14
- 1.5 Conclusion . . . 15

2 Dark Matter 16
- 2.1 History, Observations, and Detection of Dark Matter . . . 16
- 2.2 PBHs as Dark Matter Candidates . . . 19
- 2.3 Axions . . . 20
  - 2.3.1 Axions and Stars . . . 21
- 2.4 Millicharged Particles . . . 22
- 2.5 Conclusion . . . 24

3 Baryogenesis, Primordial Black Holes and MHz-GHz Gravitational Waves 25
- 3.1 Introduction . . . 25
- 3.2 PBHs mass function . . . 30
- 3.3 Baryogenesis by Hawking Evaporation . . . 31
  - 3.3.1 Evaporation of PBHs in a Radiation-Dominated Universe . . . 32
  - 3.3.2 Evaporation of PBHs in a Matter- (PBH-) Dominated Universe 38
- 3.4 MHz - GHz Gravitational Waves and Interplay with Baryogenesis . . . 42
  - 3.4.1 Scaling of strain with peak frequency . . . 46
  - 3.4.2 Gravitational Waves and PBH Domination . . . 48
- 3.5 Double-Peaked Gravitational Waves and Dark Matter-Baryogenesis Coincidence Problem . . . 49
  - 3.5.1 Bi-modal mass function . . . 51

3.5.2 Coincidence Problem . . . 52
3.5.3 Formation of Heavy Primordial Black Holes in a Matter- (PBH-) Dominated Era . . . 54
3.5.4 Double-Peaked Gravitational Waves . . . 56
3.6 Conclusions . . . 59

4 The Primordial Black Holes that Disappeared: Connections to Dark Matter and MHz-GHz Gravitational Waves 61
4.1 Introduction . . . 61
4.2 Dark Matter from Hawking Radiation . . . 64
4.2.1 Particle Production through Hawking Radiation . . . 65
4.2.2 PBH Evaporation in a Radiation-Dominated Era . . . 66
4.3 PBH Formation Mechanisms and Correlated Gravitational Waves . . . 68
4.3.1 First-order Phase Transitions . . . 68
4.3.2 Scalar Perturbations Revisited . . . 77
4.4 Results: Dark Matter and High-frequency Gravitational Waves . . . 82
4.4.1 Correlating Dark Matter Abundance: $\{\Omega_\chi h^2, m_\chi\} \to \{M_{\rm PBH}, \beta_{\rm PBH}\}$ . . . 82
4.4.2 High-frequency Gravitational Waves . . . 88
4.5 Conclusions . . . 95

5 Recycled Dark Matter 98
5.1 Introduction . . . 98
5.2 Trapped Dark Sector during FOPT . . . 103
5.2.1 Dark Sector Model . . . 103
5.2.2 Why a Multi-particle Dark Sector is Required . . . 107
5.3 Thermal History and PBH Formation . . . 111
5.3.1 Thermal History of the Dark Sector . . . 111
5.3.2 Black Hole Formation . . . 112
5.3.3 Black Hole Mass Function . . . 117
5.4 UHDM from Black Hole Evaporation . . . 120
5.4.1 UHDM from PBHs Formed by a Trapped Dark Sector . . . 122
5.4.2 Annihilation of Dark Matter after Evaporation of PBHs . . . 125
5.5 Discussions and Conclusions . . . 129

6 Introduction to Stellar Astrophysics 132
6.1 Introduction to Stellar Evolution . . . 132
6.2 MESA & Initial Conditions . . . 136
6.2.1 Nuclear Reaction Network . . . 136
6.2.2 Stopping Controls, Mesh, & Solver . . . 137
6.2.3 Wind Mass Loss, Opacity, and Equation of State . . . 138
6.2.4 Convection, Overshoot, & Mixing Length Theory . . . 139

6.2.5 Rotation . . . 141
6.3 Conclusion . . . 142

7 Blue Loops, Cepheids, and Forays into Axions 143
7.1 Introduction . . . 143
7.2 Classical Cepheid Variables and Simulation Benchmarks . . . 150
7.3 Axion Model and Primakoff Effect . . . 152
7.3.1 Axion Production in Stars . . . 152
7.3.2 Energy Loss in `MESA` Simulation . . . 158
7.4 Axions, Blue Loops, and Cepheid Variables . . . 160
7.4.1 The Blue Loop . . . 160
7.4.2 The Mirror Principle . . . 164
7.4.3 The Hydrogen Profile and the Core Potential . . . 166
7.4.4 Blue Loop Elimination as a Function of Stellar Mass . . . 168
7.5 Axion Constraints from the Existence of Massive Cepheids . . . 175
7.5.1 Constraints from Observed Cepheids and Simulations . . . 175
7.5.2 S Mus: Luminosity and the Cepheid Mass Discrepancy Problem 179
7.5.3 Incorporating Overshoot Uncertainties for $6M_\odot$ and $8M_\odot$ Models 183
7.6 Conclusions . . . 191

8 Millicharged Particles, Blue Loops, and the Cepheid Mass Discrepancy Problem 194
8.1 Introduction . . . 194
8.2 Stellar Model and Rotation . . . 199
8.2.1 Rotation . . . 199
8.2.2 Rotation in Stellar Models . . . 201
8.2.3 Rotation and Mass-Luminosity Relations . . . 202
8.2.4 Degenerate Solutions and Rotation with Varied Masses . . . 204
8.2.5 Wind Mass Loss . . . 206
8.3 Millicharged Particles . . . 208
8.3.1 Existing Constraints on Millicharged Particles . . . 208
8.3.2 MCP Models and Plasmon Decay . . . 210
8.3.3 Implementing mcp production in MESA . . . 211
8.4 Results . . . 213

9 Conclusions 218

Appendix 221
A Possible Inflaton Potentials for Multimodal PBH Distributions . . . 221
B GW Spectrum for a Smoother Power Spectrum . . . 223
C Models of Baryon Asymmetry Production from X Decay . . . 226

C.1 Model 1: Multiple (≥ 2) Flavors of Gauge Singlets X_α 226
C.2 Model 2: Multiple (≥ 2) Flavors of Iso-singlet Color Triplets X_α 227
D Constraints from $12M_\odot$ Models: Prospects and Challenges 229
E General Comments on Post-Blue Loop Evolution 231
F Inlist & Axion Code for: Blue Loops, Cepheid, and Foray into Axions 233
F.1 Inlists 233
F.2 Run Star Extras for Axion Code 242
G Inlist and Plots for: Millicharged Particles, Blue Loops, and the Cepheid Mass Discrepancy Problem 251
G.1 Inlists 251
G.2 Extra Plots for mcp paper 260

List Of Tables

7.1 Numerical values of the function $G(y_0, y_1)$ in Eq. 7.24. Each column corresponds to a different $\log y_0$, and each row corresponds to a different $\log y_1$. 159
7.2 This is the continuation of the above table. 159
7.3 Observed Cepheids with Determined Masses 179
7.4 The masses were determined from the following papers: [325, 326, 301, 327, 304, 328].The periods were obtained from [329] 179
7.5 S Mus: The mass and overshoot required to achieve $\log L/L_\odot = 3.54$ and effective temperature 5850 K in the HR diagram (red dot in Fig. 7.11). We have assumed that $g_{10} = 0$. 181
7.6 S Mus: The values of g_{10} for which the blue loop just disappears up to the red edge of the instability strip are reported, for the stellar properties listed in Table 7.5. 181

8.1 The table presents data on the mass and coupling constraints for mcps with masses of $9M_\odot$ and $10M_\odot$. The column titled "Blue Loop?" Describes whether the blue loop existed (yes) or was eliminated (no). (yes*) implies 5-9 $M_\odot$ masses where checked to see if blue loop existed. . . . 214

List Of Figures

1.1 Left: Depicts the formation of PBH in Friedmann-Walker background due to pressure gradients [14]. Right: Image from [15] depicting a drawing of the inflaton field versus the potential, showing periods of slow roll and ultra-slow roll inflation. 8

2.1 Figure from [54] Showing the interactions of the bullet cluster. The red regions represent X-rays emitted by the interacting gas, and the contours indicate the location of the majority of matter. A rotation plot of M33 from figure 6 of [53] using H1 data. Their model rotation curve is compared with the observed (black solid line). Dust rotation (long dashed), disk rotation (short dashed), and halo rotation. 17

2.2 Figure from [56] showing the fraction of PBHs that make up dark matter vs PBH mass. The fraction is defined by the ratio of PBH energy density Ω_{PBH} to dark matter energy density Ω_{DM}. Excluded regions are described in the text. The label A indicates the location of the mass range of PBHs that comprise dark matter in this study. 19

2.3 The Primakoff effect, where an axion is produced through the interaction of a real photon with a virtual photon in the stellar plasma [60]. 21

2.4 Constraints on axion mass and photon coupling [62]. 22

2.5 Bounds on the fractional charge of MCPs as a function of mass, adapted from [63]. 23

3.1 *Top-left panel*: Contours of β are drawn on the $(m_X, M_{\rm PBH})$ plane requiring the observed value of Y_B in the radiation-dominated case ($\beta < \beta_c$). We use the value $\gamma_{CP} = 10^{-2}$. The black lines show the initial abundance of PBHs that can explain the baryon asymmetry of the Universe without giving rise to an early matter-dominated era ($\beta < \beta_c$). The light gray area corresponds to $m_X < T_{\rm PBH}$ while the dark gray area marks the region in which $m_X > T_{\rm PBH}$. The white region corresponds to $\beta > \beta_c$ and a PBH-dominated era. The pink region is ruled out due to the requirement $m_X > T_{\rm eva}$, needed to avoid washout. *Top-right panel*: Contours of m_X are drawn on the $(\beta, M_{\rm PBH})$ plane requiring the observed value of Y_B in the radiation-dominated case ($\beta < \beta_c$). We use the value $\gamma_{CP} = 10^{-2}$. The different colors show the values of different choices of m_X. The gray dashed line marks β_c. *Bottom panel*: The parameter space on the plane of $M_{\rm PBH}$ vs. m_X that can produce the correct Y_B in a radiation-dominated cosmology, for different value of γ_{CP}. Each lighter shade of blue is a superset that also includes the deeper colors with smaller values of γ_{CP}. The dependence on γ_{CP} is discussed in the main text. Regions that are ruled out due to washout or that feature a PBH-dominated cosmology are indicated. We display PBH masses $M_{\rm PBH} \lesssim 10^{-5}$ g for illustrative purposes: to indicate the regime where especially small values of γ_{CP} are operational. 40

3.2 Black line shows $M_{\rm PBH}$, as a function of m_X, that explains observed value of Y_B (for $\gamma_{CP} = 10^{-2}$) when PBHs come to dominate the energy density of the Universe before their evaporation ($\beta \geq \beta_c$). Along the gray dashed line we have $m_X = T_{\rm PBH}$. The pink region is excluded to evade washout by requiring $m_X > T_{\rm rh}$. 41

3.3 *Left panel:* The energy density of GWs as a function of the frequency, for three different values of $M_{\rm PBH}$: 10^2 g (red), 10^3 g (blue), and 10^4 g (green). The observed value of Y_B is obtained for each curve, with $\gamma_{CP} = 10^{-2}$ and $m_X < T_{\rm BH}$. The details of the calculation are in the text. *Right panel:* The strain h_c is shown as a function of the frequency for the three values of $M_{\rm PBH}$ from the left panel. The orange shaded regions show the future sensitivity limit of the high frequency GW probe using the inverse Gertsenshtein effect proposed in [113]. The dark orange shade is a conservative projection of the sensitivity, while the light orange shade is an optimistic projection. 44

3.4 The strain at the peak frequency for high frequency GWs coming from light PBHs, as a function of the peak frequency (lower x-axis) and as a function of the light PBH mass (upper x-axis). The orange shaded regions show the future sensitivity limit of the high frequency GW probe using the inverse Gertsenshtein effect proposed in [113]. The darker orange region is a conservative projection of sensitivity, while the lighter orange region is an optimistic projection. 45

3.5 *Left panel:* The strain at the peak frequency for benchmark models of $m_X = 10^{13}$ GeV and different values of $\gamma_{CP} = 10^{-2}$ (red), 10^{-3} (cyan) and 10^{-4} (purple). The vertical dashed lines show the $f_{\rm GW}^{\rm peak}$ regions where successful baryogenesis can take place in a radiation-dominated universe. *Right panel:* The strain at the peak frequency for a benchmark model of $m_X = 10^4$ GeV and $\gamma_{CP} = 10^{-2}$. Note that a large γ_{CP} value is required for baryogenesis when m_X is small, as is shown in the bottom panel of Fig. 3.1. 46

3.6 *Left panel*: The initial abundance of HPBHs, β_H, as a function of the HPBH mass, assuming that HPBHs can explain all the observed abundance of DM. *Right panel*: The different options for the formation of HPBHs are displayed. The segment in red denotes a phase of LPBH (matter) domination. $k_{H,1}$, $k_{H,2}$, and $k_{H,3}$, denote, respectively, the cases when HPBHs are formed prior to, during, and after the LPBH dominate the energy density of the Universe. 57

3.7 The relative amplitude of cross term contribution to P_h as a function of wave numbers of two scalar modes. 57

3.8 *Left panel*: A benchmark GW spectrum from scalar perturbation modes. In the sub-Hz region, we show the GW radiation from perturbations that generated heavy PBH distributions peaked at $M_H = 10^{18}$ g. In the high-frequency region, we show the GW radiation from perturbations generating lighter PBHs at $M_L = 10^3$ g with initial abundance calculated assuming $m_X < T_{\rm BH}$. Sensitivities of future GW observatories are shown with black dashed curves. *Right panel*: The Signal-to-Noise Ratio of second order GW signals at the low frequency peak for future detectors like BBO (green) and DECIGO (blue). The observation time is assumed to be one year. The $M_{\rm PBH}$ is the peak mass of the heavy PBH species that make up 100% DM relic abundance. 58

4.1 The PBH mass function generated by the FOPT formation mechanism. *Upper left panel:* The dependence on $T_\star$. FOPT temperatures are chosen $T_\star = 10^{14}$ GeV (blue), 10^{15} GeV (red) and 10^{16} GeV (green), while $\beta/H_\star = 1.1$ is fixed. The peak location of $\beta_{\rm PBH}$ is determined by $T_\star$ and the abundance is relatively unchanged. *Upper right panel:* The dependence on $\beta/H_\star$. The FOPT temperature is $T_\star = 10^{15}$ GeV. The range of $\beta_{\rm PBH}$ around the peak is shown for $\beta/H_\star \in [1.0, 1.8]$. The PBH formation is suppressed with a larger β. *Lower panel:* The PBH abundance at peak location $R_\star/H_\star^{-1} = 1.5$ with varying $\beta/H_\star$ values. The PBH formation rate is very sensitive to the increase of the nucleation rate. 79

4.2 The relation between the FOPT temperature $T_\star$ (black) and the Hawking temperature $T_{\rm PBH}$ (red) of PBHs formed during a FOPT at $T_\star$, assuming the initial pocket radius is $R_\star = 1.5H_\star^{-1}$. The blue shaded region indicates that the ψ particle mass in the true vacuum should at least be above the black curve such that it can be trapped inside the false vacuum pocket. For $T_\star \lesssim 10^{18}$GeV, the PBH Hawking temperature is always smaller than m_ψ. 80
4.3 The PBH mass function generated by primordial perturbations. *Upper left panel:* The dependence on k_p. The scales of the fluctuation are chosen $k_p = 10^{21}$ Mpc^{-1} (blue), 10^{22} Mpc^{-1} (red) and 10^{23} Mpc^{-1} (green), while the amplitude $A_\zeta = 10^{-1.6}$ is fixed. The peak location of $\beta_{\rm PBH}$ is determined by k_p and the abundance is unchanged. *Upper right panel:* The dependence on A_ζ. The peak k-mode is $k_p = 10^{22}$ Mpc^{-1}. The range of $\beta_{\rm PBH}$ around the peak is shown for $A_\zeta \in [10^{-2.5}, 10^{-1.5}]$. *Lower panel:* The PBH abundance at peak location with varying A_ζ values. The PBH formation rate drops quickly when the variance of the density contrast distribution becomes smaller than the formation threshold. . . 81
4.4 Contours of $\beta_{\rm PBH}$ on the plane of $M_{\rm PBH}$ vs. m_χ after requiring $\Omega_\chi h^2 = 0.12$ from FOPTs (red) assuming $R_\star = 1.5H_\star^{-1}$, and from curvature perturbations (black). The black dashed curve show the PBH mass whose Hawking temperature is equal to the DM mass. Regions to the left of the black dashed curve means $m_\chi < T_{\rm PBH}$ and regions to the right of the black dashed curve means $m_\chi > T_{\rm PBH}$. For very light and very heavy DM masses, the relic abundance cannot be produced through Hawking radiation in a radiation-dominated Universe. These regions are shaded in blue for both mechanisms to indicate the early matter-dominated epoch. The upper bound on the PBH mass from BBN is shown in the purple shaded region. The lower bound on the PBH mass from cosmic microwave background (CMB) is shown in the orange shaded region. . 86
4.5 Same as Fig. 4.4, zoomed in on the contour $\beta_{\rm PBH} = 10^{-13}$ and requiring $\Omega_\chi h^2 = 0.12$ for the FOPT mechanism (red) and the curvature perturbation mechanism (black). We assume $R_\star = 1.5H_\star^{-1}$ for the red curve. 87
4.6 The peak frequency of ultra-high frequency GW spectra generated by sound waves during FOPTs (red) and induced by curvature perturbations (black), as a function of the PBH mass. The red curve is calculated with FOPT parameters $\alpha = 0.8$, $\beta/H_\star = 1.2$, and $v_w = 0.5$. 90

4.7 GW spectra for the case of producing $m_\chi = 1$ TeV and $\Omega_\chi h^2 = 0.12$ from light PBHs of mass $M_{\rm PBH} = 10^4$g (solid) and $M_{\rm PBH} = 10^2$g (dashed). GWs produced by sound waves during FOPTs are shown in red color, and GWs induced by curvature perturbations are shown in black color. The FOPT parameters are $v_w = 0.5$, $\alpha = 0.8$, and $\kappa \simeq 0.688$. *Left panel:* The GW density $\Omega_{\rm GW}$ as a function of the GW frequency. The current Planck 2σ constraint on GW contributions to $\Delta N_{\rm eff}$ is shown in the gray shaded region [211]. Future CMB-S4 2σ sensitivity is shown with the gray dashed curve [209]. *Right panel:* The characteristic strain h_c as a function of the GW frequency. The blue shaded regions show anticipated sensitivities of enhanced magnetic conversion detection using the inverse Gertsenshtein effect with conservative (dark blue) and optimistic (light blue) estimates. 92

4.8 The peak strain strength $h_c^{\rm peak}$ and the peak frequency $f_{\rm GW}^{\rm peak}$ of GW spectra generated in the FOPT mechanism (red) and the curvature perturbation mechanism (black) that produce the DM relic abundance during a radiation-dominated era with $m_\chi = 1$ TeV (left) and $m_\chi = 10^{15}$ GeV (right), and with varying $M_{\rm PBH}$. The FOPT parameters are $v_w = 0.5$, $\alpha = 0.8$, and $\kappa \simeq 0.688$. The induced GWs are calculated assuming the power spectrum has a finite width and there is no resonant amplification present for the induced GWs (see the text for explanation). The blue shaded regions show conservative (dark blue) and optimistic (light blue) sensitivity anticipations for future ultra-high frequency GW detection using the inverse Gertsenshtein effect. 94

5.1 The general scheme of recycled DM. **Left:** In very early Universe, a dark scalar field develops a vacuum expectation value (vev) and gives rise to a FOPT which is succeeded by formation of true vacuum bubbles. Dark sector particles, which are in kinetic equilibrium with the SM particles, are assumed to be massless in the false vacuum while they acquire a very large mass in the true vacuum. Therefore, they remain trapped in the false vacuum. **Middle:** False vacuum pockets (containing dark sector particles) that are large enough collapse into light PBHs and eventually evaporate before BBN to emit all the particles in the spectrum including dark sector particles. **Right:** The dark sector particles emitted by PBHs get diluted by the expansion of the Universe until today to explain the observed abundance of DM. 101

5.2 The trapping fraction $F^{\rm trap}$ as a function of m_d/T for different relative velocity of particle bulk motion in front of the bubble wall $\tilde{v} = 0$ (solid) and $\tilde{v} = 0.1$ (dashed). m_d denotes either m_χ or m_ϕ. The bubble wall velocity in the global plasma frame is shown in different colors $v_w = 0.5$ (blue) and $v_w = 0.2$ (red). 107

5.3 Pocket radius distribution for a fast FOPT, $\beta = 100H_\star$ (solid) and a slow one, $\beta = H_\star$ (dashed) when $v_w = 0.5$. 114
5.4 Lower bounds on $R_\star H_\star$ for $\alpha_\Lambda = 0.1$ and $v_w = 0.5$. For $\Lambda > 10^{16}\,\text{GeV}$ (yellow region) the dark sector drops out of kinetic equilibrium with the visible sector prior to the phase transition. Black solid lines show different values of $R_\star H_\star$. Within the red region, $R_\star H_\star$ becomes so small that the PBHs follow an extended mass function rather than a monochromatic one. The gray dashed contours are marked by different choices of Λ. 116
5.5 The PBH mass function for three different phase transition temperatures: $T_\star = 10^{14}\,\text{GeV}, T_\star = 10^{13}\,\text{GeV}$, and $T_\star = 10^{12}\,\text{GeV}$ as black solid, black dashed, and black dotted curves. The regions above the lower bound of PBH mass in Eq. (5.22) are shaded in red, green, and orange for the three benchmarks. The minimum $R_\star$ value for each benchmark is shown in the legend. The other parameters are set to be $\alpha_\Lambda = 0.1$, $v_w = 0.5$, $\beta = H_\star$, and $\Lambda = 10^{16}\,\text{GeV}$. 120
5.6 Value of the FOPT parameter β that generates the observed DM relic abundance is shown with solid curves. The curve colors correspond to the benchmarks used in Fig.5.5 for different FOPT temperatures. The vertical dashed curves delineate regions where the filtered DM abundance is smaller than the observed abundance. Regions to the left of the dashed curves are excluded. 125
5.7 Constraints on dark sector particles produced by PBH evaporation. **Left:** Dashed lines show the upper limits on β_{PBH} assuming PBHs evaporation explains all of the DM today. The orange and purple regions are excluded by constraints from the CMB and BBN, respectively. The dark gray region correspond to PBHs with an initial temperature larger than the mass of the DM particles. Within the light gray area, β_{PBH} is so large that it leads to an early matter-dominated era, and the abundance of DM particles produced by PBH evaporation is independent of β_{PBH}. Different colors of dashed contours correspond to different choices of $R_\star H_\star$: red, blue, and black for 0.1, 1, and 10 respectively. Solid lines with the same color show the region of the parameter space within which $50 \lesssim m/T_\star \lesssim 65$ and consequently the filtered component is suppressed. The left side of the red solid lines corresponds to $R_\star H_\star < 0.1$ which gives rise to an extended mass function for PBHs and is not compatible with the calculations in this study which are based on a monochromatic mass function for PBHs. On the right side of the black solid lines, the mass of the dark sector particles become closer to the Planck scale, and the validity of the portal model from the point of view of effective field theory becomes less reliable. **Right:** PBH mass as a function of $T_\star$ for different choices of $R_\star H_\star$. 128

6.1 The evolutionary track of a non-rotating 8 $M_\odot$ MESA model. Included are important evolutionary stages of the star and instability strips defined in MESA. The $L_\odot$ is the solar luminosity. The metallicity is set to $Z = 0.014$ and the overshoot to $\alpha_{\rm ov} = 0.0$. 135

7.1 Evolutionary tracks for two different axion couplings $g_{10} = 0$ (left panel) and $g_{10} = 2$ (right panel) for a mass range of $4-10$ $M_\odot$. The metallicity is set to $Z = 0.014$ and the overshoot to $\alpha_{\rm ov} = 0.1$. 163
7.2 Evolutionary tracks of a 6 $M_\odot$ model for $g_{10} = 0$ (black), $g_{10} = 1$ (red), and $g_{10} = 2$ (green). "A" denotes the beginning of the blue loop (where $\mathrm{Log}\, T_{\rm eff} \sim 3.605$), "C" the bluest point with the maximum effective temperature, "E" the end, while the locations of "B" and "D" are determined by taking the average age of the star between "A" and "C", and "C" and "E", respectively. The metallicity is set to $Z = 0.014$ and the overshoot to $\alpha_{\rm ov} = 0.1$. 164
7.3 Top panel: The helium core radius as a function of the stellar age for a 6 $M_\odot$ model. The axion couplings are $g_{10} = 0$ (black), $g_{10} = 1$ (red), and $g_{10} = 2$ (green). "A" denotes the beginning of the blue loop (where $\log T_{\rm eff} \sim 3.605$), "C" the bluest point with the maximum effective temperature, "E" the end, while the locations of "B" and "D" are determined by taking the average age of the star between "A" and "C", and "C" and "E", respectively. Bottom panel: The stellar radius as a function of the stellar age for the same model. For both panels, the metallicity is set to $Z = 0.014$ and the overshoot to $\alpha_{\rm ov} = 0.1$. 165
7.4 The hydrogen mass fraction X profile of a 6 $M_\odot$ model before (top panel), during (middle panel) and after (bottom panel) the blue loop stage, for axion couplings $g_{10} = 0$ (black), $g_{10} = 1$ (red), and $g_{10} = 2$ (green). The metallicity is set to $Z = 0.014$ and the overshoot to $\alpha_{\rm ov} = 0.1$. 171
7.5 Core potential as a function of age for a 6 $M_\odot$ model with $g_{10} = 0$ (black), $g_{10} = 1$ (red), and $g_{10} = 2$ (green). Different evolutionary stages are labeled with "A" through "E," as depicted in Fig. 7.2. The metallicity is set to $Z = 0.014$ and the overshoot to $\alpha_{\rm ov} = 0.1$. 172
7.6 The axion energy loss rate from Eq. 7.4, as a function of the enclosed mass for a $6M_\odot$ (top) and $8M_\odot$ model (bottom), for Stage "A" (blue), during the transit through the instability strip (purple), and Stage "E" (red) of the blue loop stage. The axion coupling is $g_{10} = 1$. The metallicity is set to $Z = 0.014$ and the overshoot to $\alpha_{\rm ov} = 0.1$. 173
7.7 Core potential as a function of age for 5 $M_\odot$ (right), 6 $M_\odot$ (middle), and 8 $M_\odot$ (left) models with $g_{10} = 0$ (black), $g_{10} = 1$ (red), and $g_{10} = 2$ (green). The metallicity is set to $Z = 0.014$ and the overshoot to $\alpha_{\rm ov} = 0.1$. 174
7.8 Core potential of a 9 $M_\odot$ model for $g_{10} = 0.83$ (solid) and $g_{10} = 0.835$ (dashed). The metallicity is set to $Z = 0.014$ and the overshoot to $\alpha_{\rm ov} = 0.1$. 176

7.9 HR diagrams corresponding to the core potentials depicted in Fig. 7.8. The left panel corresponds to $g_{10} = 0.83$ while the right panel corresponds to $g_{10} = 0.835$. Both panels are for a 9 $M_\odot$ model. The metallicity is set to $Z = 0.014$ and the overshoot to $\alpha_{\rm ov} = 0.1$. 176
7.10 Values of the axion coupling g_{10} at which the blue loop just disappears, for models simulated in the current work (red dots). The purple line provides a linear fit. 177
7.11 Reproducing the observed luminosity of the Cepheid S Mus with a $6M_\odot$ model (black) and a $6.4M_\odot$ model (purple). The metallicity is set to $Z = 0.014$ and the overshoot to $\alpha_{\rm ov} = 0.1$ for both models. Axions are absent ($g_{10} = 0$). The red dot signifies the luminosity of S Mus $\log L/L_\odot = 3.54$ following the analysis of observational data performed by [331], while for the effective temperature we have taken the value quoted in [332]. 180
7.12 The constraints on the plane of $(g_{a\gamma\gamma}, m_a)$ for a fixed value of $Z = 0.014$, for three stellar models corresponding to the observed luminosity of S Mus: $6M_\odot$ with $\alpha_{\rm ov} = 0.2$ (green), $6.4M_\odot$ with $\alpha_{\rm ov} = 0.1$ (red) and $6.6M_\odot$ with $\alpha_{\rm ov} = 0.0$ (orange). These benchmark values are taken from Table 7.6. The results for a $9M_\odot$ model with $\alpha_{\rm ov} = 0.1$ (purple) are also displayed. The constraints on the coupling are obtained from the violation of Eq. 7.2. The range of m_a depicted by hatched regions corresponds to values smaller than the star's lowest core temperature (where the majority of axion production occurs), while the range shown by shaded regions is smaller than the lowest temperature across the entire stellar profile. We also show existing constraints from the stellar R-parameter (green) [294] and R_2-parameter (light green) [295], as well as astrophysical axion dark matter searches (blue, "Astro DM") [333, 334, 335, 336, 337, 338, 339]. The constraints are obtained from [62]. . 182
7.13 The behavior of the core potential for $\alpha_{\rm ov} = 0.0, 0.1$, and 0.2 with $g_{10} = 0$ (black) and the value of g_{10} that just eliminates the blue loop in each case (green). The results depicted here are for a $6M_\odot$ model. The metallicity is set to $Z = 0.014$. 186
7.14 The behavior of the core potential for $\alpha_{\rm ov} = 0.0$, 0.1, and 0.2 with $g_{10} = 0$ (black) and the value of g_{10} that just eliminates the blue loop in each case (green). The results depicted here are for a $8M_\odot$ model. The metallicity is set to $Z = 0.014$. 187
7.15 The hydrogen mass fraction X profile of a 6 $M_\odot$ model before (top panels), during (middle panels) and after (bottom panels) the blue loop stage. The axion coupling is set to $g_{10} = 0$ for the black curves. Left column: overshoot $\alpha_{\rm ov} = 0.0$ and $g_{10} = 0.295$ (green). Right column: overshoot $\alpha_{\rm ov} = 0.2$ and $g_{10} = 1.6$ (green). The metallicity is set to $Z = 0.014$. 189

7.16 Left panel: The constraints on the plane of $(g_{a\gamma\gamma}, m_a)$ for a $6M_\odot$ model with $\alpha_{\rm ov} = 0.0$ (orange), $\alpha_{\rm ov} = 0.1$ (purple), and $\alpha_{\rm ov} = 0.2$ (red). Right panel: Corresponding constraints for a $8M_\odot$ model. The constraints on the coupling are obtained from the violation of Eq. 7.2. The metallicity is set to $Z = 0.014$. 190

8.1 HR diagram showing evolutionary tracks for stellar masses 5–9 $M_\odot$. Black curves: non-rotating models; dashed green curves: rotating models with $\Omega/\Omega_{\rm crit} = 0.5$. 203

8.2 A plot of the Log of the luminosity vs mass of the star. Each line represents a Mass-Luminosity relation. Here, the Black solid line represents rotating models from our work; the black dashed line represents non-rotating models, and the Red solid and dashed lines represent literature fits from [377, 381]. The red dots represent observed Cepheids 205

8.3 HR-diagram of 6 $M_\odot$ models showing varied $\alpha_{\rm ov}$ and $\Omega/\Omega_{\rm crit}$ creating the same observations of S mus. Here the black curve corresponds to $\alpha_{\rm ov} = 0.2$, $\Omega/\Omega_{\rm crit} = 0$ (no rotation). The green curve correspond to $\alpha_{\rm ov} = 0.1$, $\Omega/\Omega_{\rm crit} = 0.5$. The red curve represents $\alpha_{\rm ov} = 0.2$ and $\Omega/\Omega_{\rm crit} = 0.5$. The inclusion of MCP emission shifts the rotating model below the observed luminosity of S Mus (red point), while the non-rotating model remains consistent. 207

8.4 Left panel: Left panel shows varied mass without rotation with mcps included (dashed green) and without mcps (Black). The MCPs charge and mass are listed on the plot. The right panel includes MCPS with $\Omega_{crit} = 0.5$ (Dashed green curve), and the black curve represents no MCPS and no rotation. Mcps in the case above are for on-shell only. . 213

8.5 HR diagram constraining mcp mass and charge. Black line is for m = 10eV and $q_{13} = 1.63$ and red line is for the same mass, but $q_{13} = 1.64$. 215

8.6 Mass-Luminosity plot similar to Figure 8.2, including no rotation and the mcps green dashed line, as well as the mcps solid line. The mcp mass was set 25 eV and charge $q_{13} = 2 \times 10^{-13}$ for models 5-8$M_\odot$ and $q = 1.6 \times 10^{-13}$ for model 9$M_\odot$ 216

A.1 *Top-left panel*: Example power spectrum with k^4 scaling and peaks located at $k = 10^{21}$ Mpc^{-1} corresponding to $f_{\rm GW}^{\rm peak} = 1.5$ MHz. The corresponding PBH masses is $M_{\rm PBH} = 10^4$ g. The amplitude of the power spectrum is chosen for the abundance of PBHs. *Top-right panel*: The PBH mass function at formation time. *Bottom-left panel*: The energy density of induced GW signal. *Bottom-right panel*: The strain strength of induced GW signal. 225

A.2 The constraints on the plane of $(g_{a\gamma\gamma}, m_a)$ for a fixed value of $\alpha_{\rm ov} = 0.1$, $Z = 0.014$, and three stellar models: $6M_\odot$ (red), $9M_\odot$ (purple), and $12M_\odot$ (orange). The constraints on the coupling are obtained from the violation of Eq. 7.2. The range of m_a depicted by hatched regions corresponds to values smaller than the star's lowest core temperature (where the majority of axion production occurs), while the range shown by shaded regions is smaller than the lowest temperature across the entire stellar profile. The constraints from the $12M_\odot$ model are obtained from Eq. 7.28 and correspond neither to an actual observed candidate with dynamically determined mass, nor to a simulation. We also show existing constraints from the stellar R-parameter (green) [294] and R_2-parameter (light green) [295], as well as astrophysical axion dark matter searches (blue, "Astro DM") [333, 334, 335, 336, 337, 338, 339]. The constraints are obtained from [62]. 230
A.3 Log central temperature vs Log central density for a $6M_\odot$ model. Burning bounds are extrapolated from `MESA`'s pgstar plots. 232
A.4 Zoomed in of Fig. A.3. Symbols are discussed in the text. 233
A.5 An HR - diagram showing various α_{ov} with mcps mass and charge value set to lower the model value by % 10 of the luminosity. fixed rotation at 0.5 261
A.6 HR-diagram depicting the mass boundies of smus lower of 5.6 left and 6.4 right. Solid curves represent no MCPs and dashed curves include mcps with $q = 2.9 \times 10^{-13}$ and $m_\chi = 25$eV. Black, Red, and Blue curves corresonds to values of the overshoot set to $\alpha_{ov} = 0.0$, $\alpha_{ov} = 0.1$, and $\alpha_{ov} = 0.2$, respectivly. Horizontal blue-dashed line indicates 90% of Smus observed luminosity. 262
A.7 Left panel: Right panel: $m_\chi = 25eV$, Possibly add mass to figure as a string. Emphasize that the decay is on-shell only. 262

Abstract

This thesis studies two categories of objects that are relevant for studies of dark matter: primordial black holes (PBHs) and axions. (1) PBHs may be relevant to the origin of dark matter and the matter-antimatter asymmetry of the Universe. We study two different scenarios in which light PBHs disappear through Hawking evaporation, producing (*i*) dark matter and a beyond-Standard Model particle that decays to produce baryon asymmetry; and (*ii*) an ultra-heavy dark sector consisting of two or more species. These scenarios use a combination of first-order phase transitions and scalar curvature perturbations to produce PBHs. Both formation mechanisms can create a gravitational wave background in the (MHz-GHz) regime. (2) We also study axions, which can cause anomalous energy loss in Cepheid variables through their production in the stellar core and subsequent escape. We find that the elimination of the blue loop stage for Cepheids can provide bounds on the axion-photon coupling $g_{a\gamma\gamma}$. The bounds are found to be sensitive to the mass of the Cepheid and the modeling of the convection. The more massive the Cepheid, the stronger the resulting constraints on the axion-photon coupling. We also conduct a study of the effect of millicharged particles on the evolution of Cepheids, using the mass discrepancy problem to constrain the fractional charge of millicharged particles.

Chapter 1

Introduction to Primordial Black Holes

1.1 Motivation

Physics projects can often take the shape of a story, with a thrilling beginning, exciting calculations, and an ending that shows new ways of understanding nature. We hope that the reader enjoys the physics presented and the stories we created with primordial black holes and axions.

Story 1 goes as follows: primordial black holes (PBHs) form from either a first-order phase transition (FOPT) or a scalar perturbation. The mass and abundance of PBHs depend on the particle physics model and the properties of the FOPT or the amplitude of scalar perturbations. Light PBHs formed in this manner can evaporate away after formation to generate baryogenesis (Chapter 3) or produce dark matter (Chapter 4-5).

Story 1 is thus motivated by a set of questions: the origins of dark matter, baryogenesis, and the question of why there is ~ 5 more dark matter than matter. Since curvature perturbations or FOPTs also give rise to gravitational waves in the MHz-GHz regime, Story 1 connects dark matter physics and baryogenesis with the physics of high frequency gravitational waves, an exciting future observational frontier.

Story 2 involves the study of particle physics with populations of stars that are either on the tip of the red giant branch or the horizontal branch (blue loop stage of Cepheids in our case). The production of a beyond-Standard Model (BSM) species in the star, such as the axion or a millicharged particle, introduces a new form of energy

loss. This leads to changes in stellar evolution that can give rise to anomalous effects at the population level, such as the luminosity of the tip of the red giant branch or the complete elimination of the horizontal branch. Observations of stellar populations then impose constraints on the coupling and mass of the BSM species.

These two stories motivate the organization of our work into two parts. Part I (Chapters 1-5) involves PBHs, gravitational waves, and BSM particle production from PBHs. Part II (Chapters 6-8) relies on stellar evolution of Cepheid variables as a way to constrain BSM physics. Chapters (1-2) provide an introduction to Part I, while Chapter 6 provides an introduction for Part II. We conclude this work with a summary of results and possible future projects in Chapter 9.

1.2 Introduction

The following five chapters use PBHs as a probe of two problems in phenomenology: the origin of the antimatter-matter asymmetry and the origin and identity of dark matter. This chapter provides an introduction to PBHs, beginning with their history, their production, and subsequent evaporation.

Black holes (BHs) were first theorized by Karl Schwarzschild, who, in 1916, solved Einstein's field equations and discovered that for a given mass M, an object could possess an event horizon from which light cannot escape. Almost a century later, the first image of a BH, *the supermassive black hole in M87*, was captured by the Event Horizon Telescope collaboration in 2019 [1]. A possible formation mechanism for BHs involves the gravitational collapse of a massive star at the end of its life cycle. These stellar-mass black holes typically have masses ranging from a few to several tens of solar masses. However, observational constraints suggest that stellar black holes cannot account for the observed dark matter abundance, disqualifying them as viable

dark matter candidates. PBHs, in contrast, can span a vastly wider mass range and number density and are thus capable of explaining both the origin and composition of dark matter.

PBHs were first proposed in 1966 by Yakov Zel'dovich and Igor Novikov. Their existence was initially challenged by an argument involving Bondi accretion, which claimed that PBHs would quickly accrete matter and grow to the size of the cosmological horizon, thus acquiring masses too large to be consistent with observational constraints. However, it was later understood that cosmic expansion invalidates this argument, preventing such runaway growth. In 1971, Stephen Hawking conducted more detailed studies of PBHs, laying the groundwork for future research. Since the 2015 discovery of gravitational waves by the LIGO and Virgo collaborations, interest in PBHs has surged, and they have become the subject of extensive recent literature.

As the name suggests, PBHs are thought to form in the early universe and span a much broader mass spectrum than their stellar counterparts. Their mass can be estimated as a function of cosmic time t, as shown in [2]:

$$M \sim \frac{c^3 t}{G} \sim 10^{15} \left(\frac{t}{10^{-23} s} \right) \mathrm{g} \tag{1.1}$$

Here, G is Newton's gravitational constant, t is the age of the Universe, and c is the speed of light.

According to Eq. 1.1, at Planck time ($t \sim 10^{-43}\,\mathrm{s}$), the corresponding PBH mass would be roughly the Planck mass, $M \sim 10^{-5}\,\mathrm{g}$. At later times, e.g., $t \sim 1\,\mathrm{s}$, PBHs would form with masses around $10^5\,M_\odot$, indicating the vast mass range of possible PBHs.

PBHs can thus be divided into two broad categories:

- Low-mass PBHs ($M_{\rm PBH} \lesssim 10^{15}\,{\rm g}$) that have fully evaporated via Hawking radiation by today, and
- High-mass PBHs ($M_{\rm PBH} \gtrsim 10^{15}\,{\rm g}$) that are long-lived and potentially stable dark matter candidates.

This chapter focuses on particle production from evaporating PBHs. We leave a discussion of PBHs as dark matter candidates for the end of Chapter 2.

PBHs can form in the early universe from scalar perturbations, FOPTs, moduli, cosmic strings, domain walls, and quantum diffusion. For more possible scenarios and a description of each, please see [3]. Our formulation utilizes FOPTs and scalar perturbations in the process of PBH formation. The existence of gravitational waves, confirmed through the 2015 detection of black hole mergers by the LIGO and Virgo collaborations [4], has opened new possibilities for probing PBHs. Both models we consider predict the generation of a stochastic gravitational wave background (SGWB) in the MHz-GHz frequency range. The derivations and implications of such high-frequency gravitational waves are presented in this chapter.

1.3 PBH Evaporation

Stephen Hawking studied the quantum properties of black holes and determined that they possess a temperature that scales inversely with mass ($T \sim \frac{1}{M}$) and evaporate over time [5], a process now called Hawking evaporation. This is a beautiful combination of quantum physics, thermodynamics, and gravity. Hawking evaporation from PBHs has not been experimentally observed, but there are proposed observations that can be done to prove the existence of PBHs and their associated evaporation. An important method of searching for PBHs is to look for observational evidence of particles coming from them as they Hawking evaporate. This can include electron-positron

pairs, extra-Galactic gamma rays, and effects on the cosmic microwave background (CMB) and Big Bang Nucleosynthesis (BBN) [6, 7, 8, 9]. The absence of anomalies in these frontiers restricts the mass range and abundance of PBHs. Even with these constraints, however, PBHs that Hawking evaporate are extremely useful for both theory and phenomenology.

We now turn to the formal derivation of Hawking radiation from black hole producing a BSM particle. Using the Friedmann equations, Hawking radiation, and the properties of the early Universe, one can determine the production of some generic BSM particle from PBHs. Throughout this work we use natural units ($\hbar$, c, k_b, and G equal 1).

The energy density of radiation having $g_\star(T)$ relativistic degrees of freedom sharing the same temperature T is given by

$$\rho_{\rm rad}(T) = \frac{\pi^2}{30} g_\star(T) T^4, \tag{1.2}$$

and the Hubble expansion rate follows from the Friedmann equation as:

$$H^2(T) = \frac{8\pi}{3M_{\rm Pl}^2} \rho_{\rm rad}(T). \tag{1.3}$$

If PBHs form within this era at some formation time denoted by t_i, then the mass of PBHs is proportional to the horizon mass at that time, i.e.,

$$M_{\rm PBH} = \frac{4\pi}{3} \gamma \rho_{\rm rad}(T_i) H^{-3}(T_i), \tag{1.4}$$

where $\gamma \sim \omega^{3/2} \approx 0.2$, where $\omega = p/\rho$ is the equation of state parameter. The temperature of the Universe at formation time, therefore, can be expressed as:

$$T_i(M_{\rm PBH}) = \frac{\sqrt{3}\,5^{1/4}}{2\pi^{3/4}}\sqrt{\gamma}\frac{1}{g_\star^{1/4}(T_i)}\frac{M_{\rm Pl}^{3/2}}{\sqrt{M_{\rm PBH}}}. \tag{1.5}$$

The Planck mass in natural units is $M_P \sim 1.22 \times 10^{19}\,{\rm GeV}$ or $2.2 \times 10^{-5}{\rm g}$; both values are used throughout this work [10]. PBHs lose their mass by Hawking evaporation [11] during which they emit particles that are lighter than their instantaneous horizon temperature given by:

$$T_{\rm PBH}(t) = \frac{M_{\rm Pl}^2}{8\pi M_{\rm PBH}(t)}. \tag{1.6}$$

The lifetime of a PBH, $\tau_{\rm PBH}$, with initial mass $M_{\rm PBH}$ can be shown [12] to be equal to:

$$\tau_{\rm PBH} = \frac{10240\pi}{g_\star(T_{\rm PBH})}\frac{M_{\rm PBH}^3}{M_{\rm Pl}^4}. \tag{1.7}$$

Since in a radiation-dominated Universe, $H(t) = 1/(2t)$, by combining Friedmann equation with the lifetime of PBHs, one can obtain the temperature of the Universe at their evaporation time as:

$$T_{\rm eva} = \frac{\sqrt{3}\,g_\star^{1/4}(T_{\rm PBH})}{64\sqrt{2}\,5^{1/4}\pi^{5/4}}\frac{M_{\rm Pl}^{5/2}}{M_{\rm PBH}^{3/2}}. \tag{1.8}$$

The evolution of a PBH mass with the initial value of $M_{\rm PBH}(t_\star)$ at the formation time $t = t_\star$ is given by:

$$M_{\rm PBH}(t) = M_{\rm PBH}(t_\star)\left(1 - \frac{t - t_\star}{\tau_{\rm PBH}}\right)^{1/3}, \tag{1.9}$$

where

$$\tau_{\rm PBH} = \frac{10240\pi}{g_\star(T_{\rm PBH})}\frac{M_{\rm PBH}^3(t_\star)}{M_{\rm Pl}^4}, \tag{1.10}$$

denotes the lifetime of the PBH, and $g_\star(T_{\rm PBH})$ is the number of relativistic degrees of freedom at temperature $T_{\rm PBH}$ for the Hawking radiation process.

Ignoring the deviation of the Hawking radiation from the black body spectrum, which is expressed as greybody factors [13], the rate of emission of the ith particle per energy interval is related to the Hawking spectrum as:

$$\frac{d^2N_i}{dtdE} = \frac{4\pi r_{\rm S}^2}{E}\frac{d^2u_i}{dtdE}, \tag{1.11}$$

where $r_{\rm S} = 2M_{\rm PBH}/M_{\rm Pl}^2$ is the Schwarzschild radius of the PBH. The total number of bosonic (B) ith particles, emitted by one PBH is obtained as:

$$N_i = \frac{120\,\zeta(3)}{\pi^3}\frac{g_i}{g_\star(T_{\rm PBH})}\frac{M_{\rm PBH}^2(t_\star)}{M_{\rm Pl}^2}, \qquad T_{\rm PBH}(t_\star) > m_i, \tag{1.12}$$

$$N_i = \frac{15\,\zeta(3)}{8\pi^5}\frac{g_i}{g_\star(T_{\rm PBH})}\frac{M_{\rm Pl}^2}{m_i^2}, \qquad T_{\rm PBH}(t_\star) < m_i. \tag{1.13}$$

Here $\zeta(3)$ is the Riemann-Zeta function, and g_i is the relativistic degrees of freedom for particle i. The total number of fermionic species (F) is $N_F = \frac{3}{4}\frac{g_F}{g_B}N_B$.

This formalism will be applied in subsequent chapters to the production of Standard Model particles, dark sector species, and a BSM species X responsible for baryogenesis.

1.4 PBH Formation

In the introduction, we described two formation processes for PBHs relevant for our studies: scalar curvature perturbations and FOPTs. In the scalar perturbation scenario, PBHs are created due to a period of ultra-slow-roll inflation with an inflaton ϕ (in other words, the inflaton potential $V(\phi)$ is nearly flat, as shown in Figure 1.1). In the FOPT scenario, a scalar particle ϕ (not necessarily the inflaton) acquires a vacuum

expectation value (vev) and the FOPT leads to the nucleation of true vacuum pockets. PBHs are formed by true vacuum bubbles forcing the false vacuum into pockets equal to the Schwarzschild radius, leading to their collapse into a PBH. This is discussed in more depth in section 1.4.2.

1.4.1 Scalar Perturbations

PBH formation from primordial scalar perturbations has been studied in [16, 17, 18, 19, 20, 21, 22, 23, 24, 25, 26, 27]. These perturbations can be generated during the inflation era when a temporary ultra slow-roll phase [28, 29, 30, 31, 32, 33] enhances the curvature perturbation. These primordial fluctuations are frozen at super-horizon scales after they are generated during inflation and enter the causal horizon at a later time as a result of the cosmic expansion. When the overdensity enters the horizon, the gravitational attraction could overcome the pressure and lead to the gravitational collapse of a proportion of the Hubble patch into a PBH, as depicted in Figure 1.1. A short review of inflationary scenarios that can give rise to PBH formation is given in Appendix 1. We note that large amplifications of the scalar power spectrum are constrained by CMB spectral distortions [34].

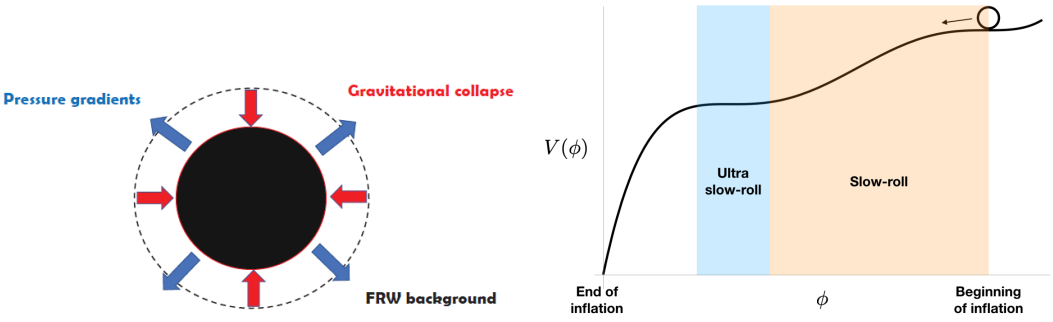


Figure 1.1: Left: Depicts the formation of PBH in Friedmann-Walker background due to pressure gradients [14]. Right: Image from [15] depicting a drawing of the inflaton field versus the potential, showing periods of slow roll and ultra-slow roll inflation.

The fraction of energy density collapsed into PBHs of mass $M_{\rm PBH}$ can be calculated from the fraction of Hubble patches that undergoes gravitational collapse in the existence of overdensities at the horizon size R. We assume the overdensities are generated by curvature perturbations $P_\zeta(k)$ from the inflationary epoch. At the re-entry time of a k-mode, $k = aH$, overdensities are generated at the scale $R = k^{-1}$ and the amplitude of the density contrast $\delta = \delta\rho/\rho$ is assumed to follow a Gaussian distribution. The black hole formation requires the local over-density surpasses a threshold value, i.e., $\delta > \delta_c$. The value of the threshold for a radiation-dominated Universe is $\delta_c \simeq \omega = 1/3$ [16]. We assume the distribution of δ in all patches is Gaussian:

$$p(\delta) = \frac{1}{\sqrt{2\pi}\sigma_0} e^{-\frac{\delta^2}{2\sigma_0^2}}. \tag{1.14}$$

The mean of the δ distribution is zero and the variance σ_0 can be calculated with

$$\sigma_0^2(k = R^{-1}) = \int_0^\infty \frac{{\rm d}k'}{k'} \frac{16}{81} (k'R)^4 W^2(k', R) P_\zeta(k'), \tag{1.15}$$

The variance is generated at a range of length scales $R \sim k_p^{-1}$ even if the curvature perturbation itself is monochromatic at k_p. This is because fluctuations are coarse-grained averaged with the window function

$$W(k, R) = \exp\left[-\frac{(kR)^2}{2}\right]. \tag{1.16}$$

Note that large variance is also generated at neighboring scales of an enhanced curvature perturbation mode as a result of the integral in Eq.(1.15). The window function suppresses contributions from perturbations at much smaller length scales. We define the abundance of PBHs in the same way as used in the FOPT case. Moreover, we assume the fraction of the energy density collapsed into the PBH is $\gamma = 0.2$.

Gravitational collapse into a PBH happens in patches where the overdensity δ is larger than the threshold δ_c. We take $\delta_c = 1/3$ when the energy density of the Universe is dominated by radiation. The number density of PBHs can be calculated by evaluating the probability of a Hubble patch having $\delta > \delta_c$ at the horizon re-entry time. The fraction of patches that collapse into PBHs is

$$\begin{aligned} \frac{n_{\rm PBH}}{n_{\rm patch}} &= \int_{\delta_c}^{\infty} d\delta \, \frac{1}{\sqrt{2\pi}\sigma_0} e^{-\frac{\delta^2}{2\sigma_0^2}} \\ &= \frac{1}{2} \, {\rm Erfc}\left(\frac{\delta_c}{\sqrt{2}\sigma_0}\right). \end{aligned} \tag{1.17}$$

We further assume that a fraction γ of the horizon mass will become the final PBH mass. The horizon mass can be expressed as:

$$M_R = 2 \times 10^4 \ {\rm g} \left(\frac{k}{10^{21} \ {\rm Mpc}^{-1}}\right)^{-2}. \tag{1.18}$$

Since $M_{\rm PBH} = \gamma M_{R=k^{-1}}$ then the PBH Mass is

$$M_{PBH} = 4 \times 10^{-3} \ {\rm g} \left(\frac{\gamma}{0.2}\right) \left(\frac{k}{10^{21} \ {\rm Mpc}^{-1}}\right)^{-2}. \tag{1.19}$$

The number density is equal to the number density of horizon patches that have large enough density contrasts for them to undergo gravitational collapse, $n_{\rm PBH} = n_{\rm patch}|_{\delta > \delta_c}$, which can be calculated by integrating the Gaussian distribution from δ_c to infinity. The mass function at the formation time $t = t_i$ can be written as:

$$\begin{aligned} \beta_{\rm PBH} = \frac{d\beta(M, t_i,)}{d \log M} &= \frac{M_{\rm PBH} \, n_{\rm PBH}}{M_R \, n_{\rm patch}} \\ &= \frac{\gamma}{2} {\rm Erfc}\left(\frac{\delta_c}{\sqrt{2}\sigma_0}\right). \end{aligned} \tag{1.20}$$

The final step is to define the power spectrum with an amplitude A_ζ and the peak location k_0 which will determine the PBH mass spectrum. This will also change the variance σ_0. Different power spectrums are presented in Chapters 3. In chapter 4 A_ζ is not constant, but changes with the PBH abundance.

1.4.1.1 Gravitational Waves from Scalar Perturbations

We will also be interested in the stochastic gravitational wave background (SGWB) created from the two PBH formation processes discussed previously. The SGWB, if observed, will play a crucial role in probing the early Universe. Currently, our knowledge of the early Universe comes from photons; for example, we use observations of the CMB, which permeates the Universe, to investigate the universe up to 10^5 years after the Big Bang. Close inspection of the primordial fluctuations of the CMB can provide even deeper insights into the early universe and offer new constraints of the inflationary epoch ($\sim 10^{-33}$ seconds after the Big Bang); however, this information is still based on observations of photons. Since gravitons are weakly coupled to the Standard Model compared to neutrinos and photons, the SGWB may provide a new direct window for observations of phenomena before BBN and after inflation, for example possible FOPTs, gauge group breaking, reheating and preheating, etc.

In Chapter 3, we study the induced second order tensor perturbations coming from scalar perturbations during an era of PBH formation. The induced gravitational waves generate an SGWB that is then tied to the subsequent signatures of the produced PBHs, providing a multi-messenger handle on models. Multimessenger studies can then be proposed for current and future detectors, such as pulsar timing arrays (PTAs), NANOGrav, next generation interferometers (advanced LIGO (aLIGO) Virgo, KAGRA) [35].

We follow [36, 37, 38] for the calculation of induced gravitational waves from scalar perturbations. The energy density of GWs normalized to the critical density per logarithmic k interval at a conformal time η is given by

$$\Omega_{\rm GW}(\eta,k) = \frac{1}{24}\left(\frac{k}{a(\eta)H(\eta)}\right)^2 P_h(\eta,k)\,. \tag{1.21}$$

The GW power spectrum can be written as

$$\begin{aligned} P_h(\eta,k) \;\simeq\; & 2\int_0^\infty dt \int_{-1}^1 ds \left(\frac{t(t+2)(s^2-1)}{(t+s+1)(t-s+1)}\right)^2 \\ & \times I^2(s,t,k\eta) P_\zeta(uk) P_\zeta(vk), \end{aligned} \tag{1.22}$$

where the dimensionless variables are $u = \frac{t+s+1}{2}$ and $v = \frac{t-s+1}{2}$. In a radiation-dominated Universe, perturbations decay quickly after horizon re-entry. The GWs are mostly produced at the re-entry time and evolve to constant values in the sub-horizon limit. Then the I^2 term can be written as

$$\begin{aligned} I^2(s,t,k\eta) \;=\; & \frac{288(s^2+t(t+2)-5)^2}{k^2\eta^2(t+s+1)^6(t-s+1)^6}\left(\frac{\pi^2}{4}\Big(s^2+t(t+2)-5\Big)^2\Theta(t-(\sqrt{3}-1)\Big)\right. \\ & +\Big(-(t+s+1)(t-s+1)+ \\ & \left.\frac{1}{2}(s^2+t(t+2)-5)\log\left|\frac{t(t+2)-2}{3-s^2}\right|\Big)^2\right), \end{aligned} \tag{1.23}$$

where $\Theta(.)$ is the Heaviside function.

The GW density today $\Omega_{\rm GW,0}$ can be calculated by red-shifting GWs together with other radiations from a time η_s when the GWs stop growing and become a fixed fraction of the total radiation energy density $\Omega_{\rm rad}$,

$$\begin{aligned}
\Omega_{\rm GW,0}(k) &= \Omega_{\rm rad,0}\,\frac{\Omega_{\rm GW}(\eta_{\rm eq},k)}{\Omega_{\rm rad,eq}} \\
&= 2\,\Omega_{\rm rad,0}\,\frac{H^2(\eta_s)\,a^4(\eta_s)}{H_{\rm eq}^2\,a_{\rm eq}^4}\,\Omega_{\rm GW}(\eta_s,k) \\
&= 2\,\Omega_{\rm rad,0}\,\frac{a^4(\eta_s)\,\rho_{\rm rad}(\eta_s)}{a_{\rm eq}^4\,2\,\rho_{\rm rad,eq}}\,\Omega_{\rm GW}(\eta_s,k) \\
&= \Omega_{\rm rad,0}\,\frac{a^4(\eta_s)\,g_\star(\eta_s)\,T^4(\eta_s)}{a_{\rm eq}^4\,g_{\star,\rm eq}\,T_{\rm eq}^4}\,\Omega_{\rm GW}(\eta_s,k) \\
&= \left(\frac{g_\star(\eta_s)}{g_{\star,\rm eq}}\right)\left(\frac{g_{\star,S}(\eta_s)}{g_{\star,S,\rm eq}}\right)^{-\frac{4}{3}}\,\Omega_{\rm rad,0}\,\Omega_{\rm GW}(\eta_s,k) \\
&= 0.83\left(\frac{g_\star(\eta_s)}{10.75}\right)^{-\frac{1}{3}}\,\Omega_{\rm rad,0}\,\Omega_{\rm GW}(\eta_s,k).
\end{aligned} \tag{1.24}$$

In the second line, we used $\Omega_{\rm rad,eq}=1/2$, $H^2=8\pi G\rho_{\rm rad}/3$ and $\rho_{\rm GW}\propto a^4$. In the fifth line, we used conservation of entropy $g_{\star,S,\rm eq}a_{\rm eq}^3T_{\rm eq}^3=g_{\star,S}(\eta_s)a^3(\eta_s)T^3(\eta_s)$. In the last line, we used $g_{\star,S,\rm eq}=3.91$, $g_{\star,\rm eq}=3.36$ and $g_\star(\eta_s)=g_{\star,S}(\eta_s)$. The energy density of radiation today is $\Omega_{\rm rad,0}=8.5\times10^{-5}$. The effective massless degrees of freedom $g_\star(\eta_s)$ at η_s is 106.75 for the PBH mass of our interest.

When the perturbation is monochromatic as defined in Eq.(4.29), the GW density at production time can be written as

$$\begin{aligned}
\Omega_{\rm GW}(k=rk_0) = \frac{3}{64}A_\zeta^2\,r^2\left(\frac{4-r^2}{4}\right)^2(2-3r^2)^2 \\
\times\left[\left(4+(3r^2-2)\log\left|\frac{3r^2-4}{3r^2}\right|\right)^2+\pi^2(3r^2-2)^2\Theta\left(\frac{2}{\sqrt{3}}-r\right)\right] \\
\times\Theta(2-r),
\end{aligned} \tag{1.25}$$

which is proportional to A_ζ^2. The $\Omega_{\rm GW}$ spectrum in Eq.(1.25) is scale-invariant, and its peak location is at $r \to 2/\sqrt{3}$ where the $\Omega_{\rm GW}$ divergence is cut off by $\Theta(\frac{2}{\sqrt{3}} - r)$. The GW density is proportional to the square of the power spectrum amplitude from the nature that GWs are induced at the second order in scalar perturbations.

1.4.2 First Order Phase Transitions

A first-order phase transition (FOPT) is characterized by a critical temperature, latent heat, and the coexistence of mixed phases. A simple example of a FOPT is a pot of boiling water; here, water acts as the medium, undergoing a transition from liquid to vapor [39]. FOPTs in the early universe typically involve a scalar field that undergoes spontaneous symmetry breaking at a specific temperature and acquires a nonzero vev. This leads to the nucleation of true vacuum bubbles, where symmetry is broken, transitioning the universe from a metastable equilibrium state to a stable equilibrium state. The formation of PBHs from FOPTs has a long history. The earliest mechanisms focused on PBH formation from the collision of bubble walls [40, 41, 42, 43, 44, 45]. Recent mechanisms have focused on the formation of PBHs by the collapse of matter or solitons in the false vacuum [46, 47, 48, 49, 50, 51].

The abundance of PBHs depends on the number of false vacuum pockets. The number of pockets depends on FOPT properties: the bubble wall velocity v_w, pocket radius $R_\star$, and length of the phase transition measured as the inverse time scale β. The initial pocket radius distribution has been studied for PBH formation in [51] with the requirement that a viable pocket should successfully shrink to form a PBH before the nucleation of new bubble seeds inside it. This is expressed as the following:

$$\frac{dn_{\rm pocket}}{dR_\star} \simeq \frac{I_\star^4\,\beta^4}{192\,v_w^3}\, e^{4\beta R_\star/v_w - I_\star\, e^{\beta R_\star/v_w}} \left(1 - e^{-I_\star e^{\beta R_\star/v_w}}\right). \tag{1.26}$$

Here $I_\star = -\ln 0.29 \simeq 1.238$. The number density of PBHs depends on the specific particle physics model. Different models change the PBH mass dependency as shown in both Chapters 4 and 5. The number of PBHs formed with a given mass depends on the probability of particles being trapped in the false vacuum. Particles with high momentum can pass through the bubble wall into the true vacuum, leading to a suppression of the number of PBHs of a given mass. FOPTs produce a SGWB discussed in the previous section. I refer the reader to Chapter 4 for a more detailed discussion of the SGWB from FOPTs.

1.5 Conclusion

This chapter introduced PBHs and their usefulness in probing the early Universe. PBHs have a variety of formation mechanisms, with the ones relevant for this work being curvature perturbations generated during inflation and FOPTs. Detailed derivations of particle production from Hawking radiation, as well PBH production from scalar perturbations, was provided. We also provided the calculation of second order induced gravitational wave. Arguably, the most crucial section of this chapter is the section on PBH evaporation, as it is used extensively in Chapters 3-5. A discussion of the observational bounds on Hawking evaporation was provided.

The next chapter provides a detailed discussion of dark matter, particularly its history, observational constraints, the popular candidates, and the candidates that we will study in this work.

Chapter 2

Dark Matter

This work focuses on BSM physics in the early and late Universe, with a particular emphasis on dark matter. It involves PBHs in the early universe while considering the effects of low-mass BSM particle production in Cepheid stars in the late universe. This chapter aims to provide the reader with an overview of dark matter, especially the dark matter candidates discussed in this work. The first section of this chapter offers a broad introduction to dark matter, while the following sections present possible candidates, provide evidence of their existence, and outline relevant constraints.

2.1 History, Observations, and Detection of Dark Matter

Zwicky first discovered the possible existence of dark matter [52] through the velocity dispersion of the Coma galaxy cluster. More recently, astronomers have used data, such as the observation of M33 [53], to obtain galaxy rotation curves and infer the existence of dark matter. Fig. 2.1 shows a rotation velocity plot vs galaxy radius for M33. The disk model data imply that $v \sim \frac{M(r)}{r^{1/2}}$ would appear for this spiral galaxy. The power law is expected for luminous matter in spiral galaxies, but it is not observed. The model data (solid line), which matches the observation (data points), can be reproduced if large amounts of non-luminous matter (dark matter) is included.

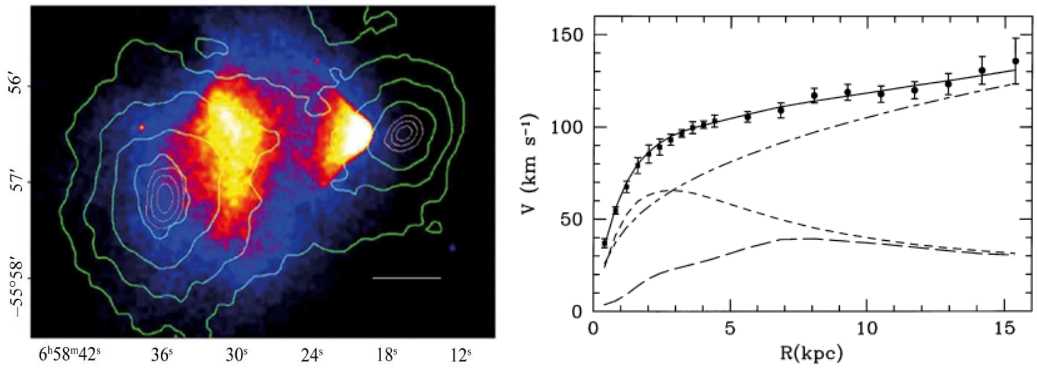


Figure 2.1: Figure from [54] Showing the interactions of the bullet cluster. The red regions represent X-rays emitted by the interacting gas, and the contours indicate the location of the majority of matter. A rotation plot of M33 from figure 6 of [53] using H1 data. Their model rotation curve is compared with the observed (black solid line). Dust rotation (long dashed), disk rotation (short dashed), and halo rotation.

The left panel of Fig. 2.1 shows X-ray observations of the bullet cluster taken with the Magellan telescopes. The galaxy clusters do not interact with each other, but the intercluster medium does. From the image, it is clear that the majority of matter in the galaxies, as indicated by the gravitational contours, did not collide with itself. This indicates that the dark matter of both galaxies interacts feebly with normal matter and with itself. An upper bound on the cross section of dark matter interacting with itself can be obtained. We note that other observations, such as the CMB power spectrum and gravitational lensing, also provide incontrovertible evidence for dark matter.

Observational evidence also provides the amount of dark matter in the Universe. It is useful to think of the matter density of the Universe to be divided into baryonic matter and dark matter. The corresponding densities for these two kinds of matter are given by Planck data [55], which shows that 80 % of the matter content of the Universe is dark matter.

Various scenarios have been modeled in particle physics to obtain the current abundance of particle dark matter. In the thermal freeze-out scenario, dark matter and

matter were in thermal equilibrium in the thermal bath, sharing the same temperature. As time progressed, dark matter decoupled from the thermal bath, leading to the relic abundance of dark matter we observe today (freeze-out). Various other scenarios have also been proposed, including so-called freeze-in, where dark matter only has extremely feeble couplings to the Standard Model, and was never in thermal equilibrium with visible matter.

There are numerous candidates for dark matter. Two of the most popular ones are motivated by two fine-tuning problems in the Standard Model: the axion (motivated by the strong CP problem in Quantum Chromodynamics discussed at the end of this chapter) and weakly interacting massive particles (WIMPs), motivated by the electroweak hierarchy problem. Dark matter candidates may also be macroscopic objects, such as Massive Compact Halo Objects (MACHOs) and PBHs. Another candidate is the millicharged particle, which is discussed further at the end of this chapter. There is a considerable amount of freedom in the mass, interaction cross-section, and possible decay width and decay products of dark matter. This work discusses two types of dark matter mentioned above: macroscopic dark matter, in our case, PBHs, and particle dark matter, in our case, axions.

There are three primary methods for detecting particle dark matter: indirect, direct, and collider searches. Indirect detection of dark matter includes observations of possible annihilation or decay products of particle dark matter and changes in a star's evolution due to dark matter production and escape. This second idea is important for us and may include alterations to the properties of white dwarfs, neutron stars, and stars at various stages of their evolutionary history. Direct detection involves detecting interactions of particle dark matter with electrons or nucleons while collider searches rely on the generation of dark matter particles, for example at the LHC, and observing possible events with missing energy.

2.2 PBHs as Dark Matter Candidates

PBHs that have mass above $M > 10^{15}$ g would be stable at the present day and possibly constitute all of dark matter. Figure 2.2 depicts the fraction of dark matter that is made up of PBHs, plotted against the PBH mass. The red-shaded region represents the observational constraints for PBHs evaporating today; a few of these constraints were discussed in Chapter 1. Letters indicate locations where PBHs may contribute a significant amount to the dark matter abundance today. Two mass regimes where PBHs can constitute all of dark matter today are the astroid to lunar mass ($10^{15} - 10^{23}$g) shown by the letter A in Fig. 2.2 and the extremely massive PBHs ($M > 10^{10}\mathrm{M}_{\odot}$) shown by letter D in the figure [3].

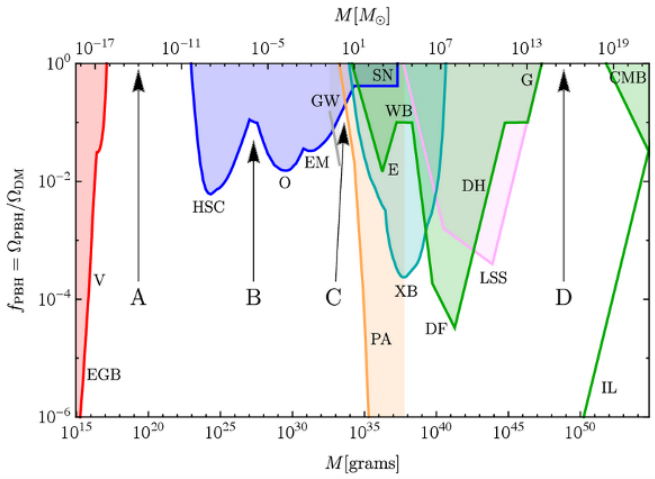


Figure 2.2: Figure from [56] showing the fraction of PBHs that make up dark matter vs PBH mass. The fraction is defined by the ratio of PBH energy density $\Omega_{\rm PBH}$ to dark matter energy density $\Omega_{\rm DM}$. Excluded regions are described in the text. The label A indicates the location of the mass range of PBHs that comprise dark matter in this study.

Several observational frontiers constrain the parameter space, including gravitational lensing (blue), CMB spectral distortions (orange), and accretion (light blue).

Labels indicate observational restrictions from sources such as gravitational waves, X-ray binaries, large-scale structures, and Planck measurements of the CMB. Light PBHs in this work have a mass range of about $10^2 - 10^4$g and exist in the far left of the figure.

2.3 Axions

The axion, a pseudoscalar boson, was first introduced through the spontaneous breaking of the Peccei–Quinn symmetry as a solution to the strong CP problem [57]. Work by Steven Weinberg and, independently, Frank Wilczek, clarified its role as dark matter [58, 59].

The origin of the axion is as a solution to the strong CP problem. We will not consider other solutions that do not rely on the axion, such as the massless up quark, or minimal parity-based solutions. The Lagrangian for the axion, written at an effective level, introduces a single new pseudoscalar a and a single new coupling f_a:

$$\mathcal{L} \supset \left(\frac{a}{f_a} + \theta\right) \frac{1}{32\pi^2} G\tilde{G} \, . \tag{2.1}$$

Both the axion and the QCD θ term have been demonstrated, and as is apparent from this term, the axion obeys an anomalous symmetry

$$a \to a + \alpha f_a, \qquad \theta \to \theta - \alpha \, . \tag{2.2}$$

This dictates the axion coupling to other particles. Every non-derivative interaction of the axion can be obtained by replacing θ with $\theta + a/f_a$. Derivative couplings are more complicated. In UV-complete models, the QCD axion can also have other couplings, such as

$$\mathcal{L} \supset \frac{a}{f_B} \frac{1}{32\pi^2} B\tilde{B} + \frac{a}{f_W} \frac{1}{32\pi^2} W\tilde{W}. \tag{2.3}$$

The axion described above is the QCD axion. In this work, we are more broadly concerned with axion-like particles (ALPs), which are ubiquitous in string theory. Of particular interest is their coupling to photons, which can be expressed as

$$\mathcal{L}_{\rm I} \supset \frac{g_{a\gamma\gamma}}{4}\, a\, F^{\mu\nu}\tilde{F}_{\mu\nu}, \tag{2.4}$$

where $F_{\mu\nu}$ is the electromagnetic field strength tensor, $\tilde{F}_{\mu\nu}$ its dual, a the axion field, and $g_{a\gamma\gamma}$ the axion–photon coupling (we will use this parametrization throughout, instead of the decay constant f_a). Later chapters will explore constraints on $g_{a\gamma\gamma}$ using Cepheid variables.

2.3.1 Axions and Stars

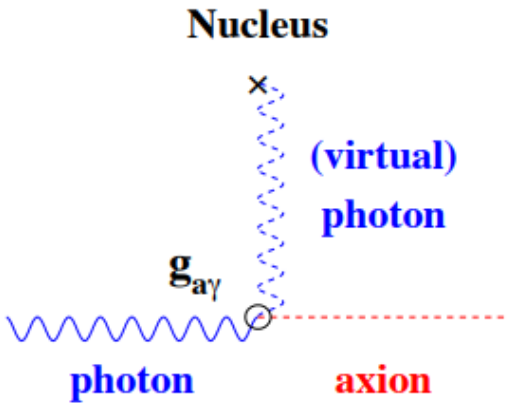


Figure 2.3: The Primakoff effect, where an axion is produced through the interaction of a real photon with a virtual photon in the stellar plasma [60].

Axion production in stellar environments has been extensively studied [61]. Production channels include interactions with photons, electrons, and nucleons in the stellar plasma. In the two-photon channel, axions are generated by the Primakoff effect, in which a real photon interacts with a virtual photon from a nucleus or electron, as

depicted in Fig. 2.3. We assume axions are free-streaming and thus carry away energy without reabsorption. This energy loss alters stellar structure and evolution, a central theme of Part II of the dissertation.

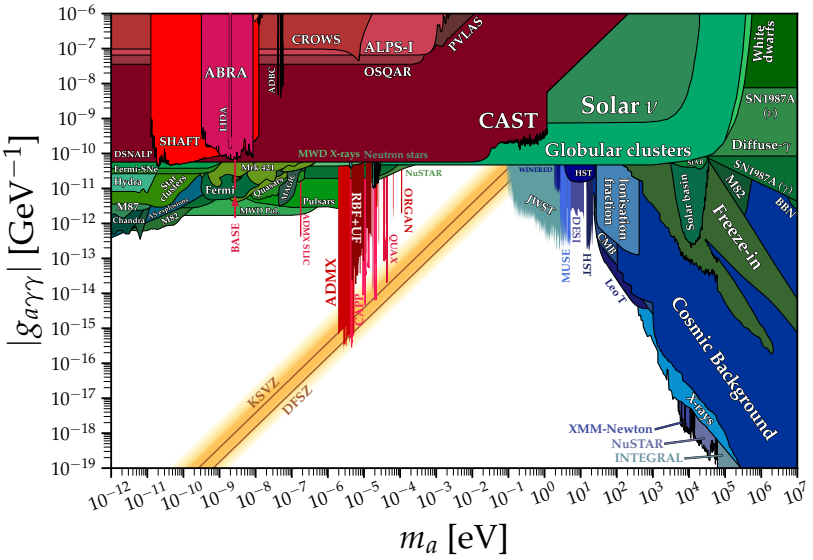


Figure 2.4: Constraints on axion mass and photon coupling [62].

The axion mass and its coupling to photons have been the focus of extensive investigation. Figure 2.4 summarizes the current limits in the coupling–mass plane. Stellar systems provide particularly strong constraints. For instance, globular cluster observations yield bounds near $g_{a\gamma\gamma} \sim 10^{-10}\,\mathrm{GeV}^{-1}$ across a broad mass range. This value, denoted g_{10}, will be used as a benchmark in Chapter 7.

2.4 Millicharged Particles

Millicharged particles (MCPs) are Dirac fermions carrying a small fractional electric charge q_χ coupled to the photon. It is convenient to parametrize q_χ as a fraction ϵ of the electric charge; thus, $q_\chi = \epsilon e$. Several mechanisms have been proposed to

introduce MCPs into the Standard Model. A typical Lagrangian consists of the MCP χ introduced via

$$\mathcal{L} \supset \epsilon e \bar{\chi} \gamma_\mu \chi A^\mu + \bar{\chi} \left(i\partial - m_\chi \right) \chi \tag{2.5}$$

The electric charge $q_\chi \ll 1$ suppresses the decay width of the production process $\gamma^* \to \chi\bar{\chi}$ from a plasmon γ^*. Other possibilities, which we will not pursue, include introducing a hidden $U(1)'$ gauge sector kinetically mixed with hypercharge Y. MCPs are well-motivated dark matter candidates, and current searches include beam-dump, collider, and neutrino experiments.

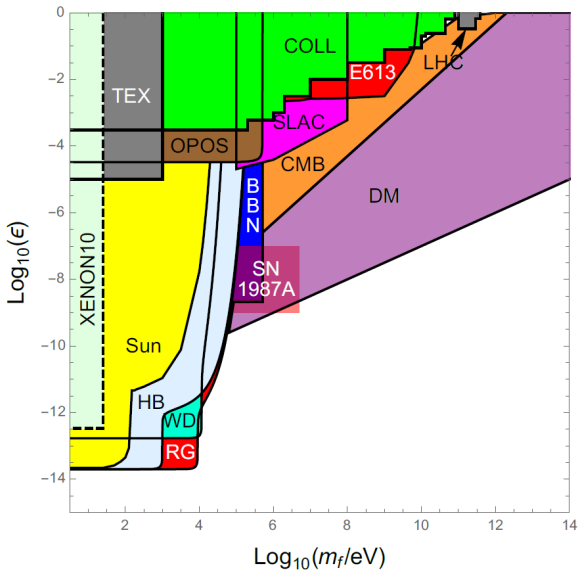


Figure 2.5: Bounds on the fractional charge of MCPs as a function of mass, adapted from [63].

Figure 2.5 shows experimental and astrophysical constraints on MCPs. Stellar evolution provides strong limits, with bounds below $\log_{10}(\epsilon) \sim -8$ derived from Supernova 1987A, the Sun [63], red giant and horizontal branch stars, and white dwarfs. Projected constraints from the tip of the red giant branch extend further, to $\log_{10}(\epsilon) \sim -14$

[64]. Chapter 8 will aim to establish constraints that improve upon these astrophysical bounds.

2.5 Conclusion

The history of the discovery of dark matter and some observational examples were provided, followed by an overview of dark matter particle candidates in general, including WIMPs. We then discussed PBHs, axions, and millicharged particles, which are the candidates relevant for the rest of the dissertation. This ends the introductory material.

Chapter 3

Baryogenesis, Primordial Black Holes and MHz-GHz Gravitational Waves

3.1 Introduction

Gravitational waves (GWs) provide a unique window to the physics of the early Universe. Current detector designs are able to probe GWs in the nHz-kHz frequency range, leaving the regime of ultra high frequency GWs, in the MHz-GHz range, relatively unexplored. It is precisely at these ultra-high frequencies, however, that one expects very early cosmological events to leave their imprints: very early phase transitions, oscillons, preheating, cosmic strings, etc. This fact has led to a recent surge of interest among particle theorists, cosmologists, and the experimental community in proposing methods to search for GWs at these frequencies. Fully understanding the cosmological and particle physics models driving such proposals is an important aspect of this endeavor. For a comprehensive review of this theoretical and experimental frontier, we refer to [65, 66].

The early Universe phenomena listed above all occur below the Big Bang Nucleosynthesis (BBN) bound in the $(h_c, f_{\rm GW})$ plane utilized to depict this frontier (we refer to Fig. 2 of [65]). Here, $f_{\rm GW}$ denotes the frequency, while h_c denotes the dimensionless characteristic strain relevant to the normalized energy density for stochastic GWs, which we will define carefully in the main text. The extremely low strain relevant

to this regime makes it a very challenging target for experimentalists. While primordial black holes (PBHs) have also been studied in this regime, it is in their avatar as stable late-Universe exotic compact objects that they have made their appearance: through inspirals, mergers, or capture (we refer to Fig. 1 of [65]). We also refer to [67, 68, 69, 70, 71, 72, 73, 74] for studies of late-Universe PBHs in the context of lower frequencies attainable at current or near-future detectors.

PBHs that evaporate before BBN could also be a target for MHz-GHz GW detectors. The source in this case would be the second order GWs produced when primordial scalar fluctuations responsible for PBH formation re-enter the horizon[1] [77, 78, 79, 80, 81, 82, 83, 84, 85, 86, 87, 88, 89, 36]. In particular, a spell of ultra slow-roll dynamics during the inflationary phase could result in a local enhancement in the spectrum of scalar perturbations, leading to PBH formation [25, 26, 90, 27, 91, 92]. While scalar, vector, and tensor fluctuations decouple at linear order, at second order the story is different: GWs can be produced with an amplitude that scales quadratically with the scalar perturbation. Since the amplitude of scalar perturbations is required to be enhanced by orders of magnitude for PBH formation, this significantly enhances the detection prospects of such GWs compared to the primordial signals from inflation. On the other hand, the peak frequency scales with the PBH mass as $f_{\rm GW}^{\rm peak} \sim M_{\rm PBH}^{-1/2}$; for PBH masses between 0.1 g and 10^4 g, this falls within the MHz-GHz range[2].

The question then is: do evaporating PBHs connect to problems of interest for particle physicists? Here the answer is very much to the affirmative. The connection of evaporating PBHs to baryogenesis has a long history [11, 93, 94, 95, 96, 97, 98, 99, 100, 101, 102]. Similarly, dark matter (DM) [103, 104, 105, 106, 12, 107] and dark radiation [108, 109, 110] produced by evaporating PBHs have been studied by many groups (we

[1] This should be contrasted to the GWs produced due to Hawking evaporation itself, which produces GWs at much higher and more challenging frequencies [75, 76].

[2] The upper bound comes from avoiding a spell of PBH domination, as we will see later.

select only a few references from the vast literature). It becomes possible, then, to study the interconnections of ultra-high frequency GW signals and baryogenesis, DM, and dark radiation induced by PBHs.

The purpose of this paper is to explore the interconnections of PBH-induced baryogenesis and GWs between MHz-GHz frequencies[3]. We briefly outline the main steps and our results, beginning with a few preliminary remarks about baryogenesis in general. The matter-anti-matter asymmetry of the Universe is usually explained by the dynamical process of baryogenesis [111], which generates the baryon density $\Omega_B h^2 = 0.02237 \pm 0.0001$ [112]. In the context of PBHs, baryogenesis proceeds as follows: a heavy species X is produced via Hawking evaporation and subsequently decays to Standard Model particles through CP and B violating operators, inducing baryogenesis.

The final baryon asymmetry is determined by (i) the initial abundance of PBHs; (ii) the number of X particles produced by evaporation per PBH and (iii) the particle physics input in the form of the amount of baryon number violation per decay of X, which we call γ_{CP}. We study the frequency and amplitude of the GWs produced by second order effects as these parameters are varied, requiring that the observed baryon asymmetry is satisfied. There are several criteria that need to be satisfied. Firstly, one must be careful to delineate the regions of parameter space where a matter- (in this case, PBH-) dominated cosmology occurs. A PBH-dominated phase would typically result in GWs peaking in a different frequency range and will be studied in future work. Secondly, one must be careful to avoid washout of the final asymmetry, which can be imposed in this case by the requirement that the mass m_X of X exceed the

[3]We leave the interconnections of high-frequency GWs with DM and dark radiation from evaporating light PBHs for future work. The interplay of DM with evaporating PBHs has been explored by several groups – we mention [104, 12]. We further note that the interconnection between *stable* PBH DM in the current Universe and low frequency induced GWs has been studied by many authors, for instance recently in [37, 38]. We refer to the review [83] and references therein.

temperature of the thermal bath at the evaporation time of the PBHs. These features are displayed in Fig. 3.1.

We do not explore the particle physics model-building (in other words, how X couples to the Standard Model) in any great detail, given the plethora of available models in the literature (for completeness, we outline a supersymmetric embedding of the model in the Appendix, based on previous work by one of the authors). Some generic features that we uncover are as follows. Since baryogenesis occurs by the interference of tree-level and one-loop decays of X, the asymmetry per decay γ_{CP} is typically a simple loop factor $\sim \mathcal{O}(1/16\pi^2)$ for $\mathcal{O}(1)$ Yukawa couplings of X. As such, we take a benchmark value of $\gamma_{CP} = 10^{-2}$ for our results. If one lowers the value of γ_{CP} to, for example, $\mathcal{O}(10^{-5})$, one needs a higher initial abundance of PBHs to achieve the observed asymmetry. However, one then runs into a PBH-dominated phase, restricting the parameter space where potentially observable GWs can be obtained. This is displayed in the bottom panel of Fig. 3.1.

We find that the range of PBH masses relevant for our scenario is 0.1 g to $\sim 3\times10^4$ g, with the upper bound coming from the threshold of hitting a PBH-dominated cosmology, assuming $\gamma_{CP} = 10^{-2}$, while the lower bound is from Hubble rate during inflation which is constrained by Cosmic Microwave Background (CMB) observations [55]. We calculate the resulting energy density of GWs as a function of the frequency for various PBH masses. These results are shown in Fig. 3.3. The strain at the peak frequency of the GW spectrum is plotted against the peak frequency in Fig. 3.4 for different choices of m_X. In these figures, we also depict a conceptual design employing the inverse Gertsenshtein effect to probe GWs in this regime[4].

[4]This was proposed in [113]. We provide this reach for the purpose of illustration only; clearly a lot of work needs to be done to probe ultra high-frequency GWs.

To get a sense of the strain values involved, we can provide a summary of our results. The strain at the peak frequency scales as

$$h_c \sim 5.5\times10^{-27} \left(\frac{1\,\mathrm{MHz}}{f_{\mathrm{GW}}^{\mathrm{peak}}}\right) \log\left[2.0\times10^{18} \left(\frac{1\,\mathrm{MHz}}{f_{\mathrm{GW}}^{\mathrm{peak}}}\right)^2 \left(\frac{\gamma_{CP}}{10^{-2}}\right)^2 \left(\frac{8.7\times10^{-11}}{Y_B}\right)^2\right]^{-1}, \tag{3.1}$$

for

$$5.41\times10^2 \left(\frac{f_{\mathrm{GW}}^{\mathrm{peak}}}{1\,\mathrm{MHz}}\right)^3 \mathrm{GeV} \lesssim m_X \lesssim 1.33\times10^8 \left(\frac{f_{\mathrm{GW}}^{\mathrm{peak}}}{1\,\mathrm{MHz}}\right)^2 \mathrm{GeV}, \tag{3.2}$$

and

$$h_c \sim 5.5\times10^{-27} \left(\frac{1\,\mathrm{MHz}}{f_{\mathrm{GW}}^{\mathrm{peak}}}\right) \log\left[5.9\times10^{14} \left(\frac{f_{\mathrm{GW}}^{\mathrm{peak}}}{1\,\mathrm{MHz}}\right)^6 \left(\frac{10^9\,\mathrm{GeV}}{m_X}\right)^4 \times \left(\frac{\gamma_{CP}}{10^{-2}}\right)^2 \left(\frac{8.7\times10^{-11}}{Y_B}\right)^2\right]^{-1}, \tag{3.3}$$

for

$$1.33\times10^8 \left(\frac{f_{\mathrm{GW}}^{\mathrm{peak}}}{1\,\mathrm{MHz}}\right)^2 \mathrm{GeV} \lesssim m_X \lesssim 1.04\times10^8 \left(\frac{\gamma_{CP}}{10^{-2}}\right)^{1/2} \times \left(\frac{8.7\times10^{-11}}{Y_B}\right)^{1/2} \left(\frac{f_{\mathrm{GW}}^{\mathrm{peak}}}{1\,\mathrm{MHz}}\right)^{5/2} \mathrm{GeV}. \tag{3.4}$$

Here, $Y_B = n_B/s \simeq 8.7\times10^{-11}$. The lower bound on m_X in Eq. (3.2) comes from avoiding washout. Eqs. (3.1) and (3.3) are of course valid as long as one stays within a radiation-dominated cosmology. The frequency of GWs is determined by the PBH mass that solves baryogenesis in a radiation-dominated universe. We found the lowest frequency is about $1.64\times(10^{-2}/\gamma_{CP})\times[Y_B/(8.7\times10^{-11})]$ MHz, which indicates MHz-GHz GWs in the parameter space of baryogenesis models.

Finally, we explore a scenario where the DM-baryogenesis coincidence problem is addressed by two populations of PBHs: one responsible for baryogenesis, and the

other stable and comprising DM today. The coincidence is then primarily driven by the ratio of the masses and abundances of the two populations. The striking feature of this scenario is a double-peaked GW spectrum.

3.2 PBHs mass function

In this Section, we introduce our notation and discuss the PBH mass function set in the introduction that will be used to address baryogenesis. The PBH mass function at time t is defined as the ratio between the PBH energy density per logarithmic mass interval and the total radiation energy density at the formation time, $t_i(M)$,

$$\frac{d\beta(M_{\rm PBH}, t_i, t)}{d\log M_{\rm PBH}} = \begin{cases} \frac{a(t)}{a(t_i)} \frac{1}{\rho_{\rm rad}(t_i)} \frac{d\rho(M_{\rm PBH})}{d\log M_{\rm PBH}} & ({\rm Radiation-dominated}), \\ \\ \frac{1}{\rho'_{\rm rad}(t,t_i)} \frac{a^3(t_i)}{a^3(t)} \frac{d\rho(M_{\rm PBH})}{d\log M_{\rm PBH}} & ({\rm PBH-dominated}). \end{cases} \tag{3.5}$$

Here $d\rho(M_{\rm PBH})/d\log M_{\rm PBH} = M_{\rm PBH} \times dn(M_{\rm PBH})/d\log M_{\rm PBH}$ and $dn(M_{\rm PBH})/d\log M_{\rm PBH}$ is the number density of PBH per logarithmic mass interval at the formation time. $a(t)$ is the scale factor. If the universe is always radiation-dominated, the radiation energy density $\rho_{\rm rad}$ scales as a^{-4} while the PBH energy density scales as a^{-3}. If there exists a PBH-dominated epoch, the energy density of radiation is determined by the reheating temperature from PBH evaporation. We denote the radiation energy density after a PBH-dominated epoch as $\rho'_{\rm rad}$. The properties of $\rho'_{\rm rad}$ is discussed in detail in Sec.3.3.2.

Following the derivations in Sec.1.4.1, we take the curvature perturbation to be monochromatic, the power spectrum can be parameterized with two parameters, the amplitude A_ζ and the peak location k_0,

$$P_\zeta(A_\zeta, k_0) = A_\zeta \, \delta\left(\log\left(\frac{k}{k_0}\right)\right), \tag{3.6}$$

while the variance is simplified to

$$\sigma_0^2(k) = A_\zeta \, \frac{16}{81} \left(\frac{k_0}{k}\right)^4 \exp\left[-\left(\frac{k_0}{k}\right)^2\right]. \tag{3.7}$$

A monochromatic power spectrum would generate a peaked PBH mass distribution, whose initial abundance can be defined in the similar way:

$$\beta(M_{\rm PBH}) = \frac{\rho(M_{\rm PBH})}{\rho_{\rm rad}(t_i(M_{\rm PBH}))} = \frac{n_{\rm PBH} \times M_{\rm PBH}}{\rho_{\rm rad}(t_i(M_{\rm PBH}))}. \tag{3.8}$$

In following sections, we assume a single PBH population of fixed mass is responsible for baryogenesis, and use Eq.(3.8) as an approximation of Eq.(1.20) in the numerical analysis.

3.3 Baryogenesis by Hawking Evaporation

A population of PBHs which undergoes Hawking evaporation can emit any particle in the spectrum which is lighter than their instantaneous temperature. In this section, we summarize baryogenesis through the CP and baryon number violating decay of a beyond-Standard Model particle X produced by Hawking evaporation of PBHs[5].

[5]This idea was initially introduced as a viable production mechanism of heavy bosons predicted by Grand Unified Theories [114, 96].

Our focus is on the production of the PBHs and the interplay of the concomitant GW signal with the mass m_X and the baryon-number-to-entropy density Y_B. For explicit particle physics models of the subsequent baryon asymmetry obtained by the decay of X, we refer to [98, 115, 101] and Appendix C, where we give details of some supersymmetric embeddings based on [116, 117, 118, 119]. If PBHs dominate the energy density of the Universe prior to their evaporation, they can initiate an early matter- (PBH-) dominated era. We will study both the case where PBHs evaporate in a radiation-dominated Universe, as well as when they themselves come to dominate the energy density.

3.3.1 Evaporation of PBHs in a Radiation-Dominated Universe

Density fluctuations, represented as δ, grow after entering the cosmological horizon in the early Universe. If that re-entering happens in a radiation-dominated epoch, the over-density may overcome the pressure and collapse into a PBH. The collapse can happen if $\delta > \omega$ where $\omega = p/\rho$ is the equation of state parameter [16]. If the energy density of the Universe is dominated by radiation, $\omega = 1/3$.

PBHs may give rise to an early matter-dominated era. Due to the fact that PBHs and radiation are diluted differently with the expansion of the Universe, the ratio of energy density of PBHs to the energy density of radiation increases with time, i.e., $\rho_{\rm PBH}(t)/\rho_{\rm rad}(t) \propto a$. Therefore, a transition from a radiation-dominated era to a matter-dominated one is inevitable if PBHs have long enough lifetimes. The critical initial abundance of PBHs, β_c, to start an early matter-dominated era can be evaluated by requiring that PBHs evaporate after the early equality time, $t_{\text{early-eq}}$, at which

$\rho_{\rm PBH}(t_{\text{early-eq}})/\rho_{\rm rad}(t_{\text{early-eq}}) \sim 1$. The temperature of the Universe at early equality time, $T_{\text{early-eq}}$, can be obtained from:

$$\frac{\rho_{\rm PBH}(T_{\text{early-eq}})}{\rho_{\rm rad}(T_{\text{early-eq}})} = \frac{\rho_{\rm PBH}(T_i)}{\rho_{\rm rad}(T_i)}\frac{T_i}{T_{\text{early-eq}}} = \beta_c \frac{T_i}{T_{\text{early-eq}}} \sim 1. \tag{3.9}$$

An early matter-dominated epoch is unavoidable provided that $t_{\text{early-eq}} \lesssim t_{\rm eva}$. This is equivalent to $\beta \geq \beta_c$, where

$$\beta_c = \frac{T_{\rm eva}}{T_i} = \sqrt{\frac{g_\star(T_{\rm PBH})}{10240\pi\gamma}}\frac{M_{\rm Pl}}{M_{\rm PBH}} \simeq 2.8\times 10^{-6}\left(\frac{g_\star(T_{\rm PBH})}{106.8}\right)^{1/2}\left(\frac{0.2}{\gamma}\right)^{1/2}\left(\frac{1\text{g}}{M_{\rm PBH}}\right). \tag{3.10}$$

If PBHs never dominate the energy density of the Universe prior to their Hawking evaporation, i.e., $\beta < \beta_c$, then they will evaporate in a radiation-dominated era at some time denoted by $t = t_{\rm eva}$.

Among other particles, PBHs emit the beyond-Standard Model particle X with a lifetime of τ_X which is added to the spectrum to explain baryogenesis by its decay at time $t = t_{\rm eva} + \tau_X$. It is customary to define the baryon asymmetry γ_{CP} produced per decay of X, given by

$$\gamma_{CP} = \sum_i B_i \frac{\Gamma(X \to f_i) - \Gamma(\bar{X} \to \bar{f}_i)}{\Gamma_X}, \tag{3.11}$$

where B_i is the baryon number of the particular final state f_i, and Γ_X is the total decay width of X. f_i and $\bar{f}_i$ denote a particle and its anti-particle, respectively. Baryogenesis is obtained by the interference between tree-level and one-loop decays of X. The exact value of γ_{CP} depends on the particle physics model; however, for $\mathcal{O}(1)$ Yukawa couplings of X to other particles, one obtains

$$\gamma_{CP} \sim \frac{1}{16\pi^2}, \tag{3.12}$$

coming from a loop suppression. As a benchmark, we use the value $\gamma_{CP} = 10^{-2}$ in our work, and keep the scaling with γ_{CP} explicit throughout.

Hawking evaporation of a population of PBHs with mass $M_{\rm PBH}$ and initial abundance β, where $\beta < \beta_c$, gives rise to baryon-number-to-entropy density, Y_B, equal to

$$\begin{aligned} Y_B &= \frac{n_B(t_0)}{s(t_0)} = \gamma_{CP}\frac{n_X(t_{\rm eva}+\tau_X)}{s(t_{\rm eva}+\tau_X)} = \gamma_{CP}\frac{n_X(t_{\rm eva})}{s(t_{\rm eva})} = \gamma_{CP}N_X\frac{n_{\rm PBH}(t_i)}{s(t_i)} \\ &= \gamma_{CP}\beta N_X\frac{1}{M_{\rm PBH}}\frac{\rho_{\rm PBH}(t_i)}{s(t_i)} = \frac{3}{4}\frac{g_\star(T_i)}{g_{\star,S}(T_i)}\gamma_{CP}\beta N_X\frac{T_i(M_{\rm PBH})}{M_{\rm PBH}}, \end{aligned} \tag{3.13}$$

where $g_{\star,S}(T_i)$ counts the number of relativistic degrees of freedom contributing to the entropy of the Universe, and N_X, is the total number of particles X emitted by one PBH given by [12]

$$N_X = \frac{15\zeta(3)}{\pi^3}\frac{g_X}{g_\star(T_{\rm PBH})}\begin{cases} \frac{8M_{\rm PBH}^2}{M_{\rm Pl}^2} & m_X < T_{\rm PBH}, \\ \\ \frac{1}{8\pi^2}\frac{M_{\rm Pl}^2}{m_X^2} & m_X > T_{\rm PBH}\,, \end{cases} \tag{3.14}$$

if X is a boson. Here, g_X denotes the number of degrees of freedom of X. We set $g_X = 1$ in all our figures, although we keep the scaling with g_X explicit in our calculations. The total number of fermionic species is $N_F = \frac{3}{4}\frac{g_F}{g_B}N_B$.

The initial abundance of PBHs which leads to a value Y_B of the baryon-number-to-entropy density can be obtained as

$$\beta = \frac{\pi^{15/4}}{45\sqrt{3}\,5^{1/4}\zeta(3)} \frac{g_\star(T_{\rm PBH}) g_\star^{1/4}(T_i)}{g_X} \gamma^{-1/2} \gamma_{CP}^{-1} Y_B \begin{cases} \left(\frac{M_{\rm Pl}}{M_{\rm PBH}}\right)^{1/2} & m_X < T_{\rm PBH}, \\ 64\pi^2 \left(\frac{M_{\rm PBH}^3 m_X^4}{M_{\rm Pl}^7}\right)^{1/2} & m_X > T_{\rm PBH}\,, \end{cases} \tag{3.15}$$

Avoiding an early matter-dominated phase, i.e., $\beta < \beta_c$ is equivalent to an upper bound on the mass of PBHs, $M_{\rm PBH} < M_c$ where

$$M_c = \begin{cases} \frac{1215\sqrt{5}\zeta^2(3)}{2048\pi^{17/2}} \frac{g_X^2}{g_\star(T_{\rm PBH}) g_\star^{1/2}(T_i)} \gamma_{CP}^2 Y_B^{-2} M_{\rm Pl} & m_X < T_{\rm PBH} \ \left(M_{\rm PBH} < \frac{M_{\rm Pl}^2}{8\pi m_X}\right), \\ \frac{3\times 5^{3/10}\zeta^{2/5}(3)}{16\times 2^{3/5}\pi^{5/2}} \frac{g_X^{2/5}}{g_\star^{1/5}(T_{\rm PBH}) g_\star^{1/10}(T_i)} \gamma_{CP}^{2/5} Y_B^{-2/5} \left(\frac{M_{\rm Pl}^9}{m_X^4}\right)^{1/5} & m_X > T_{\rm PBH} \ \left(M_{\rm PBH} > \frac{M_{\rm Pl}^2}{8\pi m_X}\right), \end{cases} \tag{3.16}$$

These conditions can be combined as

$$\begin{cases} M_{\rm PBH} < \min\left\{ \frac{1215\sqrt{5}\zeta^2(3)}{2048\pi^{17/2}} \frac{g_X^2}{g_\star(T_{\rm PBH}) g_\star^{1/2}(T_i)} \gamma_{CP}^2 Y_B^{-2} M_{\rm Pl},\ \frac{M_{\rm Pl}^2}{8\pi m_X} \right\} & m_X < T_{\rm PBH}, \\ \frac{M_{\rm Pl}^2}{8\pi m_X} < M_{\rm PBH} < \frac{3\times 5^{3/10}\zeta^{2/5}(3)}{16\times 2^{3/5}\pi^{5/2}} \frac{g_X^{2/5}}{g_\star^{1/5}(T_{\rm PBH}) g_\star^{1/10}(T_i)} \gamma_{CP}^{2/5} Y_B^{-2/5} \left(\frac{M_{\rm Pl}^9}{m_X^4}\right)^{1/5} & m_X > T_{\rm PBH}\,. \end{cases} \tag{3.17}$$

Following [120], the observational value that we use for Y_B is

$$Y_B = \frac{n_B}{s} \simeq \frac{2.515 \times 10^{-7}\,{\rm cm}^{-3}}{2891.2\,{\rm cm}^{-3}} \simeq 8.7 \times 10^{-11}. \tag{3.18}$$

It is clear from Eq. (3.16) that the critical PBH mass to avoid matter domination is determined mainly by the observed value of Y_B and the value of γ_{CP}. While this is completely true in the case that $m_X < T_{\rm PBH}$, for the case that $m_X > T_{\rm PBH}$ this statement is true up to $\sim (M_{\rm Pl}/m_X)^{1/5}$. The top two panels of Fig. 3.1 show the parameter space of PBHs that can explain baryon asymmetry of the Universe without transitioning to an early matter-dominated era. In the top-left panel of Fig. 3.1, the black lines depict the initial abundance of PBHs, i.e., β, in the $(m_X, M_{\rm PBH})$ plane. PBHs with the presented initial abundance can emit enough X particle to explain baryon asymmetry of the Universe. In the light gray region, the X particle is lighter than the initial temperature of PBHs, while in the dark gray area X is heavier than the temperature of the PBHs. The border between these two regions marks the line $T_{\rm PBH} = m_X$. Within the white region, β exceeds the critical value β_c and leads to a PBH-dominated Universe.

When X is produced from the thermal bath rather than the PBHs evaporation, this leads to the elimination of the asymmetry in the Universe. This process is called washout. To avoid washout of the baryon asymmetry generated by the decay of X, we require

$$m_X > T_{\rm eva} \ , \tag{3.19}$$

where the temperature of the Universe at evaporation time, $T_{\rm eva}$, is given by Eq. (5.33). This constraint is shown in the left panel of Fig. 3.1 by the pink region. While avoiding an early PBH-dominated era leads to an upper bound on PBH mass, i.e., $M_{\rm PBH} \lesssim 3 \times 10^4\,{\rm g}$, evading washout gives rise to a lower limit on PBH mass which varies with m_X (only for $m_X < T_{\rm PBH}$).

We note that the minimum evaporation temperature to avoid a PBH-dominated phase corresponds to $M_{\rm PBH} \simeq 3 \times 10^4\,{\rm g}$ and is given by 2.4 TeV. This also implies that m_X has to be greater than this value. We therefore have

$$T_{\rm baryo} \geq 2.4 \text{ TeV} \ . \tag{3.20}$$

To avoid subsequent sphaleron washout, the decays of X should be $B - L$ violating (Baryon (B) and Lepton L).

The top right panel of Fig. 3.1 displays limits on the mass of X particle in the $(M_{\rm PBH}, \beta)$ plane. The different colors correspond to different values of m_X. The dotted line shows β_c. For any given color, the parameter space along the diagonal line corresponds to the case where $m_X < T_{\rm PBH}$, while the sharp uptick corresponds to the case where $m_X > T_{\rm PBH}$. Along the diagonal, a given color corresponding to a fixed value of m_X starts at a point corresponding to the condition $m_X > T_{\rm eva}$. Along the uptick, the color stops at the point where $\beta = \beta_c$, i.e., where matter domination takes over.

The bottom panel of Fig. 3.1 shows the parameter space of γ_{CP} on the $(m_X, M_{\rm PBH})$ plane in a radiation-dominated cosmology that gives the correct baryon asymmetry. For a given shade of blue, the horizontal cut-off as well as the cut-off on the right diagonal come from avoiding PBH domination. The cut-off on the left diagonal comes from avoiding washout. These features are displayed in the figure. We also note that we go down to PBH masses of $\lesssim 10^{-5}$ g to indicate the regime where especially small values of γ_{CP} are operational.

3.3.2 Evaporation of PBHs in a Matter- (PBH-) Dominated Universe

If the initial abundance of PBHs is large enough, i.e., $\beta \geq \beta_c$, they can dominate the energy density of the Universe and subsequently induce an early matter- (PBH-) dominated epoch[6]. In other words, the evaporation of PBHs reheats the Universe for the second time and initiates a secondary radiation-dominated epoch. The quick equilibration of the SM particles emitted by PBHs sets the secondary reheating temperature of the Universe.

By applying the Friedemann equation very close to the Hawking evaporation of PBHs, their energy density can be expressed in terms of their lifetime as

$$H^2(\tau) = \left(\frac{2}{3\tau_{\rm PBH}}\right)^2 = \frac{8\pi\rho(\tau_{\rm PBH})}{3M_{\rm Pl}^2}, \tag{3.21}$$

where the lifetime of black hole, $\tau_{\rm PBH}$, is given by Eq. (1.7). The reheating temperature of the Universe, $T_{\rm rh}(\tau_{\rm PBH})$, given instantaneous equilibration, equals to:

$$T_{\rm rh}(\tau_{\rm PBH}) = \frac{1}{32\sqrt{2}\times 5^{1/4}\pi^{5/4}} g_\star^{1/4}(T_{\rm rh}) \left(\frac{M_{\rm Pl}^5}{M_{\rm PBH}^3}\right)^{1/2}. \tag{3.22}$$

Following Eq. (3.13), baryon-number-to-entropy density, is equal to:

$$Y_B = \gamma_{CP} N_X \frac{n_{\rm PBH}(\tau_{\rm PBH})}{s(\tau_{\rm PBH})} = \gamma_{CP} N_X \frac{1}{M_{\rm PBH}} \frac{\rho_{\rm PBH}(\tau_{\rm PBH})}{s(\tau_{\rm PBH})} = \frac{3}{4}\frac{g_\star(T_{\rm rh})}{g_{\star,S}(T_{\rm rh})} \gamma_{CP} N_X \frac{T_{\rm rh}(\tau_{\rm PBH})}{M_{\rm PBH}}, \tag{3.23}$$

where N_X is given by Eq. (3.14). Eq. (3.23) shows that when PBHs dominate the energy density of the Universe prior to their evaporation, the abundance of emitted particles is independent of initial abundance of PBHs [98].

[6]For a general review of early matter-dominated eras, we refer to [121, 122].

One can solve Eq. (3.23) for $M_{\rm PBH}$ as a function of Y_B and m_X. When $m_X < T_{\rm PBH}$, the result is independent of m_X and there is only one mass for PBHs, given by:

$$M_{\rm PBH} = \frac{405\sqrt{5}\zeta(3)^2}{512\pi^{17/2}} \frac{g_X^2}{g_\star^{3/2}(T_{\rm rh})} \gamma_{CP}^2 Y_B^{-2} M_{\rm Pl}, \tag{3.24}$$

while for $m_X > T_{\rm PBH}$, we get:

$$M_{\rm PBH} = \frac{3^{4/5} \times 5^{3/10}\zeta^{2/5}(3)}{16 \times 2^{1/5}\pi^{5/2}} \frac{g_X^{2/5}}{g_\star^{3/10}(T_{\rm rh})} \gamma_{CP}^{2/5} Y_B^{-2/5} \left(\frac{M_{\rm Pl}^9}{m_X^4}\right)^{1/5}. \tag{3.25}$$

Fig. 3.2 displays the mass of PBHs as a function of m_X when they dominate the Universe before their evaporation ($\beta \geq \beta_c$) and the X particles explain baryon asymmetry of the Universe for $\gamma_{CP} = 10^{-2}$. For $10^4\,{\rm GeV} \lesssim m_X \lesssim 2.7\times10^8\,{\rm GeV}$ where $m_X < T_{\rm PBH}$, we obtain $M_{\rm PBH} \simeq 4 \times 10^4\,{\rm g}$. By increasing the m_X and entering $m_X > T_{\rm PBH}$ region, $M_{\rm PBH}$ needs to be decreased to explain baryon asymmetry.

Our focus in this work will be on GWs produced in a radiation-dominated Universe. The interplay of baryogenesis and GWs produced during a PBH-dominated phase will be explored in the future. Nevertheless, we point out some general features of this correlation in subsection 3.4.2.

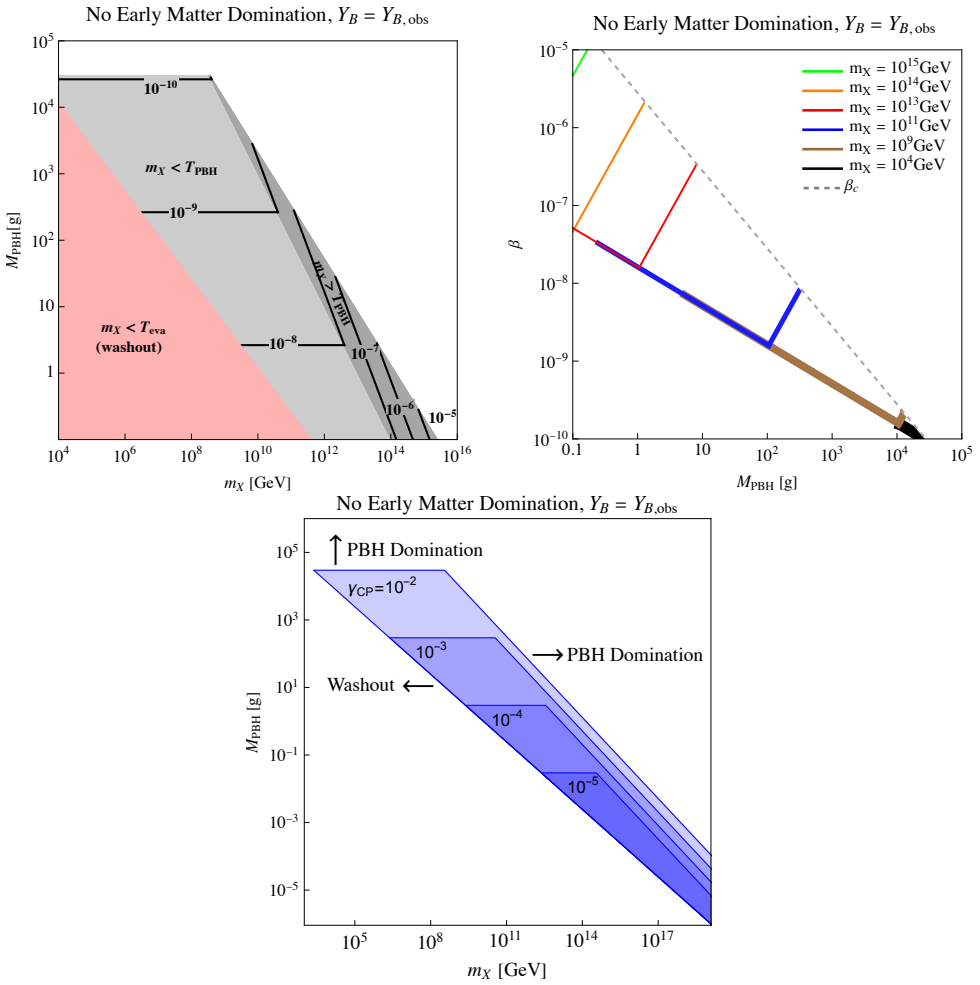


Figure 3.1: *Top-left panel*: Contours of β are drawn on the $(m_X, M_{\rm PBH})$ plane requiring the observed value of Y_B in the radiation-dominated case ($\beta < \beta_c$). We use the value $\gamma_{CP} = 10^{-2}$. The black lines show the initial abundance of PBHs that can explain the baryon asymmetry of the Universe without giving rise to an early matter-dominated era ($\beta < \beta_c$). The light gray area corresponds to $m_X < T_{\rm PBH}$ while the dark gray area marks the region in which $m_X > T_{\rm PBH}$. The white region corresponds to $\beta > \beta_c$ and a PBH-dominated era. The pink region is ruled out due to the requirement $m_X > T_{\rm eva}$, needed to avoid washout. *Top-right panel*: Contours of m_X are drawn on the $(\beta, M_{\rm PBH})$ plane requiring the observed value of Y_B in the radiation-dominated case ($\beta < \beta_c$). We use the value $\gamma_{CP} = 10^{-2}$. The different colors show the values of different choices of m_X. The gray dashed line marks β_c. *Bottom panel*: The parameter space on the plane of $M_{\rm PBH}$ vs. m_X that can produce the correct Y_B in a radiation-dominated cosmology, for different value of γ_{CP}. Each lighter shade of blue is a superset that also includes the deeper colors with smaller values of γ_{CP}. The dependence on γ_{CP} is discussed in the main text. Regions that are ruled out due to washout or that feature a PBH-dominated cosmology are indicated. We display PBH masses $M_{\rm PBH} \lesssim 10^{-5}$ g for illustrative purposes: to indicate the regime where especially small values of γ_{CP} are operational.

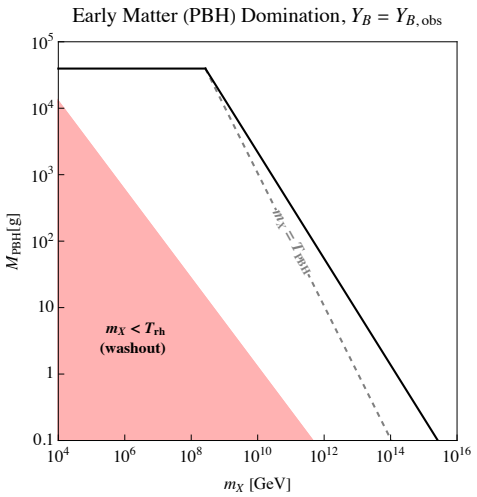


Figure 3.2: Black line shows M_{PBH}, as a function of m_X, that explains observed value of Y_B (for $\gamma_{CP} = 10^{-2}$) when PBHs come to dominate the energy density of the Universe before their evaporation ($\beta \geq \beta_c$). Along the gray dashed line we have $m_X = T_{\mathrm{PBH}}$. The pink region is excluded to evade washout by requiring $m_X > T_{\mathrm{rh}}$.

3.4 MHz - GHz Gravitational Waves and Interplay with Baryogenesis

In this section, we provide details of the calculation of the GWs coming from PBH formation. We will calculate the frequency and amplitude of the signal that is compatible with baryogenesis.

The curvature perturbations responsible for PBH formation generate GW signals (see [85, 36] for the analytical formulae of induced GWs). We note that GW production is independent of whether PBHs are actually formed. The GWs are mostly produced at the moment of horizon crossing and diluted with the expansion of the universe, becoming a stochastic GW background today. We focus on the production of GWs from scalar perturbations that enter the horizon during a radiation-dominated era. GWs are generated at the second order of the scalar mode and the abundance of them can be estimated as $\Omega_{\rm GW} \simeq A_\zeta^2$ where $A_\zeta \sim 10^{-2}$ is the amplitude of the scalar perturbations generating PBHs. The peak frequency of induced GWs is fixed by the horizon re-entry time since sub-horizon source modes decay quickly when the universe is radiation-dominated.

The calculation for the induced gravitational waves from scalar perturbations is given in Section 1.4.1.1. The GW frequency is related to k as:

$$\frac{f_{\rm GW}}{\rm Hz} = 1.546 \times 10^{-15} \frac{k}{\rm Mpc^{-1}} \ . \tag{3.26}$$

We can then write down the relation between the PBH mass and the frequency of the GW spectrum peak that comes from the perturbation as

$$f_{\rm GW}^{\rm peak} \simeq 2.82 \times \left(\frac{M_{\rm PBH}}{10^4 \ {\rm g}} \right)^{-\frac{1}{2}} {\rm MHz}. \tag{3.27}$$

The GW signal from the formation of PBHs peaks at $f_{\rm GW}^{\rm peak} \sim \mathcal{O}(\text{MHz})$, which is much higher than the observation window of future space-based GW proposals.

We can now calculate the GW spectrum that is consistent with baryogenesis. The procedure is as follows. From Eq. (3.15), we obtain the value of β required to give the correct value of Y_B, for a given $M_{\rm PBH}$. We fix $\gamma_{CP} = 10^{-2}$ and require m_X to be smaller than $T_{\rm PBH}$ such that β is independent of m_X in the light gray region in the top left panel of Fig. 3.1. Once β is obtained, the power spectrum in Eq. (4.29) that gives the correct β is calculated from the formalism outlined in Section 5.3.3. Thereafter, $\Omega_{\rm GW}$ is obtained from Eq. (1.24).

In Fig. 3.3 (left panel), we show results for $\Omega_{\rm GW}$ for several selections of PBH masses: $M_{\rm PBH} = 10^2$g, 10^3g, and 10^4g. In Fig. 3.3 (right panel), we display the strain h_c given by

$$h_c(f) = \frac{1}{f}\sqrt{\frac{3\,H_0^2\,\Omega_{\rm GW}}{4\,\pi^2}}, \tag{3.28}$$

corresponding to the three PBH benchmark masses. Since the strain of induced GWs is proportional to the amplitude of the power spectrum, $h_c \propto A_\zeta$, the characteristic strain value is $\sim 10^{-28}$ at $f_{\rm GW} \sim \mathcal{O}(\text{MHz})$.

High frequency GW detection in the MHz - GHz range is a major target of interest for theorists. The prospects and challenges for future detection are discussed in the recent review [65] (we also refer to [123, 124] and references therein). One idea that has been proposed in the frequency range of our interest employs the inverse Gertsenshtein effect [113], in which a graviton can be converted resonantly into a photon in the presence of a static background magnetic field. Small strain values are still very difficult to measure because the rate of the inverse Gertsenshtein process is suppressed by h_c^2. Instead of measuring the converted photon directly, one can also measure the

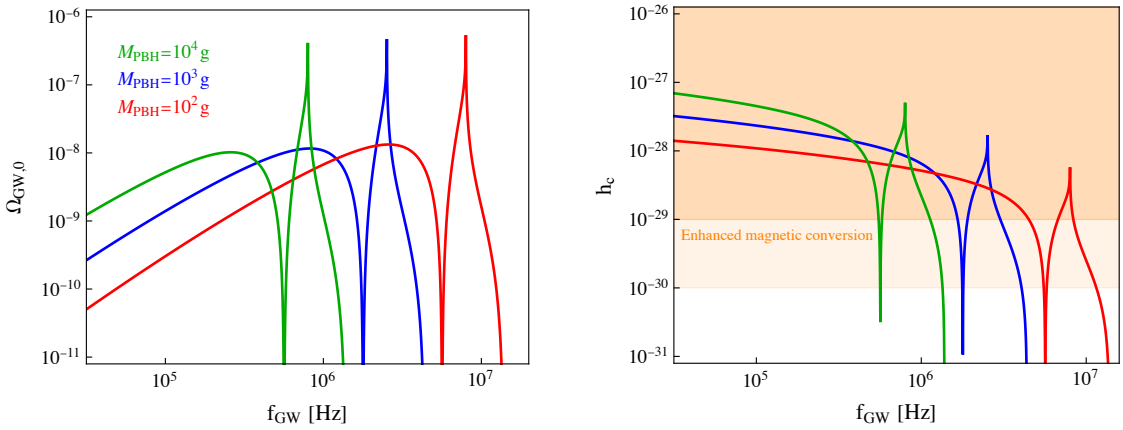


Figure 3.3: *Left panel:* The energy density of GWs as a function of the frequency, for three different values of $M_{\rm PBH}$: 10^2 g (red), 10^3 g (blue), and 10^4 g (green). The observed value of Y_B is obtained for each curve, with $\gamma_{CP} = 10^{-2}$ and $m_X < T_{\rm BH}$. The details of the calculation are in the text. *Right panel:* The strain h_c is shown as a function of the frequency for the three values of $M_{\rm PBH}$ from the left panel. The orange shaded regions show the future sensitivity limit of the high frequency GW probe using the inverse Gertsenshtein effect proposed in [113]. The dark orange shade is a conservative projection of the sensitivity, while the light orange shade is an optimistic projection.

GW conversion in a region where an auxiliary electromagnetic field is generated by placing a laser beam together with the magnetic field [125]. The event rate of the modified measurement is only linear in h_c hence the sensitivity of the proposal can be significantly improved. The initial proposal in [125] is aimed at 5 GHz frequency and a strain strength as small as $h_c \sim 10^{-30}$ (See Table 1 of [65]). The status of technology development for enhanced magnetic conversion is recently reviewed in [126] and the sensitivity to h_c is estimated to be $h_c \sim 10^{-29}$ when current state-of-art benchmarks are included. Further improvement is expected with the future development of gyrotrons, single-photon detectors and magnets. In Fig. 3.3 and Fig. 3.4, we show a conservative sensitivity projection ($h_c = 10^{-29}$) and an optimistic sensitivity projection ($h_c = 10^{-30}$) in dark and light orange shade respectively. We note that the above reach is shown for

completeness; clearly, a lot of work needs to be done by the community to probe GWs in this interesting high frequency range.

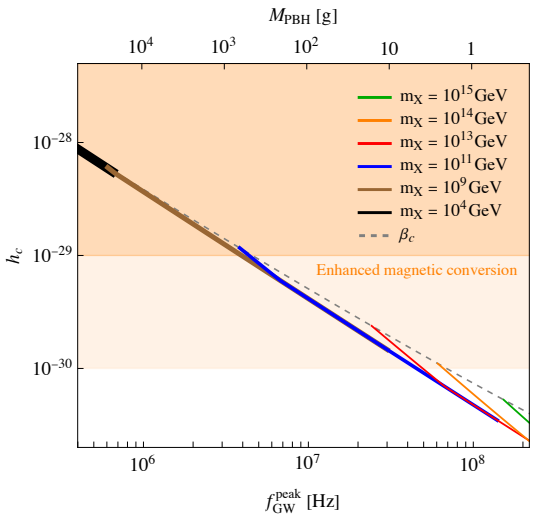


Figure 3.4: The strain at the peak frequency for high frequency GWs coming from light PBHs, as a function of the peak frequency (lower x-axis) and as a function of the light PBH mass (upper x-axis). The orange shaded regions show the future sensitivity limit of the high frequency GW probe using the inverse Gertsenshtein effect proposed in [113]. The darker orange region is a conservative projection of sensitivity, while the lighter orange region is an optimistic projection.

In Fig. 3.4, we study the strain at the peak of the GW spectrum as a function of the peak frequency (lower x-axis) and the PBH mass (upper x-axis). The different colors correspond to various values of m_X, with the color scheme following top right panel of Fig. 3.1. This calculation merits a caveat. As can be seen from Fig. 3.3, the GW signal is divergent at the peak, and the peak value for the energy density or strain actually depend on how close one approaches the peak frequency. The basic cause of this is the assumption of a delta function PBH mass function in Eq. (3.8), or, equivalently, a delta function power spectrum in Eq. (4.29). To plot the peak strain in Fig. 3.4, we instead choose a smoother power spectrum, whose details are provided in Appendix 1. The relation between β and $M_{\rm PBH}$ that gives the correct Y_B is first taken

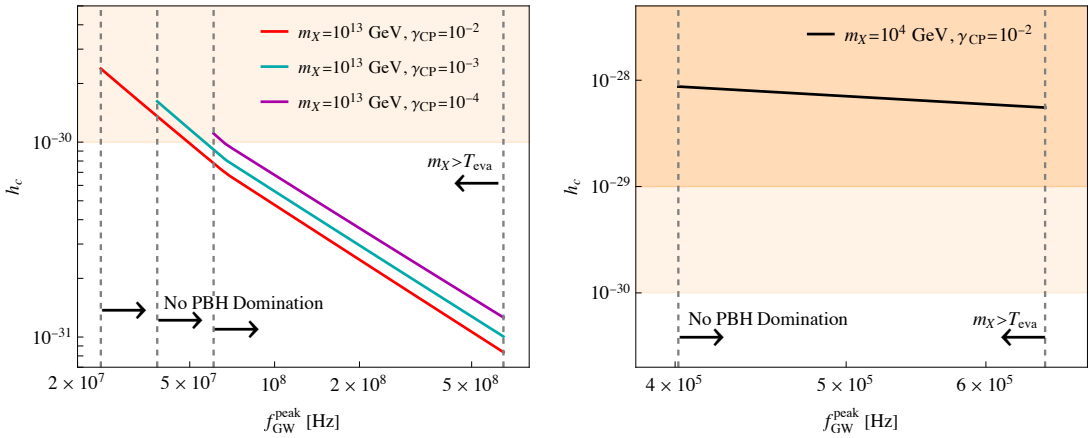


Figure 3.5: *Left panel:* The strain at the peak frequency for benchmark models of $m_X = 10^{13}$ GeV and different values of $\gamma_{CP} = 10^{-2}$ (red), 10^{-3} (cyan) and 10^{-4} (purple). The vertical dashed lines show the $f_{\rm GW}^{\rm peak}$ regions where successful baryogenesis can take place in a radiation-dominated universe. *Right panel:* The strain at the peak frequency for a benchmark model of $m_X = 10^4$ GeV and $\gamma_{CP} = 10^{-2}$. Note that a large γ_{CP} value is required for baryogenesis when m_X is small, as is shown in the bottom panel of Fig. 3.1.

from the top right panel of Fig. 3.1. Then, the amplitude of a delta function power spectrum that gives the correct β at a given $M_{\rm PBH}$ is obtained. The delta function is then "smoothed" with the spectrum that scales like k^4, depicted in the top left panel of Fig. A.1, keeping the same amplitude at the peak as the delta function. Finally, the GW spectrum is calculated with the smoothed k^4 spectrum and the value of the strain h_c at the peak frequency is obtained. The process is repeated for different PBH masses to obtain Fig. 3.4.

3.4.1 Scaling of strain with peak frequency

We are finally in a position to present our results on the $(f_{\rm GW}^{\rm peak}, h_c)$ plane for different choices of the particle physics parameters m_X and γ_{CP}. The results are shown in Fig. 3.5. In the left panel, we show the results for a choice of $m_X = 10^{13}$ GeV, for different values of $\gamma_{CP} = 10^{-2}, 10^{-3}$, and 10^{-4}. The vertical lines impose the conditions

to avoid PBH domination and washout. For each value of γ_{CP}, the curves have two scalings: the steeper one corresponds to $m_X > T_{BH}$, while the less steep portion corresponds to $m_X < T_{BH}$. In the right panel, we display the corresponding result for $m_X = 10^4$ GeV and $\gamma_{CP} = 10^{-2}$. Here, only the regime $m_X < T_{BH}$ applies.

Semi-analytic behaviors of the strain versus peak frequency curves can be found in the following way. The PBH abundance β needed to generate baryon asymmetry Y_B is calculated with Eq. (3.15) for chosen m_X, γ_{CP}, and $M_{\rm PBH}$. The power spectrum amplitude A_ζ is then obtained from β with Eq. (1.20) and Eq. (3.7) assuming contribution to baryogenesis is mainly from the peak mass.[7] The power spectrum k-mode can be solved from Eq. (1.19) and is related to the GW peak frequency $f_{\rm GW}^{\rm peak}$ in Eq. (3.26). To estimate the strain and energy density of GWs from the power spectrum, we used the approximation $\Omega_{\rm GW}(\eta_s, k) \simeq P_\zeta^2(k) \simeq A_\zeta^2$, which is shown to reproduce the correct order of magnitude at the peak frequency for log-normal power spectra in [36]. The results are:

$$h_c \sim 5.5\times10^{-27} \left(\frac{1\,\text{MHz}}{f_{\rm GW}^{\rm peak}}\right) \log\left[2.0\times10^{18} \left(\frac{1\,\text{MHz}}{f_{\rm GW}^{\rm peak}}\right)^2 \left(\frac{\gamma_{CP}}{10^{-2}}\right)^2 \left(\frac{8.7\times10^{-11}}{Y_B}\right)^2\right]^{-1}, \tag{3.29}$$

for

$$5.41\times10^2 \left(\frac{f_{\rm GW}^{\rm peak}}{1\,\text{MHz}}\right)^3 \text{GeV} \lesssim m_X \lesssim 1.33\times10^8 \left(\frac{f_{\rm GW}^{\rm peak}}{1\,\text{MHz}}\right)^2 \text{GeV}, \tag{3.30}$$

[7] We used the approximation $\text{Erfc}^{-1}(z)|_{z\to0} \simeq \sqrt{\frac{1}{2}\log[\frac{2}{\pi z^2}] - \frac{1}{2}\log[\log[\frac{2}{\pi z^2}]]} \sim \sqrt{\frac{1}{2}\log[\frac{2}{\pi z^2}]}$, with which the error is at about the 5% (9%) level for $\beta = 10^{-10}\,(10^{-5})$.

and

$$h_c \sim 5.5 \times 10^{-27} \left(\frac{1\,\mathrm{MHz}}{f_{\mathrm{GW}}^{\mathrm{peak}}}\right) \log\Bigg[5.9 \times 10^{14} \left(\frac{f_{\mathrm{GW}}^{\mathrm{peak}}}{1\,\mathrm{MHz}}\right)^6 \left(\frac{10^9\,\mathrm{GeV}}{m_X}\right)^4 \times \left(\frac{\gamma_{CP}}{10^{-2}}\right)^2 \left(\frac{8.7 \times 10^{-11}}{Y_B}\right)^2\Bigg]^{-1}, \tag{3.31}$$

for

$$1.33 \times 10^8 \left(\frac{f_{\mathrm{GW}}^{\mathrm{peak}}}{1\,\mathrm{MHz}}\right)^2 \mathrm{GeV} \lesssim m_X \lesssim 1.04 \times 10^8 \left(\frac{\gamma_{CP}}{10^{-2}}\right)^{1/2} \times \left(\frac{8.7 \times 10^{-11}}{Y_B}\right)^{1/2} \left(\frac{f_{\mathrm{GW}}^{\mathrm{peak}}}{1\,\mathrm{MHz}}\right)^{5/2} \mathrm{GeV}. \tag{3.32}$$

We note that the lower and upper bounds in Eq. (3.30) come from requiring $T_{\mathrm{eva}} < m_X$ and $m_X < T_{\mathrm{PBH}}$, respectively. Since T_{eva} and T_{PBH} are obtained in terms of M_{PBH} from Eq. (5.33) and Eq. (1.6) respectively, and M_{PBH} can be expressed in terms of the peak GW frequency through Eq. (3.27), this allows us the express the bounds on m_X in terms of $f_{\mathrm{GW}}^{\mathrm{peak}}$. Similarly, the lower and upper bounds in Eq. (3.32) are obtained by requiring $T_{\mathrm{PBH}} < m_X$ and $\beta < \beta_c$, respectively.

3.4.2 Gravitational Waves and PBH Domination

The calculation of GWs induced during a period of matter (PBH) domination has been considered by several authors. We refer to [83, 88, 127, 128, 129] for details and mention only a few major features here. Firstly, the peak frequency from secondary GWs from a PBH-dominated era lies in the $\mathcal{O}$(kHz) range and is given by [83]

$$f_{\mathrm{GW}}^{\mathrm{peak}} \sim 10^3\,\mathrm{Hz} \times \left(\frac{M_{\mathrm{PBH}}}{10^4\mathrm{g}}\right)^{-5/6}. \tag{3.33}$$

Since PBH domination occurs for $3 \times 10^4 \text{g} \lesssim M_{\text{PBH}} \lesssim 10^9$ g, the peak of the GW spectrum falls in the range of the Einstein Telescope (for the lighter end of the allowed PBH masses) and BBO or DECIGO (for the heavier end of the allowed PBH masses).

Secondly, the amplitude of the induced GWs at the peak frequency has been estimated to be

$$\Omega_{\text{GW}} \sim 10^{-7} \times \left(\frac{\beta}{10^{-6}}\right)^{16/3} \left(\frac{M_{\text{PBH}}}{10^4 \text{g}}\right)^{34/9}, \tag{3.34}$$

for very sharp mass functions, and a correspondingly suppressed amplitude for wider ones. Further exploration of GWs in an era of PBH domination is beyond the scope of the current work. We therefore delineate all regions of parameter space where PBH domination occurs and reserve them for future study.

3.5 Double-Peaked Gravitational Waves and Dark Matter-Baryogenesis Coincidence Problem

Probes of DM cover numerous possible candidates and production mechanisms and span over many decades of possible DM masses and couplings, with the aim of explaining the observed relic abundance $\Omega_{\text{CDM}}h^2 = 0.1200 \pm 0.0012$ [112]. Given that the production of DM in the early Universe is totally independent of baryogenesis, and the models employed to address the two questions are usually very different and independent of each other, it is a mystery why their abundances in the current Universe come out so close to each other: $\Omega_{\text{CDM}}/\Omega_B \sim 5$. This is the so-called coincidence problem and has led to a huge amount of work in the community. Particularly well-motivated proposals that solve the coincidence problem include asymmetric DM [130], cladogenesis and its variations [117, 116, 131], pangenesis [132], cogenesis [133, 134], hylogenesis [135], etc.

PBHs have been utilized in the context of the coincidence problem. One option is to rely on Hawking evaporation of PBHs as a source of both baryogenesis and DM production [115]; this is reminiscent of models like cladogenesis or hylogenesis, which rely on the decay of a heavy beyond-SM species such as a modulus to give rise to DM and baryons. Other ideas of addressing the coincidence problem with PBHs have also been proposed recently [136, 137, 138, 139]. The general tenor of these forays is to invoke a *single* population of PBHs to address DM, baryogenesis, or both. On the other hand, it is in some sense natural to ask whether *multiple* disparate populations of PBHs can play a role in addressing different (ostensibly correlated) cosmological phenomena. From a UV perspective , two or more phases of PBH production may be deemed "fine-tuned", although typically the inflaton potential has enough freedom to afford multiple phases of ultra slow roll[8]. The issue of fine-tuning notwithstanding, multiple PBH populations would yield spectacular gravitational wave (GW) signals, in the form of correlated multiple peaks.

In this section, we outline a solution to the DM-baryogenesis coincidence problem by invoking *two* populations of PBHs: a population of light primordial black holes (LPBH) that is responsible for baryogenesis, and a population of heavy primordial black holes (HPBH) that constitutes DM. The LPBHs induce baryogenesis by the method described in the previous sections. The DM-baryon coincidence in our scenario is obtained as a ratio of the abundances and masses of the LPBH and HPBH populations, the number of relativistic degrees of freedom at the relevant times, and, from the particle physics side, the baryon asymmetry produced per decay of X. The main observational signature of our scenario lies in the GW spectrum, since curvature perturbations responsible for PBH formation also generate GW signals. The GW

[8]For fine-tuning estimates in achieving PBH formation, we refer to [25]. At the level of a canonical single-field inflationary potential, a single phase of PBH production requires approximately one-part-in-million fine-tuning of the coefficients of the potential.

spectrum will consist of two peaks corresponding to the two populations of PBHs. For the population of heavy PBHs to be stable today in order to constitute all of DM, we need $M_{\rm HPBH} \gtrsim 10^{15}$ g and the corresponding peak frequency is $\sim \mathcal{O}(\text{Hz})$. In frequency space, this translates to a hierarchy of $\gtrsim 10^6$ Hz between the two peaks corresponding to baryogenesis and DM.

While we reserve a full study of the relevant UV physics of PBH formation for the future, we note that the main feature is that the PBH mass function is required to be bimodal. Generally speaking, if PBHs are required to play some *combination* of roles in cosmology, then a multimodal mass function becomes a necessity, and our model is a special case of the scenarios envisioned in [140][9].

3.5.1 Bi-modal mass function

We begin our discussion by appropriately modifying the PBH mass function. We assume that there are two mass function peaks and define

$$\frac{d\beta(M_{\rm PBH}, t_i, t)}{d\log M_{\rm PBH}} = \frac{d\beta_L(M_{\rm L}, t_{i,L}, t)}{d\log M_{\rm L}} + \frac{d\beta_H(M_{\rm H}, t_{i,H}, t)}{d\log M_{\rm H}}, \tag{3.35}$$

with the subscripts "L" and "H" standing, respectively, for the population of LPBHs and HPBHs. We then have

$$\beta_L = \frac{n_L(t_{i,L})M_L}{\rho(t_{i,L})}, \qquad \beta_H = \frac{n_H(t_{i,H})M_H}{\rho(t_{i,H})}. \tag{3.36}$$

[9] Multimodal PBH mass functions have been investigated in other contexts by several groups recently. They may arise from oscillations [141, 142] or multi-parametric resonances [143] in the sound speed during inflation, multiple stages of ultra slow-roll inflation [91], or oscillatory features in the power spectrum of inflation from a choice of non-Bunch-Davies vacua [140, 144].

We parameterize the double peaked power spectrum with peak locations at $k_0 = k_{\rm H/L}$ as

$$\begin{aligned} P_\zeta(k) &= P_{\zeta,H}(k) + P_{\zeta,L}(k) \\ &= A_H \delta\left(\log\left(\frac{k}{k_H}\right)\right) + A_L \delta\left(\log\left(\frac{k}{k_L}\right)\right). \end{aligned} \tag{3.37}$$

Here, $P_{\zeta,H}$ is responsible for the production of the heavy PBHs and $P_{\zeta,L}$ for the light PBHs.

3.5.2 Coincidence Problem

If HPBH formation happens within the radiation-dominated era, the contribution of HPBHs to the cold DM abundance today, which is expressed in terms of the ratio of the current HPBH mass density to that of the CDM density,

$$f = \frac{\Omega_{\rm HPBH}}{\Omega_{\rm CDM}}, \tag{3.38}$$

can be evaluated as follows [127]. In the remainder of this section, we call the masses of the two populations of PBHs as M_L and M_H, standing for light PBHs responsible for baryogenesis and HPBHs responsible for DM, respectively. Similarly, the abundances of the two species are labelled β_L and β_H.

The fraction of the energy of Universe in HPBHs at their formation time is related to their number density during the radiation era by

$$\beta_H = \frac{\rho_{\rm HPBH}(t_i)}{\rho_{\rm R}(t_i)} = \frac{M_H n_H(t_{i,H})}{\rho_{\rm R}(t_{i,H})} = \frac{4}{3}\frac{g_{\star,S}(T_{i,H})}{g_\star(T_{i,H})}\frac{M_H}{T_{i,H}}\frac{n_H(t_{i,H})}{s(t_{i,H})} = \frac{4}{3}\frac{g_{\star,S}(T_{i,H})}{g_\star(T_{i,H})}\frac{M_H}{T_{i,H}}\frac{n_H(t_0)}{s(t_0)}. \tag{3.39}$$

Therefore the current density parameter for HPBHs is given by

$$\Omega_{\rm HPBH} = \frac{M_H n_H(t_0)}{\rho_c} = \frac{3}{4}\frac{g_\star(T_{i,H})}{g_{\star,S}(T_{i,H})}\beta_H \frac{s(t_0)}{\rho_c} T_{i,H}(M_H) \tag{3.40}$$

$$= \left(\frac{2.7\times10^8}{\rm GeV}\right) h^{-2}\frac{3}{4}\frac{g_\star(T_{i,H})}{g_{\star,S}(T_{i,H})}\beta_H T_{i,H}(M_H), \tag{3.41}$$

since $s(t_0) = 2891.2\,{\rm cm}^{-3}$ and $\rho_c = 1.052\times10^{-5}h^2\,{\rm GeV\,cm}^{-3}$.

Hence

$$f = \frac{\Omega_{\rm HPBH}}{\Omega_{\rm CDM}} = \left(\frac{2.7\times10^8}{\rm GeV}\right)\left(\frac{1}{\Omega_{\rm CDM}h^2}\right)\frac{3}{4}\frac{g_\star(T_{i,H})}{g_{\star,S}(T_{i,H})}\beta_H T_{i,H}(M_H)$$

$$= \left(\frac{1}{\Omega_{\rm CDM}h^2}\right)\frac{3}{4}\beta_H\left(\frac{T_{i,H}(M_H)}{6.6\times10^{-33}{\rm g}}\right). \tag{3.42}$$

The initial abundance of HPBHs which can explain a fraction f of cold DM today is given by

$$\beta_H = \frac{8\pi^{3/4}}{3\sqrt{3}\,5^{1/4}}\frac{g_{\star,S}(T_{i,H})}{g_\star^{3/4}(T_{i,H})}\frac{\rho_c}{s(t_0)}\gamma^{-1/2}\Omega_{\rm CDM}f\left(\frac{M_H}{M_{\rm Pl}^3}\right)^{1/2}. \tag{3.43}$$

To understand the coincidence problem in the context of this scenario, we obtain the ratio f/Y_B:

$$\frac{f}{Y_B} = \frac{\beta_H}{\beta_L}\frac{1}{\gamma_{CP}}\frac{1}{\Omega_{\rm CDM}h^2}\frac{1}{N_\chi}\frac{T_{i,H}(M_H)}{T_{i,L}(M_L)}\left(\frac{M_L}{6.6\times10^{-33}{\rm g}}\right)$$

$$= \frac{\beta_H}{\beta_L}\frac{1}{\gamma_{CP}}\frac{1}{\Omega_{\rm CDM}h^2}\frac{1}{N_\chi}\left(\frac{g_\star(T_{i,L})}{g_\star(T_{i,H})}\right)^{1/4}\sqrt{\frac{M_L}{M_H}}\left(\frac{M_L}{6.6\times10^{-33}{\rm g}}\right). \tag{3.44}$$

By fixing the particle physics (m_X and γ_{CP}), the coincidence problem thus manifests itself as the right choice of PBH masses, M_L and M_H, and their initial abundances, β_L and β_H.

The left panel of Fig. 3.6 shows the upper limit on the initial abundance of HPBHs that can explain the whole abundance of DM today, as a function of the mass of

HPBHs. The lower limit on the mass of HPBHs, 10^{15} g corresponds to the minimum mass of HPBHs that can survive until today. We note that HPBHs are subject to other cosmological and astrophysical constraints that we did not show in this Figure. For an extensive review of these constraints and their current status see [145, 146, 147, 148, 149] and references within.

3.5.3 Formation of Heavy Primordial Black Holes in a Matter-(PBH-) Dominated Era

The possibility of formation of PBHs within an early matter-dominated era was first studied as a cosmological probe of grand unified theories [150, 151]. In these models, the predicted unstable heavy particles can dominate the energy density of the Universe before their decay and start an early matter-dominated epoch. While the lack of pressure enhances the probability of formation of PBHs within an early matter-dominated era, inhomogeneity and anisotropy of density perturbations can hinder formation of PBHs [150, 151, 128]. It can be shown that inhomogeneity and anisotropy of density perturbations reduce the probability of formation by a factor of $\sigma^{3/2}$ and σ^5 respectively. The probability of formation of PBHs during an early matter-dominated era is shown to be equal to [150]:

$$\beta(M_{\rm PBH}) \approx 0.02\sigma^{13/2}(M_{\rm PBH}). \tag{3.45}$$

If the early matter-dominated epoch begins at $t = t_{{\rm m},i}$ and ends at $t = t_{{\rm m},f}$, then the mass of PBHs form during this time interval falls in the following mass range [150]:

$$M_{\rm min} \sim M_{\rm hor}(t_{{\rm m},i}) \lesssim M_{\rm PBH} \lesssim M_{\rm max} \sim M_{\rm hor}(t_{{\rm m},f})\sigma(M_{\rm max})^{3/2}, \tag{3.46}$$

where $M_{\rm hor}$ denotes the horizon mass, and $M_{\rm max}$ is obtained by assuming that fluctuations at scale $M_{\rm max}$ enter the horizon at $t(M_{\rm max})$ and grow to nonlinear regime and decouple before $t_{{\rm m},f}$ [150].

A population of HPBHs can form when a population of LPBHs dominate the energy density of the Universe, if the heavy mode, k_H, which is responsible for formation of HPBHs, re-enters the horizon during LPBH domination. We assume LPBHs form at $t = t_{i,L}$ with probability β_L and with a mass equal to $M_L = \gamma M_{\rm hor}(t_{i,L})$ in a radiation-dominated Universe, they dominate the energy density at $t = t_{LD}$, and eventually they evaporate at $t = t_{L,\rm eva} = t_{i,L} + \tau_L \simeq \tau_L$, where $t_{i,L} \lesssim t_{LD} \lesssim \tau_L$. To guarantee that LPBHs come to dominate the energy density of the Universe before their evaporation, we require $\beta_L \geq \beta_c$. We denote the time of re-entry of k_H mode to horizon and equivalently the formation time of HPBHs by $t = t_{i,H}$ where $t_{LD} \lesssim t_{i,H} \lesssim \tau_L$ to make sure that formation happens within LPBHs domination. According to Eq. (3.46), production of HPBHs enhances over the mass range given by:

$$M_{\rm hor}(t_{LD}) \lesssim M_H \lesssim M_{\rm hor}(\tau_L)\sigma^{3/2}(M_{\rm Max}). \tag{3.47}$$

The initial abundance of LPBHs, β_L, selects the domination time, t_{LD}, from the range $t_{i,L} \lesssim t_{LD} \lesssim \tau_L$. For $0.5 \leq \beta_L \leq 1$, LPBHs domination happens at their formation time, i.e., $t_{LD} = t_{i,L}$, and this corresponds to the smallest possible HPBH mass. For $\beta_c \leq \beta_L < 0.5$, LPBHs domination happens before their evaporation. The maximum possible mass for HPBHs is determined by τ_L via Friedemann equation, $H(\tau_L) = 2/(3\tau_L)$. Therefore, for $\beta_L \geq \beta_c$, if k_H re-enters the horizon while LPBHs dominate the Universe, HPBHs can form within the following mass range:

$$M_L/\gamma \lesssim M_H \lesssim \frac{7680\pi}{g_\star(T_{\rm LPBH})}\frac{M_L^3}{M_{\rm Pl}^2}\sigma^{3/2}(M_{\rm Max}). \tag{3.48}$$

In Fig. 3.6 (right panel), we display the different possibilities for formation of HPBH. The heavy mode can re-enter the horizon within a radiation-dominated era succeeded by an early matter-(LPBH-) dominated era ($k_{H,1}$), or during an early matter-dominated era followed by a secondary radiation-dominated epoch ($k_{H,2}$), or in a radiation-dominated era proceeded by an early matter-dominated era ($k_{H,3}$). The treatment for HPBHs formed during an era of LPBHs domination is beyond the scope of this paper and is left for future work.

3.5.4 Double-Peaked Gravitational Waves

In this subsection, we provide a computation of the GW spectrum coming from the two populations of PBHs. As noted in Eq. (3.37), the power spectrum consists of two contributions: $P_{\zeta,H}$, which is responsible for the production of the heavy PBHs and $P_{\zeta,L}$, which is responsible for the light PBHs. We first turn to the question of whether there could be an additional contribution to the GW signal from the crossing term $P_{\zeta,H} \times P_{\zeta,L}$. In Fig. 3.7, we show the relative amplitude of the cross term contribution to P_h with arbitrary choice of two scalar modes[10]. The u/v parameter is the ratio of the chosen tensor mode wave number $k_{\rm GW}$ and the scalar modes wave number k_H/k_L. As is shown in the figure, the GW amplitude is non-vanishing only in the regions with $u \sim v \sim 1$, which is equivalent to $k_{\rm GW} \sim k_H \sim k_L$. The suppression on GW production outside this region is a result of the hierarchical splitting of the two scalar modes. Momentum conservation is satisfied only when the scalar modes are close in Fourier space. Since the the scalar modes of interest in our case have a large hierarchy $k_L/k_H \sim 10^8$, the cross term contribution is negligible in our study. We leave the

[10]Here we ignore the decay of sub-horizon modes in order to illustrate the property of the tensor mode. The decay of sub-horizon modes during radiation domination will further suppress the GW signal.

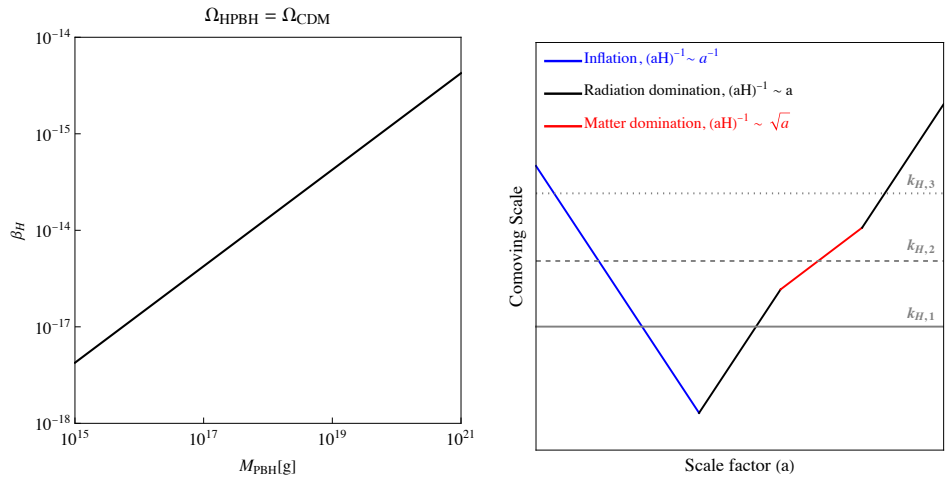


Figure 3.6: *Left panel*: The initial abundance of HPBHs, β_H, as a function of the HPBH mass, assuming that HPBHs can explain all the observed abundance of DM. *Right panel*: The different options for the formation of HPBHs are displayed. The segment in red denotes a phase of LPBH (matter) domination. $k_{H,1}$, $k_{H,2}$, and $k_{H,3}$, denote, respectively, the cases when HPBHs are formed prior to, during, and after the LPBH dominate the energy density of the Universe.

detailed study of GWs from cross terms to future work, since in certain cases where the hierarchy is smaller there could be interesting effects.

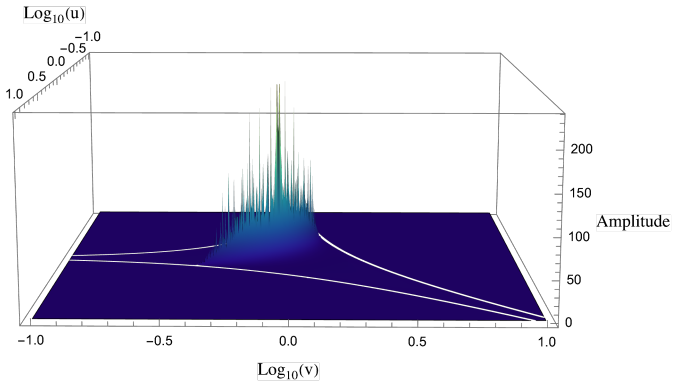


Figure 3.7: The relative amplitude of cross term contribution to P_h as a function of wave numbers of two scalar modes.

Having established that the cross term contribution is negligible in our case, we calculate the full GW spectrum signal by adding contributions calculated with each monochromatic curvature perturbation peak separately. In Fig. 3.8 (left panel), we

show the double peaked GW spectrum that results from our model. We choose a benchmark value of the scalar perturbation wavenumber that gives the peak location of heavy PBH mass function at $M_H = 10^{18}$ g. For the light PBHs, we also choose benchmarks of high-k modes that gives the peak location $M_L = 10^3$ g. We further require $f = 1$ and $Y_B = 8.7 \times 10^{-11}$ in Eq. (3.44). Since the horizon re-entry time is well defined by the horizon mass of interest, the peak location of the GW spectrum can be estimated directly from the mass of the light and heavy PBH species. Therefore the bimodal PBH mass function is strongly correlated with a double-peaked GW spectrum.

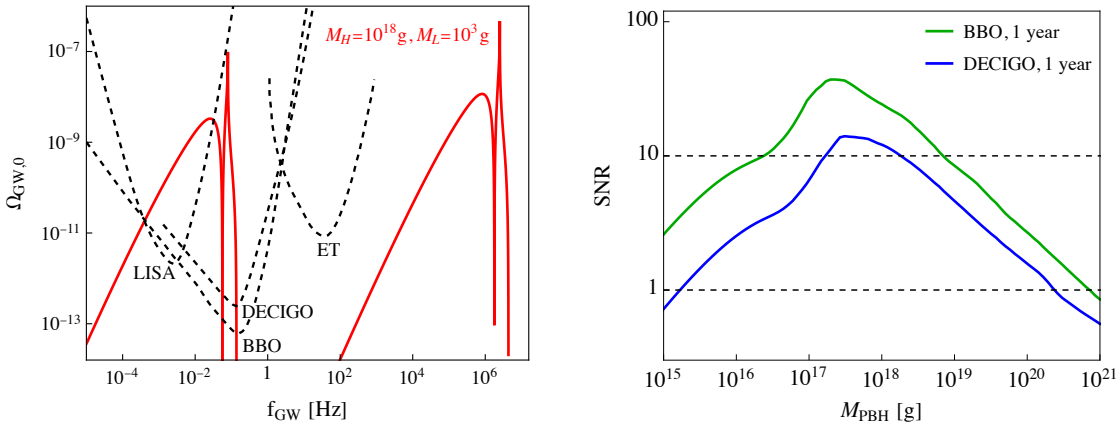


Figure 3.8: *Left panel*: A benchmark GW spectrum from scalar perturbation modes. In the sub-Hz region, we show the GW radiation from perturbations that generated heavy PBH distributions peaked at $M_H = 10^{18}$ g. In the high-frequency region, we show the GW radiation from perturbations generating lighter PBHs at $M_L = 10^3$ g with initial abundance calculated assuming $m_X < T_{\rm BH}$. Sensitivities of future GW observatories are shown with black dashed curves. *Right panel*: The Signal-to-Noise Ratio of second order GW signals at the low frequency peak for future detectors like BBO (green) and DECIGO (blue). The observation time is assumed to be one year. The $M_{\rm PBH}$ is the peak mass of the heavy PBH species that make up 100% DM relic abundance.

The GW signal from the formation of heavy PBHs peaks at $f_{\rm GW} \sim$ Hz. Future GW observatories, for example BBO [152] and DECIGO [153, 154], can perform a precise measurement of the scalar perturbations in this region. In Fig. 3.8 (right panel), we show the Signal-to-Noise Ratio (SNR) of the induced GW signals from $P_{\zeta,H}$ with

one-year measurements in BBO and DECIGO. The peak location $M_{\rm PBH}$ of the heavy PBH mass function is calculated with the horizon mass in the course of k_H re-entry in Eq.(1.19). The amplitude of $P_{\zeta,H}$ is chosen such that heavy PBHs explain the DM relic abundance in the cosmological coincidence problem. As is discussed previously, the interference between the two peaks can be neglected because of the large separation in their frequencies. We calculated the GW signal in the BBO and DECIGO frequency band with only $P_{\zeta,H}$ and checked the crossing term contribution is negligible. As a result of the large density perturbation for PBH formation, the SNRs in both detectors are larger than one for the mass region that PBH can make up DM.

The main observational feature here is the double-peaked GW signal. In Section A of the Appendix, we give an outline for constructing an inflaton potential that can give rise to two spikes in the power spectrum, through two ultra slow-roll phases.

3.6 Conclusions

The purpose of this work has been to highlight the importance of the ultra high frequency GW frontier for topics like baryogenesis that have traditionally been of interest to particle theorists. Broadly speaking, electroweak baryogenesis is the main setting where the confluence of collider and GW physics has been extensively studied (we refer to some representative papers [155, 156, 67, 157, 158, 159] in this vast literature). This is of course driven by the classic status of electroweak baryogenesis, but also by the fact that the peak frequency of the GWs in this case is in the target window of upcoming space-based detectors. In contrast, the high frequency regime where PBH-induced baryogenesis can occur is much more challenging to probe, but, in our opinion, no less important. PBHs, if they exist, provide a window into the very early inflationary era of the Universe and also connect to topics like baryogenesis, DM, and dark radiation.

We have calculated the parameter space on the strain versus peak frequency plane for baryogenesis to successfully occur, being careful to identify washout and PBH-dominated regimes. The results have been shown for different values of the particle physics inputs, such as m_X and γ_{CP}. Semi-analytic scaling have been provided. We have also outlined a scenario where two populations of PBHs: one heavy and one light - can address the DM-baryogenesis coincidence problem.

There are several future directions to explore. Firstly, in this study, we have focused on the scenario where the energy density of PBHs is always a sub-dominant component of the total energy density of the universe. Therefore, GW signals produced during horizon re-entry redshift with the cosmological expansion as a fixed fraction of radiation. On the other hand, any non-standard cosmology that dilutes the energy density of radiation will also affect the GW signal, leading to a suppressed strain today. In particular, the dilution could happen when PBHs are over-produced from a large curvature perturbation such that there was a PBH-dominated epoch in the early universe. While there is nothing inconsistent about transitioning to a PBH-dominated phase, the GW signal is typically suppressed when such a phase occurs. Nevertheless, it would be interesting to investigate how the predicted signals in our scenario change when one also has a PBH-dominated cosmology. This is especially interesting when a population of heavy PBHs starts forming in the background of a cosmology dominated by a population of light PBHs.

It is also important to probe the correlations between DM, dark radiation, PBHs, and GWs along the same lines as has been pursued in this work. The most important future direction is to creatively think about and propose detection techniques for GWs in the MHz - GHz range.

Chapter 4

The Primordial Black Holes that Disappeared: Connections to Dark Matter and MHz-GHz Gravitational Waves

4.1 Introduction

A particularly illuminating way of classifying primordial black holes (PBHs) is the following: (i) PBHs heavier than $\mathcal{O}(10^{15})g$ that are stable enough to have persisted to this day, and could constitute all or part of dark matter (DM); and (ii) PBHs lighter than $\mathcal{O}(10^{9})g$ that disappeared via Hawking evaporation before Big Bang Nucleosynthesis (BBN). In the post-LIGO era, it is the first category that has garnered a lot of attention; justifiably so, since a variety of tests can be proposed to probe their existence. We refer to [67, 68, 69, 70, 71, 72, 73, 74, 160, 161, 162, 127, 163, 164, 165, 166, 167, 168, 169, 170, 171, 172, 173, 148, 37, 174, 38, 175, 176] and references in the recent review [177, 146] as a sample of this vast literature.

In contrast, the second branch of the PBH family - those that disappeared early on - has received far less attention as far as their detection is concerned. The conventional requirement is that the Hawking evaporation should occur before BBN. More sophisticated bounds from BBN are reported in [146], using methods developed in [178, 179] for constraining the reheating temperature from the PBH evaporation. In a sense, this branch of the PBH family shares the problem of all other putative relics that could have

existed in the early Universe – compatibility with BBN necessitates that they leave the Universe in a state of thermal equilibrium by the time they vanish, obscuring their very existence, which must then be inferred indirectly. The example of cosmological moduli is instructive in this regard: their existence can be inferred from their effect on particle physics, for example the physics of DM, baryogenesis [122, 121], or cosmology [180]. This class of light PBHs are fascinating objects, serving as a portal to beyond-Standard Model physics. Since all dark/hidden sector particles couple at least to gravity, they would have been produced when PBHs underwent Hawking evaporation, providing a particularly rich and model-independent window into new physics[1]. Connections to DM [103, 104, 105, 106, 12, 107, 182, 183, 184], dark radiation [108, 109, 110, 185, 186], and baryogenesis [11, 93, 94, 95, 96, 97, 187, 98, 99, 100, 188, 101, 102, 189, 190, 191] in the primordial Universe, as well as axion-like particles at low redshift [192, 193] have been investigated by various authors.

One could then ask: could the PBHs that disappeared early on have left behind telltale signatures of their existence? Here the answer can be in the affirmative depending on the PBH formation mechanism, although it requires us to probe an extremely challenging experimental frontier: ultra-high frequency (MHz-GHz) gravitational waves (GWs) [65]. The reason is as follows. PBHs, during their formation stage, are typically accompanied by the emission of GWs. The precise origin of the GWs depends on the formation mechanism: for example, in the canonical example of PBHs coming from curvature perturbations during inflation, the source is second-order effects in perturbation theory [77, 78, 79, 80, 81, 194, 85, 36, 83, 88, 89, 86, 87, 84, 82]; on the other hand, for the case of PBHs formed during a first-order phase transition (FOPT), the FOPT itself serves as the source of GWs. The peak frequency of the emitted GWs typically scales inversely with the mass $M_{\rm PBH}$ of the PBHs; for the low mass regime

[1]This can be contrasted with the case of cosmological moduli, whose coupling to hidden sector particles is much more model-dependent [181].

relevant for the PBHs that disappeared, and for certain formation mechanisms, the frequency lies in the MHz-GHz range[2].

The purpose of this paper is to explore the signatures of PBHs in the MHz-GHz GW frontier, juxtaposed with their connection to DM. The overall scheme is as follows. PBHs are assumed to Hawking evaporate into a DM particle χ that couples to the Standard Model exclusively through gravity and yields the observed relic density. We remain agnostic to the specific nature of χ. The correct relic abundance is obtained by a combination of three parameters: the mass and abundance of the PBHs ($M_{\rm PBH}$ and $\beta_{\rm PBH}$, respectively) and the mass of the DM particle (m_χ). Given a benchmark value of m_χ, one then has a region in the plane $\{M_{\rm PBH}, \beta_{\rm PBH}\}$ where the correct relic density is achieved; in this same regime, one can calculate the correlated ultra-high frequency GWs. Ultimately, one has a DM-compatible map on the strain-frequency plane ($\{h_c, f_{\rm GW}\}$) in the ultra-high frequency GW frontier.

The map from the plane characterizing the PBH properties $\{M_{\rm PBH}, \beta_{\rm PBH}\}$ to the plane characterizing GWs $\{h_c, f_{\rm GW}\}$ depends on the PBH formation mechanism. We explore two such formation mechanisms. The first is the canonical formation of PBHs by curvature perturbations during inflation [16, 17, 18, 19, 20, 21, 22, 23, 24, 25, 26, 27]. Over-dense regions can collapse into a PBH when they enter the causal horizon. In this case, GWs originate from second-order effects. The same scalar perturbation responsible for the PBH formation contributes to tensor modes at horizon reentry. The map from the space of PBH properties to GWs is the following: $\{\Omega_\chi h^2, m_\chi\} \rightarrow \{M_{\rm PBH}, \beta_{\rm PBH}\} \rightarrow \{A_\zeta, k_p\} \rightarrow \{h_c, f_{\rm GW}\}$, where A_ζ is the amplitude of the power spectrum of the curvature perturbation and k_p is the peak location of the power spectrum.

[2]While correlations between Hawking evaporation and GWs generated during the formation of PBHs have been used to study stable PBHs [38, 175, 176], the method also holds great potential for lighter PBHs that evaporated away. For instance, baryogenesis arising from the Hawking radiation of light PBHs has been studied by the current authors [191]. The associated MHz-GHz GWs induced by curvature perturbations have been highlighted as a method to investigate the cosmology of PBHs, even if they have completely evaporated.

The second formation mechanism we explore is the formation of PBHs from first-order phase transitions (FOPTs). The possibility of forming PBHs from collision of bubble walls during FOPTs has been studied for several decades [40, 41, 42, 43, 44, 45]. Here, we choose the more recently proposed mechanism of PBH formation from the collapse of particles trapped in the false vacuum [46, 47, 48, 49, 50, 51]. The source of GWs in this case is the FOPT itself. The map from the space of PBH properties to GWs in this case is the following: $\{\Omega_\chi h^2, m_\chi\} \to \{M_{\rm PBH}, \beta_{\rm PBH}\} \to \{\alpha, \beta, T_\star, v_w\} \to \{h_c, f_{\rm GW}\}$, where $\alpha, \beta, T_\star$ and v_w are the energy density released during phase transition normalized by the radiation energy density; the inverse time scale of the phase transition; the temperature of the phase transition; and the bubble wall velocity, respectively.

One can further enquire: do the maps described above enable one to *distinguish* between PBH formation mechanisms? In other words, given $\{\Omega_\chi h^2, m_\chi\}$, does one map to different points in the space of $\{h_c, f_{\rm GW}\}$ depending on the intermediate steps? The answer turns out to be in the affirmative, holding out the promise not only that ultra-high frequency GWs will provide a connection between PBHs and DM, but also indicate the origin mechanism. A fair criticism of the kind of precision study we are advocating is that the experimental status of ultra-high frequency GWs is not mature enough to be amenable to such studies yet. Our response is that this is a frontier of critical importance, as evidenced by the many ideas for probing it that have flowered recently [195, 196, 197, 198, 199, 200, 201, 202, 123, 203, 204, 205, 124, 206, 207, 208][3].

4.2 Dark Matter from Hawking Radiation

In this section, we compute the mass and abundance of light PBHs that Hawking evaporate to give the observed relic density of DM. We will be largely agnostic about

[3]Moreover, as we will see, CMB-Stage 4 experiments [209] will come close to probing at least some formation mechanisms.

the nature of the DM particle χ, which could be fermionic or bosonic. We also discuss how the two different origin mechanisms of the PBHs affect the required mass and abundance.

4.2.1 Particle Production through Hawking Radiation

We begin with a discussion of the Hawking evaporation of PBHs into χ. PBHs which originated from a radiation-dominated era acquire negligible spin due to the pressure of the radiation [210]. Therefore, we assume that all the PBHs are Schwarzschild (non-rotating). Ignoring the deviation of the Hawking radiation from the black body spectrum which is expressed as greybody factors [13], the energy spectrum of the χ particle of mass m_χ with g_χ degrees of freedom is given by:

$$\frac{d^2 u_\chi(E,t)}{dtdE} = \frac{g_\chi}{8\pi^2} \frac{E^3}{e^{E/T_{\rm PBH}(t)} \pm 1}, \tag{4.1}$$

($+$ for fermion emission and $-$ for boson emission) where $u_\chi(E,t)$ is the total radiated energy per unit area of the BH, and E is the energy of the emitted particle.

The rate of emission of the χ particle per energy interval can be expressed as

$$\frac{d^2 N_\chi}{dtdE} = \frac{4\pi r_{\rm S}^2}{E} \frac{d^2 u_\chi}{dtdE}, \tag{4.2}$$

where $r_{\rm S} = 2M_{\rm PBH}/M_{\rm Pl}^2$ is the Schwarzschild radius of the PBH. The total number of χ particles, provided that it is a boson (B), emitted over the PBH lifetime is obtained by integrating Eq. (4.2) over energy and time:

$$N_\chi = \frac{120\,\zeta(3)}{\pi^3} \frac{g_\chi}{g_\star(T_{\rm PBH})} \frac{M_{\rm PBH}^2(t_\star)}{M_{\rm Pl}^2}, \qquad T_{\rm PBH}(t_\star) > m_\chi, \tag{4.3}$$

$$N_\chi = \frac{15\,\zeta(3)}{8\pi^5} \frac{g_\chi}{g_\star(T_{\rm PBH})} \frac{M_{\rm Pl}^2}{m_\chi^2}, \qquad T_{\rm PBH}(t_\star) < m_\chi. \tag{4.4}$$

The total number of fermionic species (F) is $N_F = \frac{3}{4}\frac{g_F}{g_B}N_B$.

4.2.2 PBH Evaporation in a Radiation-Dominated Era

The amount of DM produced via Hawking evaporation of PBHs in a radiation-dominated era can be evaluated by using conservation of entropy. The DM yield today, at t_0, is given by:

$$Y_\chi = \frac{n_\chi(t_0)}{s(t_0)} = \frac{n_\chi(t_{\rm eva})}{s(t_{\rm eva})} \simeq N_\chi \frac{n_{\rm PBH}(t_\star)}{s(t_\star)}, \tag{4.5}$$

where $n_\chi(t)$ and $n_{\rm PBH}(t)$ are the number densities of DM particles χ and PBHs, respectively. We presume there is no number changing process in the DM sector after PBH evaporation. N_χ is the total number of particles χ emitted by one PBH (Eq. (4.3) and Eq. (4.4)), and $s(t)$ is the entropy density given by

$$s(T) = \frac{2\pi^2}{45} g_{*,s}(T) T^3, \qquad g_{*,s}(T) = \sum_B g_B \left(\frac{T_B}{T}\right)^3 + \frac{7}{8}\sum_F g_F \left(\frac{T_F}{T}\right)^3. \tag{4.6}$$

The entropy from PBH evaporation is negligible when the energy density of PBHs remains a small fraction of the Universe. Assuming a fraction $\beta_{\rm PBH}$ of the energy density of the Universe collapses into PBHs at the formation time, the yield of DM is therefore

$$Y_\chi = \beta_{\rm PBH} N_\chi \frac{1}{M_{\rm PBH}} \frac{\rho_{\rm rad}(t_i)}{s(t_i)} = \frac{3}{4}\frac{g_\star(T_i)}{g_{\star,s}(T_i)} \beta_{\rm PBH} N_\chi \frac{T_i(M_{\rm PBH})}{M_{\rm PBH}}, \tag{4.7}$$

where $\rho_{\rm rad}(t_i)$ and $T_i(M_{\rm PBH})$ are the energy density and the temperature of the Universe at the PBH formation time respectively. The mass of PBHs basically follows the horizon mass at the formation time, but the exact relationship between PBHs' mass and the temperature of the Universe at the formation time depends on the formation mechanism (See Section 4.3 for two examples).

The relic abundance of DM is obtained as:

$$\Omega_\chi = \frac{\rho_{\chi(t_0)}}{\rho_c} = \frac{m_\chi Y_\chi}{\rho_c} s(t_0), \tag{4.8}$$

where $\rho_c(t_0) = 1.0537 \times 10^{-5}\, h^2$ GeV cm^{-3}, $s(t_0) = 2891.2\,(T_0/2.7255\text{K})^3\,\text{cm}^{-3}$, and $h = 0.674$ is scaling factor for Hubble expansion rate [211].

While the energy density of radiation dilutes as $\rho_{\rm rad}(t) \propto a^{-4}$ with the expansion of the Universe, the energy density of PBHs decreases as the energy density of non-relativistic matter, i.e., $\rho_{\rm PBH}(t) \propto a^{-3}$, where a is the scale factor. Since $\rho_{\rm PBH}(t)/\rho_{\rm rad}(t) \sim a$, a population of PBHs formed within a radiation-dominated era may lead to a transition to an early matter-dominated epoch before they evaporate. If PBHs are abundant enough to cause an early matter-dominated epoch, then at some time, $t_{\rm early-eq}$, which has to be before PBH evaporation ($t_{\rm early-eq} \lesssim \tau_{\rm PBH}$), they come to dominate the energy density of the Universe: $\rho_{\rm PBH}(t_{\rm early-eq})/\rho_{\rm rad}(t_{\rm early-eq}) \sim 1$. The critical initial abundance of PBHs, β_c that can initiate an early matter-dominated epoch is related to the temperature of the Universe at the formation time, T_i:

$$\frac{\rho_{\rm PBH}(T_{\text{early-eq}})}{\rho_{\rm rad}(T_{\text{early-eq}})} = \frac{\rho_{\rm PBH}(T_i)}{\rho_{\rm rad}(T_i)} \frac{T_i}{T_{\text{early-eq}}} = \beta_c \frac{T_i}{T_{\text{early-eq}}} \sim 1. \tag{4.9}$$

An early matter-dominated epoch caused by PBHs requires $\beta \gtrsim \beta_c$ with $\beta_c = T_{\rm eva}/T_i$ where $T_{\rm eva}$ denoted the temperature of the Universe at PBH evaporation time. If the energy density of PBHs ever dominated the energy density of the Universe, the reheating effect from PBH evaporation needs to be included when calculating the DM relic abundance. In this work, we focus on the scenario without early matter domination to avoid the dilution of GWs from PBH formation [4].

[4] GWs produced during a period of matter (PBH) domination has been considered in [88, 212, 129, 213].

4.3 PBH Formation Mechanisms and Correlated Gravitational Waves

In this Section, we describe two formation mechanisms of PBHs: from first-order phase transitions, and from curvature perturbations [5]. In both cases, we provide calculations of the GWs correlated with the formation mechanism.

4.3.1 First-order Phase Transitions

A simple template for the particle physics sector responsible for the formation of PBHs as well as the phase transition consists of a scalar ϕ and a fermion ψ, interacting via a Yukawa coupling y_ψ:

$$\mathcal{L} \supset \bar{\psi}\partial\!\!\!/\psi - y_\psi \phi \bar{\psi}\psi + \mathcal{L}_{SM,\chi} \ . \tag{4.10}$$

We will dub the sector containing $\{\phi, \psi\}$ as the phase transition or "PT" sector. The scalar ϕ induces a phase transition with $\langle\phi\rangle = 0$ in the false vacuum and $\langle\phi\rangle \gg T_\star$ in the true vacuum. We assume that the Standard Model sector and the $\{\phi, \psi\}$ sector are populated after reheating and evolve to the same temperature at the time of the phase transition: $T_{\rm SM} = T_{\rm PT} = T_\star$. This can be achieved, for example, by coupling ψ to the Standard Model through higher dimensional operators. We remain agnostic to the specific form of such couplings, since they do not influence the PBH formation process.

The mass of the fermion ψ is determined by the vacuum expectation value of ϕ as $m_\psi = y_\psi\langle\phi\rangle$. Since the kinetic energy of the fermions is $\mathcal{O}(T_\star)$, requiring that the mass in the true vacuum $m_\psi \gg T_\star$ will ensure that most of the ψ particles are trapped

[5] We note the PBH formation has also been studied in other mechanisms, such as scalar field fragmentations [214, 215, 216, 217], domain walls [218, 219], cosmic strings [220, 221, 222, 223], and metric preheating [224, 225]. If GWs were generated in these mechanisms, one could also correlate light PBHs with the corresponding GW signals.

in the false vacuum. Indeed, energy-momentum conservation ensures that the number of ψ particles n_ψ penetrating through the bubble wall with energy larger than m_ψ is Boltzmann suppressed: $n_\psi \propto e^{-m_\psi/T_\star}$.

Fermions trapped in the false vacuum subsequently collapse to form PBHs. However, their number density can be depleted by annihilation processes into the scalars ϕ. A detailed treatment and delineation of the parameter space of masses, couplings, temperatures, bubble wall velocity amenable to PBH formation was performed by the authors of [46, 47]. Numerically solving the associated Boltzmann equations, it was determined that benchmark values of the coupling

$$y_\psi \sim 10^{-4}\sqrt{\frac{T_\star}{10^6 \text{GeV}}}\,, \tag{4.11}$$

with bubble wall velocity $v_w = 0.5$ leads to successful PBH formation for a large range of phase transition temperatures. We assume that the trapping rate is 100% in this study. In the following, we denote both the fermion as well as the anti-fermion by ψ, except when we discuss their annihilation.

Since our interest is in light PBHs, we will concentrate on high temperature phase transitions with $T_\star \sim \mathcal{O}(10^{11-16})$ GeV. Take $T_\star = 10^{15}$ GeV as an example, the benchmark value of the coupling in such case turns out to be $y_\psi \sim 0.3$, with $m_\psi \sim 10\,T_\star$ [47]. Spherical over-dense regions with radius $R_\star$ at the onset of the phase transition typically shrink by a factor of ~ 3 before they become smaller than the Schwarzschild radius, leading to PBH formation (right panel, Fig. 4 of [47]). We discuss this process at length below, highlighting the main results of [47] and [176].

The energy density of the false vacuum is dominated by the energy density of the trapped particles ψ, whose distribution follows

$$\rho_\psi(t) \simeq \rho_\psi^{\rm eq} \left(\frac{R_\star}{R(t)}\right)^4 , \tag{4.12}$$

with $R(t)$ being the size of the trapped region at time t and $\rho_\psi^{\rm eq}$ the equilibrium distribution of ψ. The evolution of the energy density therefore depends on the ratio of the initial pocket size $R_\star$ and the pocket size $R(t)$ at time t, with the scaling being quartic because ψ number density is enhanced by the suppressed volume while ψ particles are simultaneously being heated up by the wall[6]. The mass of the PBH, $M_{\rm PBH}$ and the corresponding abundance $\beta_{\rm PBH}$ can be calculated using the methods developed in [176].

The mass $M_{\rm PBH}$ is determined by the total mass of the false vacuum pocket at the moment of gravitational collapse $t_{\rm collapse}$. The corresponding radius at $t_{\rm collapse}$ can be determined by requiring that the false vacuum pocket size equals the Schwarzschild radius r_s of a black hole whose mass equals to the total energy inside the pocket:

$$R(t_{\rm collapse}) = r_s = 2\,G\,M_{\rm pocket} \simeq \frac{8\pi G}{3}\,\frac{R_\star^4}{r_s}\,\rho_\psi^{\rm eq}, \tag{4.14}$$

[6]The total energy density of the pocket also receives contributions from Standard Model particles and is given by

$$\rho_{\rm pocket}(t) = \rho_{\rm sm}\left(\frac{t_\star}{t}\right)^2 + \rho_\psi^{\rm eq}\left(\frac{R_\star}{R(t)}\right)^4 . \tag{4.13}$$

However, contributions from trapped ψ particles dominate soon after $T_\star$. We do not include the contribution from the false vacuum energy density since it depends on the latent heat of the specific FOPT. Also, the PBH formation in our case occurs after the percolation of false vacuum pockets when vacuum energy has already been released to the radiation energy in 71% of the spatial regions.

where $G = 1/M_{\rm Pl}^2$ is the gravitational constant. The equilibrium distribution $\rho_\psi^{\rm eq}$ is evaluated at the phase transition temperature $T_\star$. The relation between the final and initial pocket size can be estimated as

$$\frac{r_s}{R_\star} \simeq \sqrt{\frac{7\,g_\psi}{8\,g_\star}}\,R_\star\,H_\star. \tag{4.15}$$

Here $g_\star = g_{\star,\rm sm} + g_{\star,\phi} + g_{\star,\psi} = 106.75 + 1 + 4\times(7/8)$ is the total number of relativistic degrees of freedom when both the Standard Model sector and the PT sector are in equilibrium.

At this point, a few comments are in order about the effect of $\psi\bar{\psi}$ annihilations on the PBH formation rate. The effect of annihilation is twofold. Firstly, annihilation dilutes the energy density in the false vacuum and thus decreases the mass of the final PBH. Secondly, for large annihilation rates, the PBH formation rate is suppressed if the Schwarzschild radius decreases faster than the pocket radius and Eq. (4.14) is never satisfied. The parametric dependence of the annihilation rate on the pocket radius is $n_\psi^2 \propto R(t)^{-6}$. If false vacuum regions survive well after the phase transition begins, *i.e.* $R(t) \ll R_\star$, a significant portion of the ψ energy density leaks into the true vacuum bubbles in the form of the annihilation final states ϕ. Therefore, PBH formation requires $R_\star/r_s \sim \mathcal{O}(1)$, implying $R_\star \gtrsim H_\star^{-1}$. For example, a benchmark value of $R_\star = 1.5\,H_\star^{-1}$ is found to allow successful PBH formation by Boltzmann equation simulations in [46, 47]. In this study, we assume the minimal initial pocket radius for PBH formation is $R_\star^{\rm min} = 1.5\,H_\star^{-1}$, below which the energy density evolution with active $\psi\bar{\psi}$ annihilation needs further inspections.

The energy density inside the pocket right before PBH formation can be calculated for arbitrary $R_\star$ as [7]

$$\rho_{\rm pocket}(t_{\rm collapse}) = \frac{g_{\star,\rm sm} + g_{\star,\phi} + g_{\star,\psi}\left(\sqrt{\frac{8g_\star}{7g_\psi}}\frac{H_\star^{-1}}{R_\star}\right)^4}{g_{\star,\rm sm} + g_{\star,\phi} + g_{\star,\psi}}\,\rho_\star\ . \tag{4.16}$$

Then, the mass of PBH from this pocket is

$$\begin{aligned} M_{\rm PBH} &= \frac{4\pi}{3} r_s^3\, \rho_{\rm pocket} \\ &= \frac{m_{\rm pl}^2}{2}\left(\frac{7g_\psi}{8g_\star}\right)^{\frac{3}{2}}\left[\frac{g_{\star,\rm sm} + g_{\star,\phi} + g_{\star,\psi}\left(\sqrt{\frac{8g_\star}{7g_\psi}}\frac{H_\star^{-1}}{R_\star}\right)^4}{g_{\star,\rm sm} + g_{\star,\phi} + g_{\star,\psi}}\right]\left(\frac{R_\star}{H_\star^{-1}}\right)^6 H_\star^{-1} \\ &\simeq 0.5\times\left(\frac{10^{15}\ \text{GeV}}{T_\star}\right)^2\left[1+32.8\left(\frac{R_\star}{H_\star^{-1}}\right)^{-4}\right]\left(\frac{R_\star}{H_\star^{-1}}\right)^6 \text{g} \\ &\simeq 16.3\times\left(\frac{10^{15}\ \text{GeV}}{T_\star}\right)^2\left(\frac{R_\star}{H_\star^{-1}}\right)^2 \text{g}. \end{aligned} \tag{4.17}$$

In the last step, we assumed that the dominant energy density contribution is from trapped particles such that $\rho_{\rm pocket} \simeq \rho_\psi$. From Eq. (4.17), it is clear that the PBH mass is only dependent on $T_\star$ when $R_\star/H_\star^{-1}$ is fixed. Lighter PBHs are therefore produced when the phase transition happens at a higher temperature.

We can also write the PBH mass in terms of the horizon mass M_H,

$$\begin{aligned} M_{\rm PBH} &= \left(\frac{g_{\star,\psi}}{g\star}\right)^{\frac{3}{2}}\left[\frac{g_{\star,\rm sm} + g_{\star,\phi} + g_{\star,\psi}\left(\sqrt{\frac{8g_\star}{7g_\psi}}\frac{H_\star^{-1}}{R_\star}\right)^4}{g_{\star,\rm sm} + g_{\star,\phi} + g_{\star,\psi}}\right]\left(\frac{R_\star}{H_\star^{-1}}\right)^6 M_H \\ &\simeq 5.4\times10^{-3}\times\left(32.8\left(\frac{R_\star}{H_\star^{-1}}\right)^2 + \left(\frac{R_\star}{H_\star^{-1}}\right)^6\right) M_H. \end{aligned} \tag{4.18}$$

[7] We assume the dilution of energy density from the annihilation process is negligible for our FOPT model parameters. This is confirmed in the numerical simulation in Fig. 2 of [46] where the increase of the trapped ψ energy density can scale approximately as $R(t)^{-4}$ given that the annihilation cross section is not too large.

For PBH formation during FOPT, the mass function peaks at $R_\star/H_\star^{-1} = 1.5$, implying the mass ratio $\gamma \equiv \frac{M_{\rm PBH}}{M_H}$ has a typical value

$$\gamma_{\rm FOPT}\Big|_{R_\star/H_\star^{-1}=1.5} \simeq 0.46. \tag{4.19}$$

The $\gamma_{\rm FOPT}$ value could be larger when the initial pocket radius is even larger than the horizon size ($\gamma_{\rm FOPT} \simeq 1$ when $R_\star/H_\star^{-1} = 2$), but the probability of having a large false vacuum pocket is highly suppressed because of the persistent nucleation of new true vacuum bubbles.

The total number of PBHs that are formed from vacuum pockets is determined by the distribution of false vacuum regions whose initial radius satisfies $R_\star > R_\star^{\rm min} = 1.5\, H_\star^{-1}$. The PBH mass is determined by the initial radius of the pocket that later collapses into the PBH, and $M_{\rm PBH}$ increases with $R_\star$ in Eq. (4.17).

The number density of remnant pockets at the false vacuum percolation time is found in [51] using the reverse time description,

$$\frac{dn_{\rm pocket}}{dR_\star} \simeq \frac{I_\star^4\,\beta^4}{192\,v_w^3}\, e^{4\beta R_\star/v_w - I_\star\, e^{\beta R_\star/v_w}} \left(1 - e^{-I_\star e^{\beta R_\star/v_w}}\right). \tag{4.20}$$

where $I_\star = -\ln(0.29) = 1.238$. The parameters that enter the double exponential suppression are $R_\star$, β and v_w. The suppression for large values of $R_\star$ implies that PBH formation is most efficient at the smallest allowed mass and drops quickly for heavier PBHs. Similarly, the suppression for large values of β can be understood as follows: since a large nucleation rate would cause new broken-phase bubbles to appear in unbroken-phase regions, an original pocket would be broken up into separate small pockets in such a scenario, and the remaining smaller pockets fail to form PBHs because of the $\psi\bar{\psi}$ annihilation. This condition of a pocket radius successfully shrinking from $R_\star$ to the Schwarzschild radius without any additional true vacuum bubble seeded inside

it gives the dominant suppression factor $e^{-I_\star\, e^{\beta R_\star/v_w}}$. PBH formation thus prefers small values of β and large values of v_w. A small β value can be realized with supercooling [226], where the order parameter of supercooled FOPTs can be larger $\langle\phi\rangle \gg T_\star$ in order to trap ψ particles with a moderate Yukawa coupling strength.

Each remnant pocket will collapse into a PBH, so that the PBH number density at formation time can be written as

$$\begin{aligned}\frac{dn_{\rm PBH}}{dM_{\rm PBH}} &= \frac{dR_\star}{dM_{\rm PBH}}\frac{dn_{\rm pocket}}{dR_\star}\Big|_{R_\star>1.5H_\star^{-1}} \\ &= \frac{R_\star}{2\,M_{\rm PBH}}\frac{dn_{\rm pocket}}{dR_\star}\Big|_{R_\star>1.5H_\star^{-1}}.\end{aligned} \tag{4.21}$$

The corresponding energy density fraction of PBHs is

$$\beta_{\rm PBH}(M_{\rm PBH}) = M_{\rm PBH}\frac{d\beta_{\rm PBH}}{dM_{\rm PBH}} = \frac{M_{\rm PBH}^2}{\rho_{\rm rad}(T_\star)}\frac{dn_{\rm PBH}}{dM_{\rm PBH}}. \tag{4.22}$$

Using Eq. (4.20)-(4.22), and the $R_\star$-$M_{\rm PBH}$ relation in Eq. (4.17), one can get

$$\beta_{\rm PBH} = \frac{M_{\rm PBH}R_\star}{2\rho_{\rm rad}}\frac{I_\star^4\,\beta^4}{192\,v_w^3}\,e^{4\beta R_\star/v_w - I_\star\, e^{\beta R_\star/v_w}}\left(1-e^{-I_\star e^{\beta R_\star/v_w}}\right)\Big|_{R_\star>1.5H_\star^{-1}}. \tag{4.23}$$

At this point, we are in a position to obtain the PBH mass spectrum ($\beta_{\rm PBH}$ vs. $M_{\rm PBH}$ for fixed values of the FOPT parameters) as well as points on the plane of $\{M_{\rm PBH}, \beta_{\rm PBH}\}$ as different selections of FOPT parameters $\{\beta, T_\star, v_w\}$ are varied, following Eq. (4.17) and Eq. (4.23). The results are displayed in Fig. 4.1. On the upper left panel of Fig. 4.1, we show the PBH mass spectrum for fixed values of $T_\star = 10^{14}$ GeV (blue), $T_\star = 10^{15}$ GeV (red), and $T_\star = 10^{16}$ GeV (green). The wall velocity is fixed at $v_w = 0.5$, while β is fixed at $\beta/H_\star = 1.1$. The PBH mass function generated through trapping particles during a FOPT is featured with a very sharp peak. The smaller PBH mass region

is cut by the requirement $R_\star^{\rm min} = 1.5 H_\star^{-1}$ to avoid excessive annihilation. The mass function for larger PBH masses is suppressed by the number density of larger pockets in Eq. (4.20). On the upper right panel of Fig. 4.1, we fix value $T_\star = 10^{15}$ GeV and $v_w = 0.5$, and vary $\beta/H_\star = 1.0 - 1.8$. In the lower panel, we show the the amplitude of the PBH mass function peak as a function of the β parameter. Larger β means a higher nucleation rate and therefore the PBH mass function is suppressed.

Before ending our discussion of PBH formation, we make a few comments about the subsequent Hawking evaporation of ψ. The Hawking production rate of ψ is determined by the relation between m_ψ and $T_{\rm PBH}$. In Fig. 4.2, we show $T_{\rm PBH}$ as a function of the formation time $T \simeq T_\star$. The requirement $m_\psi > T_\star$ is shown in blue. It is evident that for $T_\star \lesssim 10^{18}$GeV, the PBH temperature is always smaller than the particle mass so that the Hawking radiation rate of ψ is highly suppressed. Since $T_{\rm PBH}$ is also below the phase transition scale, ψ is produced at the PBH horizon as a massive degree freedom in the true vacuum. We assume that massive ψ particles that penetrated into the true vacuum during the FOPT or were produced by Hawking radiation of PBHs after the FOPT rapidly decay into the Standard Model, depleting any ψ abundance.

We now turn to a discussion of the GW signals correlated with PBH formation. We follow [227, 228] for the calculation of the GW signal from a FOPT, and focus on sound waves as the dominant contribution to the GW spectrum [229, 230, 231]. The peak frequency is given by

$$f_{\rm GW,sw}^{\rm peak} \simeq 1.9 \times 10^2 \left(\frac{1}{v_w}\right) \left(\frac{\beta}{H_\star}\right) \left(\frac{T_\star}{10^{15}\ {\rm GeV}}\right) \left(\frac{g_\star(T_\star)}{106.75}\right)^{\frac{1}{6}}\ {\rm MHz}. \tag{4.24}$$

The GWs from high temperature FOPTs that generate light PBHs have very high frequency. For $M_{\rm PBH} = 0.1$ g, the FOPT temperature is $T_\star \simeq 2 \times 10^{16}$ GeV, and the corresponding GW peak frequency is $f_{\rm GW,sw}^{\rm peak} \simeq 8.7$ GHz for the benchmark FOPT

parameters discussed above. For the heaviest PBH mass we consider in this work, $T_\star \simeq 2 \times 10^{11}$ GeV for $M_{\rm PBH} = 10^9$ g, the GW peak frequency is $f^{\rm peak}_{\rm GW,sw} \simeq 0.09$ MHz. The FOPT GW energy density today is

$$\begin{aligned}\Omega_{\rm GW,sw}(f_{\rm GW}) \;\simeq\; & 5.3 \times 10^{-6} \left(\frac{\beta}{H_\star}\right)^{-1} \left(\frac{\kappa\alpha}{1+\alpha}\right)^2 \left(\frac{106.75}{g_\star(T_\star)}\right)^{\frac{1}{3}} v_w\, \Upsilon \\ & \times \left(\frac{f_{\rm GW}}{f^{\rm peak}_{\rm GW}}\right)^3 \left(\frac{7}{4+3(f_{\rm GW}/f^{\rm peak}_{\rm GW})}\right)^{\frac{7}{2}}, \end{aligned} \tag{4.25}$$

where Υ, the suppression factor coming from the finite lifetime of sound waves, is given by [227]:

$$\Upsilon = 1 - \frac{1}{\sqrt{1 + 2\tau_{\rm sw} H_\star}}. \tag{4.26}$$

The lifetime of source can be calculated as

$$\tau_{\rm sw} \simeq \frac{R_\star}{\bar{U}_f}, \tag{4.27}$$

where the $\bar{U}_f$ is the root mean square fluid velocity which is obtained as

$$\bar{U}_f^2 = \frac{3}{4}\,\kappa\alpha. \tag{4.28}$$

The κ parameter is the fraction of vacuum energy that is released during the phase transition which goes into the fluid motion [232]. The $\Omega_{\rm GW,sw}$ is inversely proportional to β, which means the GW signal is stronger for slow FOPTs that produced PBHs. Although we fix the bubble wall velocity to $v_w = 0.5$, the GW signal is also enhanced by higher wall velocities as long as the ψ particle trapping rate is not significantly affected.

4.3.2 Scalar Perturbations Revisited

In this chapter, we use a δ-function shape for the power spectrum of the curvature perturbation for illustration of our idea,

$$P_\zeta(k) = A_\zeta \, \delta(\log k - \log k_p), \tag{4.29}$$

where k_p determines the scale of the enhanced perturbation and A_ζ determines the amplitude of the perturbation. Redefining the PBH mass from section 1.4.1

$$M_{\rm PBH}(k) = \gamma \, M_H(k) = 4 \times 10^3 \left(\frac{\gamma}{0.2}\right) \left(\frac{k}{10^{21}{\rm Mpc}^{-1}}\right)^{-2} {\rm g}. \tag{4.30}$$

Note that the ratio of the PBH mass and the horizon mass at formation time in this mechanism, $\gamma = 0.2$, is about half of the typical ratio value of the FOPT mechanism. In Fig. 4.3, we show example PBH mass functions $\{M_{\rm PBH}, \beta_{\rm PBH}\}$ generated by primordial scalar perturbations $\{A_\zeta, k_p\}$. On the upper left panel of Fig. 4.3, we show the PBH mass spectrum for fixed values of power spectrum peak locations $k_p = 10^{21}$ Mpc^{-1} (blue), $k_p = 10^{22}$ Mpc^{-1} (red) and $k_p = 10^{23}$ Mpc^{-1} (green). The amplitude of the power spectrum is chosen to be $A_\zeta = 10^{-1.6}$. The peak of the $M_{\rm PBH}$ distribution is determined by k_p with Eq. (4.30). On the upper right panel of Fig. 4.3, we show mass functions for a range of A_ζ values with fixed $k_p = 10^{22}$ Mpc^{-1}. In the lower panel, we show the peak $\beta_{\rm PBH}$ value as a function of A_ζ. The variance of δ decreases with smaller A_ζ in Eq.(3.7) such that the PBH formation rate is suppressed with small amplitudes of primordial fluctuations.

Besides the PBH formation, GWs are induced by the second-order effect when scalar modes enter the particle horizon at $aH = k_p$ [79, 80, 194, 81, 85, 36, 83]. The GW density today $\Omega_{\rm GW,0}$ is expressed as

$$\Omega_{\rm GW,0}(f_{\rm GW}) = 0.39 \left(\frac{g_\star(\eta_s)}{106.75}\right)^{-\frac{1}{3}} \Omega_{\rm rad,0}\, \Omega_{{\rm GW},\zeta}(\eta_s, k), \tag{4.31}$$

where the GW frequency and the k-mode is related by $f_{\rm GW} = 1.546\times10^{-15}(k/{\rm Mpc}^{-1})$ Hz. The $\Omega_{\rm rad,0} = 8.5\times10^{-5}$ is the energy density of radiation today normalized to the critical density. The calculation of induced GWs is given in Section 1.4.1.1 from here we can determine the peak frequency. The peak frequency of the induced GW spectrum is determined by the horizon reentry time of the power spectrum peak k_p as:

$$f^{\rm peak}_{{\rm GW},\zeta} = 1.546 \times \left(\frac{k_p}{10^{21}{\rm Mpc}^{-1}}\right) {\rm MHz}. \tag{4.32}$$

The induced GWs are generated at very high frequencies when large curvature perturbations occur at small scales. We calculate the GW peak frequency with Eq. (4.30) and Eq. (4.32), $f^{\rm peak}_{{\rm GW},\zeta} \simeq 0.3$ GHz for $M_{\rm PBH} = 0.1$ g and $f^{\rm peak}_{{\rm GW},\zeta} \simeq 3\times10^{-3}$ MHz for $M_{\rm PBH} = 10^9$ g. The GW energy density is found to be proportional to the square of the amplitude of the curvature perturbation at the formation time $\Omega_{\rm GW}(\eta_s) \simeq A^2_\zeta$ [36], thus one can estimate the present day GW signal strength to be $\Omega_{\rm GW,0} \simeq A^2_\zeta \times \Omega_{\rm rad,0} \sim 10^{-9}$.

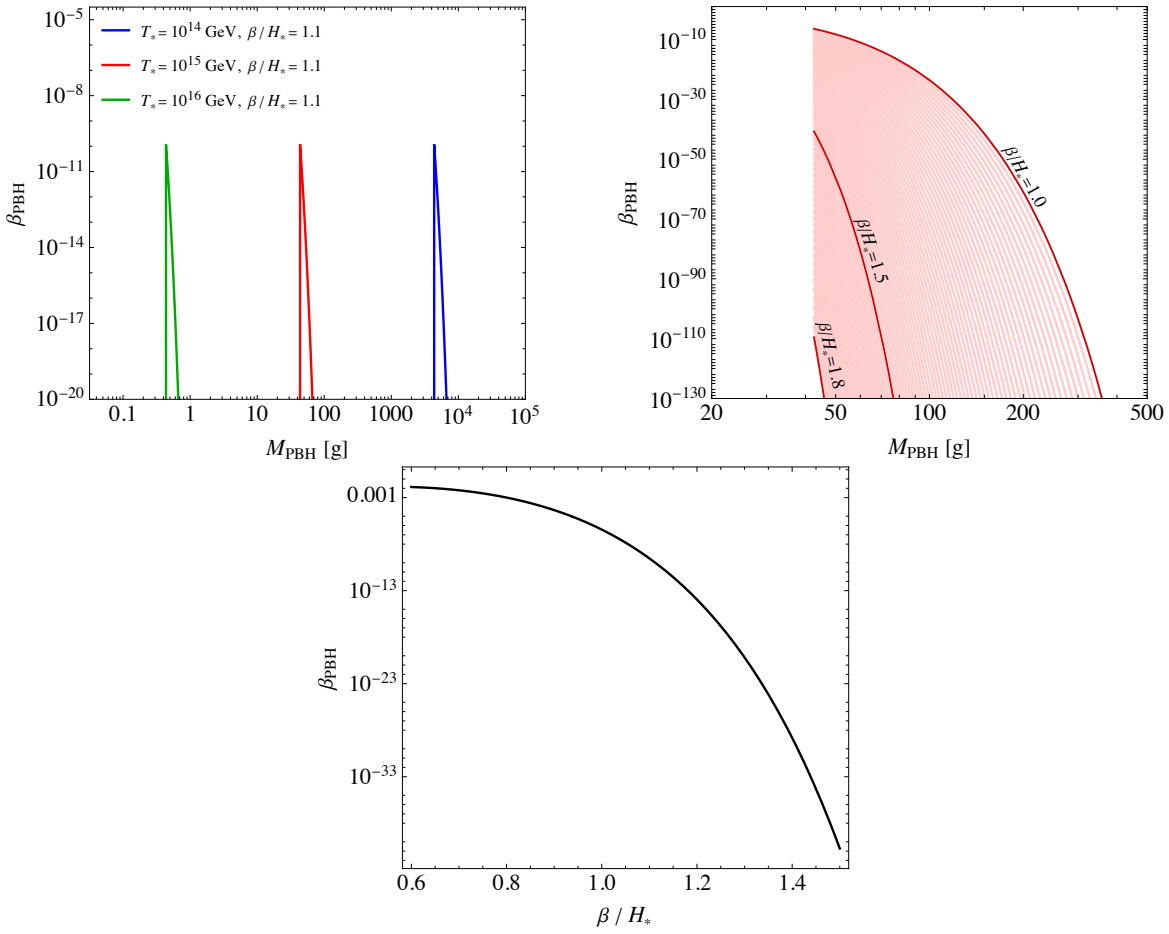


Figure 4.1: The PBH mass function generated by the FOPT formation mechanism. *Upper left panel:* The dependence on $T_\star$. FOPT temperatures are chosen $T_\star = 10^{14}$ GeV (blue), 10^{15} GeV (red) and 10^{16} GeV (green), while $\beta/H_\star = 1.1$ is fixed. The peak location of $\beta_{\rm PBH}$ is determined by $T_\star$ and the abundance is relatively unchanged. *Upper right panel:* The dependence on $\beta/H_\star$. The FOPT temperature is $T_\star = 10^{15}$ GeV. The range of $\beta_{\rm PBH}$ around the peak is shown for $\beta/H_\star \in [1.0, 1.8]$. The PBH formation is suppressed with a larger β. *Lower panel:* The PBH abundance at peak location $R_\star/H_\star^{-1} = 1.5$ with varying $\beta/H_\star$ values. The PBH formation rate is very sensitive to the increase of the nucleation rate.

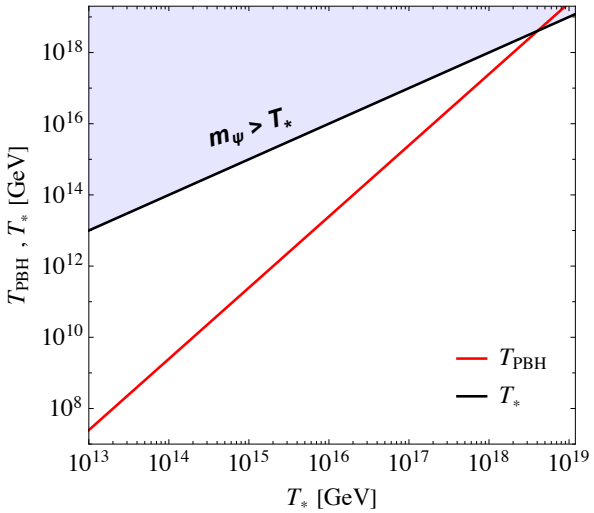


Figure 4.2: The relation between the FOPT temperature $T_\star$ (black) and the Hawking temperature $T_{\rm PBH}$ (red) of PBHs formed during a FOPT at $T_\star$, assuming the initial pocket radius is $R_\star = 1.5 H_\star^{-1}$. The blue shaded region indicates that the ψ particle mass in the true vacuum should at least be above the black curve such that it can be trapped inside the false vacuum pocket. For $T_\star \lesssim 10^{18}$GeV, the PBH Hawking temperature is always smaller than m_ψ.

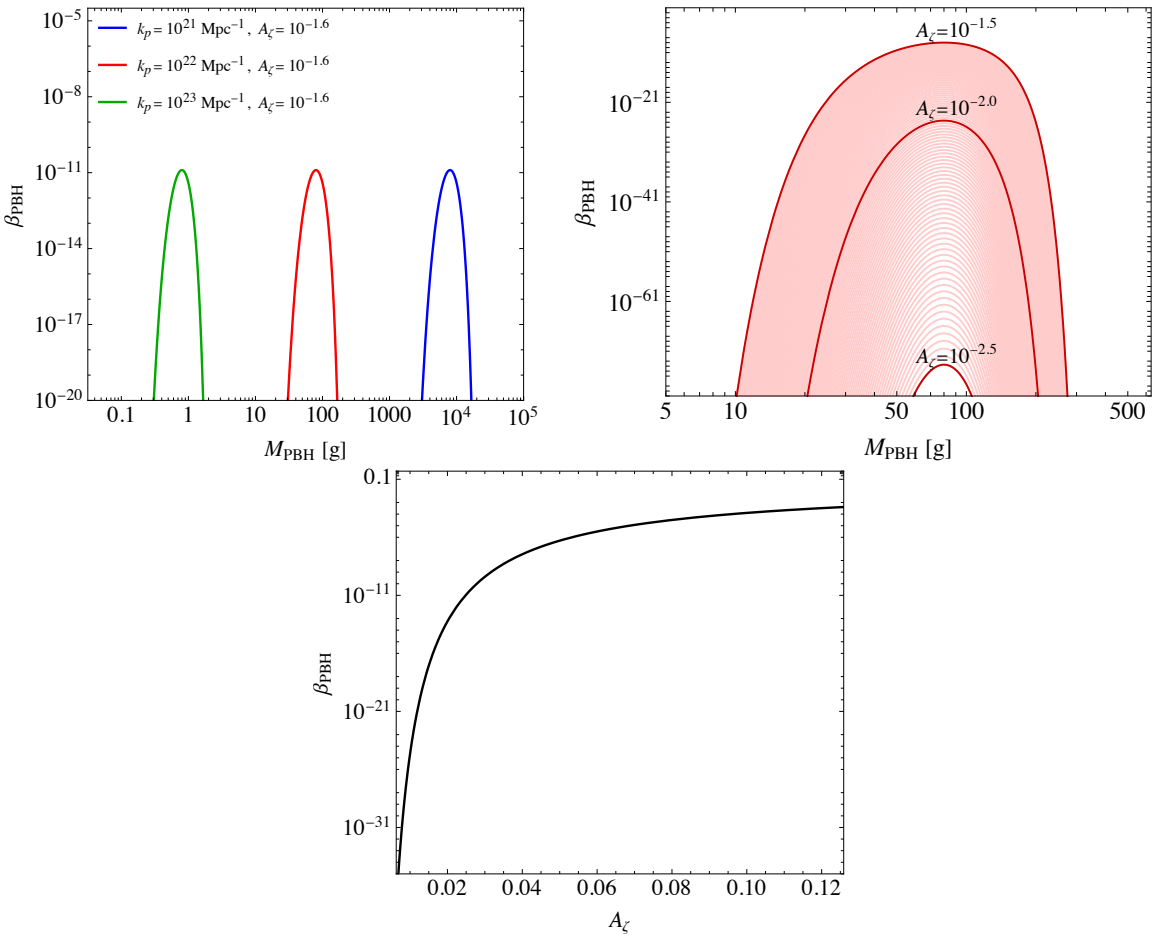


Figure 4.3: The PBH mass function generated by primordial perturbations. *Upper left panel:* The dependence on k_p. The scales of the fluctuation are chosen $k_p = 10^{21}$ Mpc^{-1} (blue), 10^{22} Mpc^{-1} (red) and 10^{23} Mpc^{-1} (green), while the amplitude $A_\zeta = 10^{-1.6}$ is fixed. The peak location of $\beta_{\rm PBH}$ is determined by k_p and the abundance is unchanged. *Upper right panel:* The dependence on A_ζ. The peak k-mode is $k_p = 10^{22}$ Mpc^{-1}. The range of $\beta_{\rm PBH}$ around the peak is shown for $A_\zeta \in [10^{-2.5}, 10^{-1.5}]$. *Lower panel:* The PBH abundance at peak location with varying A_ζ values. The PBH formation rate drops quickly when the variance of the density contrast distribution becomes smaller than the formation threshold.

4.4 Results: Dark Matter and High-frequency Gravitational Waves

In this Section, we collect our results from PBH formation and calculate the correlated GWs. Our first step will be to discuss the PBH parameter space for a given relic density and DM mass (this step constitutes the map $\{\Omega_\chi h^2, m_\chi\} \to \{M_{\rm PBH}, \beta_{\rm PBH}\}$ of our results). We will then compute the resulting GWs for the two formation mechanisms (this step constitutes the maps $\{M_{\rm PBH}, \beta_{\rm PBH}\} \to \{\alpha, \beta, T_\star, v_w\} \to \{h_c, f_{\rm GW}\}$ and $\{M_{\rm PBH}, \beta_{\rm PBH}\} \to \{A_\zeta, k_p\} \to \{h_c, f_{\rm GW}\}$ of our results).

4.4.1 Correlating Dark Matter Abundance: $\{\Omega_\chi h^2, m_\chi\} \to \{M_{\rm PBH}, \beta_{\rm PBH}\}$

We would like to understand the following question: given a mass of DM m_χ and a given value of the DM relic density $\Omega_\chi h^2$, what is the corresponding regime of $\{M_{\rm PBH}, \beta_{\rm PBH}\}$ that is covered? We can use Eq. (5.25) and Eq. (5.26) for the yield and relic density. While the results for the two formation mechanisms are similar, we treat them separately. We calculate quantities for the two example formation mechanisms with conventions "FOPT" for phase transition and "ζ" for curvature perturbations.

In the case of FOPT, we have

$$Y_{\chi,\rm FOPT} \;=\; \frac{3}{4}\beta_{\rm PBH} N_\chi \frac{T_\star}{M_{\rm PBH}} \;. \tag{4.33}$$

Solving for $T_\star$ in the third line of Eq. (4.17), the following expression can be attained

$$T_\star \simeq 7.1\times 10^{14}\sqrt{32.8+\left(\frac{R_\star}{H_\star^{-1}}\right)^4}\left(\frac{R_\star}{H_\star^{-1}}\right)\left(\frac{1\ \rm g}{M_{\rm PBH}}\right)^{\frac{1}{2}}\ \rm GeV\ , \tag{4.34}$$

To produce the relic density of a real scalar DM χ, we use Eq. (4.34) and the relic density is given as

$$\begin{aligned}\Omega_\chi h^2 \simeq 2.5 \quad &\times \quad 10^{10}\, g_\chi \left(\frac{106.75}{g_\star(T_{\rm PBH})}\right) \sqrt{32.8 + \left(\frac{R_\star}{H_\star^{-1}}\right)^4} \left(\frac{R_\star}{H_\star^{-1}}\right) \\ &\times \quad \beta_{\rm PBH} \left(\frac{M_{\rm PBH}}{1\ {\rm g}}\right)^{1/2} \left(\frac{m_\chi}{\rm TeV}\right), \qquad T_{\rm PBH} > m_\chi, \end{aligned} \tag{4.35}$$

and

$$\begin{aligned}\Omega_\chi h^2 \simeq 2.7 \quad &\times \quad 10^{18}\, g_\chi \left(\frac{106.75}{g_\star(T_{\rm PBH})}\right) \sqrt{32.8 + \left(\frac{R_\star}{H_\star^{-1}}\right)^4} \left(\frac{R_\star}{H_\star^{-1}}\right) \\ &\times \quad \beta_{\rm PBH} \left(\frac{1\ {\rm g}}{M_{\rm PBH}}\right)^{3/2} \left(\frac{10^{15}\ {\rm GeV}}{m_\chi}\right), \qquad T_{\rm PBH} < m_\chi. \end{aligned} \tag{4.36}$$

The critical abundance beyond which the Universe becomes PBH-dominated can be obtained as follows

$$\begin{aligned}\beta^{\rm FOPT}_{\rm PBH,crit} &\simeq 1.7\times 10^{-5} \left[32.8 + \left(\frac{R_\star}{H_\star^{-1}}\right)^4\right]^{-\frac{1}{2}} \left(\frac{R_\star}{H_\star^{-1}}\right)^{-1} \left(\frac{1\ {\rm g}}{M_{\rm PBH}}\right) \left(\frac{g_\star(T_\star)}{106.75}\right)^{\frac{1}{4}} \\ &\simeq 1.9\times 10^{-6} \left(\frac{1\ {\rm g}}{M_{\rm PBH}}\right) \left(\frac{g_\star(T_\star)}{106.75}\right)^{\frac{1}{4}} \Big|_{R_\star/H_\star^{-1}=1.5}. \end{aligned} \tag{4.37}$$

For scalar perturbations, the yield of DM is given by:

$$Y_{\chi,\zeta} = \frac{3}{4}\beta_{\rm PBH} N_\chi \frac{T_i(M_{\rm PBH})}{M_{\rm PBH}}\ , \tag{4.38}$$

where the temperature of the Universe at PBH formation time, $T_i(M_{\rm PBH})$, is obtained from writing Eq. (4.30) in terms of temperature as $M_{\rm PBH} = (4\pi/3)\gamma\rho_{\rm rad}(T_i)H^{-3}(T_i)$. Therefore we have:

$$T_{i,\zeta} \simeq 4.3 \times 10^{15} \left(\frac{\gamma}{0.2}\right)^{\frac{1}{2}} \left(\frac{106.75}{g_\star(T_i)}\right)^{\frac{1}{4}} \left(\frac{1\ \text{g}}{M_{\rm PBH}}\right)^{\frac{1}{2}}\ \text{GeV}, \tag{4.39}$$

is the temperature of the Universe when PBH formation is from the collapse of curvature perturbations. The relic abundance of DM from the curvature perturbation formation mechanism are as follows:

$$\begin{aligned}\Omega_\chi h^2 \simeq 1.6 \quad &\times \quad 10^{13} \left(\frac{g_*(T_i)}{106.75}\right)^{-1/4} \left(\frac{\gamma}{0.2}\right)^{1/2} \left(\frac{g_\chi}{g_*(T_{\rm PBH})}\right) \\ &\times \quad \beta_{\rm PBH} \left(\frac{M_{\rm PBH}}{1\text{g}}\right)^{1/2} \left(\frac{m_\chi}{\text{TeV}}\right), \qquad T_{\rm PBH} > m_\chi,\end{aligned} \tag{4.40}$$

and

$$\begin{aligned}\Omega_\chi h^2 \simeq 1.8 \quad &\times \quad 10^{21} \left(\frac{g_*(T_i)}{106.75}\right)^{-1/4} \left(\frac{\gamma}{0.2}\right)^{1/2} \left(\frac{g_\chi}{g_*(T_{\rm PBH})}\right) \\ &\times \quad \beta_{\rm PBH} \left(\frac{1\text{g}}{M_{\rm PBH}}\right)^{3/2} \left(\frac{10^{15}\text{GeV}}{m_\chi}\right), \qquad T_{\rm PBH} < m_\chi.\end{aligned} \tag{4.41}$$

The corresponding critical PBH abundance beyond which the Universe becomes matter-dominated in the curvature perturbation mechanism is given by

$$\beta^\zeta_{\rm PBH,crit} \simeq 2.8 \times 10^{-6} \left(\frac{g_\star(T_{\rm BH})}{106.75}\right)^{1/2} \left(\frac{0.2}{\gamma}\right) \left(\frac{1\text{g}}{M_{\rm PBH}}\right). \tag{4.42}$$

We summarize the required PBH abundance to generate the correct DM relic abundance as a function of the DM mass and the PBH mass, for the two formation mechanisms. For PBH formation during FOPT,

$$\beta_{\rm PBH} = \frac{1}{g_\chi}\left(\frac{g_\star(T_{\rm PBH})}{106.75}\right)\left[164+5\left(\frac{R_\star}{H_\star^{-1}}\right)^4\right]^{-1/2}\left(\frac{R_\star}{H_\star^{-1}}\right)^{-1}\times \times\begin{cases} 1.1\times10^{-11}\left(\frac{\rm TeV}{m_\chi}\right)\left(\frac{1\rm g}{M_{\rm PBH}}\right)^{1/2} & m_X < T_{\rm PBH}, \\ 1.0\times10^{-19}\left(\frac{m_\chi}{10^{15}\ \rm GeV}\right)\left(\frac{M_{\rm PBH}}{1\rm g}\right)^{3/2} & m_X > T_{\rm PBH}. \end{cases} \tag{4.43}$$

For PBH formation from curvature perturbations,

$$\beta_{\rm PBH} = \frac{1}{g_\chi}\left(\frac{g_*(T_i)}{106.75}\right)^{1/4}\left(\frac{0.2}{\gamma}\right)^{1/2}\left(\frac{g_*(T_{\rm PBH})}{106.75}\right)\times \times\begin{cases} 8.0\times10^{-13}\left(\frac{\rm TeV}{m_\chi}\right)\left(\frac{1\,\rm g}{M_{\rm PBH}}\right)^{1/2} & m_X < T_{\rm PBH}, \\ 7.1\times10^{-21}\left(\frac{m_\chi}{10^{15}\rm GeV}\right)\left(\frac{M_{\rm PBH}}{1\,\rm g}\right)^{3/2} & m_X > T_{\rm PBH}. \end{cases} \tag{4.44}$$

We are now in a position to describe the correlation between the DM relic density and PBHs. The results are plotted in Fig. 4.4. We show contours of $\beta_{\rm PBH}$ on the plane of $M_{\rm PBH}$ vs. m_χ, after imposing $\Omega_\chi h^2 = 0.12$ [211]. The contours corresponding to FOPT are shown in red, while the contours corresponding to scalar perturbations are shown in black. The contours for FOPT assume $R_\star/H_\star^{-1} = 1.5$. The regions shaded in blue indicate PBH-domination where the required $\beta_{\rm PBH}$ value is larger than

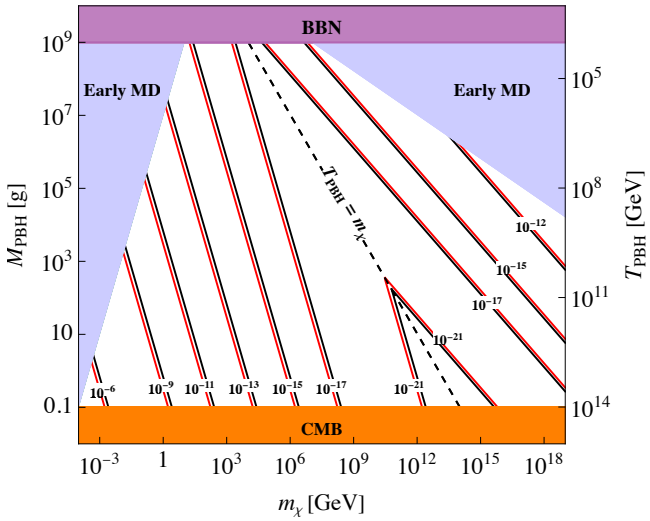


Figure 4.4: Contours of $\beta_{\rm PBH}$ on the plane of $M_{\rm PBH}$ vs. m_χ after requiring $\Omega_\chi h^2 = 0.12$ from FOPTs (red) assuming $R_\star = 1.5 H_\star^{-1}$, and from curvature perturbations (black). The black dashed curve show the PBH mass whose Hawking temperature is equal to the DM mass. Regions to the left of the black dashed curve means $m_\chi < T_{\rm PBH}$ and regions to the right of the black dashed curve means $m_\chi > T_{\rm PBH}$. For very light and very heavy DM masses, the relic abundance cannot be produced through Hawking radiation in a radiation-dominated Universe. These regions are shaded in blue for both mechanisms to indicate the early matter-dominated epoch. The upper bound on the PBH mass from BBN is shown in the purple shaded region. The lower bound on the PBH mass from cosmic microwave background (CMB) is shown in the orange shaded region.

the critical values in Eq. (4.37) and Eq. (4.42). We checked the PBH-domination regions of the two formation mechanisms are almost completely overlapping. The PBH-domination region on the top-left corner means the DM mass is too small such that the energy density of DM produced by a PBH is suppressed by the DM mass, while the PBH-domination region on the top-right corner means the suppression comes from the number of heavy DM particles that can be produced by a PBH. We focus on the PBH mass range of $0.1\text{g} \lesssim M_{\rm PBH} \lesssim 10^9\text{g}$. The upper bound is coming from the requirement that PBHs should fully evaporate before the BBN to avoid any modification from the PBH Hawking radiation on successful BBN [146]. The lower bound is set by the largest inflationary Hubble parameter $H_I/M_{\rm Pl} < 2.5 \times 10^{-5}$ that is allowed by the

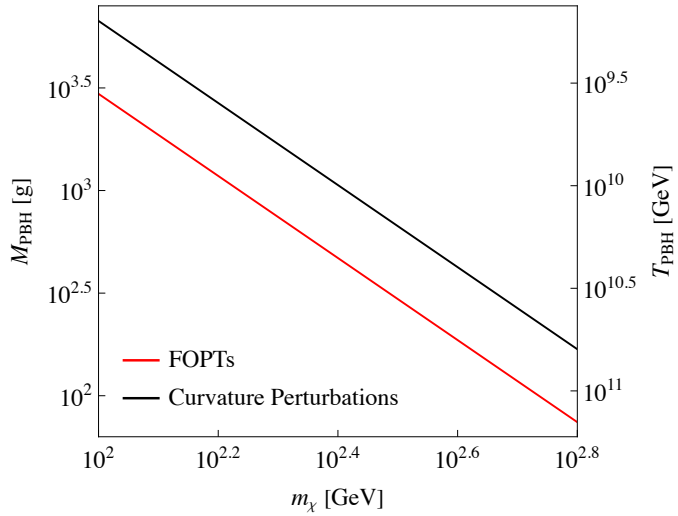


Figure 4.5: Same as Fig. 4.4, zoomed in on the contour $\beta_{\rm PBH} = 10^{-13}$ and requiring $\Omega_\chi h^2 = 0.12$ for the FOPT mechanism (red) and the curvature perturbation mechanism (black). We assume $R_\star = 1.5 H_\star^{-1}$ for the red curve.

Planck cosmic microwave background (CMB) observation [55]. The purple and orange regions show the constraints from BBN and CMB, respectively. Along the black dotted line, the initial temperature of PBHs equals to the DM mass. This line divides the parameter space into two distinct regions: $m_\chi < T_{\rm PBH}$, corresponds to the left side, and, $m_\chi > T_{\rm PBH}$, corresponds to the right side. Since these two regions coincide along the the black dotted line, the contours of initial abundance of PBHs on both sides should meet on this line, e.g, contours of $\beta_{\rm PBH} = 10^{-21}$.

It is worth mentioning that light DM produced by PBH evaporation can be warm enough to erase small-scale structures via free-streaming. It is shown that DM with no non-gravitational interactions emitted by PBHs is not cold enough for $m_\chi \lesssim 1\,\text{TeV}$ when $M_{\rm PBH} = 10^9$ g, and the lower limit on m_χ scales as $M_{\rm PBH}^{1/2}$ in order to avoid the free-streaming constraint [12]. Introducing non-gravitational interactions for DM can relax the bounds from structure formation. For example, kinetic equilibrium established with thermal contact with the SM sector after DM production can alleviate the free-streaming constraint without altering the existing DM yield (see [233] for calculations

of kinetic decoupling). DM self interactions can also relax this constraint [234], but the number changing processes can change the reported DM yield in this study.

In Fig. 4.5, we enlarge the plot for a closer view of two curves from different formation mechanisms with fixed $\beta_{\rm PBH} = 10^{-13}$. Our main take-away lesson from Fig. 4.5 is that the dependence of the DM yield on the PBH formation mechanism is from the $T_i/M_{\rm PBH}$ term in Eq. (5.25). Since both mechanisms discussed in Section 4.3 produce PBHs with the same scaling $M_{\rm PBH} \propto T_i^{-2}$, the black and red curves in Fig. 4.5 exhibit a high degree of similarity.

4.4.2 High-frequency Gravitational Waves

In this Section, we complete the maps $\{M_{\rm PBH}, \beta_{\rm PBH}\} \to \{\alpha, \beta, T_\star, v_w\} \to \{h_c, f_{\rm GW}\}$ and $\{M_{\rm PBH}, \beta_{\rm PBH}\} \to \{A_\zeta, k_p\} \to \{h_c, f_{\rm GW}\}$ from the PBH parameter space to the strain-frequency plane of GWs. Since both mechanisms generate peaked PBH mass spectra, we approximate the mass function to the monochromatic limit with the same $\{M_{\rm PBH}, \beta_{\rm PBH}\}$ values at the peak location. GW quantities appeared in this section are denoted with the subscript "sw" for sound wave contributions in the FOPT mechanism and with the subscript "ζ" for the curvature perturbation mechanism.

We first calculate the peak frequencies in the two cases. Since our focus is on light PBHs that disappeared in the early Universe, the peak frequency is much higher than existing GW detectors. The peak GW frequencies in both mechanisms have the same parametric dependence on the PBH mass $f_{\rm GW}^{\rm peak} \propto 1/\sqrt{M_{\rm PBH}}$. In the FOPT case, the peak frequency can be derived with Eqs. (4.17) and (4.24),

$$f_{\rm GW,sw}^{\rm peak} \simeq 30.1 \times \left(\frac{M_{\rm PBH}}{10^4\ {\rm g}}\right)^{-\frac{1}{2}} {\rm MHz}, \tag{4.45}$$

for the choice of FOPT parameters $v_w = 0.5$ and $\beta/H_\star = 1.2$. Adjusting v_w and β will only result in minor changes to the pre-factors and will not affect the overall scaling. On the other hand, the peak frequency of induced GWs is derived from Eqs. (4.30) and (4.32),[8]

$$f_{\mathrm{GW},\zeta}^{\mathrm{peak}} \simeq 1.4 \times \left(\frac{M_{\mathrm{PBH}}}{10^4\ \mathrm{g}}\right)^{-\frac{1}{2}} \mathrm{MHz}. \tag{4.46}$$

The $f_{\mathrm{GW}}^{\mathrm{peak}}$ vs M_{PBH} relation is shown in Fig. 4.6. GWs produced during a FOPT (red) are typically at higher frequencies than GWs induced by curvature perturbations (black). Stated differently, the PBH mass from the FOPT is about two orders heavier than that from the curvature perturbation if the identical peak frequency in GWs is thought to originate from both formation mechanisms.

In the next, we calculate the energy density of high frequency GWs for a benchmark DM mass $m_\chi = 1$ TeV in Fig. 4.7 (left). Assuming the correct DM relic abundance $\Omega_\chi h^2 = 0.12$ is emitted by PBHs formed from FOPTs (red) and curvature perturbations (black), we obtain $\{M_{\mathrm{PBH}}, \beta_{\mathrm{PBH}}\}$ with Eq. (4.43) and Eq. (4.44). There is freedom in choosing either the mass or abundance of the PBHs for a given DM mass; we choose benchmarks $M_{\mathrm{PBH}} = 10^4$g (solid) and $M_{\mathrm{PBH}} = 10^2$g (dashed). The PBH abundance is $\beta_{\mathrm{PBH}} \simeq 5.4 \times 10^{-15}$ for FOPTs and $\beta_{\mathrm{PBH}} \simeq 8.2 \times 10^{-15}$ for curvature perturbations when $M_{\mathrm{PBH}} = 10^4$g. For a smaller PBH mass $M_{\mathrm{PBH}} = 10^2$g, the corresponding β_{PBH} values need to be exactly an order of magnitude larger for both mechanisms.

The next step in the procedure for obtaining Ω_{GW} in the FOPT case is as follows. Given a point on the $\{M_{\mathrm{PBH}}, \beta_{\mathrm{PBH}}\}$ plane, we obtain the corresponding values of $T_\star$ from Eq. (4.17) assuming $R_\star/H_\star^{-1} = 1.5$. We further fix the wall velocity to be

[8] The peak location of the variance of density contrasts defined in Eq. (1.15) differs from the peak location for the monochromatic power spectrum. In the numerical simulation, we find the variance peaks at $k \simeq 0.7 k_p$. Therefore we included this factor when deriving $f_{\mathrm{GW},\zeta}^{\mathrm{peak}}$ from M_{PBH}.

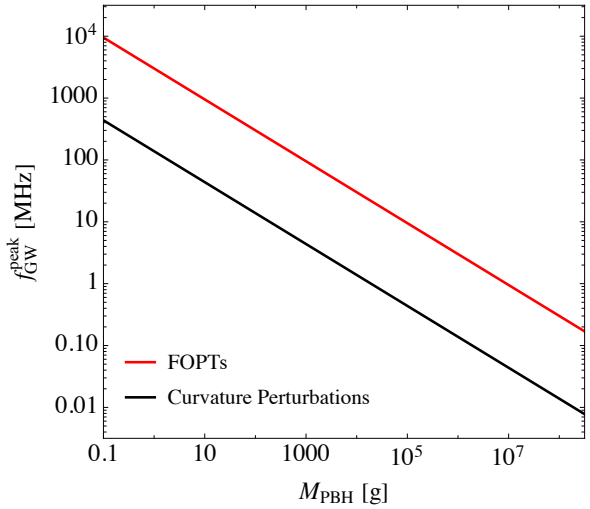


Figure 4.6: The peak frequency of ultra-high frequency GW spectra generated by sound waves during FOPTs (red) and induced by curvature perturbations (black), as a function of the PBH mass. The red curve is calculated with FOPT parameters $\alpha = 0.8$, $\beta/H_\star = 1.2$, and $v_w = 0.5$.

$v_w = 0.5$ and obtain $\beta/H_\star$ by solving Eq. (4.23) numerically. The phase transition temperature is $T_\star \simeq 6.5 \times 10^{13}$ GeV and $T_\star \simeq 6.5 \times 10^{14}$ GeV for $M_{\rm PBH} = 10^4$g and 10^2g respectively. The value of $\beta/H_\star$ is found to be about 1.2 and does not change appreciably as $\{M_{\rm PBH}, \beta_{\rm PBH}\}$ is varied. This is because the pocket distribution is double-exponentially sensitive to the nucleation rate, there a mild change in β can give the correct PBH abundance. There are two additional inputs required: α and κ, as can be seen from Eq. (4.25). We choose $\alpha = 0.8$, which is found to be allowed for $v_w = 0.5$ in Fig. 2 of [235]. We follow Appendix A of [228] to calculate the $\kappa \simeq 0.688$ in the subsonic deflagration regime for our choice of v_w. The suppression factor in Eq. (4.26) is $\Upsilon \simeq 0.71$ with our choice of parameters. This set therefore determines all the data in Eq. (4.25), which is used to obtain $\Omega_{\rm GW}$. The spectrum of GWs from sound waves has a smoother peak with the full spectrum shape determined by the shape function in the second line of Eq. (4.25).

Similarly, in the case of scalar perturbations, once a point on the $\{M_{\rm PBH}, \beta_{\rm PBH}\}$ plane is obtained for a given DM mass, Eq. (4.30) and (**??**) are used to obtain the peak location and amplitude of the monochromatic power spectrum. The primordial fluctuations appear at very small scales as $k_p \simeq 8.9 \times 10^{20}$ Mpc^{-1} and $k_p \simeq 8.9 \times 10^{21}$ Mpc^{-1} for $M_{\rm PBH} = 10^4$ g and $M_{\rm PBH} = 10^2$ g respectively. The amplitudes of monochromatic power spectra that generate heavier and lighter PBHs are $A_\zeta \simeq 0.019$ and $A_\zeta \simeq 0.020$. The benchmark power spectrum parameters are used to calculate induced GWs with Eq. (**??**). The spectrum of induced GWs exhibits a resonant peak at $k = (2/\sqrt{3})k_p$ coming from the amplification when the GW source oscillates at a frequency equals to twice the frequency of the gravitational potential. In Fig. 4.7, we show induced GWs using a delta-function power spectrum for simplicity. In the case where PBHs are generated by an extended power spectrum, the resulting GW spectrum shape is similar to the shape of the power spectrum, but without the presence of the divergent resonance.

GWs generated in the early Universe contribute to the number of effective degrees of freedom as extra radiation. As a result, they are subject to the cosmological constraint from BBN and CMB. This constraint is quantified as the effective number of neutrinos species after electron-positron annihilation, $N_{\rm eff}$. Then any extra radiation, $\Delta\rho_{\rm rad} = \rho_{\rm GW}$ in our case, can be expressed in terms of extra neutrino species, $\Delta N_{\rm eff}$ as

$$\Delta\rho_{\rm rad} = \frac{\pi^2}{30}\frac{7}{4}\left(\frac{4}{11}\right)^{\frac{4}{3}} \Delta N_{\rm eff} T_{\rm rad}^4. \tag{4.47}$$

The upper bound on $\Delta N_{\rm eff}$ sets an upper bound on $\Omega_{\rm GW}$. The Planck measurement result is $N_{\rm eff} = 2.99 \pm 0.17$ [211]. We require the GW contribution should not raise $N_{\rm eff}$ to be more than the 2σ upper bound set by Planck and shade the excluded regions in gray in the left panel of Fig. 4.7. Future CMB-Stage 4 (CMB-S4) experiment is able

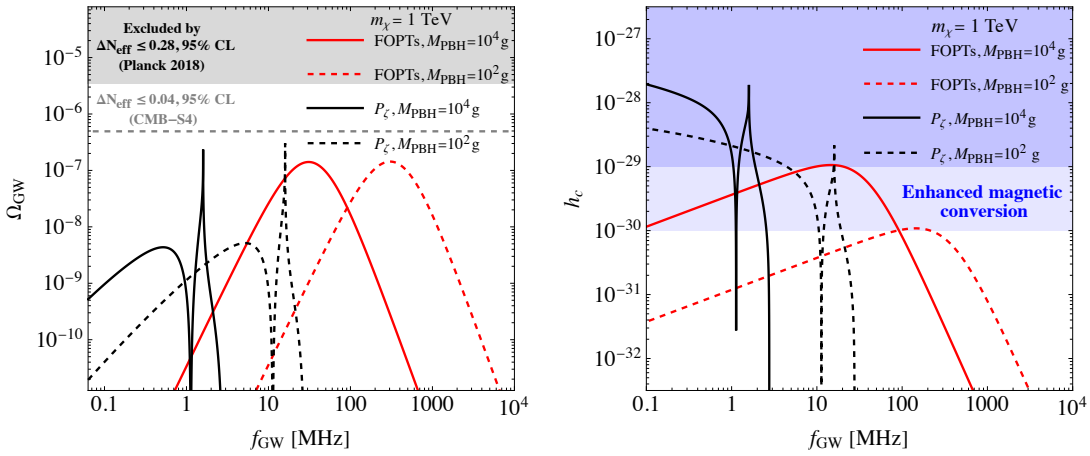


Figure 4.7: GW spectra for the case of producing $m_\chi = 1$ TeV and $\Omega_\chi h^2 = 0.12$ from light PBHs of mass $M_{\rm PBH} = 10^4$g (solid) and $M_{\rm PBH} = 10^2$g (dashed). GWs produced by sound waves during FOPTs are shown in red color, and GWs induced by curvature perturbations are shown in black color. The FOPT parameters are $v_w = 0.5$, $\alpha = 0.8$, and $\kappa \simeq 0.688$. *Left panel:* The GW density $\Omega_{\rm GW}$ as a function of the GW frequency. The current Planck 2σ constraint on GW contributions to $\Delta N_{\rm eff}$ is shown in the gray shaded region [211]. Future CMB-S4 2σ sensitivity is shown with the gray dashed curve [209]. *Right panel:* The characteristic strain h_c as a function of the GW frequency. The blue shaded regions show anticipated sensitivities of enhanced magnetic conversion detection using the inverse Gertsenshtein effect with conservative (dark blue) and optimistic (light blue) estimates.

to improve the sensitivity to $\sigma(N_{\rm eff}) \simeq 0.02$-$0.03$ [209]. We show future CMB-S4 2σ sensitivity limit $\Delta N_{\rm eff} \le 0.04$ with the gray dashed line.

While advancements in future cosmology observations continue to improve the sensitivity to primordial GWs, the positive detection of ultra-high frequency GWs remains a intriguing objective at the intersection of cosmology, particle physics and precision measurements. Various methods have been proposed to detect ultra-high frequency GWs with mechanical sensors [195, 196, 197, 198, 199, 200], interferometers [201, 202], conversion between GW and electromagnetic waves [123, 203, 204, 205, 124, 206], condensed matter systems [207] and radio telescopes [208]. In the right panel of Fig. 4.7, we

show benchmark GW spectra on the h_c vs $f_{\rm GW}$ plane. The strain strength is calculated from $\Omega_{\rm GW}$ with the definition

$$h_c = \frac{1}{f_{\rm GW}} \sqrt{\frac{3\, H_0^2\, \Omega_{\rm GW}}{4\,\pi^2}}, \tag{4.48}$$

where H_0 is the Hubble expansion rate today. In Fig. 4.7 (right), we also show expected future sensitivity reach using the inverse Gertsenshtein effect [113] to probe GWs with a Gaussian beam [236], which improves the GW conversion rate to be only proportional to h_c. The dark blue region indicates the sensitivity is assumed to be $h_c \simeq 10^{-29}$, while the light blue region is assumed to have a more optimistic sensitivity of $h_c \simeq 10^{-30}$. We plot the sensitivity in a wide range of $f_{\rm GW}$ where resonant conversion requires the Gaussian beam and the single photon detector to work at the frequency of the target GWs. See also [126] for discussions on future technological improvements to implement GW detection using Gaussian beams. In general, the future sensitivity to ultra-high frequency GWs has the potential to reach peak regions of GW spectra generated by PBH formation mechanisms.

In Fig. 4.8, we show the peak strength of GW signals for DM mass $m_\chi = 1$ TeV (left) and $m_\chi = 10^{15}$ GeV (right) produced by light PBHs, with the same color scheme used in Fig. 4.7 for two formation mechanisms. We choose PBH masses in the allowed region for the fixed DM mass in Fig. 4.4. For each $\{M_{\rm PBH}, m_\chi\}$, we calculate the peak frequency and peak strain values of GW spectra $\{f_{\rm GW}^{\rm peak}, h_c^{\rm peak}\}$, which are used to generate the curves. In the left panel, the correct DM relic abundance is always produced during the radiation-dominated era. Therefore, the left endpoints of curves are determined by the BBN constraint $M_{\rm PBH} < 10^9$ g while the right endpoints are determined by the CMB constraint $M_{\rm PBH} > 0.1$ g. In the right panel, DM is heavier

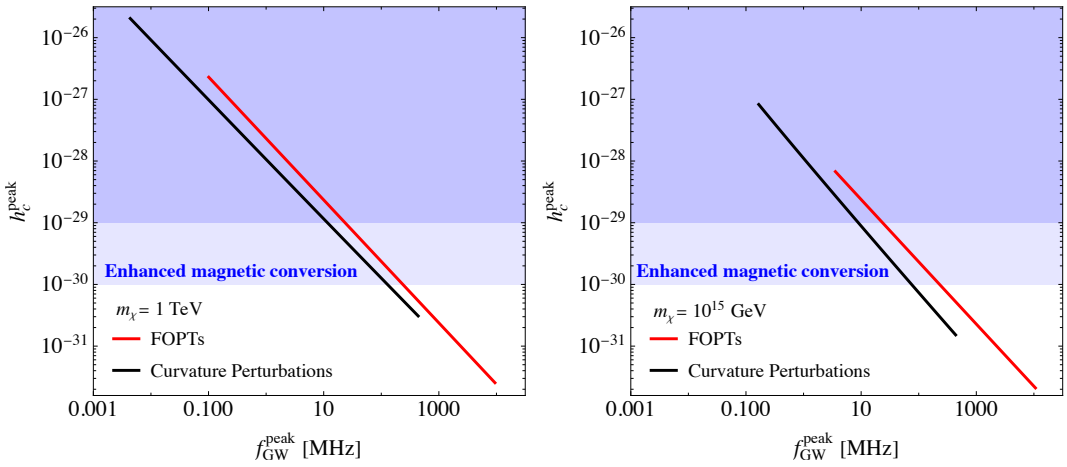


Figure 4.8: The peak strain strength $h_c^{\rm peak}$ and the peak frequency $f_{\rm GW}^{\rm peak}$ of GW spectra generated in the FOPT mechanism (red) and the curvature perturbation mechanism (black) that produce the DM relic abundance during a radiation-dominated era with $m_\chi = 1$ TeV (left) and $m_\chi = 10^{15}$ GeV (right), and with varying $M_{\rm PBH}$. The FOPT parameters are $v_w = 0.5$, $\alpha = 0.8$, and $\kappa \simeq 0.688$. The induced GWs are calculated assuming the power spectrum has a finite width and there is no resonant amplification present for the induced GWs (see the text for explanation). The blue shaded regions show conservative (dark blue) and optimistic (light blue) sensitivity anticipations for future ultra-high frequency GW detection using the inverse Gertsenshtein effect.

and its production from relatively heavy PBHs can only happen in the early matter-domination region shaded in the top-right corner of Fig. 4.4. For this reason, the left endpoints in the right panel are determined by the requirement $\beta_{\rm PBH} < \beta_{\rm PBH,crit}$, while the right endpoints are still set by the CMB constraint. We calculate the peak strain of FOPT curves (red) with Eq. (4.25). The peak strain of induced GWs (black) depends on the shape of the power spectrum. We formulated a conservative estimate by making the assumption that the power spectrum has a finite width, such that the resonant amplification has not been included in the GW spectrum. In this case, $\Omega_{\rm GW}^{\rm peak} \simeq A_\zeta^2 \times \Omega_{\rm rad,0}$ with A_ζ derived from the DM relic abundance. The peak strain $h_c^{\rm peak}$ is calculated accordingly. Both mechanisms predict ultra-high frequency GWs in the MHz-GHz range, offering a distinct signal strength benchmark for future searches.

4.5 Conclusions

We have studied the possible traces of light PBHs, which disappear before BBN, in the form of ultra-high frequency (MHz-GHz) GWs. More precisely, we have explored the signatures of PBH formation in the MHz-GHz frequency range of GW spectrum and their connections with the DM particles produced by Hawking evaporation of PBHs. The target frequency window of GWs is basically determined by the formation mechanism of PBHs.

Assuming that DM particle has only gravitational interactions, and that PBHs would never dominate the energy density of the Universe, the final abundance of DM is set by the mass and abundance of the PBHs and the mass of the DM particle. For a certain PBH formation mechanism, the part of the parameter space which gives rise to the observed relic abundance of DM today, leads to the correlated ultra-high frequency GWs and subsequently to the strain of the GWs as a function of frequency.

Although there are a variety of mechanism for light PBH formation, in this study we focused on two specific formation mechanisms: PBH formation by curvature perturbations, and formation of PBHs from the collapse of particles trapped in the false vacuum of a FOPT.

For the canonical formation of PBHs by curvature perturbations, GWs are sourced by curvature perturbations with the second-order effects, and can be described by the amplitude of the power spectrum of curvature perturbations and the peak mode of the power spectrum. For the formation of PBHs from FOPTs, the GWs, that are generated by the FOPT itself with the dominant contribution from sound waves in the fluid, are expressed in terms of the energy density released during phase transition normalized by the radiation energy density, the inverse time scale of the phase transition, the temperature of the phase transition, and the bubble wall velocity.

As we have showed, the dependence of the yield of DM on PBH formation mechanism is encoded in the ratio of the mass of the PBH to the temperature of the Universe at the formation time of the PBH. Since in both of the formation mechanisms studied in this paper, the PBH mass follows the horizon mass at the formation time, therefore, they require almost the same initial abundance of PBHs to lead to the observed value of DM abundance today.

After deriving the formation mechanism parameters by fixing the DM relic abundance, we find that GWs produced during a FOPT are typically at higher frequencies than GWs induced by curvature perturbations. For the same peak frequency, the PBH mass from the FOPT is about two orders heavier than that from the curvature perturbation. A more detailed computational treatment relying on solving Boltzmann equations for the benchmark FOPT temperature and nucleation rate from [47] in the context of evaporating PBHs will be investigated in a future work.

As an example, we evaluated the energy density of high frequency GWs generated during the formation of PBHs with masses of $M_{\rm PBH} = 10^4$g and $M_{\rm PBH} = 10^2$g provided that the observed relic abundance of DM today is explained by DM particles with a mass of $m_\chi = 1$ TeV emitted by PBHs. For FOPT formation mechanism, the necessary initial abundances of PBHs of mass $M_{\rm PBH} = 10^4$g and $M_{\rm PBH} = 10^2$g are found to be equal to $\beta_{\rm PBH} \simeq 5.4 \times 10^{-15}$ and $\beta_{\rm PBH} \simeq 5.4 \times 10^{-14}$, which then determine the temperature of FOPTs to be equal to $T_\star \simeq 6.5 \times 10^{13}$ GeV and $T_\star \simeq 6.5 \times 10^{14}$ GeV respectively. GW spectra generated by sound waves during these FOPTs peak at 30 MHz and 300 MHz respectively. Since the pocket distribution is double-exponentially sensitive to the nucleation rate, variations in the mass and initial abundance of PBHs only change the required nucleation rate slightly.

In the case of scalar perturbations, PBHs with masses equal to $M_{\rm PBH} = 10^4$g and $M_{\rm PBH} = 10^2$g with initial abundances of $\beta_{\rm PBH} \simeq 8.2 \times 10^{-15}$ and $\beta_{\rm PBH} \simeq 8.2 \times 10^{-14}$,

respectively, can explain the observed abundance of DM today. For $M_{\rm PBH} = 10^4$ g, the primordial fluctuations appear at $k_p \simeq 8.9 \times 10^{20}$ Mpc^{-1} which corresponds to GW signal with a peak frequency of 1 MHz. For $M_{\rm PBH} = 10^2$ g, these parameters are given as $k_p \simeq 8.9 \times 10^{21}$ Mpc^{-1} and 10 MHz, respectively.

Although the projected sensitivity of the future CMB-S4 experiment in probing stochastic GW signals from early Universe is almost one order of magnitude better than Planck, it is still a few times above the predicted signals by the PBH formation mechanisms studied in this paper. On the other hand, the expected future sensitivity reach of the enhanced magnetic conversion detection by utilizing the inverse Gertsenshtein effect can probe the peaks of the predicted GW signals in this study.

As we demonstrate here, PBH formation via FOPTs and curvature perturbations, both can give rise to production of ultra-high frequency (MHz-GHz) GWs. These GW signals, with distinct strength and frequency spectrum, could potentially fall into the reach of future searches and can be used to differentiate between different PBH formation mechanisms. Possible correlations of new physics with PBH formation mechanism, e.g. DM production through the Hawking evaporation of PBHs, is also coded in the associated GW signals, which make the MHz-GHz GW searches a promising frontier to pursue.

Chapter 5

Recycled Dark Matter

5.1 Introduction

Thermal freeze-out has for a long time been the preferred history of the cosmological evolution of dark matter (DM). Its most outstanding feature is the fact that DM with weak scale interactions and a thermal history reproduces the observed relic abundance. Given that new physics is expected to appear at the weak scale for completely unrelated reasons (for example the hierarchy problem), this fact presented itself as a "miracle" for several decades, leading to DM searches over numerous facilities geared at the weak scale thermal candidate.

The failure of said candidate to materialize has prompted a flurry of DM and early Universe model-building in recent years. A part of the community has focused on changing the equation of state of the early Universe (for example, by introducing an early period of matter domination [121, 122]), thereby altering the thermal evolution of DM and opening up vast regions of hitherto disallowed parameter space. Another part of the community has focused on newer mechanisms by which DM achieves the observed relic density, some of which are necessitated by the vastly different DM mass and couplings compared to the weak scale [237, 238]. Model building to go beyond the WIMP paradigm for achieving the correct relic abundance has been studied by many authors; for a flavor of recent studies, we refer to [239, 240, 241, 242, 243, 244, 245, 246, 247, 248, 249].

The purpose of this chapter is to explore one such new mechanism for the production of DM, which we dub "recycled dark matter". Recycling works as follows. A single or multiple (say, two) species of particles is/are trapped in a false vacuum region during a first order phase transition (FOPT) due to kinematics (they are very heavy in the true vacuum, and practically massless in the false vacuum). The species, which one can imagine to constitute a dark sector, maintains thermal equilibrium in its own sector and kinetic equilibrium with the Standard Model (SM) before the FOPT. The rate at which the trapped species of the dark sector leaks into the true vacuum or annihilates is suppressed enough that at some point, the false vacuum collapses into a primordial black hole (PBH) (this condition is what requires the introduction of multiple species in the dark sector, as we shall see). For phase transition temperatures high enough, the mass of the PBHs thus formed is small and they all evaporate before Big Bang Nucleosynthesis (BBN). When they evaporate, they produce ("recycle") the dark sector that originally went into forming them. At this stage, however, the dark sector species are thermally decoupled, ultra-heavy (with their true vacuum mass), and constitute a cold dark sector consisting of multiple non-interacting DM species.

One can ask: beyond the novelty of the recycling mechanism, does this production mechanism solve any outstanding issues for DM models? Our answer is in the affirmative: it presents a very useful way to think about the production of DM heavier than the Griest-Kamionkowski bound [250] – the so-called ultra heavy DM (UHDM) candidates. The logic is as follows. Ultimately, recycling arises from the fact that the PBHs all Hawking evaporate before BBN, which necessitates light PBHs and therefore phase transitions at a high temperature. But the temperature during the phase transition is set by the (also therefore high) vacuum expectation value of whatever scalar field is responsible for the symmetry breaking, which in turn sets the mass-scale of the

dark sector species. Thus, the recycling mechanism is most naturally suited for UHDM candidates.

One can then ask: how is the correct relic density obtained in this scenario? Typically, UHDM candidates beyond the Griest-Kamionkowski bound require an exponential suppression of their number density to achieve the correct relic density. This can be achieved by various mechanisms of which we mention a few (for a recent review, we refer to the Snowmass report [251] and references therein): entropy dilution [252], an enhancement of the annihilation cross section (for example through Sommerfeld enhancement [253]), specific multi-species annihilation patterns [254, 255, 256, 257], the suppression of the number density through gravitational production (for example the case of WIMPzillas [258]) and through various avatars of freeze-in and Boltzmann suppression (for example being filtered [259, 260] or squeezed out [261] during phase transitions). In contrast, for recycled DM the exponential suppression of the DM number density arises from the distribution of false vacuum pockets shown in Eq. (1.26).

It is important to contrast recycling with other UHDM production mechanisms that rely on phase transitions. The mechanisms that are most closely related are filtered DM and dark quark nuggets and Fermi-balls [262, 263, 264][1]. In filtering, the DM candidates escape from the false vacuum to the true vacuum where their number density is Boltzmann suppressed while the remaining DM particles in the false vacuum annihilate away. In recycling, on the other hand, the DM candidates cannot filter out of the false vacuum as efficiently, since their annihilation products are also massive in the true vacuum. Trapped in the false vacuum, the DM particles annihilate into each other and the annihilation products are also too heavy to escape efficiently. The dark sector maintains its own thermal equilibrium while evolving separately to a higher

[1]Mechanisms that rely on super-cooling [265] or bubble wall collision (babyZillas [266]) are quite different.

temperature than the SM sector. Finally, a PBH forms when the trapped dark sector is compressed to below its Schwarzschild radius.

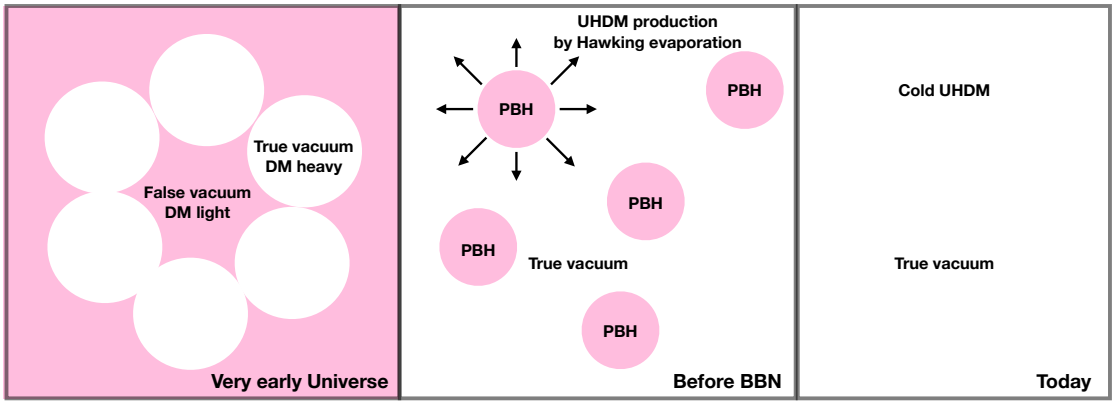


Figure 5.1: The general scheme of recycled DM. **Left:** In very early Universe, a dark scalar field develops a vacuum expectation value (vev) and gives rise to a FOPT which is succeeded by formation of true vacuum bubbles. Dark sector particles, which are in kinetic equilibrium with the SM particles, are assumed to be massless in the false vacuum while they acquire a very large mass in the true vacuum. Therefore, they remain trapped in the false vacuum. **Middle:** False vacuum pockets (containing dark sector particles) that are large enough collapse into light PBHs and eventually evaporate before BBN to emit all the particles in the spectrum including dark sector particles. **Right:** The dark sector particles emitted by PBHs get diluted by the expansion of the Universe until today to explain the observed abundance of DM.

The distinction of recycling with dark quark nuggets or Fermi-balls is that in recycling, the PBHs all completely evaporate and reproduce the dark sector that originally collapsed (i.e., the UHDM are not compact objects but simply regular GUT-scale particles formed from an evanescent intermediate PBH stage). The main stages are illustrated in Fig. 5.1.

The main goal of this chapter is to offer a proof of concept of recycling, using a simple DM sector consisting of a real scalar ϕ and a Dirac fermion χ as a template. The scalar undergoes spontaneous symmetry breaking and acquires a vev $\sim 10^{11} - 10^{15}$ GeV; consequently both the scalar and the fermion acquire large masses at this scale in the true vacuum. We compute the filtering rate and position ourselves in a region

of parameter space where the filtered DM contribution to the relic density is small. We go on to study the conditions for PBH formation in false vacuum pockets and the ensuing yield of the scalar ϕ and fermion χ from Hawking evaporation, obtaining the parameter space where the correct relic density will be produced.

There are two novel features of recycled DM that we want to emphasize. The first pertains to the PBH side of the story, while the second pertains to the UHDM side. On the PBH side, recycling features *extended PBH mass functions whose shape is controlled by IR physics*[2]. The reason is as follows. Since the products of DM annihilation in the false vacuum remain trapped there, pockets of all sizes ultimately collapse to PBHs (this can be contrasted to the situation in [259, 260]). The lower cutoff in the PBH mass function is provided by the strength of the interaction that maintains the dark and SM sectors at the same temperature at the onset of the FOPT and facilitates dark sector annihilation into SM particles that escape the pocket. The strength of this interaction provides parametric control over the shape of the mass function, which we display in Fig. 5.4. This furnishes an example of the shape of PBH mass functions being controlled by the cutoff scale and coupling of effective operators in the IR.

On the UHDM side, the novel feature is the following: recycling requires multiple dark sector species in thermal equilibrium prior to PBH formation, which are then thermally decoupled from each other after Hawking evaporation. Depending on the mass of the PBHs which produce them and also the interactions with the SM, they may or may not come back to kinetic equilibrium with the SM bath, but they cannot reach chemical equilibrium. Some (at least one) of these species will have long enough lifetimes to persist to the current Universe, and therefore the cold DM comprising the relic density today is typically composed of multiple UHDM candidates. This provides

[2]We denote by "IR physics" any physics that does not directly depend on the inflationary era, which is where PBH mass functions have typically been modelled. In our scenario, the PBH mass function can be tuned in ordinary effective field theory, without appealing to Planck-scale physics.

an example of a multi-component dark sector whose components were once in thermal equilibrium but are now thermally decoupled.

5.2 Trapped Dark Sector during FOPT

In this Section, we introduce the template dark sector Lagrangian that we will be working with. We then discuss the novel trapping behavior of the dark sector during a FOPT. This enables us to obtain the mass scales where the recycling effect is dominant for generating the observed DM abundance. In addition, we compare dark sector models that host black hole formation from the over-density of trapped particles, and introduce the idea of multi-particle dark sector.

5.2.1 Dark Sector Model

To provide an illustrative example of recycling, we introduce a scalar ϕ and a Dirac fermion χ with interactions as follows:

$$\mathcal{L} \supset -y_\chi \phi \bar{\chi}\chi + \mu^2\phi^2 - \lambda\phi^4 + \mathcal{L}_{\text{SM}-\text{DS}} \tag{5.1}$$

Here we will focus our discussion on the dark sector while refraining from making any assumptions about the specifics of the dark sector-SM interactions $\mathcal{L}_{\text{SM}-\text{DS}}$, which we only assume is strong enough to keep the two sectors with the same temperature before the FOPT. In the rest of this subsection, we use the subscript d to indicate a particle belongs to the dark sector, without specifying its detailed particle nature other than those affecting the trapping process. The result applies to both χ and ϕ particles in Eq. (5.1). We will assume that ϕ undergoes a FOPT and choose a selection of the parameters $\{\mu, \lambda, y_\chi\}$ such that $m_\chi = m_\phi = y_\chi\langle\phi\rangle$ in the true vacuum. One could also

endow the dark fermionic sector with an additional flavor structure: y_{ij}. In the rest of the chapter, we will consider a single flavor, reserving the multi-flavor case for future work.

Now we calculate the trapping rate of dark sector particles during the FOPT from the time $T = T_\star$ when false vacuum regions nucleate and keep shrinking as bubble wall are moving at a velocity of v_w. It is the gap between particle mass values on the true vacuum side and the false vacuum side of the bubble wall that determines the trapping rate. Unless sitting on the exponentially suppressed Boltzmann tail, a DM particle with a smaller mass in the false vacuum cannot enter the true vacuum due to energy momentum conservation. We keep to notation for bubble wall velocity in the $+z$ direction. To obtain the probability of particles being bounced back from the bubble wall, we can first calculate the population $\Delta N_{\rm in}$ of particles that satisfy the pass-through condition $\mathcal{T}(\vec{p})$ in front of the bubble wall area ΔA within time duration Δt [259],

$$\begin{aligned}\frac{\Delta N_{\rm in}}{\Delta A} &= \frac{g_d}{(2\pi)^3}\int d^3\vec{p}\int_{r_o}^{r_0-\frac{p_z\,\Delta t}{|\vec{p}|}} dr\,\mathcal{T}(\vec{p})\,\Theta(-p_z)\,f(\vec{p};\vec{x}) \\ &= \frac{g_d}{(2\pi)^3}\int d^3\vec{p}\,\Theta(-p_z-m_d)\,\Theta(-p_z)\,(-\frac{p_z\,\Delta t}{|\vec{p}|})\,f(\vec{p};\vec{x}). \end{aligned} \tag{5.2}$$

$\Theta(.)$ is the Heaviside step function. A particle can penetrate the wall if its momentum $\vec{p}$ projected in the perpendicular direction towards the bubble wall $-p_z$ is larger than the mass gap, meaning $\mathcal{T}(\vec{p}) = \Theta(-p_z - m_d)$. For the dark sector particle, g_d is its degree of freedom, m_d is its mass in the true vacuum side of the bubble wall, and $f(\vec{p};\vec{x})$ is its phase space distribution in the rest frame of the bubble wall. The absolute value of

the penetrated particle flux can be defined in the wall rest frame as $J_w \equiv \frac{dN}{dAdt} \simeq \frac{\Delta N}{\Delta A\,\Delta t}$, which can be written as,

$$\begin{aligned} J_w &= \frac{g_d}{(2\pi)^3}\int d^3\vec{p}\,\Theta(-p_z - m_\chi)\,\Theta(-p_z)\,f(\vec{p};\vec{x})\,(-\frac{p_r}{|\vec{p}|}) \\ &= \frac{g_d}{(2\pi)^3}\int_0^\pi d\theta\,\sin\theta\int_0^{2\pi} d\phi\int_0^\infty dp\,p^2(-\cos\theta)\,\Theta(-p\cos\theta - m_d)\,\Theta(-\cos\theta)\,f(\vec{p}). \end{aligned} \tag{5.3}$$

In the second line, we simplify the particle momentum integral in spherical coordinate system. We also assume the phase space distribution is homogeneous such that $f(\vec{p};\vec{x}) = f(\vec{p})$ only depends on the particle momentum.

The phase space distribution $f(\vec{p})$ can be obtained by imposing a Lorentz transformation on the particle equilibrium distribution from the local plasma rest frame to the bubble wall rest frame. The particle would be boosted if there was a relative motion between the bubble wall and the plasma in front of the wall. We assume the temperature of dark sector particles is T. The bulk of local plasma is moving with a velocity $\vec{\tilde{v}}$ in the $-\hat{z}$ direction towards the wall. Here bulk refers to the overall motion of the particles. Then the phase space distribution in the wall rest frame is

$$\begin{aligned} f(\vec{p}) &= \frac{1}{e^{\tilde{\gamma}\,(E - \vec{\tilde{v}}\cdot\vec{p})/T} \pm 1} \\ &\simeq \frac{1}{e^{\tilde{\gamma}\,(p + \tilde{v}\,p\,\cos\theta)/T}}. \end{aligned} \tag{5.4}$$

The Lorentz factor from $\tilde{v}$ is $\tilde{\gamma} = 1/\sqrt{1-\tilde{v}^2}$. In the last line, we approximated the phase space distribution with a Boltzmann distribution of massless particles. The difference coming from this approximation for a Bose-Einstein distribution and a Fermi-Dirac

distribution is found to be $\mathcal{O}(0.2)$ in [259]. Note that particles are massless in the false vacuum side of the bubble wall. Plugging Eq. (5.4) into Eq. (5.3), we obtain:

$$\begin{aligned} J_w &= \frac{g_d}{(2\pi)^2}\int_0^{-1} d\cos\theta\,\cos\theta\int_{-\frac{m_d}{\cos\theta}}^{\infty} dp\,\frac{p^2}{e^{\tilde{\gamma}\,(1+\tilde{v}\,\cos\theta)\,p/T}} \\ &= \frac{g_d\,T^3\,(1\,+\,\tilde{\gamma}\,m_d\,(1-\tilde{v})/T)}{4\,\pi^2\,\tilde{\gamma}^3\,(1-\tilde{v})^2}\,e^{-\tilde{\gamma}\,m_d\,(1-\tilde{v})/T}. \end{aligned} \tag{5.5}$$

Eq. (5.5) agrees with previous studies [259] up to the sign difference to account for the direction of the flux. One can see the penetrated flux is exponentially suppressed by the ratio of particle mass in the true vacuum and particle temperature in the false vacuum, indicating that we can trap most particles inside false vacuum regions.

In the end, the number density of particles penetrated into the true vacuum region seen in the global plasma frame is

$$n_d^{\text{filtered}} = \frac{J_w}{\gamma_w\,v_w}. \tag{5.6}$$

Here the bubble wall velocity in the global plasma frame is v_w, and $\gamma_w = 1/\sqrt{1-v_w^2}$. One should note the difference between velocities v_w and $\tilde{v}$, and between the Lorentz factors γ_w and $\tilde{\gamma}$. Quantities represented with tilde are defined in the bubble wall rest frame, and quantities represented without tilde are defined in the global plasma frame. The Lorentz factor γ_w in the denominator accounts for the time dilation effect experienced by the observer in the global plasma frame. The $n_{d,\text{filtered}}$ represents the number density of the dark sector species that can enter the true vacuum regardless of the sudden mass increase at the bubble wall. On the other hand, the fraction of particles that are trapped is defined

$$F^{\text{trap}} = 1 - n_d^{\text{filtered}}/n_d, \tag{5.7}$$

where n_d is the equilibrium number density of the dark sector particle.

In Fig. 5.2, we show the fraction of trapping $F^{\rm trap}$ during FOPT as a function of the particle mass-temperature ratio m_d/T. We show the limit $\tilde{v} = 0$ in solid curves where the maximum trapping rate is achieved with the assumption that the bulk gains an overall velocity to move relatively at rest with respect to the bubble wall. As a comparison, we show the case of $\tilde{v} = 0.1$ in dashed curves where the trapping rate is suppressed by the Lorentz boost on the particle phase space distribution in Eq. (5.4). We also show the bubble wall velocities $v_w = 0.5$ (blue) and $v_w = 0.2$ (red). The trapping rate is higher with a larger v_w as a result of the time dilation effect in Eq. (5.6).

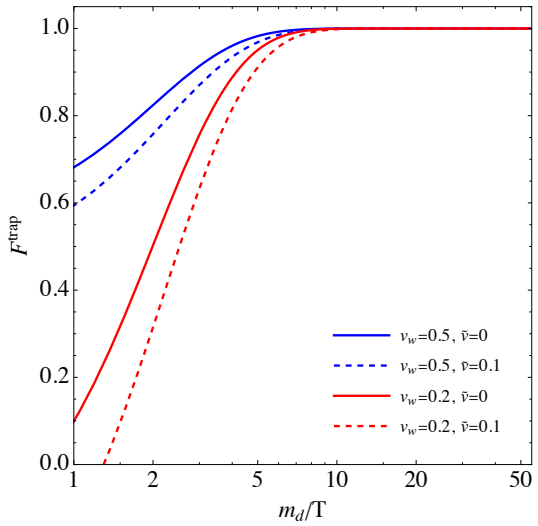


Figure 5.2: The trapping fraction $F^{\rm trap}$ as a function of m_d/T for different relative velocity of particle bulk motion in front of the bubble wall $\tilde{v} = 0$ (solid) and $\tilde{v} = 0.1$ (dashed). m_d denotes either m_χ or m_ϕ. The bubble wall velocity in the global plasma frame is shown in different colors $v_w = 0.5$ (blue) and $v_w = 0.2$ (red).

5.2.2 Why a Multi-particle Dark Sector is Required

Most models of PBH formation from phase transitions in the recent literature invoke a single fermion species that gains mass from symmetry breaking, while the scalar

responsible for the symmetry breaking remains massless. In such scenarios, the dark sector ultimately consists of only one species (the fermion). In this subsection, we discuss the challenges of implementing the recycling mechanism for such cases.

The main challenge lies in the annihilation of the fermion species χ to the scalar ϕ via $\bar{\chi}\chi \to \phi$ and $\bar{\chi}\chi \to \phi\phi$ allowed by the Yukawa coupling $y_\chi \phi \bar{\chi}\chi$. For massless scalars, the ϕ particles thus produced escape into the true vacuum. This effectively leaks out the energy density of the false vacuum pockets and inhibits PBH formation. One may be able to suppress this annihilation by reducing the Yukawa coupling, but that introduces its own problems as far as recycling is concerned. Indeed, the scaling arguments for the Yukawa coupling forwarded in [47] are instructive in this regard. The annihilation $\bar{\chi}\chi \to \phi$ scales as $y_\chi^2 T_*$ while the Hubble length scales as T_*^{-2} in a radiation-dominated Universe. Therefore, to keep the number of annihilations per Hubble length invariant, the Yukawa should scale as $y_\chi \sim 10^{-5}\sqrt{T_*/\mathrm{PeV}}$. This gives a very suppressed Yukawa at the temperatures we are interested in. As we will see in Fig. 5.6, recycling requires

$$\langle\phi\rangle \sim \mathcal{O}(55-60) \times T_* \times (1/y_\chi) \ . \tag{5.8}$$

A small Yukawa coupling therefore would imply a huge hierarchy between $\langle\phi\rangle$ and T_*.

For phase transitions at higher temperatures, the $\bar{\chi}\chi \to \phi\phi$ annihilation process becomes operational, and the appropriate scaling is $y_\chi^4 T_*$. The benchmarks studied in [47] where successful PBH formation could occur included $y_\chi = 0.3$ for $T_* = 10^{15}$ GeV. From Eq. (5.8), it is clear that this would require a large hierarchy between $\langle\phi\rangle$ and T_*. We therefore see that recycling requires large hierarchies between $\langle\phi\rangle$ and T_*, if the scalar ϕ is allowed to escape into the true vacuum. One option to ameliorate the large hierarchy could be to increase $y_\chi \sim \mathcal{O}(\sqrt{4\pi})$. However, this would only increase

the annihilation of $\bar{\chi}\chi$ into $\phi\phi$. Therefore, a heavy ϕ particle that is itself trapped in the false vacuum is necessary.

A different strategy could be pursued if one insisted on keeping ϕ massless. This would be to allow the symmetric component of χ to annihilate away to ϕ which escapes, but to have the asymmetric component remain in the false vacuum. This is the option followed in scenarios of Fermi-ball formation, about which we now make a few comments. The asymmetry in the distribution of the χ particles can be generated with a chemical potential as in usual asymmetric DM models [267, 130], or accidentally from the Gaussian statistics of the χ relic number density [261, 268]. It should be noted that both the chemical potential generated asymmetric abundance and the accidentally generated asymmetric abundance are usually discussed in the context of particles that are already out of equilibrium. In our opinion, the application of these asymmetry generation mechanisms to the massless fermionic species which is still in equilibrium in the false vacuum pocket needs further study. Such further investigation would confirm the generation of a dominant χ population over the $\bar{\chi}$ particle in the false vacuum; currently, however, we do not pursue this route.

One could imagine that the presence of the ϕ-mediated attractive force might enhance PBH formation before dark sector annihilation over-dilutes the energy density in the false vacuum. The bubble wall keeps compressing the χ and ϕ particles left within the pocket until the mean separation between χ particles becomes shorter than the range m_ϕ^{-1} of the strong Yukawa interaction mediated by ϕ. Since the Yukawa force is attractive, the additional attraction could lead to the collapse of χ particles into a PBH before the fermion degeneracy pressure becomes relevant. Moreover, the PBH formation could happen for either symmetric or asymmetric distribution between χ and $\bar{\chi}$ particles. The asymmetric distribution case has been studied for the collapse of Fermi-balls due to an internal Yukawa force in [48, 50]. A detailed simulation of

the collapse process triggered by the Yukawa interaction is necessary to determine the required strength of the Yukawa force as well as the collapse criteria (for example, how the Schwarzschild radius compares to the particle separation and the Yukawa force range). We do not comment on this possibility further in the present work.

Finally, there is one more reason why a multi-particle dark sector is required for recycling models. Typically, one requires the dark sector trapped in the false vacuum to maintain kinetic equilibrium with the SM up to the stage when the phase transition occurs. This involves couplings between the dark sector and the SM sector through higher dimensional operators suppressed by some cutoff scale. These operators can subsequently induce decays of the dark sector particles after they are produced from Hawking evaporation, jeopardizing their status as cold DM today. In the case of a single dark sector particle, this eventuality can impose severe constraints on the mass of the DM and the cutoff scale. Such a situation is avoided for multiple particles in the dark sector; even if one species decays, others can constitute cold DM in the current Universe.

We point out an important caveat here. The dark sector is required to have multiple components during the PBH formation stage and also during Hawking evaporation for reasons we have just discussed. However, after evaporation, the species that is responsible for establishing kinematic equilibrium with the SM may typically mediate early decays of other species, since we are considering UHDM. In our template model, we will choose the decaying particle to be ϕ, and the cold DM in the current Universe will be constituted by (the possibly many flavors of) the χ particles.

5.3 Thermal History and PBH Formation

In this section, we discuss the thermal history of the dark sector whose particles are trapped during the process described in Sec. 5.2.1. The trapped particles generate local over-dense regions, and if the trapping process lasts long enough, these regions collapse into PBHs. We examine the condition of forming PBHs and calculate the their mass function for our scenario[3]. As we shall see, the term $\mathcal{L}_{\rm SM-DS}$ in Eq. (5.1) that guides the interaction of the two sectors will play a critical role in this discussion.

5.3.1 Thermal History of the Dark Sector

We start with the term in the Lagrangian that mediates the interaction between the hidden sector and the SM:

$$\mathcal{L}_{\rm SM-DS} = \frac{\alpha_\Lambda}{\Lambda}\bar{\chi}\chi H^\dagger H \ , \tag{5.9}$$

where α_Λ is the coupling constant of the portal interaction, H is the SM Higgs and Λ is a cut-off scale that we will take to be near the GUT scale. Other portal operators would work as well; we take Eq. (5.9) to illustrate our main ideas. The thermal evolution of the dark sector is tracked from temperatures $T \gg \Lambda$. The dark sector and the SM are in equilibrium at the onset of the cosmic expansion. Kinetic equilibrium can be maintained until $T \simeq \Lambda$ provided that the scattering rate is larger than the Hubble expansion rate, $\Gamma_{\rm sca} = n_{\rm SM}\,\alpha_\Lambda^2/\Lambda^2 \gtrsim H(\Lambda)$. Here $n_{\rm SM}$ is the number density of SM particles that a dark sector particle can scatter with. We can derive the lower limit on α_Λ to maintain kinetic equilibrium, as a function of the energy scale Λ,

$$\alpha_\Lambda \gtrsim 0.17 \times \left(\frac{g_\star + g_\phi + \frac{7}{8}g_\chi}{106.75 + 4.5}\right)^{1/4} \left(\frac{\Lambda}{10^{16}\ \text{GeV}}\right)^{1/2} . \tag{5.10}$$

[3]For general reviews of PBHs, we refer to [177, 147].

Here $g_\star$ is the effective number of relativistic degrees of freedom for SM. The same interaction also mediates the annihilation between SM and dark sector particles $\bar{\chi}\chi \to$ SM, $\phi\phi \to$ SM. When $T \gtrsim \Lambda$, the annihilation cross section scales as $\sigma_{\rm ann} = \alpha_\Lambda^2/T^2$, thus the annihilation rate $\Gamma_{\rm ann} = n_\chi\, \alpha_\Lambda^2/T^2 \propto T$ is proportional to the temperature of the dark sector. Below the scale Λ, the cross section for the annihilation is assumed to be constant: $\sigma_{\rm ann} = \alpha_\Lambda^2/\Lambda^2$. Therefore the annihilation rate $\Gamma_{\rm ann} = n_\chi\, \alpha_\Lambda^2/\Lambda^2 \propto T^3$ is proportional to T^3, which means the energy loss from the dark sector to the SM sector is more efficient at places where the dark sector temperature is higher.

When the temperature drops to $T \lesssim \Lambda$, the two sectors start to decouple from equilibrium, because the particle number density keeps dropping while the portal cross section saturates the constant value $\alpha_\Lambda^2/\Lambda^2$. This suppresses the annihilation and scattering rate between the two sectors. Kinetic equilibrium may be kept longer than chemical equilibrium because of the larger number of degrees of freedom for target particle species for the scattering process than $g_{\chi/\phi}$ for the annihilation process. In general, we expect the two sectors to evolve separately with their own temperatures after their decoupling. We assume that there is no reheating effect during $T_\star \lesssim T \lesssim \Lambda$, such that two sectors accidentally evolve to the same temperature when the FOPT starts. A model dependent analysis could determine the deviation from this assumption, but it will not change the conclusions of this study. Therefore, we take $T_\chi = T_\phi = T_{\rm SM}$ when we study the dynamics of the dark sector during the phase transition.

5.3.2 Black Hole Formation

Since the equilibrium between the dark sector and the SM sector can be achieved with the effective coupling in Eq. (5.9), we assume $T_\chi = T_\phi = T_\star$ where $T_\star$ is the nucleation temperature of the false vacuum. Inside the bubbles, the symmetry is broken and the masses of the dark sector particles are $m_\phi = m_\chi \sim y_\chi \langle\phi\rangle$. On the

other hand, outside the bubble in the false vacuum pockets, the masses are their pole mass $m_\phi = 0$ and $m_\chi = 0$ with additional thermal corrections of $\mathcal{O}(T_\star)$. Given that their mass gaps are much larger than their kinetic energy $m_{\chi/\phi} \gg T_\star$, dark sector particles are trapped inside the false vacuum and heated up when they are bounced back from bubble walls. When the pocket radius shrinks to $R(t)$, the temperature evolves as $T_{\chi/\phi} \propto 1/R(t)$ like the behavior of radiation, while the particle number density increases as $n_{\chi/\phi} \propto (1/R(t))^3$. The enhanced energy density therefore causes the Schwarzschild radius of the whole pocket mass to grow while the physical pocket radius decreases. When $R(t)$ coincides with the Schwarzschild radius of the pocket, the dense region will collapse into a PBH (the detailed calculation of the PBH mass function is in Sec.5.3.3). The final pocket size at the time of collapse is found following the Schwarzschild criteria studied in [46, 47] for our two component dark sector,

$$R(t_c) = \sqrt{\frac{\frac{7}{8}g_\chi + g_\phi}{g_\star}} \left(\frac{R_\star}{H_\star^{-1}}\right) R_\star. \tag{5.11}$$

The pocket radius $R_\star$ at $T = T_\star$ is determined by the detailed phase transition model and could be verified with hydro-dynamical simulations of the nucleation of true vacuum bubbles. Since the initial condition of our calculation is set when most of regions are already in the true vacuum, the pocket shape is mostly spherical as a result of the surface tension of bubble walls.

Fig. 5.3 shows the pocket radius distribution for a fast FOPT corresponds to $\beta = 100H_\star$ (solid), and a slow one, corresponds to $\beta = H_\star$ (dashed) when $v_w = 0.5$. For fast FOPTs, the pocket population, which later determines the PBH mass distribution, shifts to the smaller radii region as a result of the higher bubble nucleation rates that can split a large pocket into several smaller pockets.

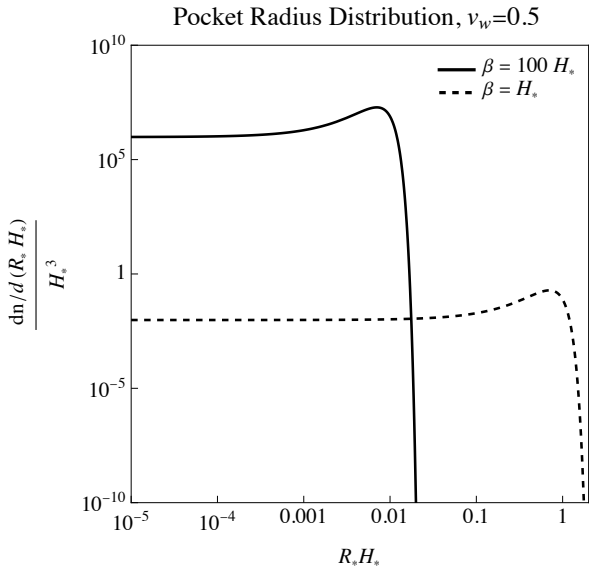


Figure 5.3: Pocket radius distribution for a fast FOPT, $\beta = 100 H_\star$ (solid) and a slow one, $\beta = H_\star$ (dashed) when $v_w = 0.5$.

The evolution of pockets of different sizes follows the same rule determined by the interaction of particles with the bubble wall. Since both the χ and ϕ particles gain a huge mass $m_{\chi/\phi} \gg T_\star$, the particles will not penetrate the bubble wall, but instead be reflected back from the bubble wall due to energy-momentum conservation. All pockets will be heated up following $T_{\chi/\phi} \propto 1/R(t)$ at the beginning, and if this process continues, all pockets are expected to collapse into PBHs spanning a extended mass range.

If PBHs are able to form for all $R_\star$ values, then the total energy budget of the dark sector collapses into PBHs and therefore the initial energy density of PBHs would be of the order of a few percent of the energy density of the radiation (the ratio of the degrees of freedom in the dark sector to the degrees of freedom of the SM). Therefore, the total PBH energy density will dominate the energy density of the universe soon after their formation, resulting in an early matter-dominated era. Such an era will continue until Hawking evaporation restores the cosmic evolution back to a radiation dominated era. However, energy loss from shrinking pockets to true vacuum regions

can halt the evolution of pockets from becoming dense enough for PBH formation. Note that in Eq. (5.11), a smaller pocket has to shrink by a larger fraction of its initial radius to reach the Schwarzschild radius of the total enclosed energy. Since the final dark sector temperature is proportional to the factor $R_\star/R(t_c) \propto R_\star^{-1}$ according to Eq. (5.11), smaller pockets are heated to a higher temperature before their collapse. This means the energy loss will be more effective for pockets with smaller values of $R_\star$. Such leakages can be achieved with the annihilation into particles that penetrate freely through the bubble wall. It was found in [47] that annihilation $\chi\bar{\chi} \to \phi, \phi\phi$ naturally stops PBH formation from pockets with $R_\star \lesssim 1.5 \times H_\star^{-1}$ for their benchmarks, assuming that ϕ is not trapped inside the false vacuum. Since both dark sector particles are DM candidates in our study and are trapped in the false vacuum, annihilation within the dark sector will not change PBH formation and the threshold of [47] is not applicable.

An alternative leakage channel is the annihilation through the operator in Eq. (5.9). To illustrate the idea, we assume that the annihilation process is $\chi + \bar{\chi} \to \text{SM} + \text{SM}$. The idea should apply to other portal models as well. The annihilate rate can be written as

$$\Gamma_{\text{ann}} = n_\chi \frac{\alpha_\Lambda^2}{\Lambda^2}, \tag{5.12}$$

where the number density of χ could be tracked using

$$\begin{aligned} n_\chi &= \frac{3}{4}\frac{\zeta(3)}{\pi^2} g_\chi T_\chi^3 \\ &= \frac{3}{4}\frac{\zeta(3)}{\pi^2} g_\chi \left(\frac{R_\star}{R(t)}\right)^3 T_\star^3. \end{aligned} \tag{5.13}$$

We can write down the expected number of annihilation events throughout the successful collapse, which takes time $t_c \simeq R_\star/v_w$. Then the PBH formation condition is set

by the range of $R_\star$ value where the expected number of annihilation events is smaller than 1,

$$\Gamma_{\rm ann} \times t_c \lesssim 1. \tag{5.14}$$

This condition translates to a lower bound on $R_\star$ below which no PBH would form because of the active annihilation,

$$R_\star > 0.23\, H_\star^{-1} \left(\frac{\alpha_\Lambda}{0.1}\right) \left(\frac{0.5}{v_w}\right)^{1/2} \left(\frac{g_\star + g_\phi + \frac{7}{8} g_\chi}{106.75 + 4.5}\right)^{1/2} \left(\frac{T_\star}{\Lambda}\right) \left(\frac{M_{\rm Pl}}{T_\star}\right)^{1/2}. \tag{5.15}$$

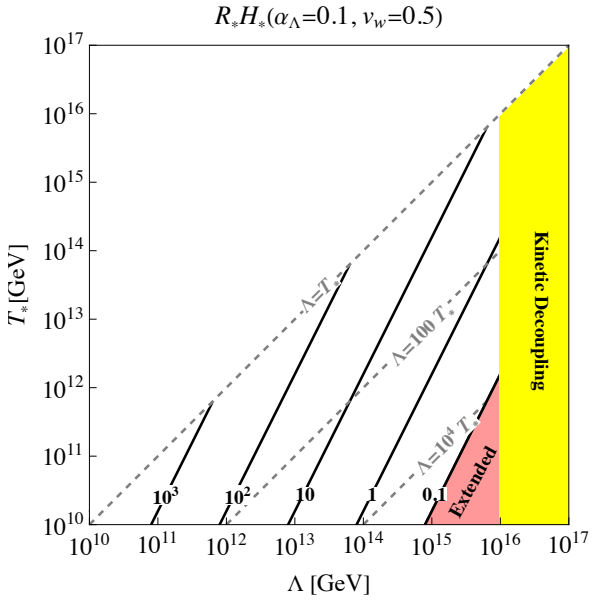


Figure 5.4: Lower bounds on $R_\star H_\star$ for $\alpha_\Lambda = 0.1$ and $v_w = 0.5$. For $\Lambda > 10^{16}\,$GeV (yellow region) the dark sector drops out of kinetic equilibrium with the visible sector prior to the phase transition. Black solid lines show different values of $R_\star H_\star$. Within the red region, $R_\star H_\star$ becomes so small that the PBHs follow an extended mass function rather than a monochromatic one. The gray dashed contours are marked by different choices of Λ.

The minimal $R_\star$ normalized to the Horizon radius is shown on the $(\Lambda - T_\star)$ plane in Fig. 5.4, for $\alpha_\Lambda = 0.1$ and $v_w = 0.5$. The gray dashed contours depicts different

values of Λ. The black solid lines are contours of minimal $R_\star$. For $R_\star \lesssim 0.1\, H_\star^{-1}$, the red shaded region, the extension of the PBH mass function cannot be ignored. In the yellow shaded region, for $\alpha_\Lambda = 0.1$, the dark sector drops out of kinetic equilibrium with the visible sector. The valid parameter space is below the diagonal $\Lambda = T_\star$ dashed line as we assume a cutoff scale above the FOPT temperature.

Eq. (5.15) is valid when the annihilation cross section remains a constant value. This means the dark sector temperature should not be heated to above Λ. We check the condition by combining Eq.(5.11) and (5.15),

$$T_{\chi/\phi}(t_c) \lesssim 0.2\,\Lambda \left(\frac{0.1}{\alpha_\Lambda}\right) \left(\frac{v_w}{0.5}\right)^{1/2} \left(\frac{T_\star}{10^{15}\ \text{GeV}}\right)^{1/2}, \tag{5.16}$$

which confirms that the calculation is valid for the range of $T_\star$ of our interest for PBH formation.

5.3.3 Black Hole Mass Function

In this section, we discuss the mass distribution of PBHs formed during a FOPT following [47, 176, 269]. The conditions for PBH formation in our model will be very similar, with one major difference: since the leakage of ϕ particles into the true vacuum is suppressed in our case, the size range of false vacuum pockets that can potentially collapse to PBHs is determined by the annihilation into SM particles, as shown in Eq. (5.15).

We start with the energy density at time $t_\star$ when the scalar and fermionic dark matter are in thermal equilibrium at some temperature $T_\star$ when the FOPT happens. The equilibrium energy densities of the scalar ϕ and the fermion χ are

$$\rho_\chi^{\text{eq}} = \frac{7\pi^2}{240} g_\chi T_\star^4\,, \quad \rho_\phi^{\text{eq}} = \frac{\pi^2}{30} g_\phi T_\star^4. \tag{5.17}$$

The energy density of the trapped dark sector increases since the particles are being compressed by bubble walls. Assume $R_\star$ is the initial pocket radius at $t_\star$, and $R(t)$ is the pocket radius at a later time t. The energy density is found to follow the scaling [47]

$$\rho_{\chi,\phi}(t) = \rho^{\rm eq}_{\chi,\phi} \left(\frac{R_\star}{R(t)}\right)^4 . \tag{5.18}$$

We define the total energy inside the pocket,

$$M_{\rm pocket} = (\rho^{\rm eq}_\phi + \rho^{\rm eq}_\chi) \left(\frac{R_\star}{R(t)}\right)^4 \frac{4\pi}{3} R(t)^3, \tag{5.19}$$

and the Schwarzschild radius corresponding to the total enclosed mass,

$$r_{\rm c} = 2\, G M_{\rm pocket}. \tag{5.20}$$

Here $G = M_{\rm Pl}^{-2}$ is the gravitational constant.

PBH formation occurs when $R(t)$ shrinks to the Schwarzschild radius $r_{\rm c} = R(t)$. We assume the energy of the whole dark sector inside the pocket is collapsed into the PBH. The PBH mass formed form a pocket of initial radius $R_\star$ is

$$M_{\rm PBH} = \left(\frac{2\pi^3}{90\, G}(g_\phi + \frac{7}{8} g_\chi)\right)^{1/2} R_\star^2\, T_\star^2. \tag{5.21}$$

The distribution of the PBH mass is determined by the distribution of the false vacuum pocket radius in Eq. (1.26) following the mass-radius relation given in Eq. (5.21). The lower bound on the pocket size, i.e., Eq.(5.15), translates into a lower bound on the

mass of PBHs. Therefore the PBH distribution, including this lower bound, can be written as:

$$\frac{dn_{\rm PBH}}{dM_{\rm PBH}} = \frac{I_\star^4\,\beta^4 M_{\rm PBH}^{-1/2}}{384\,T_\star\,v_w^3\left(\frac{2\pi^3}{90\,G}\left(g_\phi+\frac{7}{8}g_\chi\right)\right)^{1/4}}\,e^{4\beta R_\star/v_w - I_\star\,e^{\beta R_\star/v_w}}\left(1-e^{-I_\star e^{\beta R_\star/v_w}}\right) \times\Theta\left(M_{\rm PBH}-7.2\times10^{-3}\sqrt{g_\phi+\frac{7}{8}g_\chi}\,\frac{\alpha_\Lambda^2}{v_w}\,\frac{M_{\rm Pl}^4}{T_\star\Lambda^2}\right), \tag{5.22}$$

where $\Theta(.)$ is the Heaviside step function.

Fig. 5.5 shows the PBH mass function for three different phase transition temperatures: $T_\star = 10^{14}\,\text{GeV}, T_\star = 10^{13}\,\text{GeV}, T_\star = 10^{12}\,\text{GeV}$ as black solid, black dashed, and black dotted curves, and the lower bounds on the PBH mass are shaded in red, green, and orange respectively. The other parameters are set to be $\alpha_\Lambda = 0.1$, $v_w = 0.5$, $\beta = H_\star$, and $\Lambda = 10^{16}\,\text{GeV}$. In the legends, we show the minimal values of $R_\star$ below which PBH formation is halted. As one expects from Eq.(5.22), the PBH mass distribution is more peaked with a larger $R_\star H_\star$ value according to Eq.(5.15), as is shown with the red shaded distribution for $T_\star = 10^{14}$ GeV and $\Lambda = 10^{16}$ GeV.

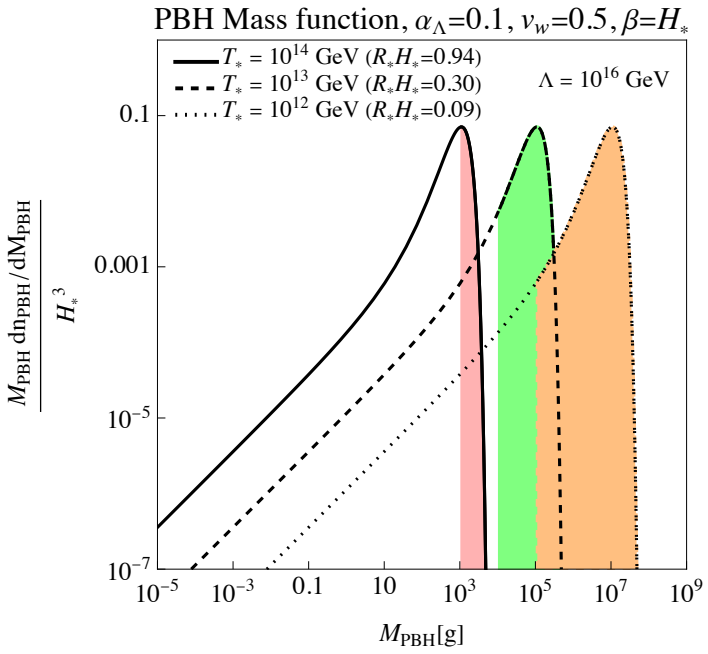


Figure 5.5: The PBH mass function for three different phase transition temperatures: $T_\star = 10^{14}\,\text{GeV}, T_\star = 10^{13}\,\text{GeV}$, and $T_\star = 10^{12}\,\text{GeV}$ as black solid, black dashed, and black dotted curves. The regions above the lower bound of PBH mass in Eq. (5.22) are shaded in red, green, and orange for the three benchmarks. The minimum $R_\star$ value for each benchmark is shown in the legend. The other parameters are set to be $\alpha_\Lambda = 0.1$, $v_w = 0.5$, $\beta = H_\star$, and $\Lambda = 10^{16}\,\text{GeV}$.

5.4 UHDM from Black Hole Evaporation

In the previous Sections, we have discussed the formation of the PBHs and their associated mass function. In this Section, we discuss their evaporation and calculate the relic density of the produced UHDM candidates χ and ϕ. DM, as a particle in the spectrum can also be emitted by Hawking evaporation of PBHs. If PBHs never dominate the energy density of the Universe, then the injected entropy in the Universe at evaporation time is negligible. Assuming the emitted DM particles by PBHs do not annihilate each

other after emission (See subsection 5.4.2 for validity of this assumption), the yield of DM today, at t_0, is related to the yield of DM at evaporation time, $t_{\rm eva}$:

$$Y_{\rm DM} = \frac{n_{\rm DM}(t_0)}{s(t_0)} = \frac{n_{\rm DM}(t_{\rm eva})}{s(t_{\rm eva})} \simeq N_{\rm DM}\frac{n_{\rm PBH}(t_\star)}{s(t_\star)}, \tag{5.23}$$

where $n_{\rm DM}(t)$ and $n_{\rm PBH}(t)$ are the number densities of DM particles and PBHs, respectively. $N_{\rm DM}$ is the total number of DM particles emitted by one PBH given by Eqs. (4.3) and (4.4). $s(t)$ is the entropy density evaluated as:

$$s(T) = \frac{2\pi^2}{45}g_{*,s}(T)T^3, \qquad g_{*,s}(T) = \sum_B g_B\left(\frac{T_B}{T}\right)^3 + \frac{7}{8}\sum_F g_F\left(\frac{T_F}{T}\right)^3. \tag{5.24}$$

The yield of DM is proportional to the number density of PBHs, and consequently is proportional to the fraction of energy density of the Universe which collapsed into PBHs at the formation time, $\beta_{\rm PBH} = d\beta_{\rm PBH}(M_{\rm PBH})/d\ln M_{\rm PBH}$. DM yield in terms of initial abundance of PBHs is given by:

$$Y_{\rm DM} = \beta_{\rm PBH}N_{\rm DM}\frac{1}{M_{\rm PBH}}\frac{\rho_{\rm rad}(t_\star)}{s(t_\star)} \simeq \frac{3}{4}\beta_{\rm PBH}N_{\rm DM}\frac{T_\star(M_{\rm PBH})}{M_{\rm PBH}}, \tag{5.25}$$

where $\rho_{\rm rad}(t_\star)$ and $T_\star(M_{\rm PBH})$ are the energy density and the temperature of the Universe at the PBH formation time respectively, and we assumed $g_\star(T_\star) \simeq g_{\star,s}(T_\star)$. The relationship between PBHs' mass and the temperature of the Universe at the formation time is dictated by PBH formation mechanism.

Finally, the relic abundance of DM is obtained as:

$$\Omega_{\rm DM} = \frac{\rho_{{\rm DM}(t_0)}}{\rho_c} = \frac{m_{\rm DM}Y_{\rm DM}}{\rho_c}s(t_0), \tag{5.26}$$

where $\rho_c(t_0) = 1.0537 \times 10^{-5}\, h^2$ GeV cm^{-3}, $s(t_0) = 2891.2\,(T_0/2.7255\text{K})^3\,\text{cm}^{-3}$, and $h = 0.674$ is scaling factor for Hubble expansion rate [211].

Since $\rho_{\rm PBH}(t)/\rho_{\rm rad}(t) \propto a$, PBHs formed in a radiation-dominated era may lead to an early matter-dominated epoch before their evaporation. The critical initial abundance of PBHs, β_c, that can lead to an early matter-dominated epoch is related to the temperature of the Universe at the formation time, $T_\star$ through:

$$\frac{\rho_{\rm PBH}(T_{\text{early-eq}})}{\rho_{\rm rad}(T_{\text{early-eq}})} = \beta_c \frac{T_\star}{T_{\text{early-eq}}} \sim 1. \tag{5.27}$$

An early matter-dominated epoch caused by PBHs is equivalent to $\beta_{\rm PBH} \gtrsim \beta_c$ where $\beta_c = T_{\rm eva}/T_\star$ and $T_{\rm eva}$ is the temperature of the Universe at PBH evaporation time.

5.4.1 UHDM from PBHs Formed by a Trapped Dark Sector

The mass of the PBHs formed by a trapped dark sector when the temperature of the Universe is $T_\star$, i.e., the temperature of the phase transition, is given by Eq. (5.21) as:

$$M_{\rm PBH} = \left[\frac{2\pi^3}{90}\left(g_\phi + \frac{7}{8}g_\chi\right)\right]^{1/2} R_\star^2\, T_\star^2\, M_{\rm Pl}. \tag{5.28}$$

It is easy to see that since we are interested in $m_\phi = m_\chi > T_\star$, the dark sector particles are always heavier than the initial temperature of the PBHs.

We are now in a position to compute the relic density of DM today. We note that the portal operator in $\mathcal{L}_{\rm SM-DS}$ can induce the decay of ϕ to SM particles in true vacuum regions, while χ remains as a stable DM candidate. Indeed, the portal operator in Eq.(5.9) induces the decay of ϕ into a pair of Higgs bosons through the χ-loop in true vacuum, and the decay width is $\Gamma_{\phi\to hh} \sim y_\chi^2\, \alpha_\Lambda^2\, m_\phi^3/(16\,\pi^2\,\Lambda^2)$. Unlike in the true vacuum, thermal masses prevent ϕ decay in the false vacuum during PBH formation.

In this case, ϕ will decay soon after being emitted by the PBH, and χ will be the only DM component in our benchmark dark sector model. However, for the relic density computation, we will present general results for the case where both χ and ϕ are stable DM candidates, in anticipation of models where the portal operator is chosen such that ϕ is stable. We will also discuss the limit that one should take when ϕ decays early.

The contribution of dark sector particles emitted by PBHs into the DM abundance today is obtained as:

$$\begin{aligned}\Omega_{\rm DM} &= \Omega_\chi + \Omega_\phi \\ &= \frac{45\sqrt{3}\times 5^{1/4}\zeta(3)}{16\times 2^{1/4}\pi^{23/4}}\frac{(3g_\chi+4g_\phi)(7g_\chi+8g_\phi)^{1/4}}{(8g_\star+7g_\chi+8g_\phi)^{3/2}}\beta_{\rm PBH}\frac{R_\star}{H_\star^{-1}}\frac{s(t_0)}{m\rho_c}\frac{M_{\rm Pl}^{7/2}}{M_{\rm PBH}^{3/2}},\end{aligned} \tag{5.29}$$

where $m_\chi = m_\phi = m$. We assumed the PBH mass function is monochromatic and take the $R_\star$ value from the minimal pocket radius in Eq. (5.15). In the case when the scalar particle ϕ decays before BBN, the Eq.(5.29) can be modified by replacing the $3g_\chi + 4g_\phi$ term in the numerator with $3g_\chi$ such that only the relic abundance of stable χ particles contributes to DM. The remaining g_ϕ dependence arises from the existence of ϕ throughout the PBH formation and evaporation, which is irrelevant to its final decay.

In Fig. 5.6, we show the FOPT parameters that allows the correct PBH formation rate $\beta_{\rm PBH}$ for different DM masses m_χ, which later produce the observed DM relic abundance $\Omega_{\rm DM}h^2 = 0.12$ through recycling. The FOPT temperatures are chosen $T_\star = 10^{14}$ GeV (red), 10^{13} GeV (green), and 10^{12} GeV (orange) corresponding to the benchmark values used in Fig.5.5 with the same filling colors. The bubble wall velocity is $v_w = 0.5$, and the $R_\star$ values are determined with $\alpha_\Lambda = 0.1$ and $\Lambda = 10^{16}$ GeV. The PBH mass is determined with $R_\star$ assuming the mass function is monochromatic, and we approximate the $\beta_{\rm PBH}$ with its peak value. The $\beta/H_\star$ is almost a constant

because of the exponential dependence in Eq. (5.22). Slow FOPTs with smaller β values are required for recycled DM to be produced by small PBHs formed during high temperature phase transitions. We also show the region of $m/T_\star$ where the filtered contribution $\Omega_{\rm DM}^{\rm filtered}$, consisting of χ and ϕ particles that penetrated into the true vacuum during the FOPT, is a subdominant fraction of the total DM abundance. The filtered DM abundance soon becomes negligible to the right of the dashed curves since the filtering rate is exponentially suppressed.

Our primary results are shown in Fig. 5.7. The left panel depicts the upper limits on the initial abundance of PBHs, $\beta_{\rm PBH}$, on the $(M_{\rm PBH}, m_\chi)$ parameter space assuming $\Omega_\chi = \Omega_{\rm DM}$, as well as excluded regions. The excluded PBH masses by BBN and CMB are shaded in purple and orange, respectively. Within the dark gray area, the initial temperature of PBHs is larger than the mass of the DM particles. The dashed contours represent the upper limits on $\beta_{\rm PBH}$ when PBHs produce all the DM after evaporation in a radiation-dominated universe. In the light gray area the required initial abundance of PBHs to produce the observed abundance of DM today, is larger than β_c and therefore gives rise to an early matter-dominated era. With the monochromatic assumption, the PBH mass is determined by the minimal pocket radius $R_\star$ and the FOPT temperature $T_\star$. Different colors of dashed contours correspond to different choices of $R_\star H_\star$: red, blue, and black for $R_\star H_\star = 0.1$, $R_\star H_\star = 1$, and $R_\star H_\star = 10$ respectively. Solid lines with the same color show the region of the parameter space within which $50 \lesssim m/T_\star \lesssim 65$ and consequently the filtered component is suppressed. The left side of the red solid lines corresponds to $R_\star H_\star < 0.1$ which leads to an extended mass function for PBHs and is not compatible with the calculations in this study which are based on a monochromatic mass function for PBHs. On the right side of the black solid lines, the mass of the dark sector particles become closer to the Planck scale, and since there

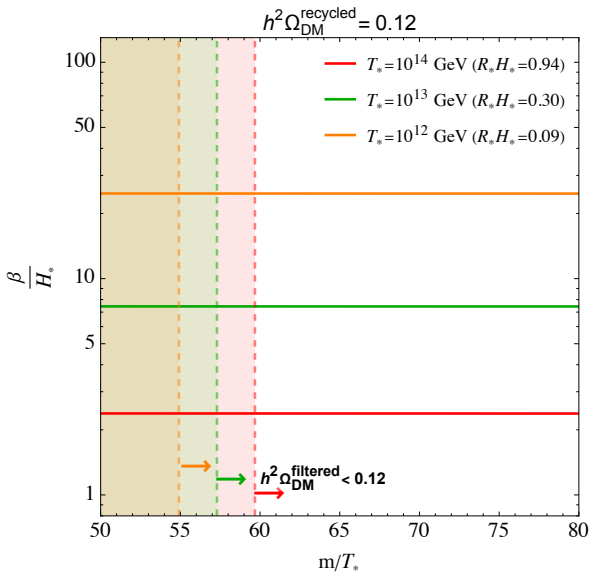


Figure 5.6: Value of the FOPT parameter β that generates the observed DM relic abundance is shown with solid curves. The curve colors correspond to the benchmarks used in Fig.5.5 for different FOPT temperatures. The vertical dashed curves delineate regions where the filtered DM abundance is smaller than the observed abundance. Regions to the left of the dashed curves are excluded.

is another scale between the vev of the dark scalar and the Planck scale, i.e., Λ, the validity of the portal model becomes less reliable. The right panel of Fig. 5.7 shows PBH mass as a function of $T_\star$ for different choices of $R_\star H_\star$.

5.4.2 Annihilation of Dark Matter after Evaporation of PBHs

If the number of DM particles emitted by PBHs are large enough, they may annihilate each other and therefore have a smaller final abundance. To examine this possibility, we need to evaluate the rate of annihilation of DM particles and compare that with the Hubble expansion rate at the evaporation time (and maybe afterwards, when produced particles are ultra relativistic).

The ratio of annihilation rate of DM particles emitted by PBHs to the Hubble expansion rate, immediately after PBH evaporation, at $t = \tau_{\rm PBH} + \epsilon$, can be estimated as:

$$\frac{\Gamma_{\rm ann}(\tau_{\rm PBH}+\epsilon)}{H(\tau_{\rm PBH}+\epsilon)} \simeq \frac{n_\chi(\tau_{\rm PBH}+\epsilon)\langle\sigma v\rangle_{\chi\chi}(\tau_{\rm PBH}+\epsilon)}{H(\tau_{\rm PBH}+\epsilon)}, \tag{5.30}$$

where

$$\begin{aligned} n_\chi(\tau_{\rm PBH}+\epsilon) = N_\chi n_{\rm PBH}(\tau_{\rm PBH}-\epsilon) &= N_\chi n_{\rm PBH}(t_\star)\frac{a^3(t_\star)}{a^3(\tau_{\rm PBH})} \\ &= N_\chi \beta_{\rm PBH}\frac{\rho_{\rm rad}(t_\star)}{M_{\rm PBH}}\frac{a^3(t_\star)}{a^3(\tau_{\rm PBH})} \\ &\simeq N_\chi \beta_{\rm PBH}\frac{\rho_{\rm rad}(t_\star)}{M_{\rm PBH}}\frac{T^3(\tau_{\rm PBH})}{T^3(t_\star)}, \end{aligned} \tag{5.31}$$

$T(\tau_{\rm PBH})$ is the temperature of the Universe at evaporation time, and annihilation cross-section is given by:

$$\langle\sigma v\rangle_{\chi\chi}(\tau_{\rm PBH}+\epsilon) \sim \frac{\alpha_\Lambda^2}{\max[\bar{E}_\chi^2, \Lambda^2]} = \frac{\alpha_\Lambda^2}{\Lambda^2}, \tag{5.32}$$

where $\bar{E}_\chi$ is the average energy of χ particles emitted by PBHs which for $m_\chi > T_{\rm PBH}$ is given by $\bar{E} \simeq 5.4 m_\chi$ [12, 103].

By using the lifetime of PBHs and Friedmann equation, one can find the temperature of the Universe at evaporation time to be equal to:

$$T(\tau_{\rm PBH}) = \frac{\sqrt{3}\, g_\star^{1/4}(T_{\rm PBH})}{64\sqrt{2}\, 5^{1/4}\pi^{5/4}}\frac{M_{\rm Pl}^{5/2}}{M_{\rm PBH}^{3/2}}. \tag{5.33}$$

Therefore, we obtain

$$\begin{aligned}\frac{\Gamma_{\rm ann}(\tau_{\rm PBH}+\epsilon)}{H(\tau_{\rm PBH}+\epsilon)} &\simeq \frac{27\sqrt{2}\zeta(3)}{33554432\times 2^{1/4}\sqrt{5}\pi^{15/2}}\frac{\sqrt{g_\star}}{(7g_\chi+8g_\phi)^{1/4}}\frac{\alpha_\Lambda^2\beta_{\rm PBH}}{R_\star H_\star}\frac{M_{\rm Pl}^9}{M_{\rm PBH}^5 m_\chi^2\Lambda^2} \\ &< \frac{27\sqrt{2}\zeta(3)}{33554432\times 2^{1/4}\sqrt{5}\pi^{15/2}}\frac{\sqrt{g_\star}}{(7g_\chi+8g_\phi)^{1/4}}\frac{\alpha_\Lambda^2\beta_{\rm PBH}}{R_\star H_\star}\frac{M_{\rm Pl}^9}{M_{\rm PBH}^5 m_\chi^4} \\ &< \frac{27\sqrt{2}\zeta(3)}{8192\times 2^{1/4}\sqrt{5}\pi^{7/2}}\frac{\sqrt{g_\star}}{(7g_\chi+8g_\phi)^{1/4}}\frac{\alpha_\Lambda^2\beta_{\rm PBH}}{R_\star H_\star}\frac{M_{\rm Pl}}{M_{\rm PBH}} \ll 1, \quad (5.34)\end{aligned}$$

where in the second step we used $\Lambda > m_\chi$, and in the third step we applied the condition that $T_{\rm PBH} = M_{\rm Pl}^2/(8\pi M_{\rm PBH}) < m_\chi$.

Since $n_\chi \propto a^{-3}$, and $H \propto a^{-2}$, $n_\chi\langle\sigma v\rangle_{\chi\chi}/H$ attains its maximum value immediately after evaporation and then decreases by the expansion of the Universe. It is clear that the rate of annihilation is always less than the Hubble rate and therefore, the yield of DM particles produced by PBHs does not change after production by PBHs. Although the DM candidates produced by PBHs do not establish chemical equilibrium with the SM bath, but they may reach kinetic equilibrium with it again due to elastic scattering processes.

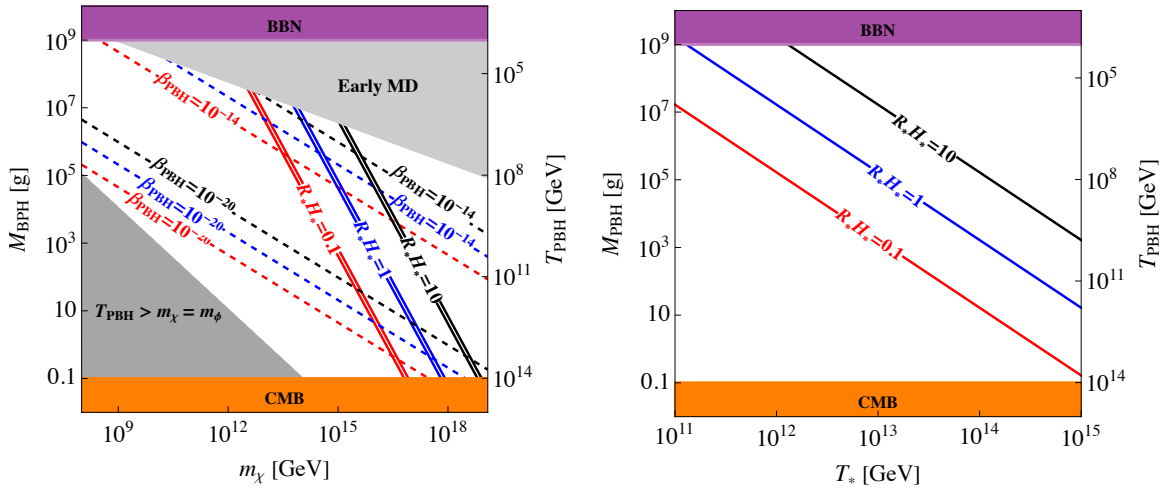


Figure 5.7: Constraints on dark sector particles produced by PBH evaporation. **Left:** Dashed lines show the upper limits on $\beta_{\rm PBH}$ assuming PBHs evaporation explains all of the DM today. The orange and purple regions are excluded by constraints from the CMB and BBN, respectively. The dark gray region correspond to PBHs with an initial temperature larger than the mass of the DM particles. Within the light gray area, $\beta_{\rm PBH}$ is so large that it leads to an early matter-dominated era, and the abundance of DM particles produced by PBH evaporation is independent of $\beta_{\rm PBH}$. Different colors of dashed contours correspond to different choices of $R_\star H_\star$: red, blue, and black for 0.1, 1, and 10 respectively. Solid lines with the same color show the region of the parameter space within which $50 \lesssim m/T_\star \lesssim 65$ and consequently the filtered component is suppressed. The left side of the red solid lines corresponds to $R_\star H_\star < 0.1$ which gives rise to an extended mass function for PBHs and is not compatible with the calculations in this study which are based on a monochromatic mass function for PBHs. On the right side of the black solid lines, the mass of the dark sector particles become closer to the Planck scale, and the validity of the portal model from the point of view of effective field theory becomes less reliable. **Right:** PBH mass as a function of $T_\star$ for different choices of $R_\star H_\star$.

5.5 Discussions and Conclusions

In this work, we studied a new mechanism for producing UHDM: recycling. While we reserve a study of the phenomenology of recycled DM for the future, there are some general novel features that we comment on.

In recycling, multiple DM candidates reside, as massless particles, in a dark sector which is initially in kinetic equilibrium with the SM. The dark sector undergoes a FOPT, and the DM candidates acquire a mass much larger than their temperature and therefore get trapped in the false vacuum. The rate of leakage of dark sector particles into the true vacuum is suppressed enough that eventually (some of or even all of) the pockets of false vacuum collapse into PBHs. If the FOPT occurs at high temperatures, the formed PBHs would be light enough to evaporate before BBN and escape all the cosmological constraints. During Hawking evaporation, PBHs reproduce (recycle) the DM candidates that initially collapsed into them. The DM particles emitted by PBHs are ultra-heavy, due to being materialized in the true vacuum, and are sparse enough to be able to explain the observed abundance of DM today without overclosing it. The suppression of DM annihilation into SM dictated by very heavy mediators leads to a lower bound on the size of the false vacuum pockets that can collapse into PBHs successfully. Therefore, the PBH mass function, in general, is an extended distribution, with a low mass cutoff determined by the IR physics. In the case that most (or all) of the the pockets collapse into PBHs, we expect an early PBH dominated Universe, since almost all the energy content of the dark sector which is of the order of percentage of the radiation energy density ends up in PBHs. It is worth mentioning that the high temperature of FOPT connected to recycling DM by PBHs gives rise to the gravitational wave signatures in the ultra high frequency MHz-GHz range [269, 191].

In this study, we focused on scenarios within which the lower bound on the mass of PBHs is not too small and therefore the resultant PBH mass function can be treated as a monochromatic distribution. Generally speaking, during the FOPT, a portion of the dark sector energy may leak into the true vacuum, while the rest gets trapped in the false vacuum. When the mass of the DM in true vacuum is larger than the phase transition temperature by a factor of ~ 55 or more, then the filtered DM contribution into the final abundance of DM becomes negligible and the recycled component emitted by PBHs afterwards would be the dominant constituent. Recycling, via formation of PBHs and their subsequent Hawking evaporation preceded by a FOPT, provides a plausible way to produce UHDM which has been in thermal equilibrium with the SM in early Universe. Depending on details of the FOPT and the particle physics model, UHDM with a mass heavier than $\sim 10^{12}\,\mathrm{GeV}$ and the right relic abundance today, can be produced by recycling mechanism initiated with FOPTs occurring at temperatures larger than $\sim 10^{11}\,\mathrm{GeV}$. Since recycling mechanism involves a dark sector which interacts with the SM, a FOPT succeeded by emission of high frequency gravitational waves, and formation of PBHs with interesting mass functions, it provides a novel UHDM production mechanism with a rich phenomenology which requires further study in the future.

This chapter concludes the primordial black hole and early universe part of this dissertation. The following three chapters will explore stellar astrophysics and the affect beyond standard model physics has on a star's evolution. The star's studied in these chapters are Cepheid variables.

Note added: As we were finalizing this work, we became aware of [270]. While there is some overlap, our study emphasises UHDM recycling with PBHs formed from the

direct collapse of the trapped dark sector, where its portal coupling to the SM controls the PBH mass distribution, as opposed to Fermi-ball formation.

Chapter 6

Introduction to Stellar Astrophysics

The first five chapters of this dissertation focused on the origin of dark matter, the creation of high-frequency gravitational waves, and the explanation of antimatter-matter asymmetry in the universe. All these questions were answered through a population of PBHs in the early universe. This chapter and the following two chapters take a large turn in terms of subject matter. The focus is on stellar evolution and how energy loss through some BSM particle production can affect a star's evolution and, therefore, can be seen at the stellar population level. This chapter's aim is first to provide an introduction to stellar evolution and second to give an introduction to the BSM species used in the following chapters. Due to the Sun's close proximity, it provides the best observations for understanding stars; therefore, we will be using it as an example throughout this chapter.

6.1 Introduction to Stellar Evolution

Stars have been studied, cataloged, and observed for thousands of years. However, it is not until more recently, with the use of computers, that we can now simulate a star's evolution. This allows for the confirmation of theory and observation. There are still many mysteries that simulations cannot reproduce. For example, the Cepheid mass discrepancy problem, where the observed mass and pulsation models match, but the simulated evolutionary mass does not. In this section, we will provide the necessary

"ingredients" to create an accurate stellar model that can closely match observations. These ingredients include the type of elements that will be mixed, the type of mixture of elements that will exist in the star, the opacity of this material, the type of nuclear reaction network that will be used, and whether the star will be rotating. These are some examples that need to be considered when developing a model. It's instructive to define the stellar evolution equations and explain how a model is affected by BSM physics. The stellar evolution equations are based on well-established physical laws, including mass conservation, energy conservation, the energy transport equation, and the equation of hydrostatic equilibrium. Asumming spherical symmetry these stellar evolution equations are defined as [271]:

$$\frac{dP(r)}{dr} = -\frac{\rho(r)GM(r)}{r^2} \tag{6.1}$$

$$\frac{dM(r)}{dr} = 4\pi r^2 \rho(r) \tag{6.2}$$

$$\frac{dT(r)}{dr} = -\frac{3k_r \rho}{64\pi r^2 \sigma T^3} L(r) \tag{6.3}$$

$$\frac{dL(r)}{dr} = 4\pi r^2 \rho(r) \epsilon(r) \tag{6.4}$$

Each equation is defined at some radius r from the center of the star. P, ρ, T, L, ϵ, and M are the pressure, density, temperature, luminosity, energy production, and mass of the star at a given radius. k_r, G, and σ are the thermal conductivity at a given radius, Newton's gravitational constant, and the Stefan-Boltzmann constant. These equations are coupled, so if one were to introduce a new particle that changes nuclear reaction rates either by slowing them or speeding them up through ϵ, then the other equations would be affected. A good example is a decrease in luminosity that affects local temperatures and densities. This effect can be shown in the central temperature vs central density plot shown in Figure A.3 in appendix D. Such changes

can lead to the removal of an evolutionary stage in a star's life cycle. A key feature that can constrain BSM physics. However, the mass in the evolution equations is not significantly affected by BSM production.

Before proceeding, it is essential to have a reference to the referred stellar evolutionary stages for Cepheid variables in the mass range of 4-12 $M_{\odot}$. The evolutionary tracks of these stars will be plotted on the Hertzsprung-Russell diagram (HR-diagram). We use the HR-digram with axis of Log_{10} of the luminosity of photons from the surface of the star divided by the luminosity of the Sun($L_{\odot}$) with the Surface temperature (T_{eff} plotted on an inverse axis. This diagram will be used extensively in the following two chapters.

We describe below, starting from the post-main-sequence stage, leading up to the entry of Cepheid variables into the instability strip and their subsequent exit. Each model presented in our work starts from the zero-age main sequence. After the star exhausts the hydrogen in its core, it expands to become a red giant, marking the initiation of the RGB stage of its evolution. The expansion of the star, which has a temporarily inert helium core surrounded by a hydrogen-burning shell, moves the star to the right (cooler temperature) in the HR diagram, constituting its first crossing through the instability strip. The instability strip on the HR diagram depicts an observed region where stars are believed to become unstable and begin pulsating. After this, crossing is rapid and typically not effective at constraining properties at the population level. The star crosses the red edge of the strip with its hydrogen shell still burning; thereafter, the helium core ignites, the star contracts and heats up, and proceeds to move to the left (hotter temperatures) on the HR diagram. The star crosses the instability strip for the second time (from the red edge), embarking on the "blue loop" phase. This helium burning phase lasts for a longer time than the first crossing

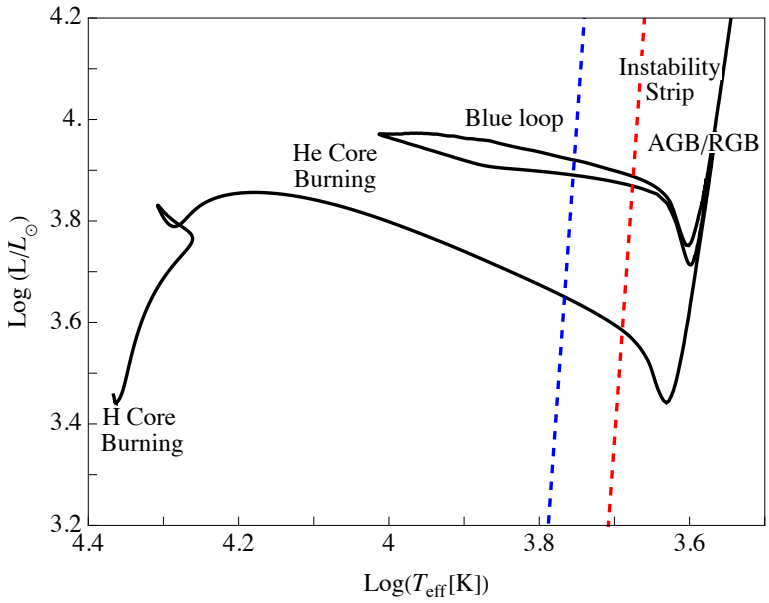


Figure 6.1: The evolutionary track of a non-rotating 8 $M_\odot$ `MESA` model. Included are important evolutionary stages of the star and instability strips defined in `MESA`. The $L_\odot$ is the solar luminosity. The metallicity is set to $Z = 0.014$ and the overshoot to $\alpha_{\rm ov} = 0.0$.

(which is typically 10^3 - 10^4 years), and the star remains in the instability strip for a long time, eventually exhausting the helium and moving right once again, to exit the strip. The star eventually climbs the AGB, with the end product being either a white dwarf or a neutron star, depending on the mass of the model. The main features of this evolutionary journey are shown for convenience in Fig. 6.1. There are many similarities between the main stages of evolution of a Cepheid star and a lower-mass star, such as the Sun. Both have a main sequence stage, red giant branch stage, horizontal branch, and an AGB stage. However, the Sun will most likely go through a Helium flash, where the depleted Hydrogen core becomes degenerate. When a critical temperature is reached, Helium begins to ignite all at once (flash). The following section describes the program we use to model Cephieds.

6.2 MESA & Initial Conditions

Modular experiments for stellar astrophysics (`MESA`) is a one-dimensional stellar evolution code written in FORTRAN 90/95 [272, 273, 274, 275, 276, 277]. It implements modularity to initialize individual FORTRAN libraries, making it very user-friendly. The modularity allows for parallel processing and shorter run times, making it usable by laptops. MESA is also designed with separate modules to easily extend the code in the `run_star_extras`. For example, this work utilizes the `other_neu` module to initialize the energy loss in stars resulting from the production of BSM particles. The `MESA` model outputs data in the form of a history file of the star or profile. The user can extend the profile and history outputs in the `run_sta_extras`, which we utilize in this work. `MESA` executes a star info structure assigned to the pointer `s`. The pointer can be used to either access a physical quantity that evolves with time or a physical value at a specific location within the star. `k` is the integer variable used to determine a specific cell within the model, where k=1 is the surface, and k increases towards the center of the star. The number of cells is set by different criteria set in MESA, such as a limit on the local temperature. As the stellar model evolves, the MESA model will merge or split a cell. The number of cells and the condition for merging or splitting can be modified by the user in the inlist as discussed below. Appendix E shows the use of the star info structure to calculate axion loss. The following are the initial conditions used in our `MESA` models:

6.2.1 Nuclear Reaction Network

Due to their larger mass, which leads to higher temperatures, densities, and pressures, the CNO cycle is more dominant in Cepheid variables than the PP chain. Therefore, a nuclear reaction network that considers the reaction rates of heavier elements and

isotopes is needed. We use the `pp_cno_extras_o18,_ne22.net` for our nuclear reaction network which consideres the following elements and isotopes: ^{1}H ,^{3}He,^{4}He, ^{12}C,^{13}C, ^{13}N, ^{14}N,^{15}N,^{14}O,^{15}O,^{16}O,^{17}O,^{18}O, ^{17}F,^{18}F, ^{19}F,^{18}Ne,^{19}Ne,^{20}Ne, ^{22}Mg, and ^{24}Mg. This nuclear reaction network encompasses the hot CNO cycle, which is essential for the later stages of nuclear burning. `MESA` uses the NACRE (Nuclear Astrophysics Compilation of Reaction Rates, [278]) for determining the reaction rates for elements and isotopes.

6.2.2 Stopping Controls, Mesh, & Solver

The user has options for when to stop the model. The stopping condition when maximum luminosity is attained is set to $\log(L/L_{\odot}) \sim 4.0 - 4.3$, since the asymptotic giant branch stage is not considered in this work. Age, mass, and a minimum element abundance in the core are other stopping conditions; however, since these vary between different mass models, they are not utilized.

The `mesh_delta_coeff` and `time_delta_coeff` control the number of cells created and the number of models produced, respectively. The more cells, the more accurate the model. Increasing the timestep time_delta_coeff yields a more precise calculation from one model to the next. Useful when models are undergoing rapid phases, such as the Helium flash. However, increasing either one leads to a substantially longer run times. In the Chapter 7 we set the mesh_delta_coeff = 2, doubling the base number of cells, but we do not alter `time_delta_coeff` . In chapter 8, we vary both the mesh and timestep due to the use of rotation in our models.

6.2.3 Wind Mass Loss, Opacity, and Equation of State

High mass stars (M $>$ 20M$_\odot$ can lose a considerable amount of mass within their lifetime. For example, Wolf-Rayet stars have roughly $\sim 10^{-5} M_\odot$/yr stemming from their high fusion rate. The radiation pressure is exceptionally high compared to the gravitational force holding on to the material in the atmosphere. This leads to large mass loss rates. Cepheid stars considered in this work are moving from the red giant branch to the horizontal branch, and then to the asymptotic giant branch. Their mass loss rates are significantly lower than those of Wolf-Rayet stars, but they still need to be considered. The mass loss rates typically increase when the star becomes large, as the gravitational force at its atmosphere decreases, leading to more mass loss. The mass loss used in this work considers the Red giant branch mass loss, which is discussed more in chapter 7.

The opacity can significantly affect the star's evolution and physical quantities. A larger opacity would mean an increase in stellar radius. As it is more difficult for radiation to escape, it effectively puffs up the star. We use opacity prescription according to [279]. We use`MESA`'s Type2 opacities for the mass range we consider. `MESA` uses the opacity tables of [280]. Opacity depends on metallicity (Everything heavier than, ^4He), which is set to galactic metallicity for this work (Z = 0.014).

In terms of the equation of state (EOS), `MESA` uses Helmholtz free energy variables. State variables are interpolated from the OPAL tables of [281] for high temperatures, and for lower temperatures, the SCVH tables are used, as described in [282]. These EOS are relevant for hydrogen abundances of 0.0¡X¡1.0 and metals 0¡Z¡0.04, covering all values in this work. If higher temperatures are reached, then `MESA` switches to the HELM EOS of [283].

6.2.4 Convection, Overshoot, & Mixing Length Theory

Stars have three primary methods of mixing: radiation, convection, and conduction. Although the strength of mixing from conduction is typically much smaller than that from radiation and convection. From stellar evolution models, a star can have a mixture of all three in its interior. We know through heliosmology that the Sun has a convection zone below its surface. It's believed that it switches to radiation transfer that exists below this convection zone. Convection can be broken down further based on the value of mean molecular weight (μ) gradients.

The conditions to have convection are defined by the Ledoux criterion [284]:

$$\nabla_{\text{rad}} < \nabla_{\text{ad}} + \frac{\phi}{\delta}\nabla_{\mu} \tag{6.5}$$

Where the above gradients and quantities are defined as follows:

$$\nabla_{\text{rad}} = \left(\frac{\partial \ln T}{\partial \ln P}\right)_{\text{rad}} \nabla_{\text{ad}} = \left(\frac{\partial \ln T}{\partial \ln P}\right)_{\text{ad}} \nabla_{\mu} = \left(\frac{\partial \ln \mu}{\partial \ln P}\right)_{\text{rad}} \tag{6.6}$$

and

$$\delta = \left(\frac{\partial \ln \rho}{\partial \ln T}\right)_{\text{P}} \quad \text{and} \quad \phi = \left(\frac{\partial \ln \rho}{\partial \ln \mu}\right)_{\text{P,T}} \tag{6.7}$$

The Ledoux criterion becomes the Schwarzschild criterion ($\nabla_{\text{rad}} < \nabla_{\text{ad}}$) in chemically uniform areas. Semiconvection takes place between the conditions of the Schwarzschild and Ledoux criteria. The semiconvection coefficient is defined in [285]. We set this coefficient to 0.1 in our inlists. The above equations imply that convection and mixing may be influenced by the changes that BSM particle production has on the star. In chapter 7, we look into the profile of the chemical abundance of hydrogen to see how

it's altered in each axion production scenario. We leave mixing and convection changes by BSM physics for future investigation.

The criterion for convection leads to a rigid boundary where a moving parcel of matter will not cross. It has become more common in the literature to consider convective overshoot. This allows the parcel of matter to go past this convective boundary and either decay afterwards or stop abruptly. Overshoot is believed to explain various astrophysical phenomena, including the main sequence width, the Cepheid mass discrepancy problem, and observations of stars that appear younger than their observed characteristics. The prescription used for overshoot can be an exponential decay or a step function. We follow [286] and use the step function prescription, which is defined as follows:

$$l_{ov} = \alpha_{\rm ov} H_{\rm P} \tag{6.8}$$

Where l_{ov} and $\alpha_{\rm ov}$ are the length of overshoot and a user-defined coefficient. H_P is the pressure scale height and is the height the pressure changes by a factor of e. Overshoot can be implemented at the top or bottom of the envelope, a burning shell, or the core of the star. Additionally, it can be applied to various stages of burning, including the hydrogen burning stage, the helium burning stage, or the fusion of heavier elements for late-stage burning. We assign it above the core of the stellar model during the hydrogen burning stage. This pulls rich hydrogen from the envelope into the core, lengthening the star's lifespan and increasing its luminosity. We set the overshoot coefficient to 0.1 unless otherwise stated.

The mixing length theory is used to define when and how a parcel of matter moves inside the star. It's characterized by a general scheme plus a coefficient α_{conv}. The

'THC' mixing scheme is used in the next chapter based on [287]. The coefficient is defined as:

$$\alpha_{conv} = \frac{l_{ml}}{H_P} \tag{6.9}$$

Here l_{ml} is the mixing length. We set $\alpha_{conv} = 1.6$ for the following two chapters. In the second chapter, we use the 'cox' mixing scheme [288]. Both implementations of mixing length theory in the inlists are shown in the last appendix E.

6.2.5 Rotation

A star gains rotation by the angular momentum attained from the infalling matter during the pre-main-sequence stage. The star's angular momentum is most significant at the start of its lifetime. Still, as the star loses mass due to winds or mass transfer from a companion star, the angular momentum will decrease over its lifespan. A star's rotation velocity can vary greatly without loss of angular momentum. The radius and mass distribution of the star vary as it undergoes its evolution. For example, the rotation rate is slow for the RGB stage and extremely slow for the AGB stage since the radius of the star is many times larger than it was on the main sequence.

Rotation modifies the stellar structure equations with a centrifugal term. High rotation implies a departure from spherical symmetry, but current 1D codes account for this. Rotation can either be modeled as a solid body or differential rotation. An example of differential rotation is the Sun's equator rotating at a faster rate than its poles. Differential rotation also occurs within a star. For the Sun, this is known as the Tachocline, where the rotation profile transitions from solid body to differential rotation. `MESA` uses [289] for a shellular approximation for differential rotation. When

rotation is used in MESA, solid body rotation is implemented first; however, it becomes differential rotation when different instabilities are employed. We incorporate the Eddington-Sweet circulation, dynamical, and secular shear instabilities into our models.

The User can implement rotation in MESA as an initial rotation velocity (v km/s), angular rotation velocity (Ω s^{-1}), or a ratio of angular rotation velocity to critical rotation velocity Ω/Ω_{crit}. Critical rotation will be defined in Chapter 8. For the following chapters, we assume no rotation in Chapter 7, but initialize different values of Ω/Ω_{crit} in Chapter 8. The MESA inlists and `run_star_extras` used for this work are listed in appendices D and E.

6.3 Conclusion

We discussed the components of stellar evolution at the beginning of this chapter. Included were 'ingredients' used by MESA when implementing a model. We discussed how BSM physics could impact various components of the star, including convection, the speed of nuclear reactions, and stellar structure. Finally, we discussed the two BSM species used in the following two chapters, axions and MCPs. Both have unique effects on stellar evolution, which can be used to provide better bounds. The last section of this chapter discusses the motivation behind this work.

Chapter 7

Blue Loops, Cepheids, and Forays into Axions

7.1 Introduction

The idea of probing Beyond Standard Model (BSM) physics with stellar objects has a venerable history [290, 291]. The last ten years, in particular, have witnessed an explosion of activity in this area, as the community has increasingly focused on sub-GeV dark sectors [292, 293]. Searches for such light BSM species have been undertaken in a host of systems: neutron stars, supernovae, white dwarfs, mergers, black holes, and various other astrophysical environments [238]. The BSM species of choice has often been the axion, or more generally, axion-like particles; the current work, too, focuses on axions.[1]

One way to organize such searches is to think of them as relating to the properties of individual stellar objects versus relating to the characteristics or behavior of entire stellar populations. Much of the recent work has been done in the context of constraints on BSM species from *individual* stellar objects, using the following cooling argument: the object cannot emit BSM particles and therefore cool anomalously fast (typically compared to cooling induced by neutrino emission). Constraints based on *population* studies, on the other hand, are argued as follows: the emission of the BSM species and the attendant cooling alters the evolutionary trajectory of stellar objects, which is reflected at the population level. Such arguments can be potent if the BSM physics

[1] We will be interested in axion-like particles in this work, but will call them "axions" throughout.

alters or eliminates a particularly long or significant portion of the evolution of a stellar population.

Stars like our Sun, as well as intermediate mass or even heavier stars, whose evolutionary histories rest on well-established theoretical models, immediately become a fertile ground for such enquiries. Various parts of the Hertzsprung-Russell (HR) diagram, which displays the evolutionary track of stars of various masses and provides a template on which stellar populations can be placed, become sites of investigation. A key target for BSM physics is evolutionary stages which feature a helium burning core, since BSM particles are efficiently produced from such cores and the resulting loss of energy reduces the duration of the corresponding evolutionary phase. This reduction then gets reflected at the population level. Classic bounds on axions using this idea have come from the study of horizontal branch stars: the reduction in the duration of this phase lowers the ratio R between the number of horizontal branch stars and red giant branch (RGB) stars in globular clusters [294]. Recently, this has been extended to population ratios between horizontal branch stars and stars on the asymptotic giant branch (AGB) [295].

A second target is constituted by the blue loop phase of intermediate mass stars. The blue loop stage on the HR diagram is the leftward movement of the evolutionary track, towards the hotter end of the HR diagram, followed by a subsequent rightward movement towards the AGB stage (cooler end). It is very sensitive to the physical properties of the star and to the various initial conditions inherited from previous phases, making it a long-standing laboratory to explore such effects (the classic text by [296] describes it as "a sort of magnifying glass, revealing relentlessly the faults of calculations of earlier phases"). Energy loss due to the emission of BSM particles can inhibit the development of the blue loop, leading to constraints on such species. The blue loop stage acquires significance due to the existence of variable stars which

fall within the instability strip. Cepheids, in particular, provide important potential sites where BSM physics may be explored, through their mass-luminosity (ML) and period-luminosity (PL) relations.

The purpose of this paper is to perform a careful study of the effect of axion emission on the blue loop stage of intermediate mass stars, using a critical physical quantity as a diagnostic measure: the core potential [297, 298, 299]. The core potential is defined in the following way

$$\phi_c \;=\; h\frac{M_c}{R_c}\;. \tag{7.1}$$

Here, M_c and R_c are the core mass and core radius, respectively, in solar units. The quantity h is a function of the change in hydrogen abundance ΔX and the corresponding change in the mass profile Δm when going from the core to the envelope across the hydrogen-burning shell: $h = h(\Delta X, \Delta m)$. The criterion for a blue loop, first introduced in [297], is as follows

$$\phi_c \;<\; \phi_{\rm crit} \quad\Rightarrow\quad \text{blue loop}, \tag{7.2}$$

where $\phi_{\rm crit}$ is determined from simulations [296]. It should be noted that the physical mechanisms behind the occurrence of a blue loop remain very much a topic of study in the astrophysics community. Nevertheless, through its dependence on the core radius and the width of the hydrogen shell, the core potential, via the criterion in Eq. 7.2, provides a relatively clean metric with which to diagnose emission due to BSM particles for benchmark values of rotation, composition, nuclear reaction rates, and convective mixing. It should be clarified right at the outset that the core potential, and in particular its critical value, are only determined for a given model once the aforementioned

physical properties are set to their benchmark values. The core potential, while providing a clean diagnostic for the onset of a loop, does not have predictive power for when or if a loop will develop.

There are two important aspects to criterion 7.2 that can be highlighted. Firstly, it is the more massive stars that obey Eq. 7.2 more robustly against changes in composition, convection, and rotation, and therefore it is these stars that have more robust blue loops. Secondly, we find that these same massive stars are much more likely to violate Eq. 7.2 and lose their blue loops once BSM couplings are switched on. The more massive stars with their hotter cores emit BSM species more efficiently (since such emission typically goes as the core temperature to some large power) and this emission inhibits the growth of the core, increases ϕ_c, and ensures that Eq. 7.2 is violated even for comparatively small BSM couplings.

We are able to perform controlled simulations of the core potential of up to $9M_\odot$ models using `Modules for Experiments in Stellar Astrophysics (MESA)` [272, 274, 275, 276, 277, 300].[2] The axion coupling that just satisfies Eq. 7.2 is obtained as a function of the Cepheid mass for simulated models up to $9M_\odot$, and a fit provides projections for higher masses. This fit is provided in Fig. 7.10 and can be used to obtain tentative constraints on the role of axions in curtailing blue loops in more massive stars, although such conclusions are not backed up by simulations and would be subject to greater uncertainties from convection models.

The main focus of our analysis are classical Cepheids in the Milky Way, with dynamically-determined masses. The determination of masses by dynamical orbital methods that are unaffected by axion physics fixes the trajectory of these candidates on the HR diagram, for benchmark values of stellar input parameters. The presence of axions, however, does affect the evolution of the star as it approaches the blue

[2]More massive Cepheids can be simulated under the assumption of zero overshoot, as we will clarify later in the paper.

loop stage, potentially halting the increase in temperature at $\phi_c \sim \phi_{\rm crit}$, prior to the star entering the instability strip. The existence of the Cepheid variable can then be used to place a constraint on the axion coupling, which cannot be so large that the condition in Eq. 7.2 is never satisfied. The most massive galactic Cepheid with a dynamically-determined mass, S Mus (with mass $6M_\odot$) [301] furnishes the most conservative constraint and is our benchmark result (the resulting constraint on the axion-photon coupling is an order of magnitude weaker than current limits from [295]). The potential future observation and mass determination of a galactic Cepheid of mass $9M_\odot$ is at the limit of models that can currently be simulated with `MESA`, and would therefore furnish the strongest projected constraint on axions if such an observation with dynamically determined mass were to be made.

Stronger constraints on axions from heavier Cepheids may very well be possible in the future. Masses of individual Cepheids determined by pulsation modeling using candidates in the Gaia DR2 galactic Cepheid database indicate a mass peak of around $\sim 5M_\odot$, with data points as large as $\sim 12M_\odot$ [302, 303]. Well-established ultra long-period Cepheids, such as OGLE-GD-CEP-1884, a galactic Cepheid with mass $7.47M_\odot$ [304] determined by pulsation models, could also serve as benchmarks. A larger sample of Cepheid observations will also become available with the Gaia DR3 catalog [305]. Stellar modeling indicates the possible existence of Cepheids of up to $20M_\odot$, and, presumably, such a heavy Cepheid would yield the strongest constraint on the axion coupling. There are two primary reasons we do not venture to put axion limits from heavier Cepheids. Firstly, we are currently unable to simulate blue loops in models with masses larger than $9M_\odot$, even in the absence of axions, for non-zero values of the overshoot (parametrized by $\alpha_{\rm ov}$ for alterations of the stellar interior structure by mixing chemical components beyond the convective boundary). Secondly, axions are expected to affect the pulsation models themselves. Nevertheless, we provide projections for

a $12M_\odot$ model, which, as expected, are very strong; we make no quantitative claims as to the robustness of those constraints. The variation of axion constraints as a function of stellar mass is discussed in Section 7.4.4, and the challenges of obtaining axion constraints for massive Cepheids is discussed in Section 7.5, which also contains our main results. *Our main message is that the detection and simulation of massive Cepheids is an important frontier in axion searches.*

One of the biggest challenges confronting axion searches with stellar physics are the benchmark assumptions about the physical properties and composition of the star, and their possible impact in limiting sensitivity to BSM physics. For the case of Cepheids in the blue loop stage within the instability strip, these questions become especially important. There is a vast literature on the effect of nuclear reaction rates, rotation, metallicity, and convection on the morphology of blue loops, and the addition of BSM physics would appear to add yet another uncertain aspect to a thicket of models. Among these astrophysical factors, we focus on the uncertainties caused by convection models, which are generally expected to be the most dominant, while keeping the metallicity at typical galactic benchmarks and excluding rotation altogether in this study. We undertake a careful study of the effect of overshoot on the core potential and probe how constraints on axions change with changing overshoot, as Eq. 7.2 is violated. Limits on the axion coupling are displayed for various assumptions of the overshoot for the case of S Mus, and a $8M_\odot$ model in Section 7.5.3.

In this context, we note the Cepheid mass discrepancy problem [306]: while Cepheid masses determined from pulsation models and binary orbital dynamics are largely in concordance with each other, they are both different from masses expected from stellar evolution. The mass discrepancy problem has been addressed by various methods, such as introducing overshoot, rotation, or pulsation-driven mass loss (we refer to [307] for a review). Axions, we find, are unlikely to either alleviate or worsen this problem, since

the effect of axions appears to be most relevant to the radius of the core and hence the core potential and the triggering of the blue loop. In other words, for a given stellar mass, axion emission does not move a blue loop vertically up or down, appreciably, in the HR diagram, but rather either allows or curtails the blue loop altogether.

Along the way, we explore various other aspects of the effect of BSM physics on the blue loop. Importantly, we note the physical origins of the blue loop come from the "mirror principle" [296]: the fact that in the presence of a hydrogen burning shell, the two sides of the shell – the envelope and the core – develop oppositely, in the sense that when one contracts the other expands, and vice versa. During the blue loop, the core expands and the envelope contracts, drawing the star away from the red giant phase with a large convective envelope towards becoming a compact blue giant. We explore the effect of BSM emission on the mirror principle in Fig. 7.3. In Fig. 7.4 we explore the change in the hydrogen profile as the axion coupling is increased. The change in the core potential of a benchmark $6M_{\odot}$ as the axion coupling is increased is depicted in Fig. 7.5; the change as the stellar mass is also increased is depicted in Fig. 7.7.

Before proceeding, we pause to comment on previous work on BSM physics and blue loops. Our results are largely complementary to those obtained by [60, 308][3] – in contrast to those studies, which focused on the relative reduction in the duration of the helium burning phase due to BSM emission, we focus on the core potential as a sharp diagnostic metric. The effects of overshoot were not considered by [308], who stressed the importance of incorporating the effect in future precision studies. Further points of distinction and contrast are detailed in the main text.

[3]We note that [308] had an error in their axion coupling computation, as already pointed out by [60].

7.2 Classical Cepheid Variables and Simulation Benchmarks

In this Section, we describe general properties of Cepheids and the various physical characteristics that affect their observational properties.

Classical galactic Cepheids are young, intermediate mass, metal-rich, radially pulsating variable stars with typical ages ranging between $10 - 300$ Myr and masses between $4-12\ M_{\odot}$. On the HR diagram, they occupy a narrow, nearly vertical band in the so-called instability strip. These luminous giant variables pulsate in the fundamental mode, the first overtone, second overtone harmonics, and multi-periodic modes.

The blue loop stage is the primary focus of our investigations. As mentioned in the Introduction, there is a vast literature on the physical attributes of the star and the various stellar processes that affect the progression of this stage. Nuclear reaction rates, rotation, metallicity, and convection have profound effects on the properties of blue loops, and hence the observational data pertaining to Cepheids. We use the 1-dimensional code `MESA` version `r23.05.1`. We follow [279] for composition and opacity settings in `MESA`. For wind mass loss, we use the "Dutch" wind scheme which follows [309, 310, 311] with a scaling factor of 0.8. For mixing length theory, we follow [287] with $\alpha_{\rm MLT} = 1.6$ for our evolutionary models [312, 313]. We use the Ledoux criterion with semi-convection parameter $\alpha_{\rm semiconv} = 0.1$ and the pp_cno_extras_o18_ne22.net for our nuclear reaction network [4]. We terminate our models during a late stage of the AGB. Our models closely follow [32–35], with the metallicity set to Z = 0.014 and a step overshoot over the hydrogen core is set to $\alpha_{ov} = 0.1$ for the primary benchmarks.

[4] We note that according to `MESA`'s 2013 instrument paper, the semi-convection is treated as a time-dependent diffusive process following [314].

We set the rotation to zero in the current work, reserving the case of non-zero rotation for the future.

We make a few brief comments about the pipeline used in previous studies. The work of [308] was the first (to our knowledge) to apply `MESA` to obtain constraints on axions from Cepheids. They used `MESA` version 3794 to generate their models, assuming solar metallicity $Z = 0.02$ and zero overshoot $\alpha_{\rm ov} = 0.0$. Their study chose $\alpha_{\rm MLT} = 1.6$ and used [279] for the opacity tables and elemental mixture. On the other hand, [60] used the `GENEVA` code, with $Z = 0.014$, $\alpha_{\rm ov} = 0.1$, and $\alpha_{\rm MLT} = 1.6$. They used the elemental abundances of [315] and isotope mixture of [316]. Moreover, [60] noted an issue with the calculation of [308]: the constant in front of Eq. (3) of [308] is off by a factor of 10 ($c = 27.2$ ergs/g/s in [308] instead of the correct value derived in Appendix A of [60], which is $c = 283.16$ ergs/g/s).

Before proceeding, we make a few comments about the position and width of the instability strip, since it will play a vital role in what follows. The exact location of the instability strip depends on several factors, such as rotation and metallicity. For detailed modeling of these aspects, we refer to [317, 318]. In this paper, we define the instability strip according to Eq. (3) from [319]. The width of the instability strip, given as $\Delta \log T_{\rm eff} = 0.08$ dex, is based on the distribution of Cepheid data from the Milky Way, Large Magellanic Cloud (LMC), and Small Magellanic Cloud (SMC) as described in [319].[5] We express their Eq. (3) in terms of $\log L = a \log T_{\rm eff} + b$, where $a = -20.83$ dex and $b = 81.2708$ dex. The red edge of the instability strip, as shown in our work, is determined by subtracting $\Delta \log T_{\rm eff} = 0.04$ dex from Eq. (3) of [319], while the blue edge is calculated by adding $\Delta \log T_{\rm eff} = 0.04$ dex to Eq. (3). It is important to note that axions may influence the location of the instability strip,

[5] We note that log in our work will have base 10, while the natural logarithm is denoted by ln.

potentially leading to observable consequences—an investigation we leave for future work [6].

7.3 Axion Model and Primakoff Effect

In this Section, we give details of our axion model, and how it is implemented in `MESA`. We use natural unit for the calculation of axion production in this section.

7.3.1 Axion Production in Stars

We introduce the axion with the Lagrangian

$$\mathcal{L}_{a\gamma\gamma} \supset \frac{1}{2}\partial_\mu a\, \partial^\mu a - \frac{1}{2}m_a^2 a^2 + \frac{g_{a\gamma\gamma}}{4} a F_{\mu\nu}\tilde{F}^{\mu\nu} \tag{7.3}$$

In this study, we consider a generalized scenario where an axion-like particle is described with its mass m_a and its coupling $g_{a\gamma\gamma}$ with the two being independent parameters. We focus on the axion-photon coupling to investigate its impact on stellar evolution through axion production, which contributes to stellar energy loss. A more detailed summary of the axion parameter space and the current constraints on $g_{a\gamma\gamma}$ can be found in [62].

The electromagnetic coupling of the axion induces its production channel via the Primakoff process $\gamma + \mathcal{Z}e \to a + \mathcal{Z}e$, where $\mathcal{Z}e$ represents target particles with charge $\mathcal{Z}$ in units of the electric charge e. These include ions (or nuclei) and electrons in the stellar medium. Photons from the hot stellar core are converted into axions in the presence of background electromagnetic fields provided by charged particles. However,

[6] We note that there are three distinct temperatures that will be used in this work: (i) $T_{\rm eff}$, the effective temperature of the surface of the star; (ii) T, which denotes the temperature of the local cell under consideration during the relevant `MESA` simulation; and (iii) T_c, which denotes the central temperature of the star.

the conversion rate is also influenced by the screening effect of the charge distribution in the dense plasma. As discussed in Sec. 7.2, energy loss in the helium core and hydrogen burning shell due to axion production could play a significant role in the evolution of Cepheids after helium ignition. This necessitates an accurate modeling of the axion Primakoff process around the burning shell. In particular, the high core temperature and density inside the shell during the post-main-sequence phase lead to an increased plasma frequency and enhanced charge screening effect, both of which are critical for determining whether the stellar evolution curve crosses the instability strip and undergoes a complete blue loop. Therefore, the calculation of photon-axion conversion requires refined treatment by accounting for the influence of plasma frequency and electron degeneracy in the stellar medium. We follow the method developed in [320] and refer readers to it for more details on the structure factor and screening scales. This method was recently employed in [295] to constrain the axion effect by analyzing the reduction in the R parameter [321] and the R_2 parameter [322] from globular cluster observations. In this approach, contributions from electrons and ions are treated independently, with each serving as a static, uniform charge density background for the other. We assume the axion mass is smaller than the temperature, making its production rate proportional only to the coupling. We also assume the axions can escape the star after being produced since the interaction strength is feeble, thus all axions contribute to additional stellar energy loss ϵ_a. In terms of Cepheids, the main axion production is from the non-degenerate medium $\epsilon_{\rm nd}$ and degenerate medium $\epsilon_{\rm d}$. The non-degenerate medium contribution dominates in the outer stellar cells while the degenerate medium contribution becomes comparable in the inner core. We can model the total axion emission rate per unit mass as,

$$\epsilon_a = (1 - w)\,\epsilon_{\rm nd} + w\,\epsilon_{\rm d}, \tag{7.4}$$

where w is a variable for the transition between the non-degenerate and the degenerate regimes. We choose w to have the same functional form as in [320],

$$w = \frac{1}{\pi}\arctan(\zeta - 3) + \frac{1}{2}. \tag{7.5}$$

Here ζ is determined by the electron number density n_e and temperature T in each specific cell of `MESA` simulation (note that the local stellar cell temperature T used in this section is different from the effective stellar temperature $T_{\rm eff}$ on the HR diagram),

$$\zeta = \frac{(3\,\pi^2\,n_e)^{\frac{2}{3}}}{2\,m_e\,T}. \tag{7.6}$$

In the high density core with non-relativistic electron gas, the value of ζ approaches the Fermi energy $E_{\rm F}$ normalized by the temperature. The transition from the non-degenerate regime to the degenerate regime occurs when ζ increases to exceed $\mathcal{O}(1)$, indicating a considerable Fermi energy for degenerate electrons. We will address the axion production rate in different stellar components due to their corresponding screening scales in the following.

In the non-degenerate medium, all charged particles behave as sources of static Coulomb field, whose screening effect reduce the axion production rate. The axion production rate from non-degenerate medium is then

$$\epsilon_{\rm nd} = \frac{g_{a\gamma\gamma}^2\,T^7}{16\pi^2\,\rho}\,y_1^2\,F(y_0, y_1). \tag{7.7}$$

The density ρ accounts for all stellar components. The function $F(y_0, y_1)$ takes the form

$$F(y_0, y_1) = \frac{1}{4\pi}\int_{y_0}^{\infty} {\rm d}y\,\frac{y^2\sqrt{y^2 - y_0^2}}{e^y - 1}\,I(y, y_0, y_1), \tag{7.8}$$

where the dummy variable $y = \omega_\gamma / T$ accounts for the initial state photon energy, and

$$I(y, y_0, y_1) = \int_{-1}^{+1} \mathrm{d}x \, \frac{1 - x^2}{(r - x)(r + s - x)}. \tag{7.9}$$

The variables r and s are chosen as

$$r = \frac{2y^2 - y_0^2}{2y\sqrt{y^2 - y_0^2}}, \tag{7.10}$$

$$s = \frac{y_1^2}{2y\sqrt{y^2 - y_0^2}}. \tag{7.11}$$

The y_0 parameter represents the dependence on the plasma frequency

$$y_0 = \frac{\omega_{\mathrm{pl}}}{T}. \tag{7.12}$$

The medium plasma frequency is

$$\omega_{\mathrm{pl}} = \sqrt{\frac{4\pi\alpha n_e}{E_{\mathrm{F}}}}, \tag{7.13}$$

and its numerical value can be approximated as [290]

$$\omega_{\mathrm{pl}} \simeq 28.7 \text{ eV} \, \frac{(Y_e \frac{\rho}{\mathrm{g\,cm^{-3}}})^{\frac{1}{2}}}{[1 + (1.019 \times 10^{-6} \, Y_e \frac{\rho}{\mathrm{g\,cm^{-3}}})^{\frac{2}{3}}]^{\frac{1}{4}}}. \tag{7.14}$$

Here α is the fine structure constant, and Y_e is the number of electrons per nucleon. While the approximation $y_0 \to 0$ is sometimes taken for horizontal branch stars, the effect of y_0 cannot be neglected for giant stars, where the plasma frequency is non-negligible compared to the temperature in the core regions. Therefore, we follow [320] and keep the non-vanishing y_0 in our simulation. When Cepheids enter the blue loop, the helium core expands, and both its core temperature and plasma frequency decrease

over time. In benchmark simulations, we observe that the value of y_0 decreases as the star crosses the instability strip during the blue loop. The y_1 parameter represents the dependence on the inverse Debye-Hückel radius

$$y_1 = \frac{k_{\rm nd}}{T}. \tag{7.15}$$

The Debye-Hückel wavenumber $k_{\rm nd}$ of the non-degenerate medium accounts for all charged particle species i

$$k_{\rm nd} = \sqrt{\frac{4\pi\alpha}{T} \sum_i \mathcal{Z}_i^2 \, n_i}, \tag{7.16}$$

with their number density n_i and electric charge $\mathcal{Z}_i$. The $k_{\rm nd}$ and the momentum transfer in the Primakoff process determines the charge screening effect in the non-degenerate stellar medium.

The degenerate medium produces axions with contributions from both electrons and ions

$$\epsilon_{\rm d} = \epsilon_{\rm ions} + \epsilon_{\rm e}. \tag{7.17}$$

In the limit of high electron degeneracy, the screening of ion charges from electron is negligible. Thus, the axion production from ions is calculated similarly to Eq. 7.7, but with y_1 replaced by y_2 to account for a reduced screening level,

$$\epsilon_{\rm ions} = \frac{g_{a\gamma\gamma}^2 T^7}{16\pi^2\rho} y_2^2 F(y_0, y_2). \tag{7.18}$$

The y_2 parameter contains only contributions from ions,

$$y_2 = \frac{k_{\rm ions}}{T}, \tag{7.19}$$

and the ionic Debye-Hückel wavenumber is

$$k_{\rm ions} = \sqrt{\frac{4\pi\alpha}{T}\sum_j \mathcal{Z}_j^2 n_j} \tag{7.20}$$

the index j runs for all ion species in the stellar medium. The degenerate electrons are correlated at a length scale set by the Thomas-Fermi wavenumber $k_{\rm TF}$, which is responsible for the charge screening in the core,

$$k_{\rm TF} = \sqrt{\frac{4\alpha m_e p_{\rm F}}{\pi}} \tag{7.21}$$

with $p_{\rm F} = (3\pi^2 n_e)^{\frac{1}{3}}$ being the Fermi momentum of degenerate electrons. The degenerate electron correlation is much weaker than other particles, as can be seen with $k_{\rm TF} \ll k_{\rm ions} \lesssim k_{\rm nd}$. The axion production from degenerate electron is less influenced by the charge screening effect, but instead gets suppressed due to Pauli blocking

$$\epsilon_e = \frac{g_{a\gamma\gamma}^2 T^7}{32\rho}\left(\frac{n_e}{3\pi\alpha m_e^3}\right)^{\frac{1}{2}} R_{\rm deg}\, y_3^3\, F(y_0, y_3). \tag{7.22}$$

The reduction factor in the degenerate core is $R_{\rm deg} = 1.5/\max(1.5, \zeta)$ with ζ defined in Eq. 7.6. The parameter y_3 is determined with the Thomas-Fermi scale as

$$y_3 = \frac{k_{\rm TF}}{T}. \tag{7.23}$$

7.3.2 Energy Loss in MESA Simulation

In this section, we discuss the implementation of axion processes in stellar evolution simulations with MESA. The axion effect has been incorporated into the run_star_extras module. To implement the axion energy loss into the simulation, we express the function $F(y_0, y_1)$ in Eq. 7.8 with a slowly varying function $G(y_0, y_1)$ as [320, 295]

$$F(y_0, y_1) = \frac{100}{1 + y_1^2} \frac{1 + y_0^2}{1 + e^{y_0}} G(y_0, y_1) \tag{7.24}$$

We calculate the numerical values of $G(y_0, y_1)$ on a grid and tabulate the results in a data table, as shown in Table 7.3.2.[7] The grid is selected to encompass a broad range of y values for the stellar profiles. In a simulation of a $6M_\odot$ star ($\alpha_{\rm ov} = 0.1$ and $Z = 0.014$) without axion emission, we observe the range: $-3.25 \lesssim \log y_0 \lesssim -0.95$, $-0.50 \lesssim \log y_1 \lesssim 1.07$, $-0.64 \lesssim \log y_2 \lesssim 0.93$, and $0.05 \lesssim \log y_3 \lesssim 2.77$. The corresponding ranges of y variables in a $8M_\odot$ model is $-3.30 \lesssim \log y_0 \lesssim -1.09$, $-1.02 \lesssim \log y_1 \lesssim 1.00$, $-1.98 \lesssim \log y_2 \lesssim 0.86$, and $-0.02 \lesssim \log y_3 \lesssim 2.76$.[8] The numerical table is interpolated in our MESA simulations in order to calculate the axion emission rate ϵ_a in each cell.

[7] We note that our evaluated values of the function $G(y_0, y_1)$ in Table 7.3.2 differ from those in Table II of [320], which use the same expressions. Our results are computed using the program Mathematica 13.0.1.0

[8] Although the minimal value of y_0 falls outside the range presented in Table 7.3.2, we have verified that the stellar evolutionary track simulated with Table 7.3.2 remains consistent with simulations with an extended table, showing a difference of less than 0.07% in the final stellar ages.

$\log y$	-3.0	-2.5	-2.0	-1.5	-1.0
-2.0	0.2240	0.2481	0.2489	0.2513	0.2543
-1.5	0.1796	0.2010	0.2013	0.2033	0.2079
-1.0	0.1375	0.1543	0.1548	0.1564	0.1603
-0.5	0.1026	0.1162	0.1166	0.1178	0.1208
0.0	0.1054	0.1216	0.1220	0.1232	0.1264
0.5	0.2253	0.2707	0.2716	0.2743	0.2815
1.0	0.4466	0.5686	0.5705	0.5763	0.5913
1.5	0.5463	0.7410	0.7436	0.7511	0.7707
2.0	0.5670	0.7740	0.7768	0.7846	0.8052
2.5	0.5674	0.7778	0.7806	0.7884	0.8091
3.0	0.5676	0.7781	0.7810	0.7888	0.8094

Table 7.1: Numerical values of the function $G(y_0, y_1)$ in Eq. 7.24. Each column corresponds to a different $\log y_0$, and each row corresponds to a different $\log y_1$.

$\log y$	-0.5	0.0	0.5	1.0	1.5
-2.0	0.2182	0.0999	0.0227	0.0071	0.0032
-1.5	0.1981	0.0995	0.0227	0.0072	0.0032
-1.0	0.1609	0.0961	0.0229	0.0072	0.0032
-0.5	0.1233	0.0868	0.0245	0.0079	0.0035
0.0	0.1297	0.1000	0.0.039	0.0141	0.0063
0.5	0.2893	0.2317	0.1250	0.0703	0.0348
1.0	0.6085	0.4948	0.3206	0.3614	0.2919
1.5	0.7933	0.6485	0.4467	0.7586	1.5992
2.0	0.8289	0.6781	0.4721	0.8774	3.0475
2.5	0.8329	0.6815	0.4750	0.8923	3.3722
3.0	0.8333	0.6818	0.4753	0.8986	3.4090

Table 7.2: This is the continuation of the above table.

7.4 Axions, Blue Loops, and Cepheid Variables

In this Section, we present our main results on the incorporation of axion emission into the evolution of intermediate mass stars, particularly the blue loop stage. We begin with a general discussion of classical Cepheid variables, emphasizing the various factors that affect the morphology of the blue loop. We then introduce the axion model, and discuss how the blue loop changes when axion emission is incorporated.

7.4.1 The Blue Loop

Since the properties of the blue loop are crucial for understanding the ML and PL relations of Cepheids, we summarize the general features of this evolutionary stage. Our discussion applies to a typical intermediate mass star, although we will show detailed results for a $6M_{\odot}$ benchmark.

During the star's evolution on the main sequence, hydrogen burning releases nuclear binding energy by its conversion to helium. The rate of energy production ϵ_H depends both on the local temperature as well as the hydrogen abundance. The timescale of central hydrogen burning scales inversely with the stellar mass as $\tau_H \sim M^{-2.5}$, for an approximate ML relation $L \sim M^{3.5}$. Moreover, the temperature sensitivity of the CNO cycle implies that in more massive stars helium production is more concentrated toward the center. While the temperature increases in the center, the hydrogen abundance decreases. A useful parameter to study the spatial variation of various physical quantities is the ratio of the enclosed to the total stellar mass $m_{\rm enc}$. With increasing stellar mass, the hydrogen profile peaks at larger values of $m_{\rm enc}$ since the mass of the helium core increases. Convective overshoot and semiconvection render the above simplified description more complex, necessitating numerical simulations; however, the broad features persist.

At the onset of the post-main sequence stage, an approximately isothermal helium core exists, surrounded by a hydrogen envelope with a hydrogen burning shell at its lowest layers. The shell then induces the so-called "mirror principle" of radial motion of material inside stars, wherein the core and envelope evolve oppositely in extent on either side of the burning shell: an expansion of the envelope above the shell source is accompanied by a contraction of the layers below. The envelope expansion rapidly converts the star into a red giant, placing it on the RGB near the Hayashi line. The contraction of the core leads to heating; when the temperature reaches $\sim 10^8$ K, the helium ignites and the core stops contracting.

The subsequent evolution of the star, in particular whether it embarks on a blue loop or not, is primarily determined by the core potential, defined in Eq. 7.1. Numerical simulations for various profiles indicate the following parametric behavior of $h = h(\Delta X, \Delta m)$ [296]

$$h \;=\; e^{\text{const.}\cdot \Delta X\, \Delta m} \;. \tag{7.25}$$

The function h can be influenced by various factors, such as the mixing length in the superadiabatic layer which determines the mixing of the outer convection zone. Under the assumption of full mixing, the hydrogen profile can exhibit a plateau, with a step-function like drop in the hydrogen abundance at the location of the shell. In this scenario, one can expect

$$\Delta m \to 0, \;\; \text{and} \;\; h \to 1 \;. \tag{7.26}$$

The star's initial transit to the RGB involves an expansion of the envelope and contraction of the core, due to the mirror principle mentioned before. Due to the decrease in core radius R_c, the core potential ϕ_c increases during this stage, following Eq. 7.1. As long as the core potential remains above the critical value ϕ_{crit} the star remains

on the RGB and ascends it. The value of $\phi_{\rm crit}$ can be determined by simulations; for example, [296] provides values of $\log(\phi_{\rm crit}) = 0.83, 0.93$, and 0.99 for stellar mass $M = 3M_\odot, 5M_\odot$, and $7M_\odot$, respectively.

We display typical evolutionary tracks for $4 - 10M_\odot$ stars on the left panel of Fig. 8.4. We take $\alpha_{\rm ov} = 0.1$ above the hydrogen core. The models in Fig. 8.4 have no rotation and are terminated midway through the AGB stage. The black tracks on the left panel correspond to the case where the axion-photon coupling

$$g_{10} \equiv \frac{g_{a\gamma\gamma}}{10^{-10}\,\mathrm{GeV}^{-1}} \tag{7.27}$$

is set to zero. It is clear that when the coupling is turned off all models except the 4 $M_\odot$ case reach the instability strip, and more massive stars have more prominent blue loops. As noted above, this is primarily due to the fact that more massive stars have larger values of $\phi_{\rm crit}$. We note that the blue loop is inhibited for the $10M_\odot$ (and heavier) models, due to the limited inward penetration of the convective envelope - a point further discussed in Section 7.5.3 [323].

As g_{10} is switched on and increased from 0 to 2, blue loops in the more massive models disappear first while the models with lower mass, e.g. 4 and 5 $M_\odot$, persist. We discuss this point in more detail in Sec. 7.4.4. The right panel of Fig. 8.4 displays the evolutionary tracks with the axion-photon coupling set to $g_{10} = 2$. Other major periods of stellar evolution, for example the main sequence, RGB, and AGB stages, appear more or less unchanged when the axion-photon coupling is increased. We note that there will in fact be a noticeable effect in the core of the star in the post blue loop evolution, as shown in Appendix E, where we plot the core temperature versus core density with and without axions. However, these differences in the core properties are

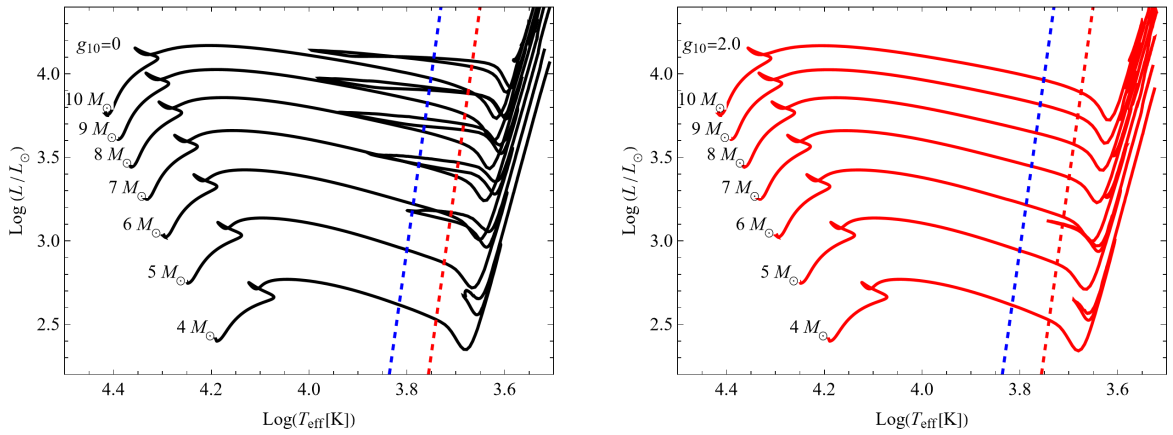


Figure 7.1: Evolutionary tracks for two different axion couplings $g_{10} = 0$ (left panel) and $g_{10} = 2$ (right panel) for a mass range of $4 - 10\ M_\odot$. The metallicity is set to $Z = 0.014$ and the overshoot to $\alpha_{\rm ov} = 0.1$.

not reflected in the overall evolutionary track of the star in the AGB, reinforcing the fact that the blue loop stage is the most sensitive stage of the evolution.

The trajectory of a $6M_\odot$ star is displayed separately in Fig. 7.2. The black curve corresponds to the case where the axion-photon coupling is set to zero. To better display the evolution of the star during the loop, we label the start of the blue loop stage by "A" (where $\log T_{\rm eff} \sim 3.605$), and the bluest point with the maximum effective temperature by "C". "E" denotes the end of the blue loop, while the locations of "B" and "D" are determined by taking the average age of the star between "A" and "C", and "C" and "E", respectively. It should be noted, therefore, that "B" and "D" indicate the midpoints of age, not the effective temperature. It is evident that while the phase from "A" to "B" produces a relatively small increase in the effective temperature, the same amount of time from "B" to "C" produces a remarkable increase in the effective temperature. A similar phenomenon occurs on the reverse passage. The red and green curves correspond to axion-photon couplings set to $g_{10} = 1$ and $g_{10} = 2$, respectively. It is evident that while $g_{10} = 1$ shortens the blue loop noticeably, the loop is entirely eliminated for $g_{10} = 2$.

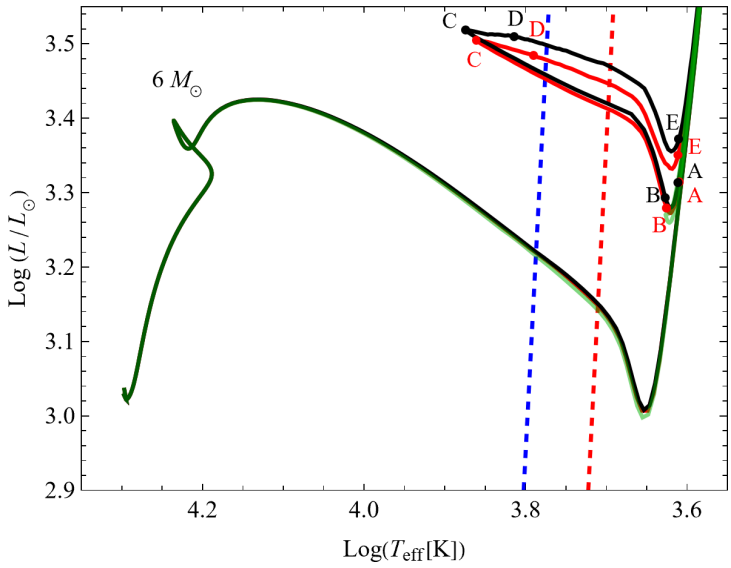


Figure 7.2: Evolutionary tracks of a 6 $M_\odot$ model for $g_{10} = 0$ (black), $g_{10} = 1$ (red), and $g_{10} = 2$ (green). "A" denotes the beginning of the blue loop (where $\mathrm{Log}\, T_{\rm eff} \sim 3.605$), "C" the bluest point with the maximum effective temperature, "E" the end, while the locations of "B" and "D" are determined by taking the average age of the star between "A" and "C", and "C" and "E", respectively. The metallicity is set to $Z = 0.014$ and the overshoot to $\alpha_{\rm ov} = 0.1$.

7.4.2 The Mirror Principle

Given a star with an initial value of the core potential $\phi_{c,\rm init}$, this value can fall below $\phi_{\rm crit}$ due to a reduction in $h = h(\Delta X, \Delta m)$ as the shell burns, or an increase in the core radius, or both. This initiates the leftward movement along the blue loop. During this stage, the core expands, leading to a further drop in the core potential. Due to the mirror principle, the envelope contracts, moving the star further to the left on the HR diagram. At some point, the core potential reaches its minimal value $\phi_{c,\rm min}$. The core subsequently contracts and the envelope expands, leading to an increase in ϕ_c. The star moves to the right in the HR diagram, completing the blue loop. After ϕ_c becomes larger than $\phi_{\rm crit}$, the star exits the blue loop and ascends the AGB.

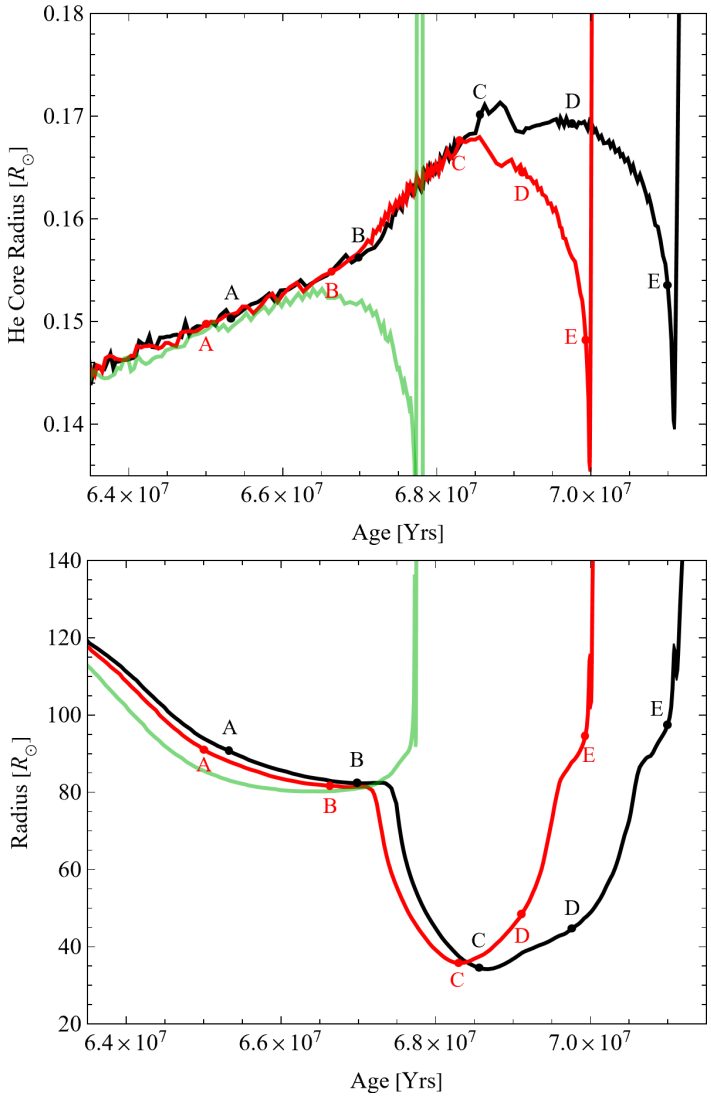


Figure 7.3: Top panel: The helium core radius as a function of the stellar age for a 6 $M_\odot$ model. The axion couplings are $g_{10} = 0$ (black), $g_{10} = 1$ (red), and $g_{10} = 2$ (green). "A" denotes the beginning of the blue loop (where $\log T_{\rm eff} \sim 3.605$), "C" the bluest point with the maximum effective temperature, "E" the end, while the locations of "B" and "D" are determined by taking the average age of the star between "A" and "C", and "C" and "E", respectively. Bottom panel: The stellar radius as a function of the stellar age for the same model. For both panels, the metallicity is set to $Z = 0.014$ and the overshoot to $\alpha_{\rm ov} = 0.1$.

The black curves in Fig. 7.3 show the evolution of the core (top panel) and envelope (bottom panel) during the blue loop phase, in unit of the solar radius $R_\odot$, for a $6M_\odot$ star. The age in all figures signifies time elapsed since the zero age main sequence

stage. From the top panel, it is evident that at the onset of the blue loop ("A" around age $\sim 6.5 \times 10^7$ yrs) the core radius starts increasing. The radius reaches a maximum value of $\sim 0.17 R_\odot$ at the bluest point ("C" at age $\sim 6.9 \times 10^7$ yrs) after which it rapidly shrinks until it reaches a radius of $\sim 0.15 R_\odot$ ("E" at age $\sim 7.2 \times 10^7$ yrs). From the bottom panel, it is evident that the envelope follows the mirror principle at each stage of the progression. It should be noted that the vertical axis of the top panel, depicting the core radius, is substantially magnified (ranging from $0.135 - 0.18 R_\odot$) compared to the vertical axis of the bottom panel, depicting the extent of the envelope (ranging from $20 - 140 R_\odot$).

The red and green curves in Fig. 7.3 correspond to the cases where the axion-photon coupling is set to $g_{10} = 1$ and $g_{10} = 2$, respectively. From the top panel, it is evident that with increasing g_{10} the maximum value of the core radius is reduced compared to the case when axions are absent. Indeed, for the case of $g_{10} = 1$, the value of the core radius at the position "C" is $R_c \sim 0.166 R_\odot$, compared to the value at the position of the black triangle $R_c \sim 0.17 R_\odot$, a reduction of $\sim 2\%$. The value of the core radius is even further reduced in the case of $g_{10} = 2$, with $R_c \sim 0.150$, a reduction of $\sim 11\%$ compared to the black peak. Increasing the axion-photon coupling leads to an increase in energy loss which causes the star to go through helium burning more rapidly and reduces the size of the core compared to the case when $g_{10} = 0$. Since the energy loss $\epsilon_a \propto g_{10}^2$, increasing the coupling from $g_{10} = 1$ to $g_{10} = 2$ correspond to a four-fold increase in energy loss. From the red and green curves in the bottom panel, it is evident that the envelope follows the mirror principle for each axion-photon coupling.

7.4.3 The Hydrogen Profile and the Core Potential

The hydrogen profile as a function of the enclosed mass, $m_{\rm enc}$, is displayed in Fig. 7.4, for three stages of the blue loop: stage "A" (top panel), during the transit through

the instability strip (middle panel), and stage "E" (bottom panel). The black, red, and green curves indicate the cases of $g_{10} = 0$, $g_{10} = 1$, and $g_{10} = 2$, respectively. The black profile shows the expected behavior in the absence of axions. Reading from left to right in the top or middle panels, one has: (*i*) the convective inner core where helium converts to carbon and the radiative outer core (these are flat lines on the hydrogen profile); (*ii*) the sharp first increase in the hydrogen profile, which marks the hydrogen-burning shell; (*iii*) the second more steady increase where the old convective core retreats; and (*iv*) finally, the jump which flat-lines into the envelope composition on the right.

In stage "A", a jump in the hydrogen profile appears due to the first dredge-up, when the convective zone of the envelope penetrates into the region where hydrogen is being burnt in the core. The old composition profile is truncated and matter from the core is redistributed to the envelope. In the middle panel, both the inner core and the burning shell move outwards when plotted against the enclosed mass fraction. In the final panel, the burning shell attenuates the zone where the composition steadily changes, and reaches the jump. The presence of axions during the instability strip preserves the overall morphology of the hydrogen profile, shifting it leftward towards smaller enclosed mass.

It is clear how the function h would behave, based on Fig. 7.4. Following the black curve with $g_{10} = 0$, it is clear that as the blue loop progresses, the value of Δm decreases from $\Delta m \sim 0.1$ (top panel), $\Delta m \sim 0.06$ (middle panel) until the change in the hydrogen profile becomes almost smooth and $\Delta m \sim 0.01$ (bottom panel). Since $\Delta X \sim 0.7$ remains constant in the three stages, it is clear that the function h decreases from its value at the onset of the blue loop, ultimately reaching $h \to 1$ at the end. It is, therefore, a combination of the fact the h decreases and R_c increases in Fig. 7.3 that

leads to a decrease in ϕ_c and a blue loop is initiated. From Fig. 7.4, it is clear that non-zero axion couplings do not produce a substantial difference in the values of Δm and ΔX, and hence in the behavior of h, compared to the case where the couplings are zero. The main difference is that as the axion coupling becomes stronger, the same qualitative jump in the hydrogen profile occurs at smaller $m_{\rm enc}$, reflecting a smaller core size. We note that the core mass M_c increases in both in the absence as well as in the presence of the axion coupling.

Finally, the evolution of the core potential as a function of the age of the star is displayed in Fig. 7.5. The black curve displays the case where the axion coupling is zero. It is evident that at the beginning of the blue loop ("A" at age $\sim 6.5 \times 10^7$ yrs) the core potential is at its maximum value of ~ 0.91, which is larger than $\phi_{\rm crit}$ for a $6M_\odot$ star. Thereafter, the core potential decreases, falls below $\phi_{\rm crit}$, reaches its minimum value and subsequently increases. On the other hand, the reduction in the core potential is less pronounced for the red curve, and almost completely absent for the green curve. This demonstrates that the blue loop is eliminated for $g_{10} = 2$ because the core potential remains too high, which is primarily driven by the fact that the core radius R_c remains too small.

7.4.4 Blue Loop Elimination as a Function of Stellar Mass

More massive stars lose their blue loops first compared to less massive stars, when axions are switched on, even though the massive ones have more robust loops to begin with (Fig. 8.4). Constraints on axions coming from stars of different masses have different levels of robustness and are of different strengths, and we explore these questions in this section.

The emission rates within a stellar cell, plotted as a function of the enclosed mass, are shown in Fig. 7.6 for a $6M_\odot$ model (top panel) and a $8M_\odot$ model (bottom panel). The instantaneous axion emission rate is calculated using Eq. 7.4 and the stellar profile generated from the `MESA` simulation. We assume an axion coupling of $g_{10} = 1.0$, a metallicity of $Z = 0.014$, and an overshoot parameter of $\alpha_{\rm ov} = 0.1$. The color curves represent emission rates at different stages of the star's evolution: before (blue), during (purple), and after (red) the blue loop phase along the evolutionary track. Several features are evident: (*i*) Firstly, the helium burning core overwhelmingly dominates axion production. Energy loss within the core (boundary indicated by the dashed line) dominates due to its high temperature and falls off dramatically by several orders of magnitude beyond $m_{\rm enc} \sim 10\%$ of the star mass, for all stages before, during, and right after the blue loop. For larger values of the axion coupling, axion emission leads to excessive energy loss in the core, accelerates helium burning, and eventually eliminates the blue loop phase. (*ii*) Secondly, axion emission is more efficient in heavier stars. We compare the local emission rate of a representative stellar cell, located where $m_{\rm enc}$ is 10% of the star mass, between the $8M_\odot$ model and the $6M_\odot$ model shown in Fig. 7.6. The corresponding ratios are about 2.2 before (blue), 2.9 during (purple), and 2.0 (red) after the blue loop phase. Additionally, the ratios of the total axion emission power between the $8M_\odot$ model and the $6M_\odot$ model are about 2.5 (blue), 2.8 (purple), and 2.1 (red), respectively. The variation in emission rates calculated using Eq. 7.4 arises from the core mass difference by a factor of approximately 1.4, and from differences in core temperatures and densities. In our simulation, we find the ratios of the highest core temperatures are 1.07 (blue), 1.09 (purple), and 1.03 (red). Therefore, we expect the sensitivity to g_{10} to improve by a factor of a few as the stellar mass increases in our benchmarks.

In Fig. 7.7, we show the evolution of the core potential as a function of the age of the star, for several selections of stellar masses: 5 $M_\odot$ (right, dashdotted), 6 $M_\odot$ (middle, dashed), and 8 $M_\odot$ (left, solid). The black, red, and green curves for a given mass correspond to $g_{10} = 0$, $g_{10} = 1$, and $g_{10} = 2$. In the absence of axions (black curves), the value of $\phi_{\rm crit}$ increases with increasing stellar mass [296]. For a blue loop to be initiated, ϕ_c must fall below $\phi_{\rm crit}$; massive stars typically satisfy $\phi_{c,\rm init} \sim \phi_{\rm crit}$ on the RGB and a blue loop is initiated and relatively robust. On the other hand, for less massive stars, $\phi_{\rm crit}$ is already so low that the beginning value of ϕ_c may satisfy $\phi_{c,\rm init} \gg \phi_{\rm crit}$ and the blue loop never gets initiated, or is heavily dependent on the composition, rotation, and convection. The situation is quite different once the axion coupling is turned on. Clearly, for $g_{10} = 2$ (green), the core potential in the case of the 5 $M_\odot$ star satisfies $\phi_c < \phi_{\rm crit}$, initiating the blue loop, while for heavier stars this condition is violated and the blue loop disappears.

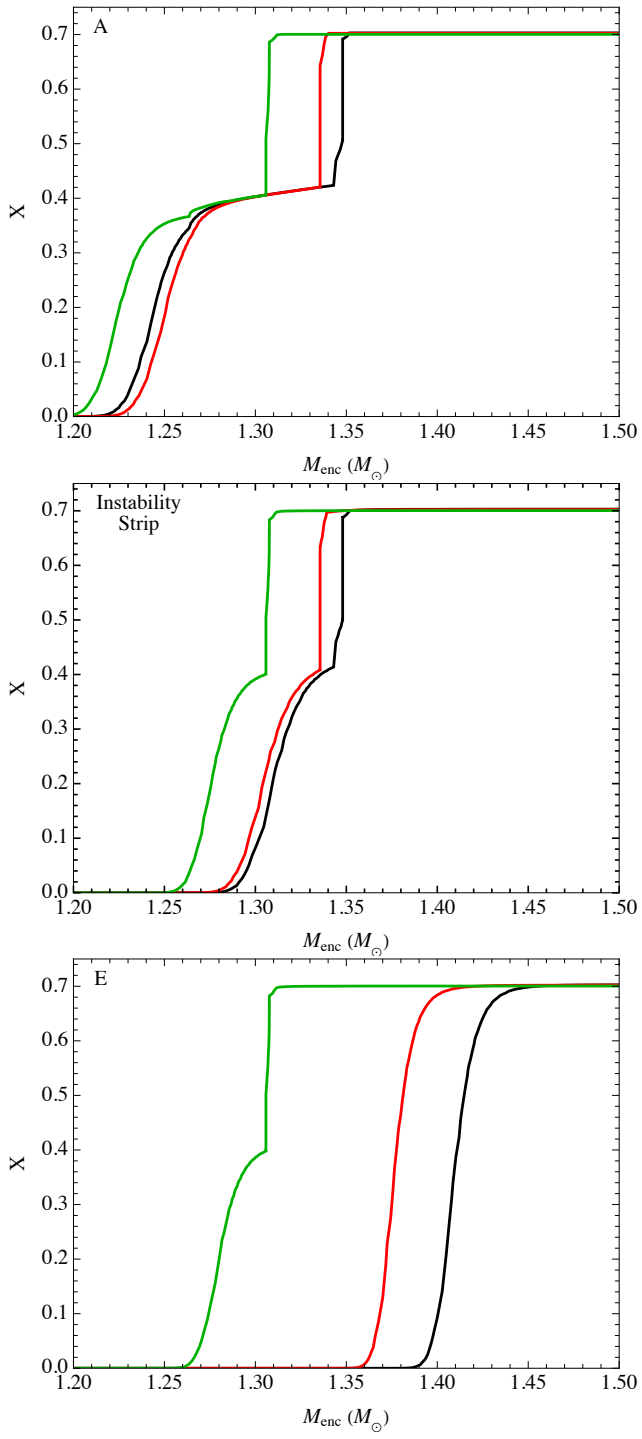


Figure 7.4: The hydrogen mass fraction X profile of a 6 $M_\odot$ model before (top panel), during (middle panel) and after (bottom panel) the blue loop stage, for axion couplings $g_{10} = 0$ (black), $g_{10} = 1$ (red), and $g_{10} = 2$ (green). The metallicity is set to $Z = 0.014$ and the overshoot to $\alpha_{ov} = 0.1$.

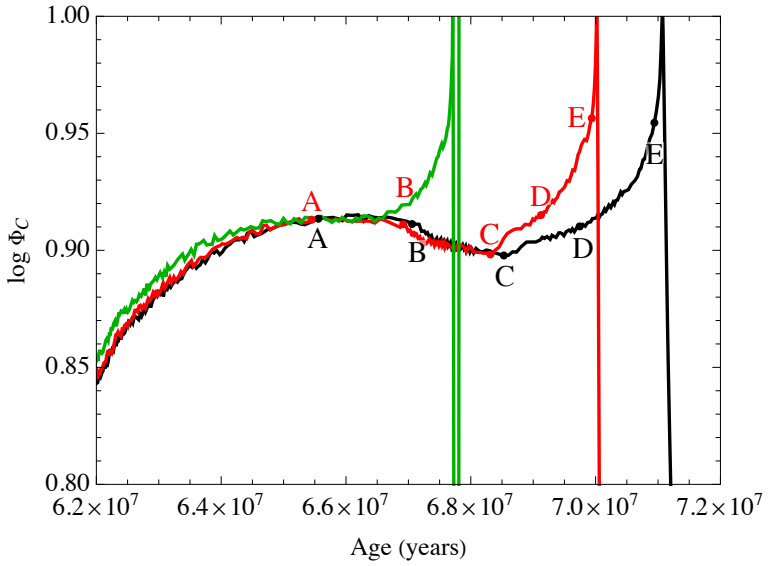


Figure 7.5: Core potential as a function of age for a 6 $M_\odot$ model with $g_{10} = 0$ (black), $g_{10} = 1$ (red), and $g_{10} = 2$ (green). Different evolutionary stages are labeled with "A" through "E," as depicted in Fig. 7.2. The metallicity is set to $Z = 0.014$ and the overshoot to $\alpha_{\rm ov} = 0.1$.

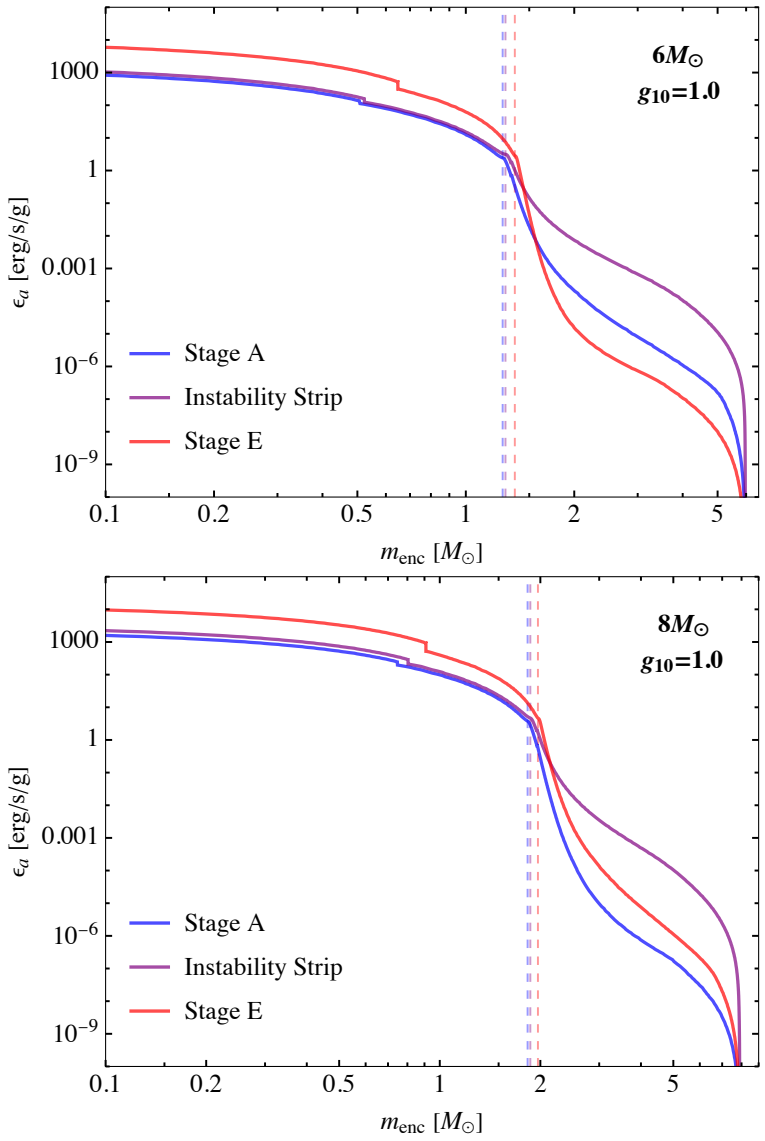


Figure 7.6: The axion energy loss rate from Eq. 7.4, as a function of the enclosed mass for a $6M_\odot$ (top) and $8M_\odot$ model (bottom), for Stage "A" (blue), during the transit through the instability strip (purple), and Stage "E" (red) of the blue loop stage. The axion coupling is $g_{10} = 1$. The metallicity is set to $Z = 0.014$ and the overshoot to $\alpha_{\rm ov} = 0.1$.

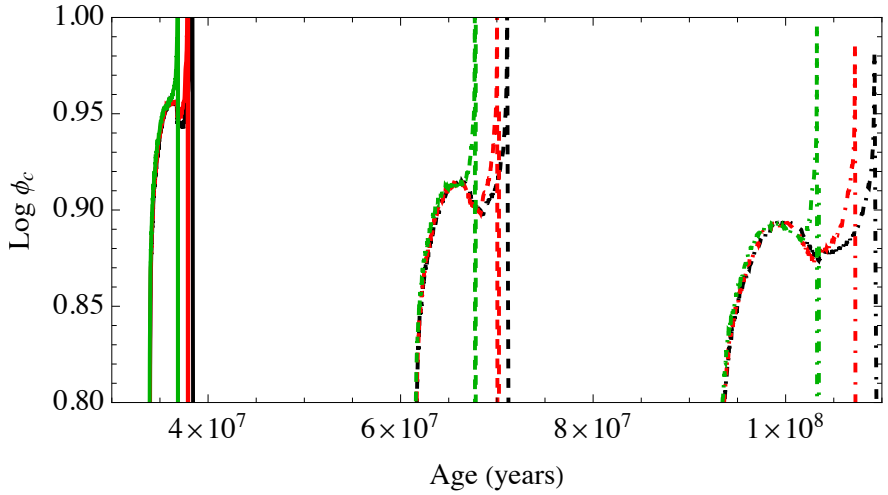


Figure 7.7: Core potential as a function of age for 5 $M_\odot$ (right), 6 $M_\odot$ (middle), and 8 $M_\odot$ (left) models with $g_{10} = 0$ (black), $g_{10} = 1$ (red), and $g_{10} = 2$ (green). The metallicity is set to $Z = 0.014$ and the overshoot to $\alpha_{\rm ov} = 0.1$.

7.5 Axion Constraints from the Existence of Massive Cepheids

In this section, we establish constraints on the axion-photon coupling using the criterion of blue loop elimination in Cepheid models corresponding to both existing observations and future expectations.

7.5.1 Constraints from Observed Cepheids and Simulations

It is evident from the discussion in Sec. 7.4.4 that requiring the existence of blue loops in more massive stars leads to more stringent constraints on g_{10}. Not only does the blue loop in more massive stars vanish for smaller values of g_{10}, the constraints obtained are more robust against assumptions in composition, rotation, and convection, since the blue loop without axions is more robust. In Fig. 7.8, we show the evolution of the core potential as a function of age for a $9M_{\odot}$ model. The solid curve corresponds to $g_{10} = 0.83$, while the dashed curve corresponds to $g_{10} = 0.835$. It is clear that the blue loop disappears (stops before reaching the edge of the red instability strip) for $g_{10} = 0.835$, a fact that we have verified by the star's track on the HR diagram in Fig. 7.9.

While stopping the evolution right at the edge of the red strip is our criterion, for heavier stars this criterion is sometimes difficult to fulfill since the evolution becomes highly sensitive to changes in energy loss. A small change in the coupling, at the level of $\Delta g_{10} \sim \mathcal{O}(10^{-4})$, can completely remove the blue loop instead of stopping it at the red edge. To address this, we create two models: one where the blue loop is entirely eliminated with a slightly higher coupling, and another where the blue loop persists with a lower coupling. For example, in the 8 $M_{\odot}$ model, the blue loop is eliminated

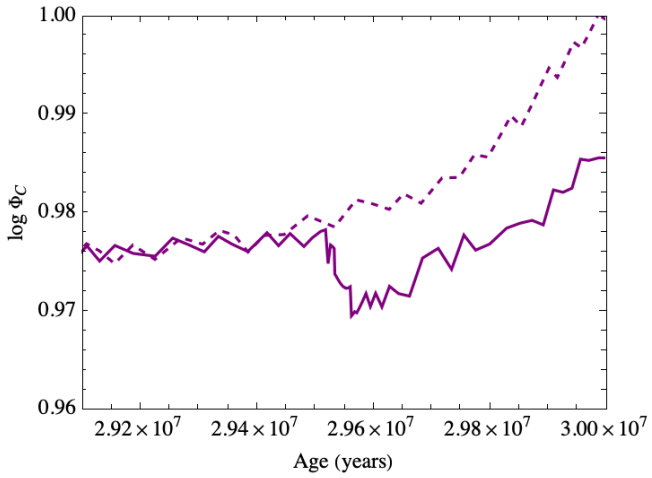


Figure 7.8: Core potential of a 9 $M_\odot$ model for $g_{10} = 0.83$ (solid) and $g_{10} = 0.835$ (dashed). The metallicity is set to $Z = 0.014$ and the overshoot to $\alpha_{\rm ov} = 0.1$.

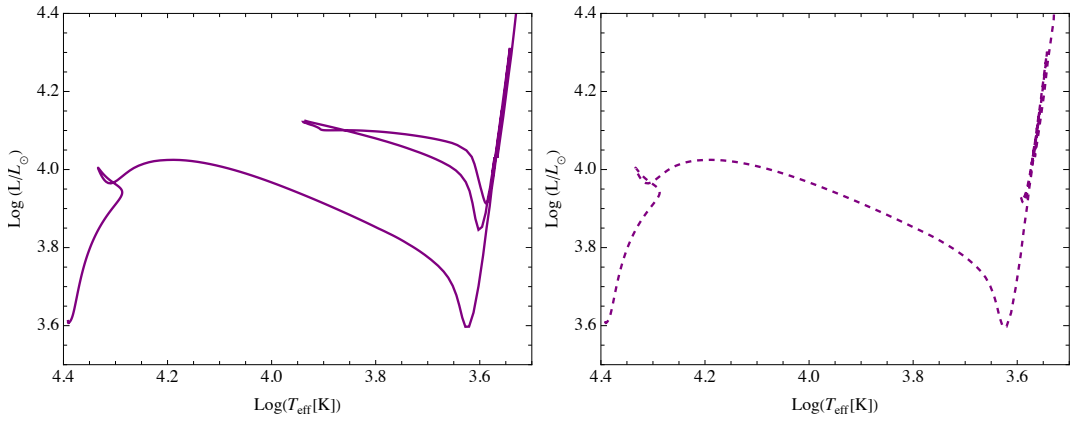


Figure 7.9: HR diagrams corresponding to the core potentials depicted in Fig. 7.8. The left panel corresponds to $g_{10} = 0.83$ while the right panel corresponds to $g_{10} = 0.835$. Both panels are for a 9 $M_\odot$ model. The metallicity is set to $Z = 0.014$ and the overshoot to $\alpha_{\rm ov} = 0.1$.

at $g_{10} = 1.2254$, while it remains at $g_{10} = 1.2253$. Instead of selecting a single model to calculate the axion constraint presented later in Eq. 7.28, we employ both models. This approach is applied to models with masses greater than 7 $M_\odot$.

At this stage, the fact that values of g_{10} must be so finely tuned to eliminate the blue loop might give reasons to pause; the elimination, at that level of precision, may be an artifact of the stellar evolution interpolation in `MESA`, rather than an accurate

representation of the effect of axions. To a certain extent, this ambiguity is difficult to resolve without adopting a finer resolution for the cell thickness in the simulations, or upgrading the simulations in other non-trivial ways. The elimination of the blue loop for such extremely small changes of g_{10} could also be due to underlying physical processes, which would require further study and more extensive simulations. However, it should be kept in mind that this is not a precision study: the blue loop does in fact vanish, for example in the case of the $9M_{\odot}$ model, between $g_{10} = 0.83$ and $g_{10} = 0.84$, or, being even less precise, between $g_{10} = 0.8$ and $g_{10} = 0.9$. Presenting our results with fewer significant digits would not alter the overall physics statement that axion energy loss causes the blue loop to vanish, or improve/diminish the strengths of our constraints in a very meaningful way. As such, we choose to display as many significant digits in g_{10} as we obtain from the current `MESA` simulation.

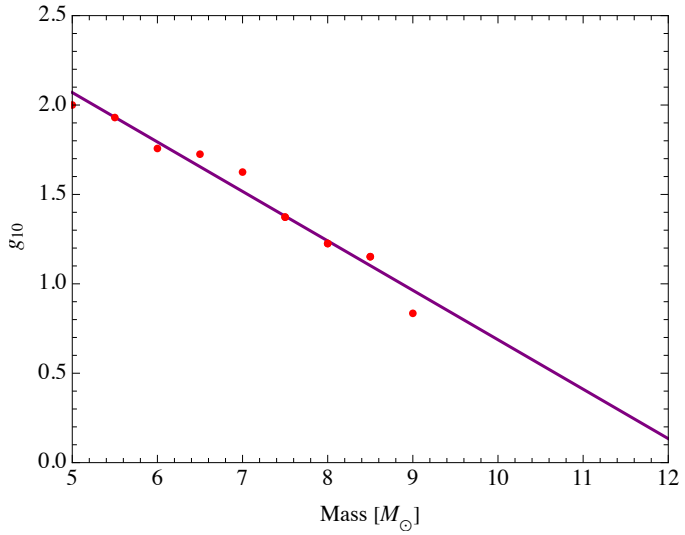


Figure 7.10: Values of the axion coupling g_{10} at which the blue loop just disappears, for models simulated in the current work (red dots). The purple line provides a linear fit.

In Fig. 7.10, we plot the value of g_{10} at which the blue loop just stops at the red edge of the instability strip, for models simulated in our work. The purple line

provides a linear fit. We were unable to generate blue loops for models with masses larger than $9M_\odot$ on `MESA` for $\alpha_{\rm ov} = 0.1$, even with $g_{10} = 0$. The inability of stellar evolutionary codes to produce blue loops for Cepheids above $9M_\odot$ as long as overshoot is incorporated, even with reasonable conditions for other input parameters, has been observed generally across various simulation suites - for more details, we refer to [323]. The blue loop is inhibited for $10M_\odot$ and heavier models at solar metallicities due to the limited inward penetration of the convective envelope.

At this point, one can begin to translate the results we have obtained into statements about constraints on the plane of $(g_{a\gamma\gamma}, m_a)$. The constraints come from requiring that a tentative Cepheid loses its blue loop due to axion emission; the criterion hinges on the behavior of the core potential, as displayed in Fig. 7.8 for the case of a $9M_\odot$ model. The requirement is that a blue loop should be curtailed just as it reaches the outer edge of the red edge of the instability strip. One can take these results, and compare them against Cepheids that have *actually* been observed, preferably with masses determined by methods that are independent of any processes involving axions. In Table 7.3, we summarize the current observational status of galactic Cepheids with dynamical mass determination. We note that Large Magellanic Cloud candidates, for example OGLE-LMC-CEP0227 [324] with mass $3.74M_\odot$ are not considered in our work.

The existence of the Cepheids S Muscae (S Mus) [301] and OGLE-GD-CEP-1884 [304] with dynamically and pulsation determined masses, respectively, serve as two potential benchmark observations. We note that Cepheids with dynamically determined masses are inherently more conservative with respect to constraining axions. The reason is that axions are expected to alter both stellar evolution models (as we have shown in this work) as well as stellar pulsation models (which is the subject of future work by

Table 7.3: Observed Cepheids with Determined Masses

Name	Mass ($M_\odot$)	Period (days)	Mass Determination	Location
SU Cyg	5.9	3.8455	Dynamical	galactic
V350 Sgr	5.2	5.154	Dynamical	galactic
S Mus	6.0	9.66	Dynamical	galactic
Polaris	4.5	3.9715	Dynamical	galactic
OGLE-GD-CEP-1884	7.47	78.14	Pulsation model	galactic
V1334 Cyg	4.288	3.331	Dynamical	galactic

Table 7.4: The masses were determined from the following papers: [325, 326, 301, 327, 304, 328].The periods were obtained from [329]

the current authors [330]). Dynamical mass determination, conducted through measurements of binary orbital parameters, is immune to axion physics.[9] S Mus, with a dynamically determined mass, thus serves as our most conservative benchmark.

7.5.2 S Mus: Luminosity and the Cepheid Mass Discrepancy Problem

Utilizing observational data from Cepheids to constrain axions immediately runs into a complication. While dynamical mass determination fixes the mass of S Mus as shown in Table 7.3, taking this same mass as a benchmark in evolutionary models leads to a Cepheid with lower luminosity than required to match data. This is the well-known mass discrepancy problem, already described in the Introduction. We illustrate this problem in the case of S Mus in Fig. 7.11 with a $6M_\odot$ model (black) and a $6.4M_\odot$

[9]In this context, we note in passing the Cepheid mass discrepancy problem [306]: while Cepheid masses determined from pulsation models and binary orbital dynamics are largely in concordance with each other, they are both different from masses expected from stellar evolution. Axions are unlikely to alleviate this problem, since the effect of axions appears to be most relevant to the radius of the core and hence the core potential and the triggering of the blue loop.

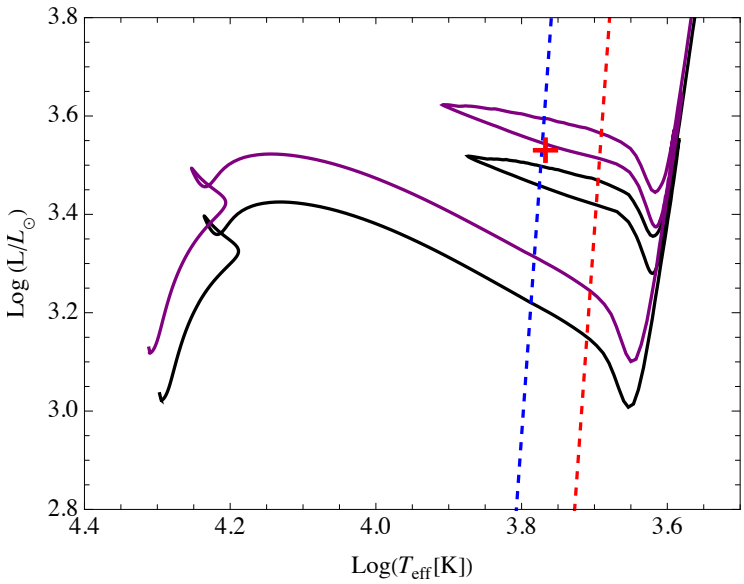


Figure 7.11: Reproducing the observed luminosity of the Cepheid S Mus with a $6M_\odot$ model (black) and a $6.4M_\odot$ model (purple). The metallicity is set to $Z = 0.014$ and the overshoot to $\alpha_{\rm ov} = 0.1$ for both models. Axions are absent ($g_{10} = 0$). The red dot signifies the luminosity of S Mus $\log L/L_\odot = 3.54$ following the analysis of observational data performed by [331], while for the effective temperature we have taken the value quoted in [332].

model (purple). The metallicity is set to $Z = 0.014$ and the overshoot to $\alpha_{\rm ov} = 0.1$ for both models. Axions are absent ($g_{10} = 0$). The red dot signifies the observed luminosity of S Mus $\log L/L_\odot = 3.54$, according to the analysis of observational data performed by [331]. It should be noted that the observational collaboration did not report uncertainties in the luminosity. which therefore could not be incorporated in our study. On the other hand, the benchmark effective temperature is taken to be 5850 K, following the determination by [332]. These authors took a pulsation period of 9.6 days, a pulsation mass of $6M_\odot$, and interpolated evolution models with luminosities between $\log L/L_\odot = 3.50 - 3.75$. While uncertainties in the temperature also undoubtedly exist, we do not incorporate them in our benchmark depiction in Fig. 7.11, since they have not been reported in the aforementioned study.

It is clear that a $6M_\odot$ model is unable to reach the required luminosity to match with observation, even after incorporating $\alpha_{\rm ov} = 0.1$, while a $6.4M_\odot$ model does so. Moreover, these conclusions would change as $\alpha_{\rm ov}$ is varied, and also with variations in the exact position of S Mus in the instability strip: the second crossing, versus the third, and so on, which is also unknown. Therefore, the situation depicted in Fig. 7.11 is a benchmark among a variety of possible evolutionary tracks. We report these possibilities in Table 7.5, varying the mass and overshoot.

Table 7.5: S Mus: The mass and overshoot required to achieve $\log L/L_\odot = 3.54$ and effective temperature 5850 K in the HR diagram (red dot in Fig. 7.11). We have assumed that $g_{10} = 0$.

Mass	$\alpha_{\rm ov}$
$6.0\,M_\odot$	0.2
$6.4\,M_\odot$	0.1
$6.6\,M_\odot$	0.0

Table 7.6: S Mus: The values of g_{10} for which the blue loop just disappears up to the red edge of the instability strip are reported, for the stellar properties listed in Table 7.5.

Mass	$\alpha_{\rm ov}$	g_{10}
$6.0\,M_\odot$	0.2	1.6
$6.4\,M_\odot$	0.1	1.7
$6.6\,M_\odot$	0.0	0.35

Switching on axion emission and requiring the blue loop to vanish would lead to different constraints on g_{10}, depending on the mass of the model, the value of $\alpha_{\rm ov}$, and the position of S Mus in the instability strip. Of these options, we keep the position of S Mus fixed, and report the constraints on g_{10} as the overshoot and mass are varied in

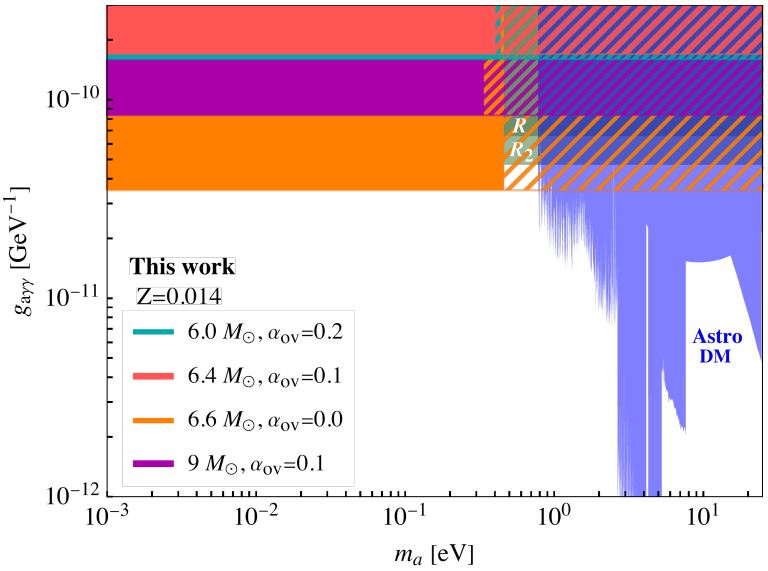


Figure 7.12: The constraints on the plane of $(g_{a\gamma\gamma}, m_a)$ for a fixed value of $Z = 0.014$, for three stellar models corresponding to the observed luminosity of S Mus: $6M_\odot$ with $\alpha_{ov} = 0.2$ (green), $6.4M_\odot$ with $\alpha_{ov} = 0.1$ (red) and $6.6M_\odot$ with $\alpha_{ov} = 0.0$ (orange). These benchmark values are taken from Table 7.6. The results for a $9M_\odot$ model with $\alpha_{ov} = 0.1$ (purple) are also displayed. The constraints on the coupling are obtained from the violation of Eq. 7.2. The range of m_a depicted by hatched regions corresponds to values smaller than the star's lowest core temperature (where the majority of axion production occurs), while the range shown by shaded regions is smaller than the lowest temperature across the entire stellar profile. We also show existing constraints from the stellar R-parameter (green) [294] and R_2-parameter (light green) [295], as well as astrophysical axion dark matter searches (blue, "Astro DM") [333, 334, 335, 336, 337, 338, 339]. The constraints are obtained from [62].

Table 7.6. The procedure we have followed is as follows. The mass and overshoot for a given model that achieves the position of S Mus on the HR diagram in the absence of axions is first taken from Table 7.5, and then the value of g_{10} that just nullifies the loop up to the red edge of the instability strip for that mass and overshoot is reported. The corresponding constraints on the plane of $(g_{a\gamma\gamma}, m_a)$ coming from S Mus are depicted in Fig. 7.12.

The results for a $9M_\odot$ model, which is the heaviest model that was simulated in the current work, are also shown. In the absence of simulations of blue loops at higher

stellar masses, and hence information about the effect of axions on such blue loops, we instead attempt to deduce such information from the linear fit in Fig. 7.10. We obtain

$$g_{10} = (-0.28 \pm 0.02)\,\frac{M}{M_\odot} + (3.5 \pm 0.1)\ . \tag{7.28}$$

We show the constraints corresponding to the largest model we can simulate, the $9M_\odot$ model corresponding to Fig. 7.8, in purple regions in Fig. 7.12.

The fact that we display the results for a $6.6M_\odot$ model may be open to criticism, given that it is outside of the range for the allowed dynamical mass of S Mus, which only goes up to $6.4M_\odot$. Moreover, the fact that we first determine the mass and overshoot to match the observed luminosity of S Mus, and *then* vary g_{10} until the blue loop vanishes, is not the most precise method to set limits. More correctly, what should be done is to scan the three-dimensional parameter space comprising $\{M, \alpha_{\rm ov}, g_{10}\}$ and select the subspace where the observed luminosity of S Mus is achieved *and* the blue loop vanishes; the values of g_{10} from that subspace would furnish the constraints on the axion coupling. While we do not pursue this method, our results indicate that in the large mass - small overshoot regime ($\sim 6.6M_\odot$) the constraints on the axion are likely to become stringent. This further underscores our main point: that heavy, luminous Cepheids are a fertile target for these kinds of studies.

7.5.3 Incorporating Overshoot Uncertainties for $6M_\odot$ and $8M_\odot$ Models

In this Section, we investigate how our results change with changes in overshoot.

The most important physical quantity influencing the development and morphology of the blue loop is the size of the core. The dependence of the core radius on the composition for a fixed core mass has been studied by various authors [340, 323] and

generally while composition is important, it is not the dominant factor in determining the blue loop. The main determinant in the development of the blue loop is the outward motion of the hydrogen burning shell that is evident in the progressive panels labelled "A", "Instability Strip", and "E" in Fig. 7.4 [297, 340, 323]. This outward motion reduces the amount of excess helium above the shell, which is a critical requirement for the blue loop to occur.

The position of the discontinuous jump in the hydrogen profile in panel "A" of Fig. 7.4 marks the innermost point of convective penetration (the first dredge-up). The further inwards (smaller values of $m_{\rm enc}$) this penetration occurs in stage "A", the more robust the ensuing blue loop. Conversely, the inward penetration of the convective envelope is limited for stars with mass above $9M_{\odot}$ at solar metallicity, inhibiting the blue loop in such cases [323]. The efficiency of convective mixing in the core [341, 342] and the efficiency below the convective envelope [299, 343] play an important role in determining the size of the convective core.

Models using the Ledoux criterion require overshooting to match observations [344], since overshooting extends the core beyond the convective boundary predicted by stellar theory. Convective cells in the stellar core penetrate into the radiative regions due to their non-negligible velocity, an effect parametrized by $\alpha_{\rm ov}$. Larger overshoot results in larger stellar cores and higher luminosities, as well as higher stellar radii. Constraining $\alpha_{\rm ov}$ has been a focus of activity, with efforts ranging from using eclipsing binary stars ($\alpha_{\rm ov}$ between 0.25 and 0.32 for stars between 2.5 and 7 $M_{\odot}$) [345] to asteroseismological measurements ($\alpha_{\rm ov} = 0.44 \pm 0.07$ for θ Ophiuchi) [346] and non-rotating evolutionary models ($\alpha_{\rm ov}$ between 0.25 and 0.30) [347]. Based on VLT Flames survey of massive stars ranging from $5 - 60M_{\odot}$, [348] found $\alpha_{\rm ov} = 0.335$. In Sec. 7.4, we followed the initial conditions of [349] who constrained overshoot using the main sequence width for mass ranges between $1.35 - 9M_{\odot}$. The overshoot was set to $\alpha_{\rm ov} = 0.1$ during hydrogen

and helium burning for masses above 1.7 $M_\odot$, making it applicable for our case. We now show how our results change as $\alpha_{\rm ov}$ is varied.

We show the behavior of the core potential for $\alpha_{\rm ov} = 0.0, 0.1$, and 0.2 for a $6M_\odot$ model in Fig. 7.13 and for a $8M_\odot$ model in Fig. 7.14, respectively. The black curves show the case of $g_{10} = 0$, while the green curves show the core potential for values of g_{10} at which the blue loop is just curtailed at the red edge of the instability strip. There are two features that are important in Fig. 7.13. Firstly, as $\alpha_{\rm ov}$ becomes larger, the critical value of the core potential $\phi_{\rm crit}$ increases. This is because as the overshoot increases, the core becomes enlarged both in mass as well as in radius. Secondly, as $\alpha_{\rm ov}$ increases, the core potential displays a more pronounced dip when it falls below $\phi_{\rm crit}$ and thus the blue loop is more robust; it therefore requires a larger value of g_{10} to attenuate it. On the other hand, for smaller $\alpha_{\rm ov}$, the core potential becomes flatter and just barely dips below the corresponding value of $\phi_{\rm crit}$; even a small value of g_{10} is sufficient to disrupt the blue loop in this case. We note that the constraints on g_{10} do not change appreciably for larger values of $\alpha_{\rm ov}$ in the $6M_\odot$ model. Ultimately, both the $6M_\odot$ model as well as the $8M_\odot$ model lose their blue loops for large enough overshoot. This is because the large overshoot increases the mass of the core to an extent that the core potential acquires a large value and no longer dips below $\phi_{\rm crit}$. It should be noted that the overshoot physics of an $8M_\odot$ model can differ substantially from that of a $6M_\odot$ model, as axions are switched on. Thus, in Fig. 7.14, it is clear that the constraint coming from $\alpha_{\rm ov} = 0.2$ is substantially stronger than that coming from $\alpha_{\rm ov} = 0.1$, and even $\alpha_{\rm ov} = 0.0$.

We pause to warn the reader against a possible misperception emanating from Figs. 7.13 and 7.14. The core potential should not be misconstrued as a quantity with predictive power: indeed, the fact that ϕ_c before the loop increases with increasing

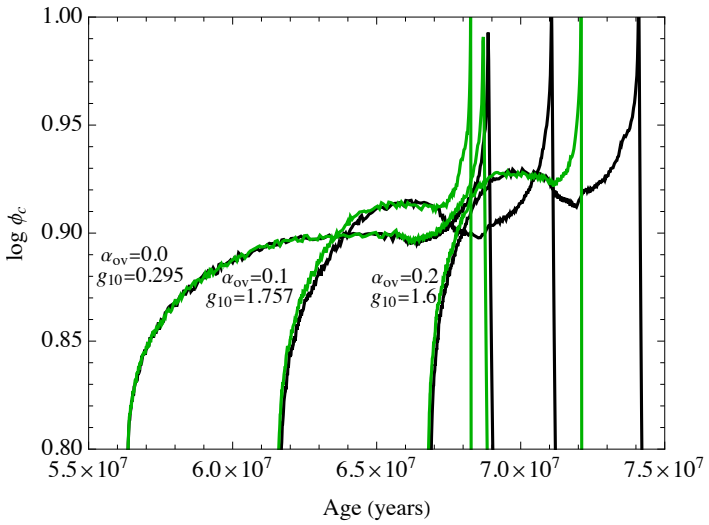


Figure 7.13: The behavior of the core potential for $\alpha_{\rm ov} = 0.0, 0.1$, and 0.2 with $g_{10} = 0$ (black) and the value of g_{10} that just eliminates the blue loop in each case (green). The results depicted here are for a $6M_{\odot}$ model. The metallicity is set to $Z = 0.014$.

overshooting does not predict that a higher g_{10} value is needed to suppress the loop. Similarly, after the onset of the loop, ϕ_c tends to increase again, although the loop is still in its blue-sided part (and vice versa). A more correct way to think of the core potential is as a diagnostic for the onset of a loop.

In Fig. 7.15, we display the hydrogen mass fraction of a 6 $M_{\odot}$ model with $\alpha_{\rm ov} = 0.0$ (left) and $\alpha_{\rm ov} = 0.2$ (right), respectively, for $g_{10} = 0$ and the value of g_{10} that just switches off the blue loop in each case. For each column, the top panel shows the profile at stage "A", the middle panel shows the profile at a point in the instability strip, while the bottom panel shows the profile at stage "E". The first feature to note is that in the absence of axions (black curves), as $\alpha_{\rm ov}$ becomes larger, the location of the first dredge-up moves outwards, enlarging the core and creating a more robust blue loop. For stage "A", the location of the jump in the hydrogen profile occurs at $m_{\rm enc} = 1.28$, 1.35, and 1.49 for $\alpha_{\rm ov} = 0.0, 0.1$, and 0.2, respectively, as can be seen from Fig. 7.15 and Fig. 7.4. The effect of axions is to shift the hydrogen profiles, especially

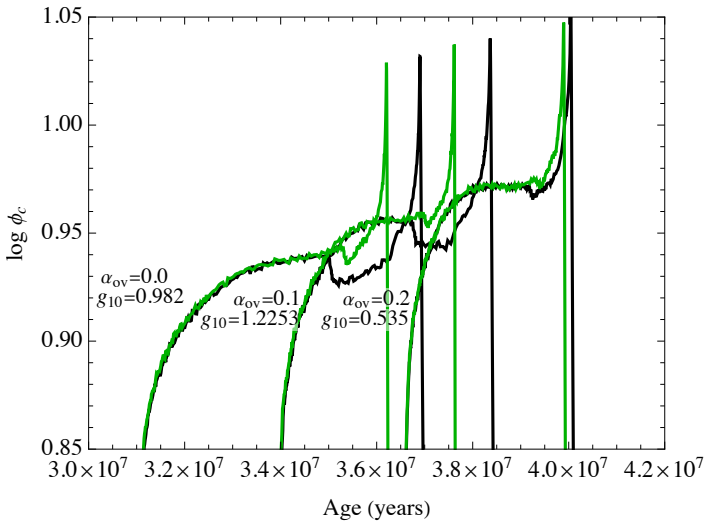


Figure 7.14: The behavior of the core potential for $\alpha_{\rm ov} = 0.0$, 0.1, and 0.2 with $g_{10} = 0$ (black) and the value of g_{10} that just eliminates the blue loop in each case (green). The results depicted here are for a $8M_\odot$ model. The metallicity is set to $Z = 0.014$.

the location of the first dredge-up, to the left. This is especially evident in the cases of $\alpha_{\rm ov} = 0.1, 0.2$ where the jump in the profile is relocated to 1.30 (a reduction of 3.7%) and 1.47 (a reduction of 1.3%), respectively. The case of $\alpha_{\rm ov} = 0.0$ shows a barely perceptible left-ward shift of the profile at the first dredge-up, showing how sensitive the system is to changes in the core. The location of the hydrogen burning shell at stage "A" for the $\alpha_{\rm ov} = 0.0$ model is at slightly larger enclosed mass for $g_{10} = 0.295$ compared to $g_{10} = 0$, although by stage "E" the situation is reversed.

In Fig. 7.16, we depict constraints on the plane of $(g_{a\gamma\gamma}, m_a)$ for two benchmark models: a $6M_\odot$ model (left panel) and $8M_\odot$ model (right panel), and for each model we vary values of $\alpha_{\rm ov} = 0.0$ (orange), $\alpha_{\rm ov} = 0.1$ (purple), and $\alpha_{\rm ov} = 0.2$ (red). As discussed above, the blue loop phase becomes more robust with an increase in overshoot from 0.0 to 0.1, requiring a larger $g_{a\gamma\gamma}$ coupling to completely eliminate the phase. Conversely, the blue loop phase becomes unstable when $\alpha_{\rm ov} \sim 0.2$, as can be seen from the black

curves in Fig. 7.13 and Fig. 7.14. This leads to an enhanced sensitivity in the red-shaded regions of Fig. 7.16, especially in the case of the $8M_{\odot}$ model.

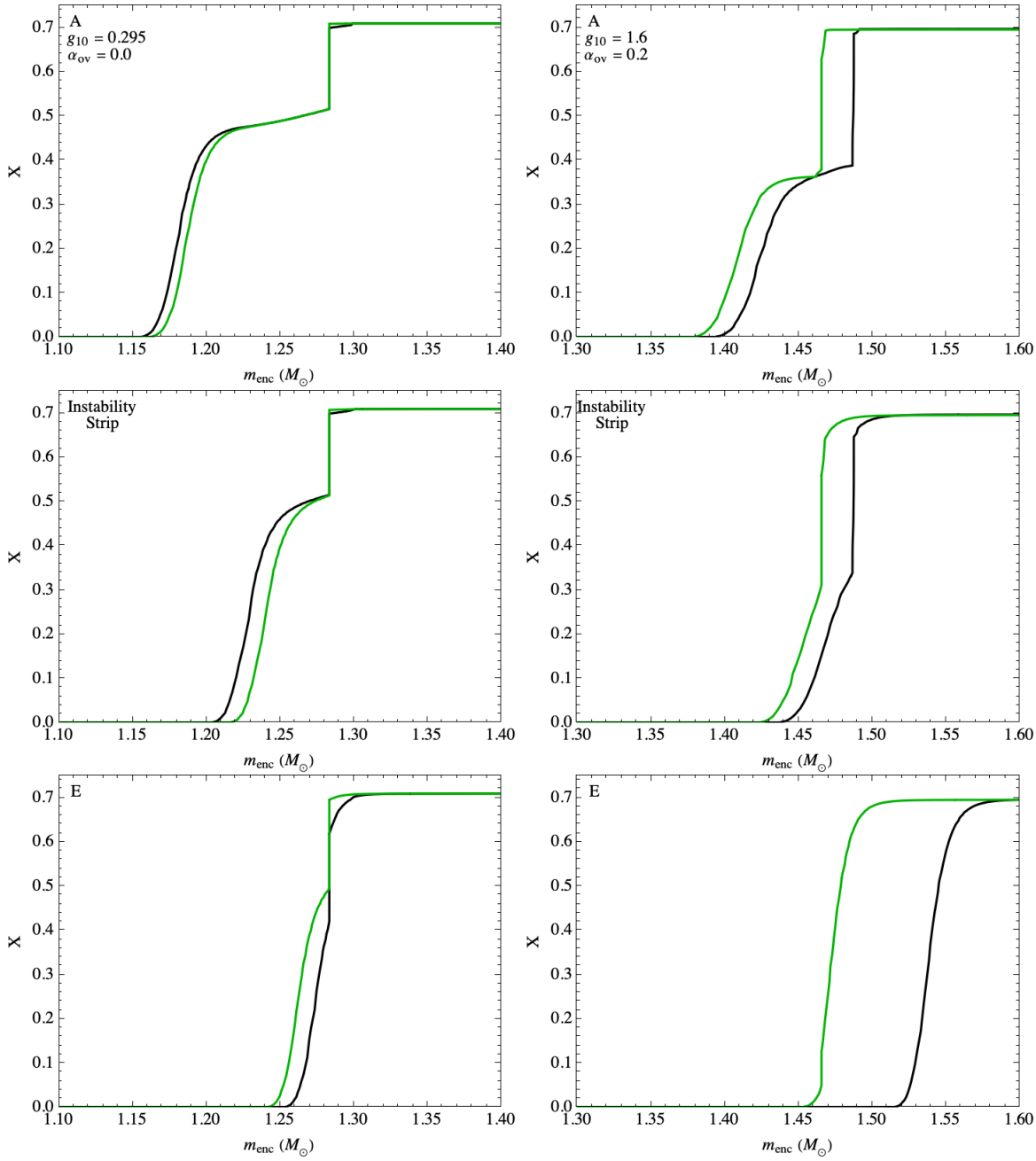


Figure 7.15: The hydrogen mass fraction X profile of a 6 $M_\odot$ model before (top panels), during (middle panels) and after (bottom panels) the blue loop stage. The axion coupling is set to $g_{10} = 0$ for the black curves. Left column: overshoot $\alpha_{ov} = 0.0$ and $g_{10} = 0.295$ (green). Right column: overshoot $\alpha_{ov} = 0.2$ and $g_{10} = 1.6$ (green). The metallicity is set to $Z = 0.014$.

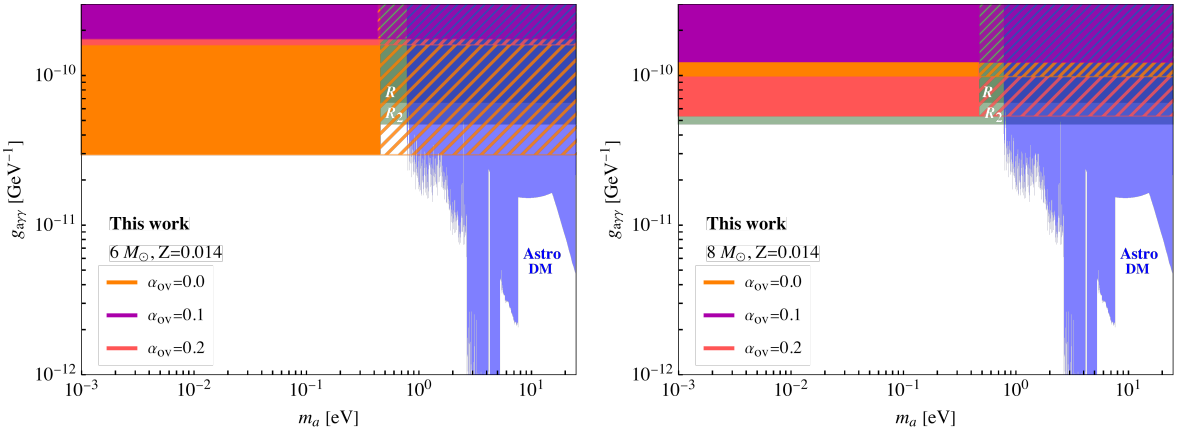


Figure 7.16: Left panel: The constraints on the plane of $(g_{a\gamma\gamma}, m_a)$ for a $6M_\odot$ model with $\alpha_{\rm ov} = 0.0$ (orange), $\alpha_{\rm ov} = 0.1$ (purple), and $\alpha_{\rm ov} = 0.2$ (red). Right panel: Corresponding constraints for a $8M_\odot$ model. The constraints on the coupling are obtained from the violation of Eq. 7.2. The metallicity is set to $Z = 0.014$.

7.6 Conclusions

In this paper, we have explored the effect of axion emission on the development of the blue loop stage of intermediate mass stars, taking the core potential as a diagnostic for the onset of the blue loop. As we have stressed in Sec. 7.5.3, the amount of convective overshooting drastically changes the critical value of the axion coupling for which loops are suppressed; moreover, the core potential also depends on the detailed chemical composition (as a function of the radius) of the star, as depicted in Fig. 7.4. Rotation, metallicity, and nuclear reaction rates also affect the core potential. The critical value of the core potential, $\phi_{\rm crit}$, is determined from simulations and thus $\phi_{\rm crit}$ can only be determined from the models, i.e., once the loop sets in. In particular, it should be understood that $\phi_{\rm crit}$ has no predictive power and can be used only as a diagnostic or even proxy for the onset of a loop.

Assuming galactic metallicity and $\alpha_{\rm ov} = 0.1$, the existence of the Cepheid S Mus with dynamically determined mass $6M_\odot$ has been used to constrain the axion-photon coupling. The effect of different choices of the overshoot on the underlying physics has been studied. Results have also been provided for $9M_\odot$ models, which constitute the limits of our simulation. Prospects and challenges for obtaining reliable bounds from the simulation of heavier Cepheids have been discussed, and tentative projected bounds for a $12M_\odot$ model is presented in Appendix D. Although the blue loop stage of more massive stars is more robust in the absence of energy loss via axion emission, our findings suggest that, for a given overshoot, axions have a greater impact on more massive stars by eliminating their blue loops due to their higher core temperatures. Consequently, observational evidence from more massive Cepheid stars could impose stronger constraints on the $g_{a\gamma\gamma}$ coupling.

Compared to the previous study of axion effect on Cepheids [308], our study included axion energy loss from both degenerate medium and non-degenerate medium in the simulation for a more precise description of axions originating from the dense helium core, whereas the previous study only took into account the non-degenerate medium contribution. Further improvements can be included in future works to reduce the uncertainty in the simulation of Cepheids. Firstly, we used the variable ζ in Eq. 7.6 to classify stellar regions with and without degenerate electron contributions. A refined approach could be taken when a more sophisticated model of the transition region around the hydrogen-burning shell is available. Regarding the charge screening effect due to high charge density, we treated the electron screening and the ion screening independently since their correlation wavenumbers differ significantly. Future studies could explore the correlations in the emission regions near the core boundary. Finally, the uncertainty in calculating the emission rate can be reduced by adopting a finer resolution for the cell thickness in `MESA` simulations, as the $\epsilon_a \propto T^7$ dependence on the stellar temperature profile makes the calculation highly sensitive to even small variations in T.

Further future directions have been described at various points in the main text. Axions may influence the location of the instability strip, potentially leading to observable consequences. The effect of axions on the PL relations of Cepheids is a very interesting direction to pursue, especially since the performance of Cepheids as standard candles hinges on percent-level control over systematic uncertainties, which may very well be challenged by the emission of axions. The incorporation of rotation and different values of the metallicity, and their interplay with axion physics, is another interesting future direction. We remark that in our simulations axions more readily eliminate the blue loop phase of heavier stars when assuming larger $\alpha_{\rm ov}$ values, while

lighter stars are more easily affected under null overshooting. This calls for more comprehensive overshoot models to refine future axion constraints from Cepheids.

One of the goals of our paper has been to motivate the simulation community to further investigate the prospects of simulating blue loops for heavier stars with overshoot, given the importance of the heavier stars for fundamental physics that we have emphasized. Of course, it is also possible that current simulations are adequate and Cepheids above $9M_{\odot}$ do not exist.

Blue loops have acquired a reputation, in our opinion undeserved, of being disfavored for setting constraints on axions, due to uncertainties in the microphysics and numerical description [350]. Such an evaluation may be premature, given the advances in numerical simulations and evolution and pulsation models on the one hand, and the anticipated discovery of dynamically mass-determined Cepheids from Gaia on the other. *Our main message is that the observation, dynamical mass determination, and reliable blue loop simulation of heavy Cepheids is likely to yield strong constrains on the axion-photon coupling.*

Chapter 8

Millicharged Particles, Blue Loops, and the Cepheid Mass Discrepancy Problem

8.1 Introduction

The helium burning cores of stars are a promising site to explore new physics. The high temperatures attained in these cores provide suitable conditions for the production of beyond-Standard Model (BSM) species, which then typically escape the star. This energy loss mechanism alters or even hinders the further development of the helium core and the associated stages of stellar evolution, which are reflected at the level of stellar population observations. These avenues for searching for BSM physics go back to the classic work of Raffelt [290, 291] and have seen a recent resurgence as the focus of the community has increasingly turned to light BSM species [292, 293]. At least one standard exclusion region on the axion parameter space comes directly from these arguments: the loss of energy due to axions from the helium burning core of horizontal branch stars reduces the duration of this stage and hence its population; such loss (and hence the coupling of axions to the Standard Model) can therefore be constrained by directly by observations [294, 295].

A more recent development has been the focus on the blue loop stage of intermediate mass stars, which also feature a helium burning core [351]. The production of BSM species can curtail the blue loop stage, which can lead to the disappearance of

known Cepheid variable stars, and therefore constraints on the strength of the axion couplings. Heavier Cepheids have hotter helium cores that produce axions more copiously; hence, the discovery of such Cepheids would place extremely stringent bounds on the axion-photon coupling. In recent work [351], the current authors have emphasized the importance of both reliable simulations of heavy Cepheids as well as observations of such candidates (preferably with mass determination performed through dynamical methods). For example, the observation and simulation of a $12M_{\odot}$ Cepheid would outperform existing constraints on the axion-photon coupling coming from horizontal branch stars.

While the total disappearance of a blue loop, and hence a known Cepheid, furnishes the most striking footprint of BSM physics, subtler hints may also be of interest. The prospects may seem daunting here, since any change in the morphology or broad physical characteristics of a star would seem to require BSM species that are trapped - typically relevant for larger couplings to the Standard Model that are already constrained by other methods. Moreover, the proper treatment of trapped species would presumably require comprehensive simulations that can adequately account for changes in the hydrodynamic and transport properties of the stellar interior induced by the BSM species. A clear direction of interest is whether BSM species, trapped inside a Cepheid, can induce changes to the Cepheid's pulsation period, with observational consequences. This is a work in progress by the current authors.

A slightly simpler question, still within the regime of couplings where the BSM species escapes the star, is whether observable changes can be induced without necessarily requiring the blue loop to be curtailed entirely. Put differently, can the reduction of stellar luminosity induced by BSM particles have observational consequences? One fruitful avenue to explore is the effect of BSM species on a classic problem in the Cepheid community, which, by now, has been relevant for over fifty years: the so-called

Cepheid mass discrepancy problem (we refer to [306] for an accessible review). This is the systematic offset between the mass of Cepheids inferred from evolutionary models and that inferred from other methods, such as binary dynamics or pulsation models. The level of disagreement is typically $\mathcal{O}(10-20)\%$. Masses determined by binary dynamics furnish the most striking examples of this discrepancy; in our galaxy, such Cepheids include SU Cyg [325] with mass $5.9M_\odot$; V350 Sgr [326] with mass $5.2M_\odot$; S Mus [301] with mass $6.0M_\odot$; Polaris [327] with mass $4.5M_\odot$; and V1334 Cyg [328] with mass $4.288M_\odot$. One can also include the Cepheid OGLE-LMC-CEP0227 [352] in the Large Magellanic Cloud with mass $4.14M_\odot$. In every case, the mass agrees well with that derived from pulsation models, while disagreeing with masses derived from evolutionary models.

It is important to note that the discrepancy is such that evolutionary models corresponding to a dynamically or pulsation-determined mass predict a luminosity that is lower than that observed for a given Cepheid. Stated equivalently, the mass predicted from evolutionary models is typically higher than that predicted from dynamical or pulsation models for a given observed Cepheid luminosity. Solving the discrepancy problem, then, comes down to introducing mechanisms that increase the luminosity of a Cepheid without increasing its mass. During the blue loop stage, this amounts to introducing mechanisms that enrich the core. Two such mechanisms are considered standard in the literature: convective overshoot and rotation[1]. Convective core overshooting, for example, enriches the core by mixing hydrogen into it, which leads to a more massive helium core after the star departs from the main sequence. Rotation, which we discuss in detail, has a similar effect [349, 354, 355, 356, 357]; as detailed in [349] for a $7M_\odot$ model, once rotation is incorporated, the star crosses the Hertzsprung gap at a higher luminosity. The higher luminosity persists in subsequent stages and

[1] A third, pulsation-driven wind loss, is not relevant for our work. We refer to [353] for details.

in particular, the corresponding Cepheid stage has a luminosity 0.15 dex higher than the case where there is no rotation. This corresponds to a 15% reduction in the mass deduced from evolution, resolving the mass discrepancy problem.

The emission of BSM species from the core and the consequent lowering of the stellar luminosity can be expected to have the opposite effect and make the mass discrepancy problem more severe. If one posits standard benchmark values for one or both of convective overshoot and rotation that resolve the mass discrepancy problem for a given Cepheid, then switching on BSM couplings would reduce the luminosity below levels that are compatible with data. This would potentially lead to constraints on the BSM couplings, if the reduction is drastic enough (for example, down to a level that nullifies the effect of overshoot and/or rotation). While such constraints would not be as robust as requiring the disappearance of the blue loop, they could be stronger, especially if the reduction in luminosity is substantial for feebler BSM couplings, before the couplings are increased and the blue loop vanishes entirely. Clearly, such prospects are best for species whose production rates have a milder dependence on the temperature; for steep dependencies, such as $\sim T^7$ in the case of axions, the blue loop vanishes *before* a substantial reduction of the luminosity can be achieved, as one increases the axion-photon coupling.

In this context, millicharged particles (MCPs) fit the relevant BSM candidate perfectly. A key feature of MCP production in stellar interiors is the strong dependence of the emissivity on temperature, typically scaling as $\epsilon_\chi \propto T^3$ in the regime where plasmon decay dominates [61, 358, 64]. The physical origin of this scaling lies in the thermal phase space distribution of longitudinal plasmons, whose population density

follows a Bose-Einstein distribution and grows rapidly with temperature. Specifically, the emissivity can be written in the form

$$\epsilon_\chi(T,\rho) \simeq C\,\omega_P^2(T,\rho)\,T^3\,e^{-m_\chi/T}\,q_\chi^2, \tag{8.1}$$

where ω_P is the plasma frequency (which depends weakly on density ρ), m_χ is the MCP mass, and q_χ is the electric millicharge. The T^3 scaling arises from the integral over the plasmon phase space, reflecting both the increasing thermal occupation number of plasmons and the available phase space volume for their decay into MCP pairs.

While the emissivity for MCPs produced via plasmon decay scales approximately as $\epsilon_\chi \propto T^3$, the corresponding temperature dependence for axion-like particles (ALPs) produced via the Primakoff process is qualitatively different and typically steeper. In the Primakoff process, thermal photons convert to ALPs in the Coulomb field of charged particles (mainly ions), with a cross section that grows with energy. As a result, the Primakoff emissivity exhibits a stronger temperature sensitivity, scaling approximately as [61, 358, 359]

$$\epsilon_a \propto T^7\,\kappa^{-2}, \tag{8.2}$$

where κ is the Debye screening scale of the plasma. The T^7 scaling reflects both the Bose-enhanced number of high-energy photons and the energy dependence of the Primakoff cross section, which favors higher temperatures.

The purpose of this paper is to constrain MCPs by studying their effect on the Cepheid mass discrepancy problem. As mentioned before, this possibility arises due to the much milder T dependence of the MCP emissivity compared to axions, which opens the possibility of studying their effect on the luminosity of the star during its blue loop stage, rather than the entire nullification of the blue loop.

8.2 Stellar Model and Rotation

In this Section, we describe our simulation pipeline. We perform simulations with the 1-dimensional code `MESA` version `r23.05.1` [272, 274, 275, 276, 277, 300]. The opacity tables, equation of state, and nuclear reaction networks closely follow our previous work on axions [351]. Compared to our previous work, we have increased the number of grid points in our simulations by increasing the number of cells in each model by a factor of 4 and the number of models by a factor of about 1.5, for a given fully evolved star. We have also implemented changes to the mixing length theory and mass-loss prescription, as described below. Instead of using time-dependent convection (TDC) for the mixing length theory which follows [287] and becomes Cox mixing length theory at long times, we have switched to Henyey [360]. All models implement a galactic metallically of $Z = 0.014$ with composition set to solar following [279]. Models start on the zero-age main sequence and are terminated during the AGB stage.

As mentioned in the Introduction, a major new aspect of this study is the incorporation of rotation and its interplay with BSM physics. Rotation impacts almost every aspect of stellar models and has been extensively studied by various groups [361, 362, 363, 364, 365, 366, 367, 368, 369]. Through its effect on stellar lifetimes, nucleosynthesis and evolution, rotation leaves its imprint on models of both population synthesis and chemical evolution of star clusters and galaxies. The aspect of rotation we will primarily be interested in is its relevance to the mass discrepancy problem.

8.2.1 Rotation

Rotation is known to be a critical factor in resolving the long-standing Cepheid mass discrepancy problem. The inclusion of rotation modifies stellar evolution in several

ways that help resolve this discrepancy. Anderson *et al.* [317] and Ekström *et al.* [370] have shown that self-consistent inclusion of rotation in Geneva stellar models yields:

- **Extended main-sequence lifetimes:** Rotational mixing transports fresh hydrogen into the stellar core, prolonging hydrogen burning.
- **Increased blue-loop luminosity:** Rotational mixing leads to more massive helium cores, resulting in higher luminosity during the blue-loop phase.
- **Modified mass-luminosity (M-L) relation:** The M-L relation acquires a dependence on both initial rotation rate and evolutionary crossing number of the instability strip.
- **Surface abundance changes:** Rotation-induced mixing can enhance surface abundances of processed material, such as ^{14}N.

For a $7\,M_\odot$ star with initial angular velocity $\Omega/\Omega_{\rm crit} \approx 0.4$, Ekström *et al.* find that the blue-loop luminosity increases by ~ 0.15 dex compared to non-rotating models [370]. This boost reduces the inferred evolutionary mass at fixed luminosity by $\sim$ 15%, bringing it into agreement with dynamical and pulsation masses. Main-sequence lifetimes are extended by $\sim$ 20–25% due to rotational mixing. Anderson et al. (2014) [317] also employ the Geneva stellar evolution models, which include a homogeneous and self-consistent treatment of axial rotation, and arrive at similar conclusions.

Rotation also affects the core structure. The centrifugal force reduces the effective gravity, which would tend to lower the core density and temperature; however, rotational mixing dominates, leading to larger core masses and higher luminosity overall [371]. Surface abundance anomalies, such as ^{14}N enrichment, offer observational tracers of past rotational history [372]. Moreover, rotation-induced mixing leads to

surface abundance patterns that can mimic those produced by dredge-up processes, complicating the interpretation of observational data.

8.2.2 Rotation in Stellar Models

We follow prior literature in implementing rotation in our MESA models. Observations of main-sequence B-type stars, believed to be the progenitors of Cepheids, suggest initial rotation rates corresponding to $v/v_{\rm crit} \sim 0.3$–0.4 [373]. We adopt an initial rotation rate $\Omega/\Omega_{\rm crit} = 0.5$ to match the rotation rates used in [370, 317, 374].

The critical surface velocity $v_{\rm crit}$ is defined as:

$$v_{\rm crit} = \sqrt{\frac{2}{3}\frac{GM}{R_p}}, \tag{8.3}$$

where R_p is the polar radius at critical rotation. Correspondingly, the critical angular velocity $\Omega_{\rm crit}$ is given by:

$$\Omega_{\rm crit} = \sqrt{\Gamma\frac{GM}{R_p^3}}, \tag{8.4}$$

where $\Gamma = 1 - \min\left[L/L_{\rm Edd}, 0.9999\right]$ accounts for the Eddington factor.

Cepheids themselves are observed to rotate slowly, with surface velocities $\sim$ 10–20 km/s [372], consistent with strong angular momentum loss during post-main-sequence evolution. However, the initial rotation rate on the main sequence strongly influences the subsequent evolution and the blue-loop luminosity. In MESA, we initialize rotation via $\Omega/\Omega_{\rm crit}$, and adopt convective core overshoot $\alpha_{\rm ov} = 0.1$ unless otherwise specified. We include key rotational instabilities and circulations: dynamical shear instability, secular shear instability, Solberg-Høiland instability, Eddington-Sweet circulation, and Goldreich-Schubert-Fricke instability. We follow [317, 375] and set the angular momentum transport efficiency parameter to unity. The rotational diffusion

coefficient f_c is set to 1/30 [375], and the mean molecular weight gradient parameter ∇_μ is set to 0.05. We do not include magnetic fields or angular momentum transport via the Spruit-Taylor dynamo [376], consistent with the Geneva models [370]. Our models reproduce the expected trends: rotation increases the luminosity of blue loops across 5–9 $M_\odot$, bringing evolutionary masses into closer agreement with observed Cepheid masses.

8.2.3 Rotation and Mass-Luminosity Relations

Rotation has a direct impact on the mass-luminosity (M-L) relation of Cepheids, as demonstrated in previous work [317, 377]. Figure 8.2 shows evolutionary tracks for stellar models with masses in the range 5–9 $M_\odot$, both with and without rotation. Black solid curves correspond to non-rotating models, while dashed green curves show models with $\Omega/\Omega_{\rm crit} = 0.5$. The inclusion of rotation systematically increases the luminosity of stars during the blue-loop phase, across all masses shown. On the main sequence, rotation lowers the effective temperature and luminosity at a given mass, because the centrifugal force inflates the stellar radius and reduces the effective gravity. In contrast, during the blue-loop phase, rotational mixing leads to a larger helium core and enhanced luminosity at fixed mass. The net result is an upward shift of the M-L relation for Cepheids, consistent with previous findings [377]. Moreover, rotation shortens the duration of the blue loop [377], since the more massive helium core accelerates helium burning. This effect is visible in our models as a reduced extent of the blue loop in the HR diagram for rotating stars.

Figure 8.2 shows the empirical M-L relation for Cepheids, plotting $\log(L/L_\odot)$ versus $\log(M/M_\odot)$, in comparison with our model predictions. We include dynamical mass measurements from Evans et al. [378, 379, 380], as well as the M-L relations reported

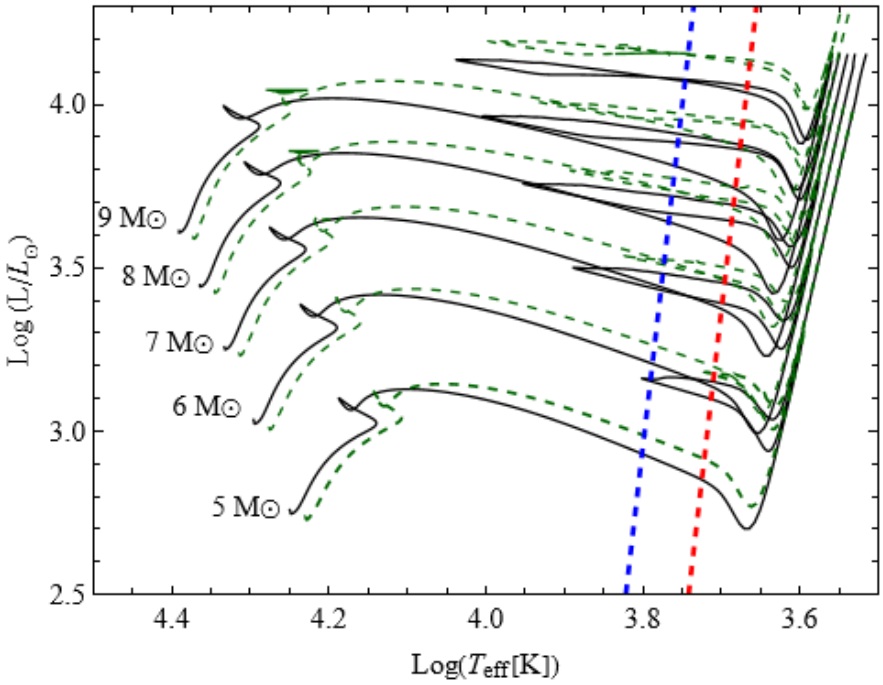


Figure 8.1: HR diagram showing evolutionary tracks for stellar masses 5–9 $M_{\odot}$. Black curves: non-rotating models; dashed green curves: rotating models with $\Omega/\Omega_{\rm crit} = 0.5$.

in [377, 381]. The observed luminosities are derived from Evans et al. [379] and bolometric corrections from [382]. For example, the mass of T Mon is inferred from stellar modeling with $\alpha_{\rm ov} = 0.2$, yielding 9.1 $M_{\odot}$. The mass and luminosity of W Sgr lie on our rotating model M-L relation. The location of AW Per is consistent with models without overshoot and rotation, although observational uncertainties allow for some overlap. For S Mus, our rotating models bring the predicted M-L relation closer to the observed dynamical mass and luminosity.

The M-L relations derived from our simulations are as follows, with and without rotation, for comparison with literature fits (Our fits are on top):

Non-rotating models:

$$\log(L/L_\odot) = (0.636 \pm 0.03) + (3.59 \pm 0.04)\log(M/M_\odot), \tag{8.5}$$

$$\log(L/L_\odot) = 0.72 + 3.35\log(M/M_\odot) + 1.36\log(Y/0.28) - 0.24\log(Z/0.02), \tag{8.6}$$

Rotating models ($\Omega/\Omega_{\rm crit} = 0.5$):

$$\log(L/L_\odot) = (0.539 \pm 0.06) + (3.78 \pm 0.07)\log(M/M_\odot), \tag{8.7}$$

$$\log(L/L_\odot) = (0.712 \pm 0.124) + (3.594 \pm 0.712)\log(M/M_\odot). \tag{8.8}$$

In our non-rotating models $Z = 0.014$ and $Y = 0.268$. Our rotating M-L relation is in excellent agreement with the Geneva model results reported in [377], and the inclusion of rotation improves agreement with observed Cepheid masses and luminosities, especially for S Mus.

8.2.4 Degenerate Solutions and Rotation with Varied Masses

The combined effects of rotation and convective core overshoot can produce degenerate solutions in the Hertzsprung-Russell (HR) diagram: different combinations of initial rotation rate $\Omega/\Omega_{\rm crit}$ and overshoot parameter $\alpha_{\rm ov}$ can yield blue loop evolutionary tracks with similar luminosity and effective temperature. This degeneracy is relevant for interpreting observations of Cepheid variables such as S Mus, whose observed luminosity and effective temperature can be reproduced by both rotating and non-rotating models with different $\alpha_{\rm ov}$. In Figure 8.3, we show evolutionary tracks for a $6\,M_\odot$ model using two different combinations of parameters:

- A non-rotating model ($\Omega/\Omega_{\rm crit} = 0$) with $\alpha_{\rm ov} = 0.2$,

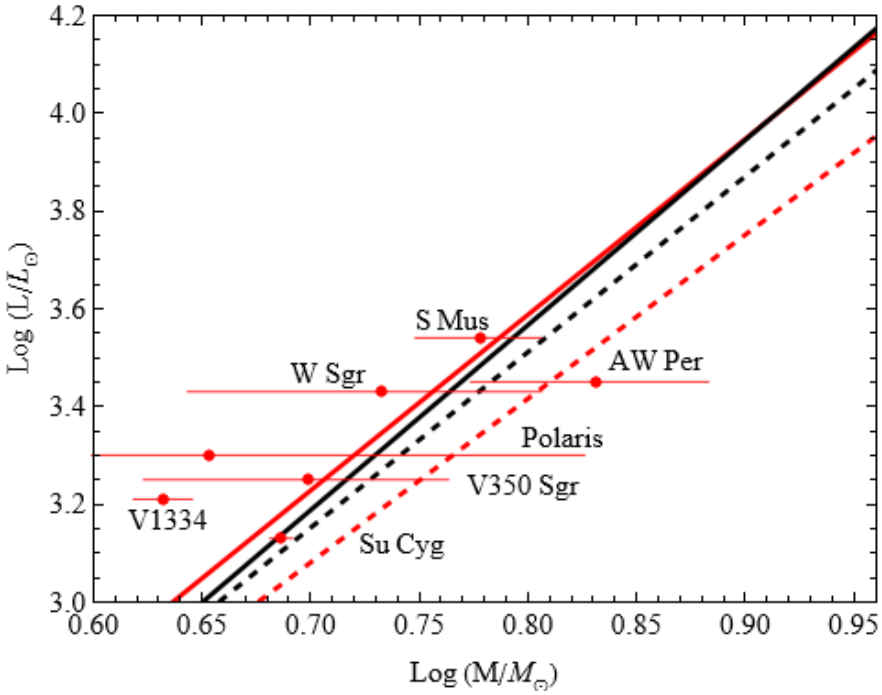


Figure 8.2: A plot of the Log of the luminosity vs mass of the star. Each line represents a Mass-Luminosity relation. Here, the Black solid line represents rotating models from our work; the black dashed line represents non-rotating models, and the Red solid and dashed lines represent literature fits from [377, 381]. The red dots represent observed Cepheids

- A rotating model ($\Omega/\Omega_{\rm crit} = 0.5$) with $\alpha_{\rm ov} = 0.1$.

Both models cross the observed location of S Mus in the HR diagram ($\log L/L_\odot = 3.54$, $T_{\rm eff} \approx 5850$ K), illustrating the degeneracy between overshoot and rotation in determining Cepheid luminosity.

Introducing MCP emission into the models affects this degeneracy. The additional energy loss reduces stellar luminosity and shortens the duration of the blue-loop phase. As shown in Figure 8.3, for the rotating model with $\alpha_{\rm ov} = 0.1$ and $\Omega/\Omega_{\rm crit} = 0.5$, including MCP emission reduces the luminosity sufficiently to no longer match S Mus. Conversely, the non-rotating model with $\alpha_{\rm ov} = 0.2$ remains consistent with S Mus when MCP emission is included.

This behavior provides a powerful means of constraining combinations of $\alpha_{\rm ov}$, $\Omega/\Omega_{\rm crit}$, and MCP coupling. If MCP-induced luminosity suppression is too strong, some combinations of overshoot and rotation will be excluded by the requirement of reproducing observed Cepheid properties. For example, in our $6\,M_\odot$ models, we can exclude the combination $\alpha_{\rm ov} > 0.2$ and $\Omega/\Omega_{\rm crit} > 0.5$ when MCP emission is included at the benchmark couplings studied here.

Degeneracies of this kind emphasize the need to carefully model rotation and overshoot together when using Cepheid observations to constrain BSM physics. Accurate dynamical mass measurements and improved characterization of Cepheid surface abundances can help break these degeneracies.

8.2.5 Wind Mass Loss

Our stellar evolution models incorporate wind mass loss following standard prescriptions. The baseline wind scheme is the `Dutch` wind scheme in MESA, which combines multiple literature prescriptions optimized for different stellar phases [309, 310, 311]. In our models, we tune this scheme to match prior work on Cepheid evolution.

For the red giant branch (RGB), we adopt the Reimers prescription [383], using a scale factor of 0.6 to match empirical RGB mass-loss rates for $5\,M_\odot$ Cepheids, consistent with the MESA test suite and recent literature. For the asymptotic giant branch (AGB), we apply the Blöcker prescription [384] with MESA's default scaling factor of 0.5, noting that the AGB phase is not the focus of this work. For hot stars with $T_{\rm eff} > 11{,}000$ K, we employ the prescription of Vink *et al.* [310].

When considering the effect of rotation on mass loss, we note that many studies implement rotation-enhanced mass-loss prescriptions [385, 375, 371, 386]. While the detailed implementation can vary, our approach follows that of MESA's built-in

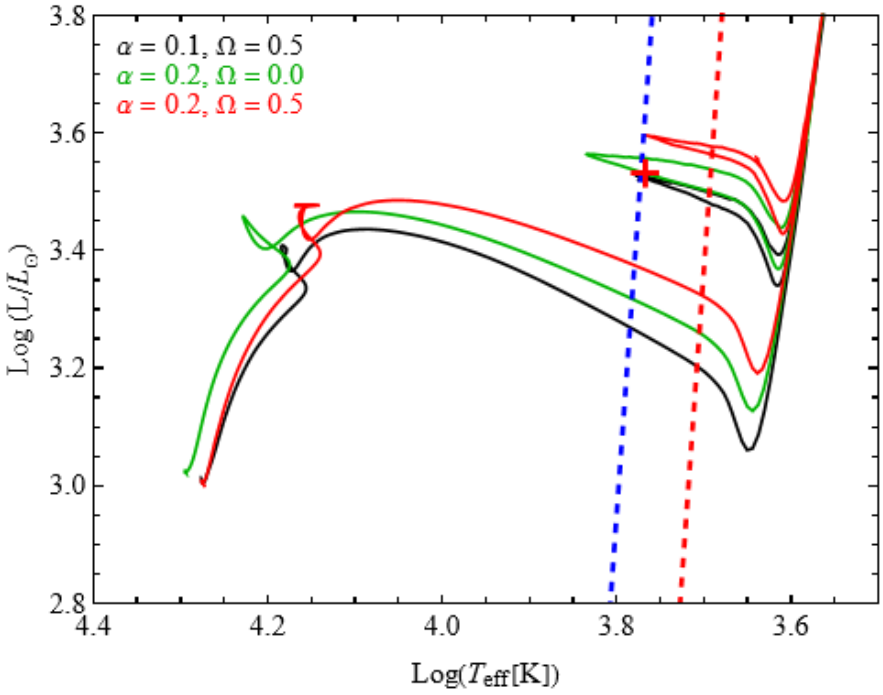


Figure 8.3: HR-diagram of 6 $M_\odot$ models showing varied $\alpha_{\rm ov}$ and $\Omega/\Omega_{\rm crit}$ creating the same observations of S mus. Here the black curve corresponds to $\alpha_{\rm ov} = 0.2$, $\Omega/\Omega_{\rm crit} = 0$ (no rotation). The green curve correspond to $\alpha_{\rm ov} = 0.1$, $\Omega/\Omega_{\rm crit} = 0.5$. The red curve represents $\alpha_{\rm ov} = 0.2$ and $\Omega/\Omega_{\rm crit} = 0.5$. The inclusion of MCP emission shifts the rotating model below the observed luminosity of S Mus (red point), while the non-rotating model remains consistent.

scheme, which is consistent with prior Geneva models [370, 317]. Specifically, we use the following rotation-enhanced mass-loss prescription:

$$\dot{M}(\Omega) = \dot{M}(0)\left(\frac{1}{1-\Omega/\Omega_{\rm crit}}\right)^{\xi}, \tag{8.9}$$

where $\dot{M}(0)$ is the mass-loss rate without rotation, Ω is the surface angular velocity, $\Omega_{\rm crit}$ is the critical angular velocity at the stellar surface, and $\xi = 0.43$ is an empirically motivated parameter [385, 386]. Here, $\Omega_{\rm crit}$ corresponds to the angular velocity at which centrifugal forces would disrupt the star's equatorial surface layers. Including

rotation-enhanced mass loss is important for accurately capturing the angular momentum evolution of intermediate and high-mass stars, and for self-consistency with our rotationally mixed models.

In summary, we adopt well-established mass-loss prescriptions across all evolutionary phases, with rotation-enhanced mass loss treated following MESA defaults and prior literature. These choices ensure consistency with recent modeling efforts on Cepheids and provide a robust baseline for assessing the impact of MCPs on stellar evolution.

8.3 Millicharged Particles

8.3.1 Existing Constraints on Millicharged Particles

Millicharged particles (MCPs) are hypothetical particles carrying a small electric charge ϵe, where $\epsilon \ll 1$. They arise generically in extensions of the Standard Model involving kinetic mixing between the photon and a new massless $U(1)_D$ gauge boson [387], and have been proposed in a range of contexts, from dark matter to hidden sector physics [388, 389].

Experimental searches for MCPs span multiple energy and distance scales. Laboratory-based bounds arise from tests of Coulomb's law [390], beam dump experiments such as SLAC [391], and collider constraints (e.g. from LEP and LHC via monophoton plus missing energy searches). However, for MCP masses below a few hundred MeV, the strongest bounds come from astrophysical and cosmological considerations.

In particular, the energy loss of stars via MCP emission places powerful constraints on the MCP parameter space. The most stringent limits in the mass range $m_\chi \lesssim 100$ keV come from observations of red giants, white dwarfs, and horizontal branch (HB) stars. These stars would cool anomalously fast if MCPs were produced

efficiently in their interiors. The corresponding emissivity scales with the third power of temperature, $\dot{\epsilon}_\chi \propto T^3$, for the regime where MCPs are produced via plasmon decay and escape freely [392, 393]. As a result, the core temperatures of such stars — in the range of 10–100 keV — provide particularly sensitive probes of ϵ.

Recent global fits to stellar energy loss rates, including data from HB and RG stars, yield a robust upper bound on the MCP electric charge:

$$\epsilon \lesssim 2 \times 10^{-14}, \quad \text{for } m_\chi \lesssim 10 \text{ keV}, \tag{8.10}$$

as reported in [393]. This is complemented by X-ray constraints from Sun-like stars and solar modeling, which place slightly weaker bounds but remain competitive [394].

For larger masses $m_\chi \gtrsim 100$ keV, MCPs are not efficiently produced in low-mass stellar cores, and the corresponding stellar bounds become weaker. In this mass range, constraints from early universe cosmology and the Cosmic Microwave Background (CMB) become dominant, particularly from spectral distortions and limits on extra relativistic degrees of freedom (e.g., $N_{\rm eff}$). CMB constraints require MCPs to decouple before Big Bang Nucleosynthesis (BBN), yielding $\epsilon \lesssim 10^{-8}$–$10^{-10}$ for MeV-scale masses [392, 395].

Our work focuses on an intermediate region of parameter space, where millicharged particles can be produced inside the cores of Cepheid stars via plasmon decay. These stars have core temperatures $T_c \sim 1$–3×10^8 K, or ~ 10–30 keV, placing them within the window of maximum sensitivity to MCPs with $m_\chi \lesssim 100$ keV. While the HB and RG constraints dominate globally, Cepheids provide a unique test environment because their luminosity and evolutionary timescale are tightly constrained by observation. As we demonstrate below, this allows us to derive complementary and competitive

constraints on MCP production using their impact on the luminosity and lifetime of the blue-loop phase.

8.3.2 MCP Models and Plasmon Decay

The main contribution to mcp production in the stellar medium is from the decay of plasmons. We follow the [396, 397, 398] for the calculation of plasmon distributions and the decay rate.

The mcp particle χ is introduced with the Lagrangian

$$\mathcal{L} \supset q_\chi e \bar{\chi} \gamma_\mu \chi A^\mu + \bar{\chi} \left(i\partial - m_\chi \right) \chi \tag{8.11}$$

The electric charge $q_\chi \ll 1$ suppresses the decay width of the production process $\gamma^* \to \chi\bar{\chi}$ from a plasmon γ^*. In the dense Cepheid medium, photons gain a plasmon mass due to the interaction with the electron distribution

$$\omega_p^2 = \frac{4\pi\alpha n_e}{\sqrt{p_{\rm F}^2 + m_e^2}} \tag{8.12}$$

with $p_{\rm F} = (3\pi^2 n_e)^{1/3}$ the Fermi momentum, which consistently taking into account the degeneracy of electrons. The plasmon properties is studies in [399] with approximations valid up to the wavenumber scale $k_{\rm max} \simeq \mathcal{O}(\omega_p)$.

The on-shell decay process dominates the mcp production when the medium plasmon mass is larger than twice the mcp mass $\omega_p \geq 2m_\chi$. The mcp production rate per unit mass is ϵ_χ for transverse plasmon decay,

$$\epsilon_\chi = \frac{q^2 e^2}{6\pi^2 \rho} \sqrt{1 - \frac{4m^2}{\omega_p^2}} (\omega_p^2 + 2m^2) \int \frac{k^2 dk}{1 - e^{\omega/T}}, \tag{8.13}$$

and for the longitudinal plasmon decay

$$\epsilon_\chi = \frac{q^2 e^2 \omega_p^2}{12\pi^2 \rho} \int k^2 dk \sqrt{1 - \frac{4m^2}{\omega_p^2 - k^2}} \frac{\omega_p^2 - k^2 + 2m^2}{(\omega_p^2 - k^2)(1 - e^{\omega/T})}. \tag{8.14}$$

Note in Eq. 8.13 and Eq. 8.14, the plasmon is assumed to be on-shell and the integral of wavenumber k is bounded by the dispersion relations.

In the case of heavier mcps or the outer region of the star, $\omega_p < 2m_\chi$, the mcp production is through the off-shell plasmon process, which is suppressed by the density of off-shell plasmons in the medium [400]. The off-shell plasmon contribution is mainly determined by its self-energy in the medium, whose real part set the plasmon dispersion and the imaginary part originates from the damping of plasmons due to scattering (mostly Thomson scattering).

The overall production rate depends highly on the temperature and electron density profiles. The total rate peaks at $\omega_p = 2m_\chi$ due to the on-shell decay, while the off-shell plasmon decay rate is kinematically/Boltzmann suppressed.

8.3.3 Implementing mcp production in MESA

We introduce approximations of the integral of plasmon phase space, and obtain analytic expressions for the mcp production in different scenarios for the `MESA` stellar simulation.

In the case of heavy plasmon mass that enable the efficient on-shell decay production, $\omega_p \geq 2m_\chi$, we find the approximation depends on the stellar medium temperature, and the plasmon polarization. For transverse modes, we find

$$\epsilon_\chi \simeq \frac{q^2e^2}{6\pi^2\rho}\sqrt{1-\frac{4m^2}{\omega_p^2}}(\omega_p^2+2m^2)\times\begin{cases}2\zeta(3)T^3, & \omega_p < T\\ \\ T^3\left(1+\frac{1}{2}\frac{\omega_p}{T}+\frac{3}{8}\left(\frac{\omega_p}{T}\right)^2\right)e^{-\frac{\omega_p}{T}}, & \omega_p > T\end{cases} \tag{8.15}$$

For the longitudinal modes, we find the approximation

$$\epsilon_\chi \simeq \frac{q_\chi^2e^2\omega_p^2}{12\pi^2\rho}\frac{1}{1-e^{\omega_p/T}}\left[\frac{1}{3}(\omega_p^2-4m^2)^{3/2}+\frac{m^4}{\omega_p}\ln\left|\frac{\omega_p+\sqrt{\omega_p^2-4m^2}}{\omega_p-\sqrt{\omega_p^2-4m^2}}\right|-\frac{m^2}{2}\sqrt{w_p^2-4m^2}\right] \tag{8.16}$$

In our `MESA` simulations, we only include the on-shell decay since it dominated the mcp production rate. Therefore, our results impose conservative constraints on mcp mass below half of the plasmon frequency, while future simulations including the complete off-shell decay will refine the limits.

We find that the integral approximation has an error of less than 2% (typically $\mathcal{O}(0.1\%)$) throughout the evolution process up until the mid to late AG phase.

We use the steps below to justify the approximation: (1) simulate in MESA with Eq.8.15 and 8.15; (2) save the star profile and emission rate calculated within MESA; (3) use the star profile to calculate Q_χ with complete expression; (4) compare the rates calculated analytically and the ones with MESA. (5) We need to make sure the deviations (approximation of on-shell, and also the neglect of off-shell contribution) are less than MESA uncertainties, for example, the temperature difference between cells (below 0.1% in axion simulations).

8.4 Results

In Fig. 8.4 we plot evolutionary tracks for a mass range of $4 - 9M_{\odot}$ with $\alpha_{\rm ov} = 0.1$ above the Hydrogen core and $\alpha_{\rm ov} = 0.1$ below and above the Hydrogen burning shell. All presented models have no rotation. Models are stopped midway through AGB stage since we're only interested in the blue loop stage. We remain agnostic about the coupling we choose. We use $q = 2.9 \times 10^{-13}$ and $m_{\chi} = 25$eV to eliminate the blue loops of the majority of the models. When we increased the fractional charge from 1.63×10^{-13} to 2.9×10^{-13} more massive models disappear first while lower mass models, e.g. 5 & $6M_{\odot}$, appear to be incentive to the increase energy loss from axions. Other major periods of evolution appear unchanged, e.g. MS, RG, and AGB stages, when increasing the coupling. The MCPS in our scenario are free streaming and leave the star.

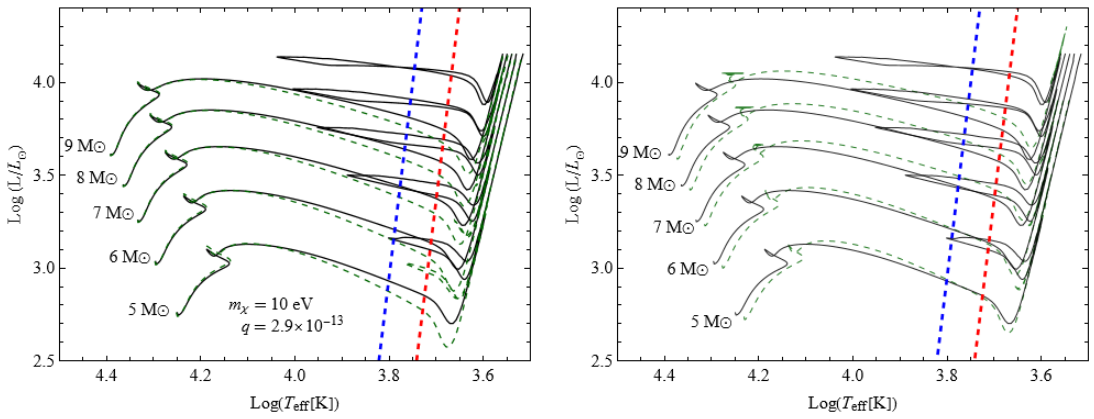


Figure 8.4: Left panel: Left panel shows varied mass without rotation with mcps included (dashed green) and without mcps (Black). The MCPs charge and mass are listed on the plot. The right panel includes MCPS with $\Omega_{crit} = 0.5$ (Dashed green curve), and the black curve represents no MCPS and no rotation. Mcps in the case above are for on-shell only.

Mass ($M_\odot$)	$\Omega_{crit,i}$	m_χ (eV)	q (10^{-13})	Blue Loop?
9	0	10	1.64	no
9	0	0.1	1.63	no
9	0	1	1.63	no
9	0	10	1.63	yes
9	0	100	1.63	no
9	0	1	1.5	yes*
9	0.5	10	1.0	yes
9	0.5	10	1.3	no
10	0	10	0.9	no
10	0.5	10	0.7	no
10	0.5	10	0.5	yes

Table 8.1: The table presents data on the mass and coupling constraints for mcps with masses of $9M_\odot$ and $10M_\odot$. The column titled "Blue Loop?" Describes whether the blue loop existed (yes) or was eliminated (no). (yes*) implies 5-9 $M_\odot$ masses where checked to see if blue loop existed.

We varied mcp parameters near the point of elimination of the blue loops for 9 $M_\odot$ and 10 $M_\odot$ as shown in Table 8.1. We found that the varying m_χ from 0.1 to 100 eV leaves q unchanged when eliminating the blue loop. This is shown by the sampling of the 9 $M_\odot$ models for $q = 1.63 \times 10^{-13}$ in the table. This result is similar to the bottom of the figure shown in the MCP section in Chapter 2. Figure 8.5 shows the elimination of the blue loop by increasing the q value for a 9 $M_\odot$ model from the table. It is clear in Table 8.1 that increasing the mass of the Cepheid leads to greater constraint on q. A similar correlation between mass and coupling was found for the axion coupling in our previous work [351].

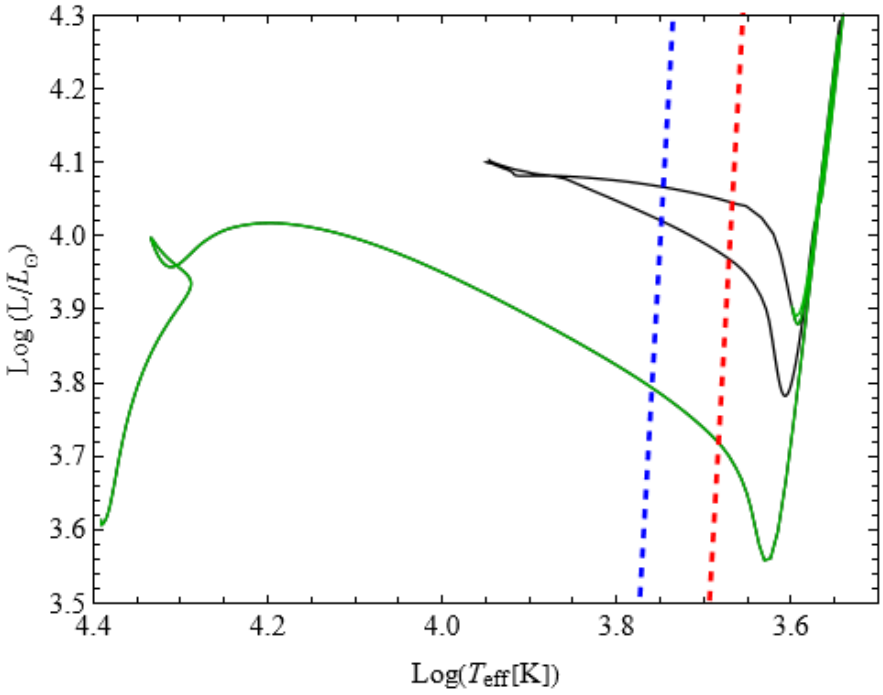


Figure 8.5: HR diagram constraining mcp mass and charge. Black line is for m = 10eV and $q_{13} = 1.63$ and red line is for the same mass, but $q_{13} = 1.64$

Non-rotating models with MCPs:

$$\log(\mathrm{L}/\mathrm{L}_\odot) = (0.568 \pm 0.017) + (3.65 \pm 0.02)\mathrm{Log}(\mathrm{M}/\mathrm{M}_\odot), \tag{8.17}$$

Rotating models with MCPS:

$$\log(\mathrm{L}/\mathrm{L}_\odot) = (0.359 \pm 0.024) + (3.97 \pm 0.03)\mathrm{Log}(\mathrm{M}/\mathrm{M}_\odot). \tag{8.18}$$

Equations 8.17-8.18 represent the linear fits shown in the Mass-Luminosity plot of Figure 8.6 (Mcps solid green and green dashed lines). This plot is similar to figure 8.2. Unlike the previous plot, where we are trying to eliminate the blue loop, in Figure 8.6 we include mcps but do not eliminate the blue loop. This leads to a slightly stronger constraint on the coupling. The inclusion of mcps lowers the luminosity of the star when

it enters the RGB stage and results in a lower luminosity during the Blue loop stage. The dashed green line shows that with no rotation, mcps leads to an overall decrease in luminosity. This gives the impression that the mass of the star has increased. Using S Mus as an example, this puts mcps without rotation outside the uncertainty of S Mus. This leads to a larger mass discrepancy between the observed mass of S Mus.

The inclusion of rotation brings us closer to the observed mass of S Mus as discussed above. With the inclusion of mcps this lowers the luminosity and gives the impression of increased mass of the stars. We note that at higher masses, the inclusion of mcps does not affect the luminosity as it does for lower masses. One possible reason could be the critical rotation rate is reached when the star has an isothermal core and is moving towards the red giant branch. This happens for both the

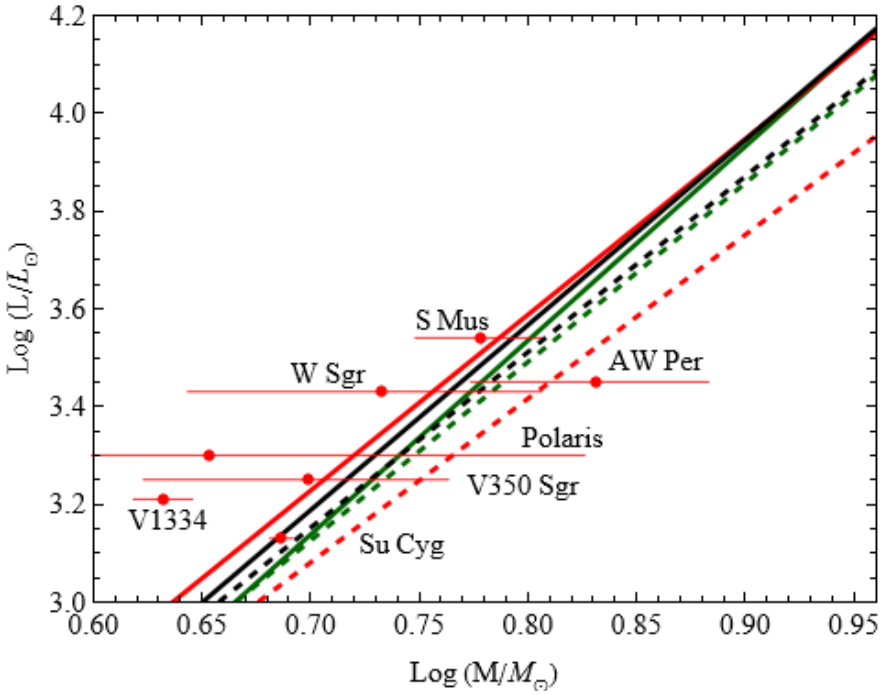


Figure 8.6: Mass-Luminosity plot similar to Figure 8.2, including no rotation and the mcps green dashed line, as well as the mcps solid line. The mcp mass was set 25 eV and charge $q_{13} = 2 \times 10^{-13}$ for models 5-8$M_{\odot}$ and $q = 1.6 \times 10^{-13}$ for model 9$M_{\odot}$

We showed in our previous work that the increase in the mass of a cepheid puts a stronger constraint on BSM physics. T Mon does exist in a binary system though its orbital period is long and observations of it's companion mass is still need to be determined We stress a dynamical mass measurement of this Cephied would provide greater constraints for our work.

Chapter 9

Conclusions

In this work, we investigated populations of primordial black holes (PBHs) and their potential formation mechanisms as solutions to long-standing problems in physics. In Chapter 3 we presented a model producing both light PBHs ($M < 10^{15}$ g) and heavy PBHs. This framework addressed baryogenesis and the origin of dark matter. In our scenario, a population of light PBHs formed from scalar curvature perturbations and evaporated before Big Bang Nucleosynthesis. These PBHs produced a particle X with CP-violating decays, characterized by the parameter $\gamma \sim 10^{-2}$, which generated the matter–antimatter asymmetry of the Universe. Combining light PBH-induced baryogenesis with dark matter offered a possible explanation of the dark matter-baryon coincidence problem. The signature is a double-peaked stochastic gravitational-wave background in the MHz–GHz range, potentially detectable by future detectors.

In Chapter 4 we considered dark matter in the form of a fermionic particle χ that is produced from evaporating PBHs. We compared two PBH formation mechanisms: scalar perturbations and first-order phase transitions. We explored the associated gravitational wave background for PBH formation in the MHz-GHz frequency range and its connections to the properties of the DM particles produced by Hawking evaporation. The target frequency window of GWs is basically determined by the formation mechanism of PBHs. A 100% trapping scenario was assumed for PBH formation inside false-vacuum pockets. We found no significant difference in the production of χ with respect to PBH mass or temperature between the two formation channels. However,

the associated gravitational-wave background did differ: first-order phase transitions produced a weaker characteristic strain.

In Chapter 5 we explored a novel scenario in which a dark sector consisting of a scalar ϕ and a fermion χ is recycled by a first-order phase transition into PBHs, which then evaporate back into the dark sector. Here, 100% trapping was not assumed, but under suitable initial conditions most of the dark sector could still be confined in the false pockets. This led to the generation of ultra-heavy dark sector particles. In recycling the dark sector is initially in kinetic equilibrium with the Standard Model. Then the dark sector undergoes a FOPT, and the DM candidates acquire a mass much larger than their temperature. They therefore get trapped in the false vacuum. For FOPTs at high temperatures, the formed PBHs are light enough to evaporate before BBN and escape all the cosmological constraints.

In the last two chapters (7–8), we used MESA models of Cepheid variables to constrain the axion–photon coupling and the millicharged particle coupling. We found that higher-mass Cepheids are more sensitive to additional energy loss, leading to stronger constraints on both couplings. We examined the impact of varying the convective overshoot coefficient and the axion–photon coupling constant, noting that overshoot significantly alters the resulting constraints. The trend, however, is not monotonic; increasing or decreasing overshoot can affect the coupling bounds in nontrivial ways. We compared these results with observational data from the Cepheid S Mus. The $6.6\,M_\odot$ model with $\alpha_{\rm ov} = 0.0$ provided the tightest bound, though this lies outside the observational mass constraint of $6.4\,M_\odot$ for S Mus.

We then incorporated both rotation and overshoot when investigating the coupling and mass of millicharged particles. Using the Cepheid mass discrepancy problem, we constrained the MCP coupling constant. Unlike axions, which suppress the blue loop entirely, MCPs reduce its luminosity, thereby increasing the discrepancy between

observed and modeled Cepheid masses. By including both rotation and overshoot, we assessed how MCP energy loss affects the mass–luminosity relation, providing new bounds on the coupling.

Looking forward, future work will extend MESA modeling to include Cepheid pulsation periods, enabling additional constraints via the period–luminosity and period–radius relations, both of which are tightly constrained by observations. Since the period–luminosity relation is fundamental to Hubble constant determinations, even small changes due to exotic couplings would have significant implications. Another promising direction is the construction of a finer grid of stellar models probing the parameter space $\{\alpha_{\rm ov}, \Omega, g_{10}, M\}$ for axions or $\{\alpha_{\rm ov}, \Omega, m_\chi, M\}$ for MCPs, to yield sharper constraints. Other avenues include exploring superradiance as a mechanism for particle production in the early Universe.

The future detection of PBHs, the stochastic gravitational-wave background, or stellar signatures of new particles will be decisive. Confirming the existence of PBHs through gravitational-wave observations would mark a breakthrough, while null results would increasingly constrain the PBH mass–abundance parameter space. Upcoming data from Gaia DR4 may reveal more massive Cepheids, tightening bounds on axion–photon and MCP couplings. Together, these developments could usher in a new era for our understanding of dark matter, baryogenesis, and fundamental particle physics.

Appendix A

A Possible Inflaton Potentials for Multimodal PBH Distributions

The formation of PBHs is exponentially sensitive to the ratio of the density perturbation to the critical density. This implies that modulations to the primordial power spectrum can have a drastic effect on the mass function. In particular, multimodal PBH mass functions have been discussed in three broad classes of UV settings: (*i*) specific features of the inflaton potential that induce distinct phases of ultra slow-roll, such as multiple inflection points [25, 26, 90, 27, 91, 92]; (*ii*) oscillatory features in the primordial spectrum emanating from the ambiguity in defining the vacuum state inflation [401], [144]; and (*iii*) oscillatory features in the speed of sound during inflation [141]. Of these, only the option of multiple ultra slow-roll phases is able to achieve multiple peaks separated by a large hierarchy in frequencies, as is required in our case.

For completeness, we briefly provide a road map for achieving multiple ultra slow-roll phases at the level of an effective description of the scalar potential. A generic potential for a scalar field ϕ can be characterized as

$$V(\phi) \,=\, V_0 \sum_n c_n \left(\frac{\phi}{\Lambda}\right)^n , \tag{A.1}$$

where V_0 is the overall scale of the potential, c_n are tunable coefficients, and Λ is a cutoff scale. Requiring j inflection points imposes the following conditions on $V(\phi)$:

$$V'(\phi_i) \,=\, 0,\; V''(\phi_i) \,=\, \alpha_i \sim 0, \qquad \forall\; i = 1 \ldots j\;. \tag{A.2}$$

Here, the α_i denote values of the second derivatives of the potential at the ϕ_i. The set $\{\phi_i, \alpha_i\}$ can be tuned to the specific values needed by the model of interest by choosing the coefficients c_n.

The values of $\{\phi_i, \alpha_i\}$ are set by requiring PBH formation during multiple stages of ultra slow-roll at different k-modes. The conditions for PBH formation can be obtained by starting with the evolution of the background. The FRW and scalar field equations are given by

$$\begin{aligned} H^2 &= \frac{1}{2}\dot{\phi}^2 + V(\phi), \\ \ddot{\phi} &+ 3H\dot{\phi} + V'(\phi) = 0. \end{aligned} \tag{A.3}$$

Here, the dots refer to derivatives with respect to time, while the prime refers to derivatives with respect to ϕ. The number of e-foldings is given by $dN = Hdt$.

The slow-roll parameters are given by

$$\epsilon_H = -\frac{\dot{H}}{H^2}, \qquad \eta_H = -\frac{\ddot{H}}{2H\dot{H}}. \tag{A.4}$$

The power spectrum is given by

$$\mathcal{P}_\mathcal{R}(k) = \frac{1}{8\pi^2}\frac{H^2}{\epsilon_H}. \tag{A.5}$$

We note that Eq. (A.5) underestimates the power spectrum and to obtain the precise value, one needs to numerically solve the Mukhanov-Sasaki equations. However, Eq. (A.5) is sufficient to understand the qualitative behavior of the power spectrum. The requirement for PBH formation with masses $M_{\rm LPBH} = 10^3$g and $M_{\rm HPBH} = 10^{18}$g is

$$\mathcal{P}_\mathcal{R}(k) \gtrsim 10^{-2} \quad \text{at} \quad \log_{10} k \sim \{14.1, 21.6\}\ . \tag{A.6}$$

Eq. (A.6) is easily satisfied for choices of $\{\phi_1, \phi_2, \alpha_1, \alpha_2\}$, which in turn can be attained by choices of c_{2-6}. One option is to perform a scan at the level of the coefficients c_{2-6} to obtain the dynamics one needs.

A more structured algorithm has been advanced recently in the form of reverse engineering the inflaton potential given the shape of the power spectrum [25, 90]. In this approach, one would start from the conditions in Eq. (A.6), and work out the evolution of $H(k)$, $\epsilon_H(k)$ and $\eta_H(k)$, ultimately trading these dependencies to obtain $V(\phi)$. This can be done either working with functions of the comoving wave number k or the number of e-foldings, in which case Eq. (A.6) roughly translates to the condition $\mathcal{P}_{\mathcal{R}}(N) \sim 10^{-2}$ at $N \sim 33$ and $N \sim 49$. We leave a full reconstruction and study of the inflaton potential corresponding to our scenario for future work.

Appendix B

B GW Spectrum for a Smoother Power Spectrum

In this Appendix, we display the smoother power spectrum employed to obtain Fig. 3.4 of the main text. In particular, we start with a power spectrum that is displayed on the top left panel of Fig. A.1[1]. The power spectrum is chosen to have peaks at $k = 10^{21}$ Mpc^{-1} corresponding to $f_{\rm GW}^{\rm peak} = 1.5$ MHz. The corresponding PBH mass is $M_{\rm LPBH} = 10^4$ g. The power spectrum is taken to have a k^4 rise and fall for each side of the peak, following the results of [402]. We note that the results will not change qualitatively for other power-law behaviors.

[1]While a smoothed power spectrum captures the most important features of the original delta-function power spectrum, we modify the peak location by a factor of 1.5 and the peak amplitude by a factor of 2, in order to reproduce the PBH mass function.

The PBH mass function corresponding to our power spectrum is shown in the top right panel of Fig. A.1. On the bottom panels, we display the resulting GW spectrum. We note that in contrast to the GW spectrum depicted in Fig. 3.8 resulting from the delta function power spectrum, the peaks in the GW spectrum are smoother.

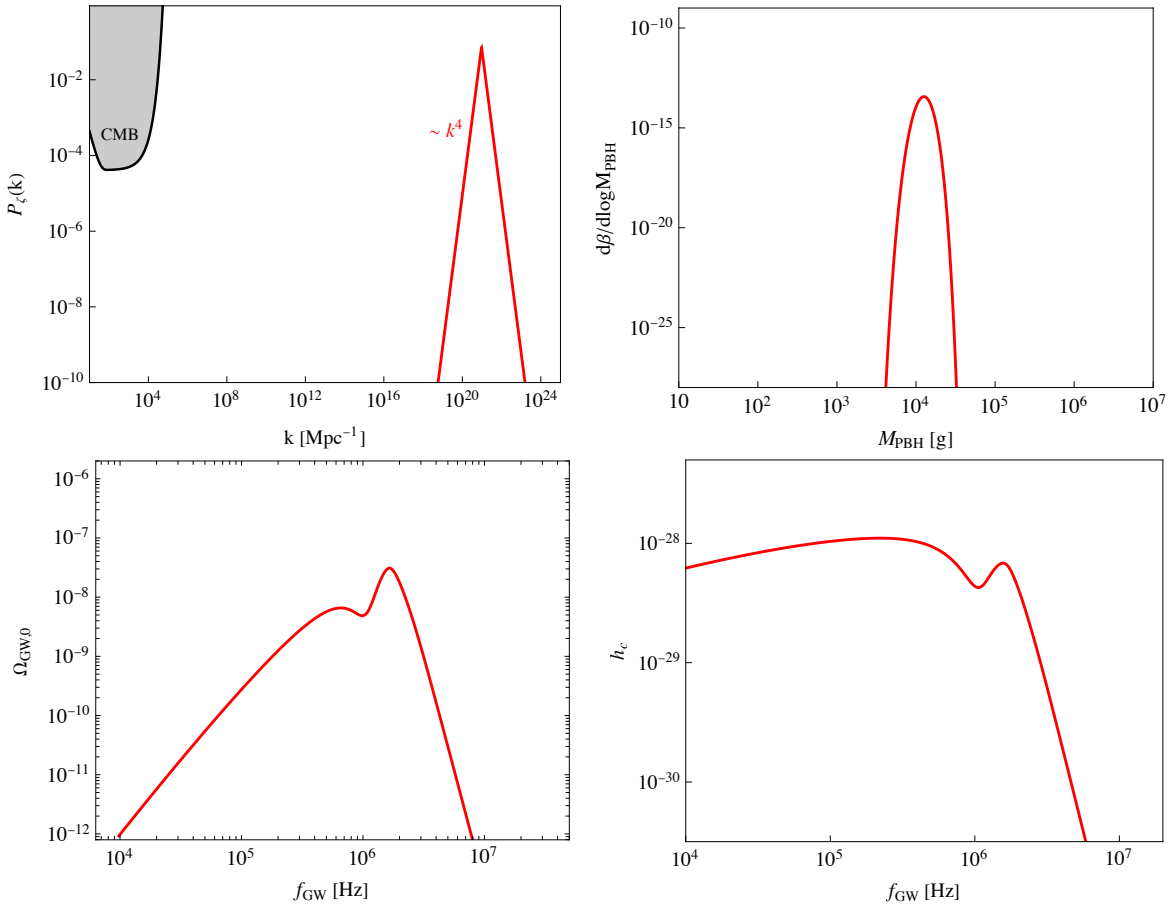


Figure A.1: *Top-left panel*: Example power spectrum with k^4 scaling and peaks located at $k = 10^{21}$ Mpc^{-1} corresponding to $f_{\rm GW}^{\rm peak} = 1.5$ MHz. The corresponding PBH masses is $M_{\rm PBH} = 10^4$ g. The amplitude of the power spectrum is chosen for the abundance of PBHs. *Top-right panel*: The PBH mass function at formation time. *Bottom-left panel*: The energy density of induced GW signal. *Bottom-right panel*: The strain strength of induced GW signal.

Appendix C

C Models of Baryon Asymmetry Production from X Decay

There are many possibilities for baryogenesis model-building once the species X has been produced by Hawking radiation. Here, we give two examples with a supersymmetric embedding. Both break $B-L$ symmetry. Since the DM in our scenario is comprised primarily of PBHs, the lightest neutralino is not required to reproduce the observed relic density or even be stable. Although not the focus of our work, this can open up considerable freedom in the supersymmetric model-building side.

C.1 Model 1: Multiple (≥ 2) Flavors of Gauge Singlets X_α

We consider the Minimal Supersymmetric Standard Model (MSSM) extended with the following superfields: a single flavor of iso-singlet color triplets N, $\bar{N}$ and at least two flavors of singlets X_α. The superpotential of the theory is given by the MSSM superpotential along with

$$W_{\text{extra}} = \lambda_{i\alpha} X_\alpha u_i^c N + \lambda'_{ij} d_i^c d_j^c \overline{N} + \frac{M_\alpha}{2} X_\alpha X_\alpha + M_N N \overline{N} \,. \tag{A.7}$$

The interference between tree-level and one-loop self-energy and vertex diagrams result in a baryon asymmetry (for $M_\alpha > M_N$). For $X_\alpha \to N^* u_i^{c*}$ decay (with X_α being the fermionic component of the X superfield), the asymmetry generated is

$$\gamma_{CP} = \frac{\sum_{i,j,\beta} \text{Im}\left(\lambda_{i\alpha}\lambda^*_{i\beta}\lambda^*_{j\beta}\lambda_{j\alpha}\right)}{24\pi \sum_i \lambda^*_{i\alpha}\lambda_{i\alpha}} \left[3\mathcal{F}_S\left(\frac{M_\beta^2}{M_\alpha^2}\right) + \mathcal{F}_V\left(\frac{M_\beta^2}{M_\alpha^2}\right)\right], \tag{A.8}$$

where

$$\mathcal{F}_S(x) = \frac{2\sqrt{x}}{x-1} \quad , \quad \mathcal{F}_V = \sqrt{x}\,\ln\left(1+\frac{1}{x}\right). \tag{A.9}$$

The extra factor of 3 in the denominator compared to standard expressions for the asymmetry in leptogenesis appears due to the final state having baryon number $+1/3$. The factor 3 in the self energy contribution $\mathcal{F}_S$ comes from the sum over colors in intermediate states. The total asymmetry in this model can be obtained by summing up over contributions from scalar and fermionic components of all flavors of X, and the desired baryon asymmetry can be obtained by suitable choices of the couplings $\lambda_{i\alpha}$.

C.2 Model 2: Multiple (≥ 2) Flavors of Iso-singlet Color Triplets X_α

A different variation is the case where the MSSM is extended by the following fields: ≥ 2 flavors of iso-singlet color triplets $X_\alpha,\ \bar{X}_\alpha$ which have hypercharges $+4/3, -4/3$ respectively; and a field N that is a singlet under the SM gauge symmetry, but may be charged under a larger gauge group. The superpotential for the augmented sector is W_{extra}, where

$$W_{\text{extra}} = \lambda_{i\alpha} N u_i^c X_\alpha + \lambda'_{ij\alpha} d_i^c d_j^c \overline{X}_\alpha + \frac{M_N}{2} NN + M_\alpha X_\alpha \overline{X}_\alpha\ . \tag{A.10}$$

Here $i,\ j$ denote MSSM flavor indices with color indices suppressed. The couplings $\lambda'_{ij\alpha}$ are antisymmetric under $i \leftrightarrow j$. The fermionic components of N and $X,\ \bar{X}$ are assigned charges $+1$ and -1, respectively, under R-parity. While this ensures R-parity conservation, this is not strictly required since we do not demand that the lightest supersymmetric particle constitutes the majority of DM. We denote by $X_\alpha,\ \psi_\alpha,\ \bar{X}_\alpha,\ \bar{\psi}_\alpha$

the scalar and fermionic components of the superfields X_α. Scalar components of a given flavor have mass eigenvalues given by

$$m_\alpha^2 = |M_\alpha|^2 + \tilde{m}_\alpha^2 \pm |B_\alpha M_\alpha|, \tag{A.11}$$

where $\tilde{m}_\alpha$ is the soft mass of scalars and B_α is the B-term associated with the superpotential mass term $M_\alpha X_\alpha \bar{X}_\alpha$.

The baryon asymmetry obtained in this model can be obtained as follows. For simplicity, we consider two flavors of color triplets, which is the minimum number required to obtain an asymmetry, and focus on decays with supersymmetry conserving interactions. For the fermionic component ψ_1, the relevant decay modes (if kinematically allowed) are $\bar{\psi}_1 \to d_i^{c*} \tilde{d}_j^{c*}$, with $\Delta B = +2/3$, and $\bar{\psi}_1 \to \tilde{N} u_k^c,\ N \tilde{u}_i^c$ for which $\Delta B = -1/3$. Here $N, \tilde{N}$ are the fermionic and scalar components of the superfield N. The interference between the tree-level decay diagram and the one-loop self-energy diagram results in a baryon asymmetry from $\bar{\psi}_1$ and $\bar{\psi}_1^*$ decays (if $M_1 > M_N$) as follows:

$$\epsilon_1 = \frac{1}{8\pi} \frac{\sum_{i,j,k} \mathrm{Im}\left(\lambda_{k1}^* \lambda_{k2} \lambda_{ij1}'^* \lambda_{ij2}'\right)}{\sum_{i,j} \lambda_{ij1}'^* \lambda_{ij1}' + \sum_k \lambda_{k1}^* \lambda_{k1}} \mathcal{F}_S\left(\frac{M_2^2}{M_1^2}\right), \tag{A.12}$$

where, for $M_2 - M_1 > \Gamma_{\bar{\psi}_1}$,

$$\mathcal{F}_S(x) = \frac{2\sqrt{x}}{x-1}. \tag{A.13}$$

This is similar to the result in standard leptogenesis [403] with the difference that in this model there are no vertex diagrams. The same asymmetry is obtained from ψ_1 and ψ_1^* decays, since $\bar{\psi}_1$ and ψ_1^c constitute a four-component spinor with hypercharge $-4/3$. The same asymmetry is also obtained from the decay of scalars $X_1,\ \bar{X}_1$ and their antiparticles $X_1^*,\ \bar{X}_1^*$, in the limit of unbroken supersymmetry; when supersymmetry is broken the asymmetries from scalar and fermion decays are similar if their masses

are similar, $m_{1,2} \sim M_{1,2}$. For $M_2 > M_N$ scalar and fermionic components of $X_2, \bar{X}_2$ will decay to produce an asymmetry ϵ_2, which can be obtained from the expression for ϵ_1 with $1 \leftrightarrow 2$. The total asymmetry in this model can be obtained as $\epsilon_1 + \epsilon_2$.

Appendix D

D Constraints from $12M_\odot$ Models: Prospects and Challenges

Given the fact that constraints on axions are projected to be very powerful for a $12M_\odot$ model, we make a few brief comments about the prospects of converting such bounds into reality.

Firstly, although Cepheids of such mass have not been confirmed through dynamical methods, there are tentative indications that such candidates may have appeared in Gaia data, with masses determined by pulsation models. In particular, we comment on the treatment of [302], where nonlinear convective pulsation models were developed for a wide selection of stellar input parameters, and then applied to a sample of the Gaia DR2 Galactic Cepheids database. Mass-dependent Period-Wesenheit relations in the Gaia bands were derived, which enables mass-dependent estimates of individual distances, and hence, after matching with astrometric distances, individual masses of Cepheids. The DR2 sample peaked at $5.6M_\odot$ and $5.4M_\odot$ for variables pulsating in the fundamental and first overtone modes, respectively. After parallax offset, the peaks moved to $5.2M_\odot$ and $5.1M_\odot$, respectively. In both cases, at least one candidate with mass $12M_\odot$ was obtained, as can be seen from Fig. 2 of [302]. These trends broadly match earlier studies of Galactic Cepheids using Gaia DR2, for example that of [303].

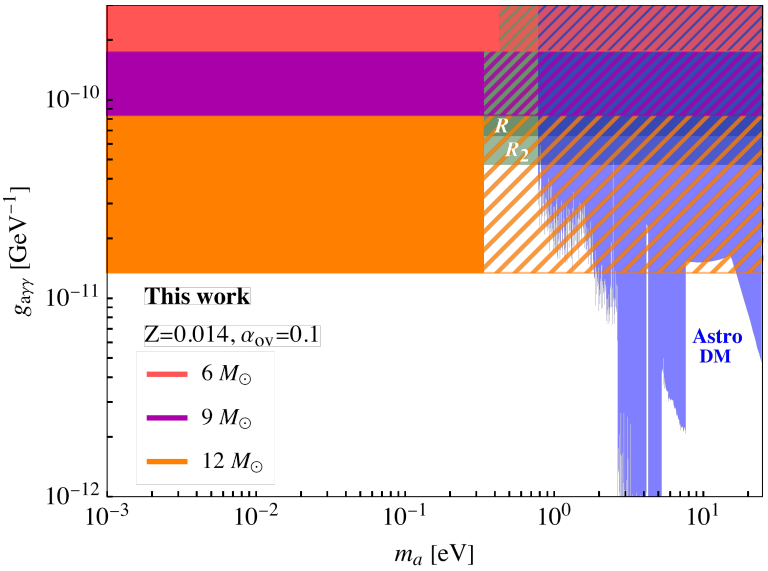


Figure A.2: The constraints on the plane of $(g_{a\gamma\gamma}, m_a)$ for a fixed value of $\alpha_{\rm ov} = 0.1$, $Z = 0.014$, and three stellar models: $6M_\odot$ (red), $9M_\odot$ (purple), and $12M_\odot$ (orange). The constraints on the coupling are obtained from the violation of Eq. 7.2. The range of m_a depicted by hatched regions corresponds to values smaller than the star's lowest core temperature (where the majority of axion production occurs), while the range shown by shaded regions is smaller than the lowest temperature across the entire stellar profile. The constraints from the $12M_\odot$ model are obtained from Eq. 7.28 and correspond neither to an actual observed candidate with dynamically determined mass, nor to a simulation. We also show existing constraints from the stellar R-parameter (green) [294] and R_2-parameter (light green) [295], as well as astrophysical axion dark matter searches (blue, "Astro DM") [333, 334, 335, 336, 337, 338, 339]. The constraints are obtained from [62].

Of course, it is important to issue the appropriate caveats here. We reiterate that the mass estimate by [302] is not conclusive since it is based on 1-d pulsation models. Similarly, the "calibration" with the results from [303] is done for much lower stellar masses. Moreover, neither the models predict loops, as we discuss below.

If one were to take the observation of a $12M_\odot$ Cepheid as a given, there are still two obstacles to obtaining a trustworthy bound on axions. The first, and most important one, is that we were unable to simulate a blue loop for such a model in `MESA` even in the absence of an axion, let alone study the effects of axion emission in such models. For

the $12M_\odot$ model, the inability to obtain a blue loop persists even for $\alpha_{\rm ov} = 0.0$. For a $10M_\odot$ or $11M_\odot$ model, on the other hand, blue loops cannot be obtained for $\alpha_{\rm ov} = 0.1$, although they can be obtained for $\alpha_{\rm ov} = 0.0$. As we noted previously, this appears to be a general feature of current stellar evolution codes, including the Cambridge STARS code [323]. At this conjuncture, we are unable to resolve this problem. The second obstacle is that the pulsation models may themselves be affected by axion emission. This obstacle offers a promising route to study axions that instead relies on their effects on pulsation, rather than their effects in curtailing the blue loop itself. This is left for future work.

The projections for a $12\,M_\odot$ model are depicted in Fig. A.2. We utilize the linear fit in Fig. 7.10 and Eq. 7.28. The $12M_\odot$ model constraints should be considered with the appropriate caveat that they are obtained neither from simulation nor from observation; moreover, we cannot justify the linear fit in Eq. 7.28 at a theoretical level. However, Eq. 7.28 and the limits coming from the $12M_\odot$ model do underscore the general physics point: *the observation and mass determination of heavier Cepheids would correspond to stronger constraints on axions.*

Appendix E

E General Comments on Post-Blue Loop Evolution

In this section, we make a few preliminary comments about the possible effects of axions on the post-blue loop evolution of stars. A full treatment is kept for future work.

The first comment pertains to Fig. 7.3, which shows the evolution of the stellar and core radius versus age. The production of axions not only reduces the maximum

size of the core radius, but also ushers in the AGB stage sooner in the evolutionary history. This is clear by the fact that the onset of the AGB occurs at $\sim 7.2 \times 10^7$ years, $\sim 7.1 \times 10^7$ years, and $\sim 6.9 \times 10^7$ years, for $g_{10} = 0$ (black), $g_{10} = 1$ (red), and $g_{10} = 2$ (green), respectively. This confirms that the helium burning stage is shortened with the inclusion of axion loss, a fact also discussed in [60].

In Fig. A.3, we depict the evolutionary trajectory of a $6M_\odot$ model on the plane of $\log T_c$ vs $\log \rho_c$. Fig. A.4 shows the same evolution, zoomed in on the blue loop stage, and displaying the various stages "A" through "E" described before. It is clear from the zoomed in figure that an increase in g_{10} lowers T_c and increases ρ_c during the blue loop stage. The effect is exacerbated during the AGB stage of evolution, as depicted by the deviation from the black line in Fig. A.3. A decrease in luminosity from axion emission near the core leads to a decrease in the temperature.

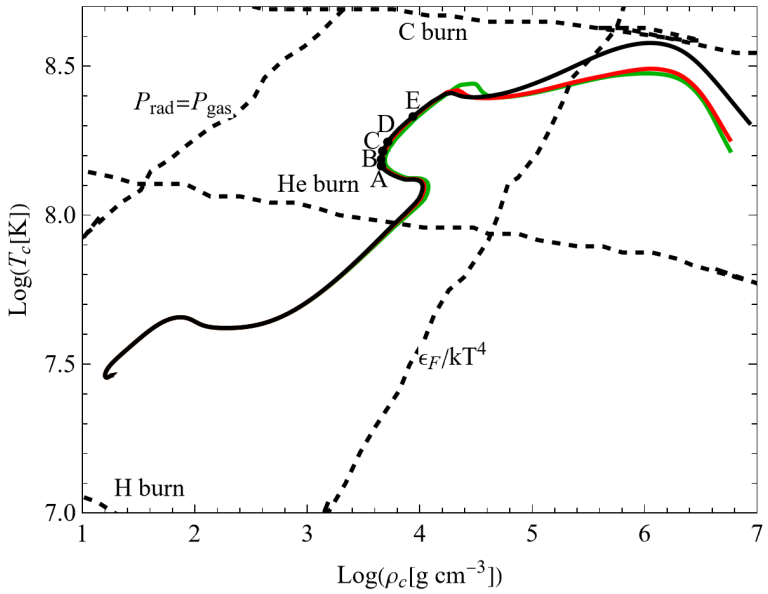


Figure A.3: Log central temperature vs Log central density for a $6M_\odot$ model. Burning bounds are extrapolated from `MESA`'s pgstar plots.

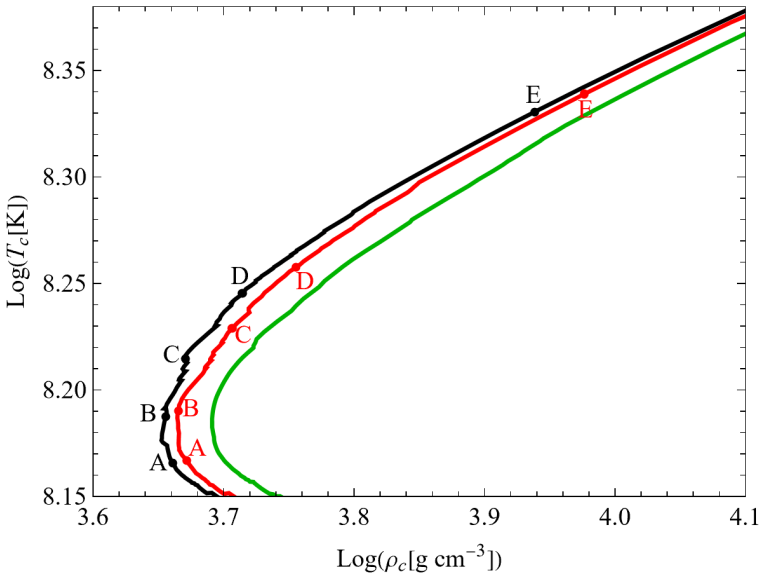


Figure A.4: Zoomed in of Fig. A.3. Symbols are discussed in the text.

Appendix F

F Inlist & Axion Code for: Blue Loops, Cepheid, and Foray into Axions

F.1 Inlists

```
! For the sake of future readers of this file (yourself included),
! ONLY include the controls you are actually using.  DO NOT include
! all of the other controls that simply have their default values.

&star_job
```

```
  ! see star/defaults/star_job.defaults

    show_log_description_at_start = .false.

    load_saved_model = .true.
    load_model_filename = 'zams/zams9.mod'

    pause_before_terminate = .true.

  ! ============= Nuclear Reaction Network ==============!
    change_net = .true.
    new_net_name = 'pp_cno_extras_o18_ne22.net'
  ! ====================================================!



    report_retries = .false.
    profile_columns_file = 'profile_columns.list'


  ! display on-screen plots
    pgstar_flag = .true.

/ ! end of star_job namelist

&eos
```

```
  ! eos options
  ! see eos/defaults/eos.defaults

/ ! end of eos namelist



&kap
  ! kap options
  ! see kap/defaults/kap.defaults
   kap_file_prefix = 'gs98' !a09 ! ! Grevesse & Sauval 1998
   kap_lowT_prefix = 'lowT_fa05_gs98'
   kap_CO_prefix = 'gs98_co' !a09_co
   use_Type2_opacities = .true. ! false for higher mass
   Zbase = 0.014 ! 0.014

/ ! end of kap namelist



&controls
  ! see star/defaults/controls.defaults
  ! smooth_convective_bdy = .true. NLE
  ! convective_bdy_weight = 1 NLE

  ! =========== Starting Specifications=================!
    initial_mass = 9.0 ! in Msun units
    initial_z = 0.014 ! 0.014
```

```
! ======================================================!



! ================= Stopping Conditions ========================!
  max_model_number = 8000
  xa_central_upper_limit_species(1) = 'ne20'
  xa_central_upper_limit(1) = 1d-1
  log_center_density_upper_limit = 12d0
  log_center_temp_upper_limit = 10.3d0
! ============================================================!



! ================  Wind Mass Loss ========================!
  hot_wind_scheme = 'Vink'
  cool_wind_RGB_scheme = 'Dutch'
  cool_wind_AGB_scheme = 'Dutch'
  RGB_to_AGB_wind_switch = 1d-4
  Dutch_scaling_factor = 0.8


    ! Dutch papers
    ! Glebbeek, E., et al, A&A 497, 255-264 (2009)
    [more Dutch authors!]
    ! Vink, J.S., de Koter, A., & Lamers,
    H.J.G.L.M., 2001, A&A, 369, 574.
    ! Nugis, T.,& Lamers, H.J.G.L.M., 2000, A&A, 360, 227
```

```
      ! Some folks use 0.8 for non-rotating mdoels
      (Maeder & Meynet, 2001).
  ! ========================================================


  ! ================== Mesh & Solver ======================
    xa_scale = 1d-5
  ! newton_itermin = 2 Possibly RD as solver_itermin = 2
    solver_itermin = 2 ! uses two iterations for hydro solver
    mesh_delta_coeff = 2

!    time_delta_coeff = 1 ! 2.5d-1 ! Change this to get better results
!    max_years_for_timestep = 2d5

    mass_change_full_on_dt = 1d7 ! (seconds)
    mass_change_full_off_dt = 1d6 ! (seconds)
    min_timestep_limit = 1d-12 ! (seconds)
  ! ========================================================

  ! ================== Mixing ============================
    mixing_length_alpha = 1.6 !1.5 for rsp 1.0 for M> 30 set to 1.6
    screening_mode = 'extended' ! empty string means no screening
    MLT_option = 'TDC' ! Added mimicing ! Khufuss 1986 model.
    Reduces to Cox at long times.

    use_Ledoux_criterion = .true.
```

```
  alpha_semiconvection = 0.1 ! Not in original file

  predictive_mix(1) = .true.
  predictive_zone_type(1) = 'any'
  predictive_zone_loc(1) = 'core'
  predictive_bdy_loc(1) = 'any'

  predictive_mix(2) = .true.
  predictive_zone_type(2) = 'any'
  predictive_zone_loc(2) = 'surf'
  predictive_bdy_loc(2) = 'any'
  make_gradr_sticky_in_solver_iters = .true.

! for core He-burning, to prevent splitting of the core
convection zone and/or core breathing pulses

  predictive_superad_thresh(1) = 0.01
  predictive_avoid_reversal(1) = 'he4'
! ======================================================!

! ================== Output ======================!
! photostep = 100 RD as photo_interval
  photo_interval = 100
  history_interval = 1
  profile_interval = 10
  log_directory = 'history_referee/9msun_g10083'
```

```
! log_cnt = 10 RD as history_interval
  terminal_interval = 10
  write_header_frequency = 10
! ================================================!

! ============== Overshoot ========================!
                overshoot_scheme(1) = 'step'!
                overshoot_zone_type(1) = 'burn_H'
                overshoot_zone_loc(1) = 'core'
                overshoot_bdy_loc(1) = 'top'
                overshoot_f(1) = 0.105 !0.105 0.365
                overshoot_f0(1) = 0.005 ! 0.05 0.03
! ================================================!




   ! options for energy conservation (see MESA V, Section 3)
   energy_eqn_option = 'dedt'
   use_gold_tolerances = .true.

! our addition to the routine to run the
  axion equations from run_star_extras

! ========== Energy Loss ====================!
  use_other_neu = .true.
```

```
    x_ctrl(1) = 0.47 ! axion_g10 for FGW
    x_ctrl(2) = 2.2d-14 ! mf for mcp 2015 paper
    x_ctrl(3) = 25 ! mf mcp 2015 paper
    x_ctrl(4) = 0.83 ! 0.468
    x_integer_ctrl(1)=3
  ! Options are: 1: axion_neu,2: mcp_neu, and  3:axion_neu_volkas
  ! ============================================!

/ ! end of controls namelist

&pgstar

 ! show HR diagram
  ! this plots the history of L,Teff over many timesteps
    HR_win_flag = .true.

  ! set static plot bounds
    HR_logT_min = 3.5
    HR_logT_max = 4.6   !4.6  !5.2
    HR_logL_min = 2.4   !2.4  !3.0
    HR_logL_max = 5.0   !4.7   !5.8 3.54 is for s mus

   show_HR_classical_instability_strip = .true.
   show_HR_target_box = .false.
   HR_target_n_sigma = -3
   HR_target_logL = 0.67d0
```

```
   HR_target_logL_sigma = 0.05d0
   HR_target_logT = 3.785d0
   HR_target_logT_sigma = 0.00461d0

  ! set window size (aspect_ratio = height/width)
    HR_win_width = 8
    HR_win_aspect_ratio = 0.7

  ! file output
   HR_file_flag = .true.
   HR_file_dir = 'hr_referee/9msun_g10083hr' !
   HR_file_prefix = 'hr'
   HR_file_interval = 10
  ! output when mod(model_number,HR_file_interval)==0
   HR_file_width = -1
   HR_file_aspect_ratio = -1
  ! negative means use same value as for window


/ ! end of pgstar namelist
```

F.2 Run Star Extras for Axion Code

Axion code used from [404] using a different table shown in Chap. 7. This code has been adjusted to fit the margins of this work. We have added a "*" where the code has been broken into the next line.

```
real(dp) :: original_diffusion_dt_limit
real(dp) :: postAGB_check = 0.0
real(dp) :: rot_set_check = 0.0
logical :: wd_diffusion = .false.
real(dp) :: X_C_init, X_N_init

integer :: time0, time1, clock_rate

! Parameters necessary for axion energy-loss
real(dp) :: axion_g10
real(dp) :: g_x_array(6)
real(dp) :: g_y_array(10)
real(dp) :: g_data(6,10)
real(dp) :: wk_array(3,6,10)
integer :: initiate_load, data_loaded

subroutine f_function(y0, y1, log_y0, log_y1, g_data, g_x_list,
  g_y_list, wk_array, fval, ierr)
```

```
    use interp_2d_lib_db, only: interp_rgbi3p_db

    real(dp), intent(in) :: y0, y1, g_data(6,10), g_x_list(6),
    g_y_list(10), & log_y0(1), log_y1(1)
    real(dp), intent(inout) :: fval, wk_array(3, 6, 10)
    integer, intent(inout) :: ierr
    real(dp) :: g_value(1)

    call interp_rgbi3p_db(2, 6, 10, g_x_list, g_y_list, g_data, &
    1, log_y0, log_y1, g_value, ierr, wk_array)

    fval = 100*(1+y0**2)*g_value(1)/((1+y1**2)*(1+exp(y0)))

    !write(*,*) log_y0, log_y1, g_value, fval

end subroutine



! consult star/other/README for general usage instructions
! control name: use_other_neu = .true.
! procedure pointer: s% other_neu => my_routine

!Friedland-Giannotti-Wise
subroutine axion_neu_volkas(  &
      id, k, T, log10_T, Rho, log10_Rho,
      *abar, zbar, log10_Tlim, flags,
```

```
   & loss, sources, ierr)
use neu_lib, only: neu_get
use neu_def
use interp_2d_lib_db, only: interp_rgbi3p_db

integer, intent(in) :: id
! id for star
integer, intent(in) :: k
! cell number or 0 if not for a particular cell
real(dp), intent(in) :: T
! temperature
real(dp), intent(in) :: log10_T
! log10 of temperature
real(dp), intent(in) :: Rho
! density
real(dp), intent(in) :: log10_Rho
! log10 of density
real(dp), intent(in) :: abar
! mean atomic weight
real(dp), intent(in) :: zbar
! mean charge
real(dp), intent(in) :: log10_Tlim
logical, intent(inout) :: flags(num_neu_types)
! true if should include the type of loss
real(dp), intent(inout) :: loss(num_neu_rvs)
! total from all sources
```

```
real(dp), intent(inout) :: sources(num_neu_types, num_neu_rvs)
integer, intent(out) :: ierr

! Stellar variables
real(dp) :: ye
! Mean number of free electrons per nucleon
real(dp) :: w
! Parameter for smoothly interpolating between deg
! and non-deg energy-loss
real(dp) :: R_deg
! degeneracy factor
real(dp) :: R_deg_max
real(dp) :: zeta
! degeneracy parameter

! y factors
real(dp) :: y_0, log_y_0(1)
! Temperature normalised plasma frequency
real(dp) :: y_1, log_y_1(1)
! Temperature normalised Debye-Huckel wavenumber
real(dp) :: y_ions, log_y_ions(1)
! y_1, but only including ions in the sum
real(dp) :: y_TF, log_y_TF(1)
! kappa_TF/T - Temperature normalised Thomas-Fermi wavenumber

! Emission rates (erg/g/s)
```

```
real(dp) :: f_nd
! f function for non-degenerate case
real(dp) :: eps_nd
! non-degenerate Primakoff energy-loss rate
real(dp) :: f_ions
! f function for case of ions only
real(dp) :: eps_ions
! Primakoff energy-loss rates to ions only
real(dp) :: f_el
! f function for (degenerate) electrons
real(dp) :: eps_el
! Energy-loss rate to (degenerate) electrons
real(dp) :: eps_deg
! Degenerate energy-loss rate (eps_ions + eps_el)
real(dp) :: eps_total
! Total energy-loss rate, defined below

! Others
integer :: i
real(dp) :: y0_test(1), y1_test(1), ans(1), test_T, test_Rho

type (star_info), pointer :: s

include 'formats'

ierr = 0
```

```
call star_ptr(id, s, ierr)
if (ierr /= 0) return

call neu_get(  &
   T, log10_T, Rho, log10_Rho, abar, zbar, log10_Tlim,
   *flags, &
   loss, sources, ierr)
if (ierr /= 0) return

!.. Add axion production and energy loss through
!   the Primakoff process.

if (initiate_load /= 1) then
    initiate_load = 1

    axion_g10 = s\% x_ctrl(4)     ! was s% %job extras_rpar(4)

    ! Load x and y arrays
    do i = 1,6
        g_x_array(i) = -1.0 + (i-1)*0.5
    end do

    do i = 1,10
        g_y_array(i) = -2.0 + (i-1)*0.5
    end do
```

```
    ! Load table from file
    open(1, file =
    "Insert_file_name", status =
    'old', &
         access = 'sequential', form = 'formatted',
         *action = 'read')
    read(1,*) g_data
    close(1)

    ! Set up interpolation
    y0_test = 0.123
    y1_test = -0.43

    call interp_rgbi3p_db(1, 6, 10, g_x_array, g_y_array,

    g_data, &
            1, y0_test, y1_test, ans, ierr, wk_array)

    data_loaded = 1
end if



! First calculate the degeneracy parameters
ye = zbar/abar
zeta = (3.01d5)*(Rho*ye)**(2./3.)/(T)
w = atanpi(zeta-3)+0.5
```

```
R_deg_max = max(1.50d0, zeta)
R_deg = 1.50/R_deg_max



! Second: Calculate y factors
y_0 = (3.33d5/T)*sqrt(Rho*ye)/
(1+(1.019d-6*Rho*ye)**(2./3.))**(1./4.)
*log_y_0 = log10(y_0)
y_1 = sqrt(6.632d20*((zbar**2/abar)+ye)*Rho/(T*T*T))
!switched from z2bar to zbar**2
log_y_1 = log10(y_1)
y_ions = sqrt(6.632d20*(zbar**2/abar)*Rho/(T*T*T)) !
switched from z2bar to zbar**2
log_y_ions = log10(y_ions)
y_TF = (5.74d7/T)*(Rho*ye)**(0.16666666667)
log_y_TF = log10(y_TF)

! Energy-loss rates - f functions
if (data_loaded == 1) then
    call f_function(y_0, y_1, log_y_0, log_y_1,
    g_data, g_x_array, g_y_array, wk_array, f_nd, ierr)
    call f_function(y_0, y_ions, log_y_0, log_y_ions,
    g_data, g_x_array, g_y_array, wk_array, f_ions, ierr)
    call f_function(y_0, y_TF, log_y_0, log_y_TF,
    g_data, g_x_array, g_y_array, wk_array, f_el, ierr)
else
```

```
    f_nd = 0.
    f_ions = 0.
    f_el = 0.
end if

! Energy-loss rates
eps_nd = (7.1d-52)*axion_g10**2*T**7*y_1**2*f_nd/Rho
eps_ions = (7.1d-52)*axion_g10**2*T**7*y_ions**2*f_ions/Rho
eps_el = 4.7d-31*axion_g10**2*R_deg*T**4*f_el*ye

eps_deg = eps_ions + eps_el

!Total energy-loss
eps_total = (1-w)*eps_nd + w*eps_deg

loss(ineu) = loss(ineu) + eps_total
!loss(idneu_dT) = loss(idneu_dT) + d_sprimakoff_dT
!loss(idneu_dRho) = loss(idneu_dRho) + d_sprimakoff_dRho



!if (k == s% nz) write(*,3) 'axioncsi', s% model_number,
k, axioncsi
!if (k == s% nz) write(*,3) 'faxioncsi', s% model_number,
k, faxioncsi
!if (k == s% nz) write(*,3) 'sprimakoff', s% model_number,
```

```
         k, sprimakoff


      end subroutine axion_neu_volkas
```

Appendix G

G Inlist and Plots for: Millicharged Particles, Blue Loops, and the Cepheid Mass Discrepancy Problem

G.1 Inlists

```
    ! For the sake of future readers of this file (yourself included),
! ONLY include the controls you are actually using.  DO NOT include
! all of the other controls that simply have their default values.

&star_job
  ! see star/defaults/star_job.defaults



     load_saved_model = .true.
     load_model_filename = 'zams/zams6.mod'


     set_initial_age = .true.
     initial_age = 0
```

```
 ! ========== Nuclear Reaction Network =========== !
   change_net = .true.
   new_net_name = 'pp_cno_extras_o18_ne22.net'
 ! ================================================ !

 !=================== Initial Rotation ====================!
     new_rotation_flag = .true.
     change_rotation_flag = .true.
     change_initial_rotation_flag = .true.

 !    relax_omega_div_omega_crit = .true.
 !    relax_initial_omega_div_omega_crit = .true.
 !    near_zams_relax_omega_div_omega_crit = .true.

     new_omega_div_omega_crit = 0.3 !
     for v_crit = 0.4
     set_omega_div_omega_crit = .true.
     set_initial_omega_div_omega_crit = .true.
!=====================================================!

   profile_columns_file = 'profile_columns.list'

   pgstar_flag = .true.

   required_termination_code_string = 'log_L_upper_limit'
```

```
    pause_before_terminate = .true.

/ ! end of star_job namelist


&eos
  ! eos options
  ! see eos/defaults/eos.defaults

/ ! end of eos namelist


&kap
  ! kap options
  ! see kap/defaults/kap.defaults
  kap_file_prefix = 'gs98'
  kap_lowT_prefix = 'lowT_fa05_gs98'
  kap_CO_prefix = 'gs98_co'
  use_Type2_opacities = .true. ! false for higher masses
  Zbase = 0.014

/ ! end of kap namelist


&controls
```

```
! see star/defaults/controls.defaults

! ========= starting specifications ============== !
  initial_mass = 6 ! in Msun units
  initial_z = 0.014
! ================================================ !

! ========== when to stop ============== !
   max_model_number = 10000
   log_L_upper_limit = 4.4d0 !4.3 for 7M - 4.15 for 6M - 4.0 for 5M
! ====================================== !

! =========== Wind ============== !

  cool_wind_RGB_scheme = 'Reimers'
  Reimers_scaling_factor = 0.6
  cool_wind_AGB_scheme = 'Blocker'
  Blocker_scaling_factor = 0.5
  RGB_to_AGB_wind_switch = 1d-4

! only use the cool_wind_scheme
  cool_wind_full_on_T = 1d10  !K
  hot_wind_full_on_T = 1.1d10 !K
  hot_wind_scheme = 'Vink'

! enhanced mass loss due to rotation
```

```
      mdot_omega_power = 0.43d0

   ! ================================

   ! atmosphere

   ! ========== ROTATION ==============

   !======== ROTATIONAL INSTABILITIES =========!
     am_nu_factor = 1d0
   !================================
     am_D_mix_factor =  0.033333333333d0 ! diffusion coefficient for mixing of material
   ! (Anderson uses 0.03333333d0 in other works set to 0.0228d0 brott 2011)
   !================================
     D_DSI_factor = 1 ! dynamical shear instability
     D_SH_factor = 1 ! Solberg-Hoiland
     D_SSI_factor = 1 ! secular shear instability
     D_ES_factor = 1 ! Eddington-Sweet circulation
     D_GSF_factor = 1 ! Goldreich-Schubert-Fricke I'm not sure if this one is used in A
     D_ST_factor = 0 ! Spruit-Tayler dynamo


! this is for ang.mom. transport
     am_nu_DSI_factor = 1
     am_nu_SH_factor = 1
     am_nu_SSI_factor = 1
```

```
    am_nu_ES_factor = 1
    am_nu_GSF_factor = 1
    am_nu_ST_factor = 0 ! Eskomer does not use the spruit-tayler dynamo
!
    am_gradmu_factor = 0.05d0 ! Heger, Langer, and Woosley 2000


  ! element diffusion

  ! ======== mlt ============ !
    MLT_option = 'Henyey'
    mixing_length_alpha = 1.6
    screening_mode = 'extended'

    use_Ledoux_criterion = .true.
  ! ==========================

  ! ===== mixing ========= !
    alpha_semiconvection = 0.1

    predictive_mix(1) = .true.
    predictive_zone_type(1) = 'any'
    predictive_zone_loc(1) = 'core'
    predictive_bdy_loc(1) = 'any'

    predictive_mix(2) = .true.
```

```
  predictive_zone_type(2) = 'any'
  predictive_zone_loc(2) = 'surf'
  predictive_bdy_loc(2) = 'any'
  make_gradr_sticky_in_solver_iters = .true.




  predictive_superad_thresh(1) = 0.01
  predictive_avoid_reversal(1) = 'he4'

  do_element_diffusion = .false.

! ================================== !

! =========== overshoot ============ !
    overshoot_scheme(1) = 'step'
    overshoot_zone_type(1) = 'burn_H'
    overshoot_zone_loc(1) = 'core'
    overshoot_bdy_loc(1) = 'top'
    overshoot_f(1) = 0.105
    overshoot_f0(1) = 0.005
! ====================================

! =========== mesh & timesteps =============== !
  solver_itermin = 2
  mesh_delta_coeff = 0.5
```

```
  time_delta_coeff = 0.7



  mass_change_full_on_dt = 1d7 ! (seconds)
  mass_change_full_off_dt = 1d6 ! (seconds)
  min_timestep_limit = 1d-12 ! (seconds)
! ============================================



! solver
   ! options for energy conservation (see MESA V, Section 3)
   energy_eqn_option = 'dedt'
   use_gold_tolerances = .true.

! ============ output ========================== !
  num_trace_history_values = 2
  trace_history_value_name(1) = 'surf_avg_v_rot'
  trace_history_value_name(2) = 'surf_avg_omega_div_omega_crit'

  photo_interval = 100
  history_interval = 1
  profile_interval = 10
  log_directory = 'history_Omega/history_omega03_6msun'
  terminal_interval = 10
  write_header_frequency = 10
```

```
  ! ============================================== !



  ! ======= Energy Loss ================ !
    use_other_neu = .false.
    x_ctrl(1) = 25  ! mf mass in eV
    x_ctrl(2) = 1.2d-13     ! q charge
  ! ===================================



/ ! end of controls namelist


&pgstar

  ! show HR diagram
  ! this plots the history of L,Teff over many timesteps
    HR_win_flag = .true.


  ! set static plot bounds
    HR_logT_min = 3.5
    HR_logT_max = 4.4   !4.6  !5.2
    HR_logL_min = 2.7   !2.4  !3.0
    HR_logL_max = 5.3   !4.7   !5.8


   show_HR_classical_instability_strip = .true.
   show_HR_target_box = .true.
```

```
   HR_target_n_sigma = 1
   HR_target_logL = 3.388126d0
   HR_target_logL_sigma = 0.169406d0
   HR_target_logT = 3.72782d0
   HR_target_logT_sigma = 0.1d0

  ! set window size (aspect_ratio = height/width)
    HR_win_width = 8
    HR_win_aspect_ratio = 0.7

  ! file output
   HR_file_flag = .true.
   HR_file_dir = 'hr_omega/6msun_omega03_hr'
   HR_file_prefix = 'hr'
   HR_file_interval = 20
   HR_file_width = -1
   HR_file_aspect_ratio = -1

/ ! end of pgstar namelist
```

G.2 Extra Plots for mcp paper

Our MCP work is still ongoing, and the following plots will be included in our published paper. However, they are not absolutely necessary for the discussions in Chapter 8

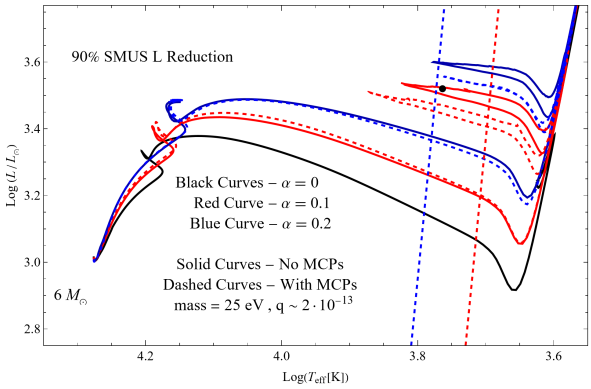


Figure A.5: An HR - diagram showing various α_{ov} with mcps mass and charge value set to lower the model value by % 10 of the luminosity. fixed rotation at 0.5

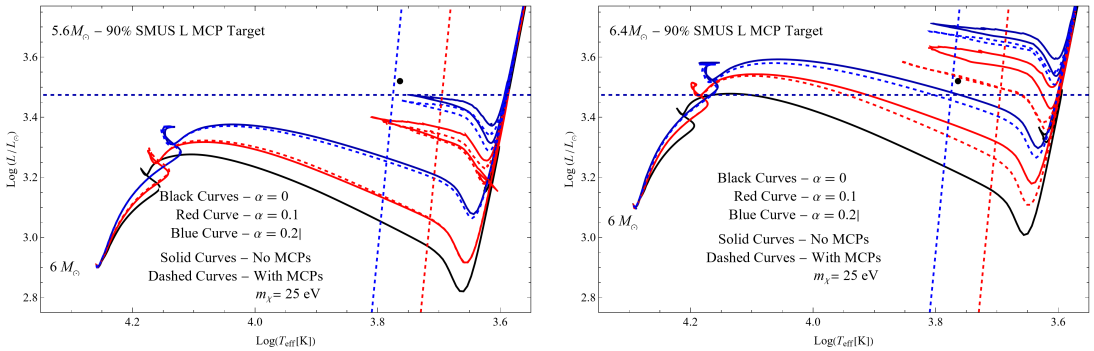


Figure A.6: HR-diagram depicting the mass boundies of smus lower of 5.6 left and 6.4 right. Solid curves represent no MCPs and dashed curves include mcps with $q = 2.9 \times 10^{-13}$ and $m_\chi = 25$eV. Black, Red, and Blue curves corresonds to values of the overshoot set to $\alpha_{ov} = 0.0$, $\alpha_{ov} = 0.1$, and $\alpha_{ov} = 0.2$, respectivly. Horizontal blue-dashed line indicates 90% of Smus observed luminosity.

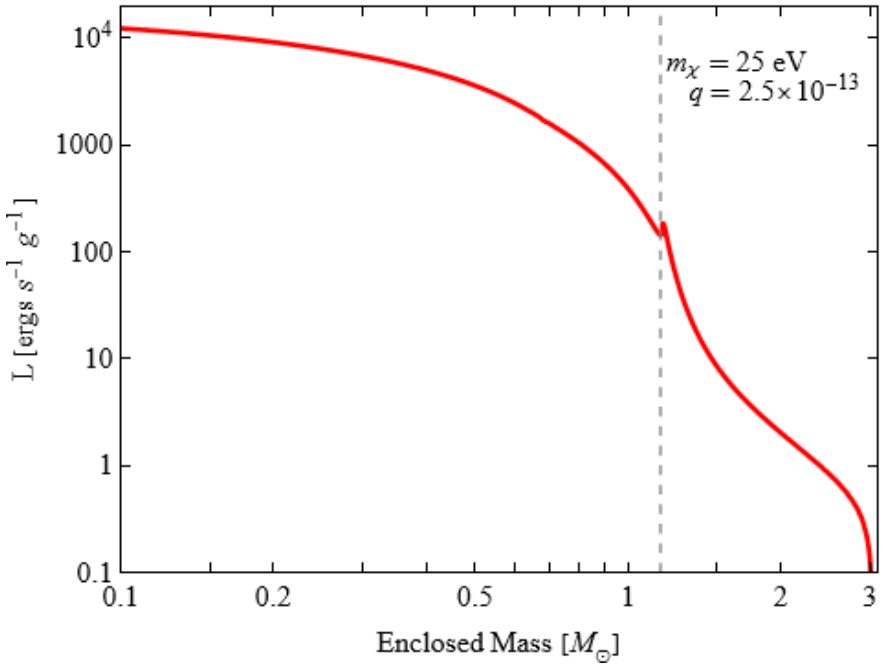


Figure A.7: Left panel: Right panel: $m_\chi = 25eV$, Possibly add mass to figure as a string. Emphasize that the decay is on-shell only.

Reference List

[1] D. Ball, C.-k. Chan, P. Christian, B.T. Jannuzi, J. Kim, D.P. Marrone et al., *First m87 event horizon telescope results. i. the shadow of the supermassive black hole*, .

[2] B. Carr and F. Kühnel, *Primordial black holes as dark matter candidates*, *SciPost Physics Lecture Notes* (2022) .

[3] B. Carr and F. Kühnel, *Primordial black holes as dark matter candidates*, *SciPost Physics Lecture Notes* (2022) 048.

[4] B.P. Abbott, R. Abbott, T. Abbott, M. Abernathy, F. Acernese, K. Ackley et al., *Observation of gravitational waves from a binary black hole merger*, *Physical review letters* **116** (2016) 061102.

[5] S.W. Hawking, *Black hole explosions?*, Nature **248** (1974) 30.

[6] K. Kohri and J. Yokoyama, *Primordial black holes and primordial nucleosynthesis: Effects of hadron injection from low mass holes*, *Phys. Rev. D* **61** (1999) 023501.

[7] H. Tashiro and N. Sugiyama, *Constraints on primordial black holes by distortions of the cosmic microwave background*, *Physical Review D* **78** (2008) .

[8] S.J. Clark, B. Dutta, Y. Gao, L.E. Strigari and S. Watson, *Planck constraint on relic primordial black holes*, *Physical Review D* **95** (2017) .

[9] V. Poulin, J. Lesgourgues and P.D. Serpico, *Cosmological constraints on exotic injection of electromagnetic energy*, *Journal of Cosmology and Astroparticle Physics* **2017** (2017) 043–043.

[10] N. Aghanim, Y. Akrami, M. Ashdown, J. Aumont, C. Baccigalupi, M. Ballardini et al., *Planck 2018 results-vi. cosmological parameters*, *Astronomy & Astrophysics* **641** (2020) A6.

[11] S.W. Hawking, *Particle Creation by Black Holes*, *Commun. Math. Phys.* **43** (1975) 199.

[12] P. Gondolo, P. Sandick and B. Shams Es Haghi, *Effects of primordial black holes on dark matter models*, *Phys. Rev. D* **102** (2020) 095018 [2009.02424].

[13] D.N. Page, *Particle Emission Rates from a Black Hole: Massless Particles from an Uncharged, Nonrotating Hole*, *Phys. Rev. D* **13** (1976) 198.

[14] P. Zyla and P. Eerola, *Review of particle physics*, *Progress of Theoretical and Experimental Physics* **2020** (2020) .

[15] P. Cole, *Small-scale probes of the early universe*, .

[16] B.J. Carr, *The Primordial black hole mass spectrum*, *Astrophys. J.* **201** (1975) 1.

[17] P. Ivanov, P. Naselsky and I. Novikov, *Inflation and primordial black holes as dark matter*, *Phys. Rev. D* **50** (1994) 7173.

[18] J. Garcia-Bellido, A.D. Linde and D. Wands, *Density perturbations and black hole formation in hybrid inflation*, *Phys. Rev. D* **54** (1996) 6040 [astro-ph/9605094].

[19] J. Silk and M.S. Turner, *Double Inflation*, *Phys. Rev. D* **35** (1987) 419.

[20] M. Kawasaki, N. Sugiyama and T. Yanagida, *Primordial black hole formation in a double inflation model in supergravity*, *Phys. Rev. D* **57** (1998) 6050 [hep-ph/9710259].

[21] J. Yokoyama, *Formation of MACHO primordial black holes in inflationary cosmology*, *Astron. Astrophys.* **318** (1997) 673 [astro-ph/9509027].

[22] S. Choudhury and S. Pal, *Fourth level MSSM inflation from new flat directions*, *JCAP* **04** (2012) 018 [1111.3441].

[23] S. Choudhury and A. Mazumdar, *Primordial blackholes and gravitational waves for an inflection-point model of inflation*, *Phys. Lett. B* **733** (2014) 270 [1307.5119].

[24] S. Pi, Y.-l. Zhang, Q.-G. Huang and M. Sasaki, *Scalaron from R^2-gravity as a heavy field*, *JCAP* **05** (2018) 042 [1712.09896].

[25] M.P. Hertzberg and M. Yamada, *Primordial Black Holes from Polynomial Potentials in Single Field Inflation*, *Phys. Rev. D* **97** (2018) 083509 [1712.09750].

[26] O. Özsoy, S. Parameswaran, G. Tasinato and I. Zavala, *Mechanisms for Primordial Black Hole Production in String Theory*, *JCAP* **07** (2018) 005 [1803.07626].

[27] M. Cicoli, V.A. Diaz and F.G. Pedro, *Primordial Black Holes from String Inflation*, *JCAP* **06** (2018) 034 [1803.02837].

[28] N.C. Tsamis and R.P. Woodard, *Improved estimates of cosmological perturbations*, *Phys. Rev. D* **69** (2004) 084005 [astro-ph/0307463].

[29] W.H. Kinney, *Horizon crossing and inflation with large eta*, *Phys. Rev. D* **72** (2005) 023515 [gr-qc/0503017].

[30] J. Martin, H. Motohashi and T. Suyama, *Ultra Slow-Roll Inflation and the non-Gaussianity Consistency Relation*, *Phys. Rev. D* **87** (2013) 023514 [1211.0083].

[31] H. Motohashi, A.A. Starobinsky and J. Yokoyama, *Inflation with a constant rate of roll*, *JCAP* **09** (2015) 018 [1411.5021].

[32] L. Anguelova, P. Suranyi and L.C.R. Wijewardhana, *Systematics of Constant Roll Inflation*, *JCAP* **02** (2018) 004 [1710.06989].

[33] K. Dimopoulos, *Ultra slow-roll inflation demystified*, *Phys. Lett. B* **775** (2017) 262 [1707.05644].

[34] H. Ragavendra, P. Saha, L. Sriramkumar and J. Silk, *Primordial black holes and secondary gravitational waves from ultraslow roll and punctuated inflation*, *Physical Review D* **103** (2021) .

[35] K. Inomata and T. Nakama, *Gravitational waves induced by scalar perturbations as probes of the small-scale primordial spectrum*, *Physical Review D* **99** (2019) 043511.

[36] K. Inomata and T. Nakama, *Gravitational waves induced by scalar perturbations as probes of the small-scale primordial spectrum*, *Phys. Rev. D* **99** (2019) 043511 [1812.00674].

[37] J. Kozaczuk, T. Lin and E. Villarama, *Signals of primordial black holes at gravitational wave interferometers*, *Phys. Rev. D* **105** (2022) 123023 [2108.12475].

[38] K. Agashe, J.H. Chang, S.J. Clark, B. Dutta, Y. Tsai and T. Xu, *Correlating gravitational wave and gamma-ray signals from primordial black holes*, *Phys. Rev. D* **105** (2022) 123009 [2202.04653].

[39] M. Hindmarsh, M. Lüben, J. Lumma and M. Pauly, *Phase transitions in the early universe*, *SciPost Physics Lecture Notes* (2021) .

[40] S.W. Hawking, I.G. Moss and J.M. Stewart, *Bubble Collisions in the Very Early Universe*, *Phys. Rev. D* **26** (1982) 2681.

[41] M. Crawford and D.N. Schramm, *Spontaneous Generation of Density Perturbations in the Early Universe*, *Nature* **298** (1982) 538.

[42] H. Kodama, M. Sasaki and K. Sato, *Abundance of Primordial Holes Produced by Cosmological First Order Phase Transition*, *Prog. Theor. Phys.* **68** (1982) 1979.

[43] I.G. Moss, *Black hole formation from colliding bubbles*, gr-qc/9405045.

[44] B. Freivogel, G.T. Horowitz and S. Shenker, *Colliding with a crunching bubble*, *JHEP* **05** (2007) 090 [hep-th/0703146].

[45] M.C. Johnson, H.V. Peiris and L. Lehner, *Determining the outcome of cosmic bubble collisions in full General Relativity*, *Phys. Rev. D* **85** (2012) 083516 [1112.4487].

[46] M.J. Baker, M. Breitbach, J. Kopp and L. Mittnacht, *Primordial Black Holes from First-Order Cosmological Phase Transitions*, 2105.07481.

[47] M.J. Baker, M. Breitbach, J. Kopp and L. Mittnacht, *Detailed Calculation of Primordial Black Hole Formation During First-Order Cosmological Phase Transitions*, 2110.00005.

[48] K. Kawana and K.-P. Xie, *Primordial black holes from a cosmic phase transition: The collapse of Fermi-balls*, *Phys. Lett. B* **824** (2022) 136791 [2106.00111].

[49] T.H. Jung and T. Okui, *Primordial black holes from bubble collisions during a first-order phase transition*, 2110.04271.

[50] P. Huang and K.-P. Xie, *Primordial black holes from an electroweak phase transition*, *Phys. Rev. D* **105** (2022) 115033 [2201.07243].

[51] P. Lu, K. Kawana and K.-P. Xie, *Old phase remnants in first-order phase transitions*, *Phys. Rev. D* **105** (2022) 123503 [2202.03439].

[52] F. Zwicky, *Die Rotverschiebung von extragalaktischen Nebeln*, *Helvetica Physica Acta* **6** (1933) 110.

[53] E. Corbelli and P. Salucci, *The extended rotation curve and the dark matter halo of m33*, *Monthly Notices of the Royal Astronomical Society* **311** (2000) 441–447.

[54] D. Clowe, M. Bradač, A.H. Gonzalez, M. Markevitch, S.W. Randall, C. Jones et al., *A direct empirical proof of the existence of dark matter*, *The Astrophysical Journal* **648** (2006) L109.

[55] Planck collaboration, *Planck 2018 results. X. Constraints on inflation*, *Astron. Astrophys.* **641** (2020) A10 [1807.06211].

[56] B. Carr and F. Kühnel, *Primordial black holes as dark matter: Recent developments*, *Annual Review of Nuclear and Particle Science* **70** (2020) 355.

[57] R.D. Peccei and H.R. Quinn, CP *conservation in the presence of pseudoparticles*, *Phys. Rev. Lett.* **38** (1977) 1440.

[58] S. Weinberg, *A new light boson?*, *Phys. Rev. Lett.* **40** (1978) 223.

[59] F. Wilczek, *Problem of strong p and t invariance in the presence of instantons*, *Phys. Rev. Lett.* **40** (1978) 279.

[60] A. Choplin, A. Coc, G. Meynet, K.A. Olive, J.-P. Uzan and E. Vangioni, *Effects of axions on Population III stars*, A&A **605** (2017) A106 [1707.01244].

[61] G.G. Raffelt, *Stars as Laboratories for Fundamental Physics: The Astrophysics of Neutrinos, Axions, and Other Weakly Interacting Particles*, University of Chicago Press (1996).

[62] C. O'Hare, "cajohare/axionlimits: Axionlimits." https://cajohare.github.io/AxionLimits/, July, 2020. 10.5281/zenodo.3932430.

[63] N. Vinyoles and H. Vogel, *Minicharged particles from the sun: a cutting-edge bound*, *Journal of Cosmology and Astroparticle Physics* **2016** (2016) 002–002.

[64] K.C. Fung, T. Lin, M. Pospelov, Y. Zhao and Y.-D. Tsai, *Beyond stellar cooling: Constraints on light particles from radial oscillations of red giants*, *arXiv preprint* (2023) [2309.06465].

[65] N. Aggarwal et al., *Challenges and opportunities of gravitational-wave searches at MHz to GHz frequencies*, *Living Rev. Rel.* **24** (2021) 4 [2011.12414].

[66] G. Franciolini, A. Maharana and F. Muia, *The Hunt for Light Primordial Black Hole Dark Matter with Ultra-High-Frequency Gravitational Waves*, 2205.02153.

[67] R. Caldwell et al., *Detection of Early-Universe Gravitational Wave Signatures and Fundamental Physics*, 2203.07972.

[68] S. Bird, I. Cholis, J.B. Muñoz, Y. Ali-Haïmoud, M. Kamionkowski, E.D. Kovetz et al., *Did LIGO detect dark matter?*, *Phys. Rev. Lett.* **116** (2016) 201301 [1603.00464].

[69] S. Clesse and J. García-Bellido, *The clustering of massive Primordial Black Holes as Dark Matter: measuring their mass distribution with Advanced LIGO*, *Phys. Dark Univ.* **15** (2017) 142 [1603.05234].

[70] M. Sasaki, T. Suyama, T. Tanaka and S. Yokoyama, *Primordial Black Hole Scenario for the Gravitational-Wave Event GW150914*, *Phys. Rev. Lett.* **117** (2016) 061101 [1603.08338].

[71] C. Kouvaris, P. Tinyakov and M.H.G. Tytgat, *NonPrimordial Solar Mass Black Holes*, *Phys. Rev. Lett.* **121** (2018) 221102 [1804.06740].

[72] Y. Ali-Haïmoud, E.D. Kovetz and M. Kamionkowski, *Merger rate of primordial black-hole binaries*, *Phys. Rev. D* **96** (2017) 123523 [1709.06576].

[73] H.-K. Guo, K. Sinha and C. Sun, *Probing Boson Stars with Extreme Mass Ratio Inspirals*, *JCAP* **09** (2019) 032 [1904.07871].

[74] H.-K. Guo, J. Shu and Y. Zhao, *Using LISA-like Gravitational Wave Detectors to Search for Primordial Black Holes*, *Phys. Rev. D* **99** (2019) 023001 [1709.03500].

[75] R. Anantua, R. Easther and J.T. Giblin, *GUT-Scale Primordial Black Holes: Consequences and Constraints*, *Phys. Rev. Lett.* **103** (2009) 111303 [0812.0825].

[76] R. Dong, W.H. Kinney and D. Stojkovic, *Gravitational wave production by Hawking radiation from rotating primordial black holes*, *JCAP* **10** (2016) 034 [1511.05642].

[77] K. Tomita, *Non-Linear Theory of Gravitational Instability in the Expanding Universe*, *Progress of Theoretical Physics* **37** (1967) 831.

[78] S. Mollerach, D. Harari and S. Matarrese, *CMB polarization from secondary vector and tensor modes*, *Phys. Rev. D* **69** (2004) 063002 [astro-ph/0310711].

[79] K.N. Ananda, C. Clarkson and D. Wands, *The Cosmological gravitational wave background from primordial density perturbations*, *Phys. Rev. D* **75** (2007) 123518 [gr-qc/0612013].

[80] D. Baumann, P.J. Steinhardt, K. Takahashi and K. Ichiki, *Gravitational Wave Spectrum Induced by Primordial Scalar Perturbations*, *Phys. Rev. D* **76** (2007) 084019 [hep-th/0703290].

[81] V. Acquaviva, N. Bartolo, S. Matarrese and A. Riotto, *Second order cosmological perturbations from inflation*, *Nucl. Phys. B* **667** (2003) 119 [astro-ph/0209156].

[82] C. Yuan and Q.-G. Huang, *A topic review on probing primordial black hole dark matter with scalar induced gravitational waves*, 2103.04739.

[83] G. Domènech, *Scalar Induced Gravitational Waves Review*, *Universe* **7** (2021) 398 [2109.01398].

[84] S. Pi and M. Sasaki, *Gravitational Waves Induced by Scalar Perturbations with a Lognormal Peak*, *JCAP* **09** (2020) 037 [2005.12306].

[85] K. Kohri and T. Terada, *Semianalytic calculation of gravitational wave spectrum nonlinearly induced from primordial curvature perturbations*, *Phys. Rev. D* **97** (2018) 123532 [1804.08577].

[86] J.R. Espinosa, D. Racco and A. Riotto, *A Cosmological Signature of the SM Higgs Instability: Gravitational Waves*, *JCAP* **09** (2018) 012 [1804.07732].

[87] M. Braglia, D.K. Hazra, F. Finelli, G.F. Smoot, L. Sriramkumar and A.A. Starobinsky, *Generating PBHs and small-scale GWs in two-field models of inflation*, *JCAP* **08** (2020) 001 [2005.02895].

[88] K. Inomata, K. Kohri, T. Nakama and T. Terada, *Enhancement of Gravitational Waves Induced by Scalar Perturbations due to a Sudden Transition from an Early Matter Era to the Radiation Era*, *Phys. Rev. D* **100** (2019) 043532 [1904.12879].

[89] K. Inomata, M. Kawasaki, K. Mukaida, Y. Tada and T.T. Yanagida, *Inflationary primordial black holes for the LIGO gravitational wave events and pulsar timing array experiments*, *Phys. Rev. D* **95** (2017) 123510 [1611.06130].

[90] G. Franciolini and A. Urbano, *Primordial black hole dark matter from inflation: the reverse engineering approach*, 2207.10056.

[91] F. Zhang, J. Lin and Y. Lu, *Double-peaked inflation model: Scalar induced gravitational waves and primordial-black-hole suppression from primordial non-Gaussianity*, *Phys. Rev. D* **104** (2021) 063515 [2106.10792].

[92] T.-J. Gao, *NANOGrav Signal from double-inflection-point inflation*, 2110.00205.

[93] I.B. Zeldovich, *Charge asymmetry of the universe as a consequence of evaporation of black holes and of the asymmetry of the weak interaction*, *ZhETF Pisma Redaktsiiu* **24** (1976) 29.

[94] B.J. Carr, *Some cosmological consequences of primordial black-hole evaporations.*, ApJ **206** (1976) 8.

[95] D. Toussaint, S.B. Treiman, F. Wilczek and A. Zee, *Matter-antimatter accounting, thermodynamics, and black-hole radiation*, *Phys. Rev. D* **19** (1979) 1036.

[96] M.S. Turner, *BARYON PRODUCTION BY PRIMORDIAL BLACK HOLES*, *Phys. Lett. B* **89** (1979) 155.

[97] A.F. Grillo, *Primordial black holes and baryon production in grand unified theories*, *Physics Letters B* **94** (1980) 364.

[98] D. Baumann, P.J. Steinhardt and N. Turok, *Primordial Black Hole Baryogenesis*, hep-th/0703250.

[99] T. Fujita, M. Kawasaki, K. Harigaya and R. Matsuda, *Baryon asymmetry, dark matter, and density perturbation from primordial black holes*, *Phys. Rev. D* **89** (2014) 103501 [1401.1909].

[100] A. Hook, *Baryogenesis from Hawking Radiation*, *Phys. Rev. D* **90** (2014) 083535 [1404.0113].

[101] L. Morrison, S. Profumo and Y. Yu, *Melanopogenesis: Dark Matter of (almost) any Mass and Baryonic Matter from the Evaporation of Primordial Black Holes weighing a Ton (or less)*, *JCAP* **05** (2019) 005 [1812.10606].

[102] N. Bernal, C.S. Fong, Y.F. Perez-Gonzalez and J. Turner, *Rescuing high-scale leptogenesis using primordial black holes*, *Phys. Rev. D* **106** (2022) 035019 [2203.08823].

[103] P. Sandick, B.S. Es Haghi and K. Sinha, *Asymmetric reheating by primordial black holes*, *Phys. Rev. D* **104** (2021) 083523 [2108.08329].

[104] R. Allahverdi, J. Dent and J. Osinski, *Nonthermal production of dark matter from primordial black holes*, *Phys. Rev. D* **97** (2018) 055013 [1711.10511].

[105] N.F. Bell and R.R. Volkas, *Mirror matter and primordial black holes*, *Phys. Rev. D* **59** (1999) 107301 [astro-ph/9812301].

[106] O. Lennon, J. March-Russell, R. Petrossian-Byrne and H. Tillim, *Black Hole Genesis of Dark Matter*, *JCAP* **04** (2018) 009 [1712.07664].

[107] N. Bernal, F. Hajkarim and Y. Xu, *Axion Dark Matter in the Time of Primordial Black Holes*, *Phys. Rev. D* **104** (2021) 075007 [2107.13575].

[108] A. Arbey, J. Auffinger, P. Sandick, B. Shams Es Haghi and K. Sinha, *Precision calculation of dark radiation from spinning primordial black holes and early matter-dominated eras*, *Phys. Rev. D* **103** (2021) 123549 [2104.04051].

[109] D. Hooper, G. Krnjaic and S.D. McDermott, *Dark Radiation and Superheavy Dark Matter from Black Hole Domination*, *JHEP* **08** (2019) 001 [1905.01301].

[110] I. Masina, *Dark Matter and Dark Radiation from Evaporating Kerr Primordial Black Holes*, *Grav. Cosmol.* **27** (2021) 315 [2103.13825].

[111] M. Dine and A. Kusenko, *The Origin of the matter - antimatter asymmetry*, *Rev. Mod. Phys.* **76** (2003) 1 [hep-ph/0303065].

[112] Planck collaboration, *Planck 2018 results. I. Overview and the cosmological legacy of Planck*, *Astron. Astrophys.* **641** (2020) A1 [1807.06205].

[113] M. Gertsenshtein, *Wave resonance of light and gravitional waves*, *Sov Phys JETP* **14** (1962) 84.

[114] M.S. Turner and D.N. Schramm, *The Origin of Baryons in the Universe and the Astrophysical Implications*, *Nature* **279** (1979) 303.

[115] N. Smyth, L. Santos-Olmsted and S. Profumo, *Gravitational baryogenesis and dark matter from light black holes*, *JCAP* **03** (2022) 013 [2110.14660].

[116] R. Allahverdi, B. Dutta, R.N. Mohapatra and K. Sinha, *A Supersymmetric Model for Dark Matter and Baryogenesis Motivated by the Recent CDMS Result*, *Phys. Rev. Lett.* **111** (2013) 051302 [1305.0287].

[117] R. Allahverdi, B. Dutta and K. Sinha, *Cladogenesis: Baryon-Dark Matter Coincidence from Branchings in Moduli Decay*, *Phys. Rev. D* **83** (2011) 083502 [1011.1286].

[118] B. Dutta and K. Sinha, *Affleck-Dine Baryogenesis in Effective Supergravity*, *Phys. Rev. D* **82** (2010) 095003 [1008.0148].

[119] R. Allahverdi, B. Dutta and K. Sinha, *Baryogenesis and Late-Decaying Moduli*, *Phys. Rev. D* **82** (2010) 035004 [1005.2804].

[120] Particle Data Group collaboration, *Review of Particle Physics*, *PTEP* **2020** (2020) 083C01.

[121] R. Allahverdi et al., *The First Three Seconds: a Review of Possible Expansion Histories of the Early Universe*, 2006.16182.

[122] G. Kane, K. Sinha and S. Watson, *Cosmological Moduli and the Post-Inflationary Universe: A Critical Review*, *Int. J. Mod. Phys. D* **24** (2015) 1530022 [1502.07746].

[123] A. Berlin, D. Blas, R. Tito D'Agnolo, S.A.R. Ellis, R. Harnik, Y. Kahn et al., *Detecting high-frequency gravitational waves with microwave cavities*, *Phys. Rev. D* **105** (2022) 116011 [2112.11465].

[124] V. Domcke, C. Garcia-Cely and N.L. Rodd, *Novel Search for High-Frequency Gravitational Waves with Low-Mass Axion Haloscopes*, *Phys. Rev. Lett.* **129** (2022) 041101 [2202.00695].

[125] F. Li, N. Yang, Z. Fang, R.M.L. Baker, Jr., G.V. Stephenson and H. Wen, *Signal Photon Flux and Background Noise in a Coupling Electromagnetic Detecting System for High Frequency Gravitational Waves*, *Phys. Rev. D* **80** (2009) 064013 [0909.4118].

[126] A. Ringwald, J. Schütte-Engel and C. Tamarit, *Gravitational Waves as a Big Bang Thermometer*, *JCAP* **03** (2021) 054 [2011.04731].

[127] B.J. Carr, K. Kohri, Y. Sendouda and J. Yokoyama, *New cosmological constraints on primordial black holes*, *Phys. Rev. D* **81** (2010) 104019 [0912.5297].

[128] T. Harada, C.-M. Yoo, K. Kohri, K.-i. Nakao and S. Jhingan, *Primordial black hole formation in the matter-dominated phase of the Universe*, *Astrophys. J.* **833** (2016) 61 [1609.01588].

[129] T. Papanikolaou, V. Vennin and D. Langlois, *Gravitational waves from a universe filled with primordial black holes*, *JCAP* **03** (2021) 053 [2010.11573].

[130] K.M. Zurek, *Asymmetric Dark Matter: Theories, Signatures, and Constraints*, *Phys. Rept.* **537** (2014) 91 [1308.0338].

[131] G. Kane, J. Shao, S. Watson and H.-B. Yu, *The Baryon-Dark Matter Ratio Via Moduli Decay After Affleck-Dine Baryogenesis*, *JCAP* **11** (2011) 012 [1108.5178].

[132] N.F. Bell, K. Petraki, I.M. Shoemaker and R.R. Volkas, *Pangenesis in a Baryon-Symmetric Universe: Dark and Visible Matter via the Affleck-Dine Mechanism*, *Phys. Rev. D* **84** (2011) 123505 [1105.3730].

[133] J. March-Russell and M. McCullough, *Asymmetric Dark Matter via Spontaneous Co-Genesis*, *JCAP* **03** (2012) 019 [1106.4319].

[134] K. Kamada and M. Yamaguchi, *Asymmetric Dark Matter from Spontaneous Cogenesis in the Supersymmetric Standard Model*, *Phys. Rev. D* **85** (2012) 103530 [1201.2636].

[135] H. Davoudiasl, D.E. Morrissey, K. Sigurdson and S. Tulin, *Hylogenesis: A Unified Origin for Baryonic Visible Matter and Antibaryonic Dark Matter*, *Phys. Rev. Lett.* **105** (2010) 211304 [1008.2399].

[136] Y.-P. Wu, E. Pinetti and J. Silk, *Cosmic Coincidences of Primordial-Black-Hole Dark Matter*, *Phys. Rev. Lett.* **128** (2022) 031102 [2109.09875].

[137] S. Balaji, J. Silk and Y.-P. Wu, *Induced gravitational waves from the cosmic coincidence*, *JCAP* **06** (2022) 008 [2202.00700].

[138] J. García-Bellido, B. Carr and S. Clesse, *Primordial Black Holes and a Common Origin of Baryons and Dark Matter*, *Universe* **8** (2021) 12 [1904.11482].

[139] B. Carr, S. Clesse and J. García-Bellido, *Primordial black holes from the QCD epoch: Linking dark matter, baryogenesis and anthropic selection*, *Mon. Not. Roy. Astron. Soc.* **501** (2021) 1426 [1904.02129].

[140] B. Carr and F. Kuhnel, *Primordial black holes with multimodal mass spectra*, *Phys. Rev. D* **99** (2019) 103535 [1811.06532].

[141] Y.-F. Cai, X. Tong, D.-G. Wang and S.-F. Yan, *Primordial Black Holes from Sound Speed Resonance during Inflation*, *Phys. Rev. Lett.* **121** (2018) 081306 [1805.03639].

[142] Y.-F. Cai, C. Chen, X. Tong, D.-G. Wang and S.-F. Yan, *When Primordial Black Holes from Sound Speed Resonance Meet a Stochastic Background of Gravitational Waves*, *Phys. Rev. D* **100** (2019) 043518 [1902.08187].

[143] A. Addazi, S. Capozziello and Q. Gan, *Induced Gravitational Waves from Multi-Sound Speed Resonances during Cosmological Inflation*, 2204.07668.

[144] C. Armendariz-Picon and E.A. Lim, *Vacuum choices and the predictions of inflation*, *JCAP* **12** (2003) 006 [hep-th/0303103].

[145] B. Carr, F. Kuhnel and M. Sandstad, *Primordial Black Holes as Dark Matter*, *Phys. Rev. D* **94** (2016) 083504 [1607.06077].

[146] B. Carr, K. Kohri, Y. Sendouda and J. Yokoyama, *Constraints on primordial black holes*, *Rept. Prog. Phys.* **84** (2021) 116902 [2002.12778].

[147] B. Carr and F. Kuhnel, *Primordial Black Holes as Dark Matter: Recent Developments*, *Ann. Rev. Nucl. Part. Sci.* **70** (2020) 355 [2006.02838].

[148] A.M. Green and B.J. Kavanagh, *Primordial Black Holes as a dark matter candidate*, *J. Phys. G* **48** (2021) 043001 [2007.10722].

[149] P. Villanueva-Domingo, O. Mena and S. Palomares-Ruiz, *A brief review on primordial black holes as dark matter*, *Front. Astron. Space Sci.* **8** (2021) 87 [2103.12087].

[150] M.Y. Khlopov and A.G. Polnarev, *PRIMORDIAL BLACK HOLES AS A COSMOLOGICAL TEST OF GRAND UNIFICATION*, *Phys. Lett. B* **97** (1980) 383.

[151] A.G. Polnarev and M.Y. Khlopov, *Dustlike Stages in the Early Universe and Constraints on the Primordial Black-Hole Spectrum*, *Sov. Astron.* **26** (1982) 391.

[152] V. Corbin and N.J. Cornish, *Detecting the cosmic gravitational wave background with the big bang observer*, *Class. Quant. Grav.* **23** (2006) 2435 [gr-qc/0512039].

[153] N. Seto, S. Kawamura and T. Nakamura, *Possibility of direct measurement of the acceleration of the universe using 0.1-Hz band laser interferometer gravitational wave antenna in space*, *Phys. Rev. Lett.* **87** (2001) 221103 [astro-ph/0108011].

[154] S. Kawamura et al., *Current status of space gravitational wave antenna DECIGO and B-DECIGO*, *PTEP* **2021** (2021) 05A105 [2006.13545].

[155] M.J. Ramsey-Musolf, *The electroweak phase transition: a collider target*, *JHEP* **09** (2020) 179 [1912.07189].

[156] S. Profumo, M.J. Ramsey-Musolf and G. Shaughnessy, *Singlet Higgs phenomenology and the electroweak phase transition*, *JHEP* **08** (2007) 010 [0705.2425].

[157] A. Alves, T. Ghosh, H.-K. Guo and K. Sinha, *Resonant Di-Higgs Production at Gravitational Wave Benchmarks: A Collider Study using Machine Learning*, *JHEP* **12** (2018) 070 [1808.08974].

[158] A. Alves, T. Ghosh, H.-K. Guo, K. Sinha and D. Vagie, *Collider and Gravitational Wave Complementarity in Exploring the Singlet Extension of the Standard Model*, *JHEP* **04** (2019) 052 [1812.09333].

[159] P. Huang, A.J. Long and L.-T. Wang, *Probing the Electroweak Phase Transition with Higgs Factories and Gravitational Waves*, *Phys. Rev. D* **94** (2016) 075008 [1608.06619].

[160] A. Coogan, L. Morrison and S. Profumo, *Direct Detection of Hawking Radiation from Asteroid-Mass Primordial Black Holes*, *Phys. Rev. Lett.* **126** (2021) 171101 [2010.04797].

[161] S. Clark, B. Dutta, Y. Gao, Y.-Z. Ma and L.E. Strigari, *21 cm limits on decaying dark matter and primordial black holes*, *Phys. Rev. D* **98** (2018) 043006 [1803.09390].

[162] R. Laha, J.B. Muñoz and T.R. Slatyer, *INTEGRAL constraints on primordial black holes and particle dark matter*, *Phys. Rev. D* **101** (2020) 123514 [2004.00627].

[163] R. Laha, *Primordial Black Holes as a Dark Matter Candidate Are Severely Constrained by the Galactic Center 511 keV γ -Ray Line*, *Phys. Rev. Lett.* **123** (2019) 251101 [1906.09994].

[164] M. Boudaud and M. Cirelli, *Voyager 1 $e^{\pm}$ Further Constrain Primordial Black Holes as Dark Matter*, *Phys. Rev. Lett.* **122** (2019) 041104 [1807.03075].

[165] V. Poulin, J. Lesgourgues and P.D. Serpico, *Cosmological constraints on exotic injection of electromagnetic energy*, *JCAP* **03** (2017) 043 [1610.10051].

[166] S. Clark, B. Dutta, Y. Gao, L.E. Strigari and S. Watson, *Planck Constraint on Relic Primordial Black Holes*, *Phys. Rev. D* **95** (2017) 083006 [1612.07738].

[167] M.Y. Khlopov, *Primordial Black Holes*, *Res. Astron. Astrophys.* **10** (2010) 495 [0801.0116].

[168] K.M. Belotsky, A.D. Dmitriev, E.A. Esipova, V.A. Gani, A.V. Grobov, M.Y. Khlopov et al., *Signatures of primordial black hole dark matter*, *Mod. Phys. Lett. A* **29** (2014) 1440005 [1410.0203].

[169] K.M. Belotsky, V.I. Dokuchaev, Y.N. Eroshenko, E.A. Esipova, M.Y. Khlopov, L.A. Khromykh et al., *Clusters of primordial black holes*, *Eur. Phys. J. C* **79** (2019) 246 [1807.06590].

[170] S.V. Ketov and M.Y. Khlopov, *Cosmological Probes of Supersymmetric Field Theory Models at Superhigh Energy Scales*, *Symmetry* **11** (2019) 511.

[171] W. DeRocco and P.W. Graham, *Constraining Primordial Black Hole Abundance with the Galactic 511 keV Line*, *Phys. Rev. Lett.* **123** (2019) 251102 [1906.07740].

[172] H. Kim, *A constraint on light primordial black holes from the interstellar medium temperature*, *Mon. Not. Roy. Astron. Soc.* **504** (2021) 5475 [2007.07739].

[173] A.K. Saha and R. Laha, *Sensitivities on nonspinning and spinning primordial black hole dark matter with global 21-cm troughs*, *Phys. Rev. D* **105** (2022) 103026 [2112.10794].

[174] S. Mittal, A. Ray, G. Kulkarni and B. Dasgupta, *Constraining primordial black holes as dark matter using the global 21-cm signal with X-ray heating and excess radio background*, *JCAP* **03** (2022) 030 [2107.02190].

[175] D. Marfatia and P.-Y. Tseng, *Correlated signals of first-order phase transitions and primordial black hole evaporation*, *JHEP* **08** (2022) 001 [2112.14588].

[176] K.-P. Xie, *Pinning down the primordial black hole formation mechanism with gamma-rays and gravitational waves*, 2301.02352.

[177] A. Escrivà, F. Kuhnel and Y. Tada, *Primordial Black Holes*, 2211.05767.

[178] M. Kawasaki, K. Kohri and N. Sugiyama, *MeV scale reheating temperature and thermalization of neutrino background*, *Phys. Rev. D* **62** (2000) 023506 [astro-ph/0002127].

[179] T. Hasegawa, N. Hiroshima, K. Kohri, R.S.L. Hansen, T. Tram and S. Hannestad, *MeV-scale reheating temperature and thermalization of oscillating neutrinos by radiative and hadronic decays of massive particles*, *JCAP* **12** (2019) 012 [1908.10189].

[180] B. Shams Es Haghi, *Baryogenesis and primordial black hole dark matter from heavy metastable particles*, *Phys. Rev. D* **107** (2023) 083507 [2212.11308].

[181] R. Allahverdi, M. Cicoli, B. Dutta and K. Sinha, *Nonthermal dark matter in string compactifications*, *Phys. Rev. D* **88** (2013) 095015 [1307.5086].

[182] A. Cheek, L. Heurtier, Y.F. Perez-Gonzalez and J. Turner, *Primordial black hole evaporation and dark matter production. I. Solely Hawking radiation*, *Phys. Rev. D* **105** (2022) 015022 [2107.00013].

[183] A. Cheek, L. Heurtier, Y.F. Perez-Gonzalez and J. Turner, *Primordial black hole evaporation and dark matter production. II. Interplay with the freeze-in or freeze-out mechanism*, *Phys. Rev. D* **105** (2022) 015023 [2107.00016].

[184] N. Bhaumik, A. Ghoshal, R.K. Jain and M. Lewicki, *Distinct signatures of spinning PBH domination and evaporation: doubly peaked gravitational waves, dark relics and CMB complementarity*, 2212.00775.

[185] A. Cheek, L. Heurtier, Y.F. Perez-Gonzalez and J. Turner, *Redshift effects in particle production from Kerr primordial black holes*, *Phys. Rev. D* **106** (2022) 103012 [2207.09462].

[186] T. Papanikolaou, *The H_0 tension alleviated through ultra-light primordial black holes: an information insight through gravitational waves*, in *CORFU2022: 22th Hellenic School and Workshops on Elementary Particle Physics and Gravity*, 3, 2023 [2303.00600].

[187] S. Alexander and P. Meszaros, *Reheating, Dark Matter and Baryon Asymmetry: A Triple Coincidence in Inflationary Models*, hep-th/0703070.

[188] Y. Hamada and S. Iso, *Baryon asymmetry from primordial black holes*, *PTEP* **2017** (2017) 033B02 [1610.02586].

[189] S. Datta, A. Ghosal and R. Samanta, *Baryogenesis from ultralight primordial black holes and strong gravitational waves from cosmic strings*, *JCAP* **08** (2021) 021 [2012.14981].

[190] N. Bhaumik, A. Ghoshal and M. Lewicki, *Doubly peaked induced stochastic gravitational wave background: testing baryogenesis from primordial black holes*, *JHEP* **07** (2022) 130 [2205.06260].

[191] T.C. Gehrman, B. Shams Es Haghi, K. Sinha and T. Xu, *Baryogenesis, primordial black holes and MHz–GHz gravitational waves*, *JCAP* **02** (2023) 062 [2211.08431].

[192] K. Agashe, J.H. Chang, S.J. Clark, B. Dutta, Y. Tsai and T. Xu, *Detecting Axion-Like Particles with Primordial Black Holes*, 2212.11980.

[193] Y. Jho, T.-G. Kim, J.-C. Park, S.C. Park and Y. Park, *Axions from Primordial Black Holes*, 2212.11977.

[194] H. Assadullahi and D. Wands, *Constraints on primordial density perturbations from induced gravitational waves*, *Phys. Rev. D* **81** (2010) 023527 [0907.4073].

[195] G.M. Harry, T.R. Stevenson and H.J. Paik, *Detectability of gravitational wave events by spherical resonant mass antennas*, *Phys. Rev. D* **54** (1996) 2409 [gr-qc/9602018].

[196] A. Arvanitaki and A.A. Geraci, *Detecting high-frequency gravitational waves with optically-levitated sensors*, *Phys. Rev. Lett.* **110** (2013) 071105 [1207.5320].

[197] N. Aggarwal, G.P. Winstone, M. Teo, M. Baryakhtar, S.L. Larson, V. Kalogera et al., *Searching for New Physics with a Levitated-Sensor-Based Gravitational-Wave Detector*, *Phys. Rev. Lett.* **128** (2022) 111101 [2010.13157].

[198] M. Goryachev and M.E. Tobar, *Gravitational Wave Detection with High Frequency Phonon Trapping Acoustic Cavities*, *Phys. Rev. D* **90** (2014) 102005 [1410.2334].

[199] M.A. Page et al., *Gravitational wave detectors with broadband high frequency sensitivity*, *Commun. Phys.* **4** (2021) 27 [2007.08766].

[200] M. Goryachev, W.M. Campbell, I.S. Heng, S. Galliou, E.N. Ivanov and M.E. Tobar, *Rare Events Detected with a Bulk Acoustic Wave High Frequency Gravitational Wave Antenna*, *Phys. Rev. Lett.* **127** (2021) 071102 [2102.05859].

[201] A.S. Chou, R. Gustafson, C. Hogan, B. Kamai, O. Kwon, R. Lanza et al., *MHz gravitational wave constraints with decameter michelson interferometers*, *Physical Review D* **95** (2017) .

[202] T. Akutsu et al., *Search for a stochastic background of 100-MHz gravitational waves with laser interferometers*, *Phys. Rev. Lett.* **101** (2008) 101101 [0803.4094].

[203] A. Berlin et al., *Searches for New Particles, Dark Matter, and Gravitational Waves with SRF Cavities*, 2203.12714.

[204] N. Herman, L. Lehoucq and A. Fúzfa, *Electromagnetic Antennas for the Resonant Detection of the Stochastic Gravitational Wave Background*, 2203.15668.

[205] N. Herman, A. Füzfa, L. Lehoucq and S. Clesse, *Detecting planetary-mass primordial black holes with resonant electromagnetic gravitational-wave detectors*, *Phys. Rev. D* **104** (2021) 023524 [2012.12189].

[206] A. Berlin, D. Blas, R. Tito D'Agnolo, S.A.R. Ellis, R. Harnik, Y. Kahn et al., *MAGO 2.0: Electromagnetic Cavities as Mechanical Bars for Gravitational Waves*, 2303.01518.

[207] A. Ito, T. Ikeda, K. Miuchi and J. Soda, *Probing GHz gravitational waves with graviton–magnon resonance*, *Eur. Phys. J. C* **80** (2020) 179 [1903.04843].

[208] V. Domcke and C. Garcia-Cely, *Potential of radio telescopes as high-frequency gravitational wave detectors*, *Phys. Rev. Lett.* **126** (2021) 021104 [2006.01161].

[209] CMB-S4 collaboration, *CMB-S4 Science Book, First Edition*, 1610.02743.

[210] V. De Luca, V. Desjacques, G. Franciolini, A. Malhotra and A. Riotto, *The initial spin probability distribution of primordial black holes*, *JCAP* **05** (2019) 018 [1903.01179].

[211] Planck collaboration, *Planck 2018 results. VI. Cosmological parameters*, *Astron. Astrophys.* **641** (2020) A6 [1807.06209].

[212] K. Inomata, M. Kawasaki, K. Mukaida, T. Terada and T.T. Yanagida, *Gravitational Wave Production right after a Primordial Black Hole Evaporation*, *Phys. Rev. D* **101** (2020) 123533 [2003.10455].

[213] T. Papanikolaou, *Gravitational waves induced from primordial black hole fluctuations: the effect of an extended mass function*, *JCAP* **10** (2022) 089 [2207.11041].

[214] E. Cotner and A. Kusenko, *Primordial black holes from supersymmetry in the early universe*, *Phys. Rev. Lett.* **119** (2017) 031103 [1612.02529].

[215] E. Cotner and A. Kusenko, *Primordial black holes from scalar field evolution in the early universe*, *Phys. Rev. D* **96** (2017) 103002 [1706.09003].

[216] E. Cotner, A. Kusenko and V. Takhistov, *Primordial Black Holes from Inflaton Fragmentation into Oscillons*, *Phys. Rev. D* **98** (2018) 083513 [1801.03321].

[217] E. Cotner, A. Kusenko, M. Sasaki and V. Takhistov, *Analytic Description of Primordial Black Hole Formation from Scalar Field Fragmentation*, *JCAP* **10** (2019) 077 [1907.10613].

[218] S.G. Rubin, M.Y. Khlopov and A.S. Sakharov, *Primordial black holes from nonequilibrium second order phase transition*, *Grav. Cosmol.* **6** (2000) 51 [hep-ph/0005271].

[219] S.G. Rubin, A.S. Sakharov and M.Y. Khlopov, *The Formation of primary galactic nuclei during phase transitions in the early universe*, *J. Exp. Theor. Phys.* **91** (2001) 921 [hep-ph/0106187].

[220] S.W. Hawking, *Black Holes From Cosmic Strings*, *Phys. Lett. B* **231** (1989) 237.

[221] A. Polnarev and R. Zembowicz, *Formation of Primordial Black Holes by Cosmic Strings*, *Phys. Rev. D* **43** (1991) 1106.

[222] J.H. MacGibbon, R.H. Brandenberger and U.F. Wichoski, *Limits on black hole formation from cosmic string loops*, *Phys. Rev. D* **57** (1998) 2158 [astro-ph/9707146].

[223] R. Brandenberger, B. Cyr and H. Jiao, *Intermediate mass black hole seeds from cosmic string loops*, *Phys. Rev. D* **104** (2021) 123501 [2103.14057].

[224] J. Martin, T. Papanikolaou and V. Vennin, *Primordial black holes from the preheating instability in single-field inflation*, *JCAP* **01** (2020) 024 [1907.04236].

[225] J. Martin, T. Papanikolaou, L. Pinol and V. Vennin, *Metric preheating and radiative decay in single-field inflation*, *JCAP* **05** (2020) 003 [2002.01820].

[226] L. Delle Rose, G. Panico, M. Redi and A. Tesi, *Gravitational Waves from Supercool Axions*, *JHEP* **04** (2020) 025 [1912.06139].

[227] H.-K. Guo, K. Sinha, D. Vagie and G. White, *Phase Transitions in an Expanding Universe: Stochastic Gravitational Waves in Standard and Non-Standard Histories*, *JCAP* **01** (2021) 001 [2007.08537].

[228] H.-K. Guo, K. Sinha, D. Vagie and G. White, *The benefits of diligence: how precise are predicted gravitational wave spectra in models with phase transitions?*, *JHEP* **06** (2021) 164 [2103.06933].

[229] M. Hindmarsh, S.J. Huber, K. Rummukainen and D.J. Weir, *Gravitational waves from the sound of a first order phase transition*, *Phys. Rev. Lett.* **112** (2014) 041301 [1304.2433].

[230] M. Hindmarsh, S.J. Huber, K. Rummukainen and D.J. Weir, *Numerical simulations of acoustically generated gravitational waves at a first order phase transition*, *Phys. Rev. D* **92** (2015) 123009 [1504.03291].

[231] M. Hindmarsh, S.J. Huber, K. Rummukainen and D.J. Weir, *Shape of the acoustic gravitational wave power spectrum from a first order phase transition*, *Phys. Rev. D* **96** (2017) 103520 [1704.05871].

[232] J.R. Espinosa, T. Konstandin, J.M. No and G. Servant, *Energy Budget of Cosmological First-order Phase Transitions*, *JCAP* **06** (2010) 028 [1004.4187].

[233] T. Bringmann and S. Hofmann, *Thermal decoupling of WIMPs from first principles*, *JCAP* **04** (2007) 016 [hep-ph/0612238].

[234] N. Bernal and O. Zapata, *Self-interacting Dark Matter from Primordial Black Holes*, *JCAP* **03** (2021) 007 [2010.09725].

[235] A. Alves, D. Gonçalves, T. Ghosh, H.-K. Guo and K. Sinha, *Di-Higgs Production in the 4b Channel and Gravitational Wave Complementarity*, *JHEP* **03** (2020) 053 [1909.05268].

[236] F.-Y. Li, M.-X. Tang and D.-P. Shi, *Electromagnetic response of a Gaussian beam to high frequency relic gravitational waves in quintessential inflationary models*, *Phys. Rev. D* **67** (2003) 104008 [gr-qc/0306092].

[237] J. Cooley et al., *Report of the Topical Group on Particle Dark Matter for Snowmass 2021*, 2209.07426.

[238] M. Baryakhtar et al., *Dark Matter In Extreme Astrophysical Environments*, in *Snowmass 2021*, 3, 2022 [2203.07984].

[239] F. D'Eramo and J. Thaler, *Semi-annihilation of Dark Matter*, *JHEP* **06** (2010) 109 [1003.5912].

[240] Y. Hochberg, E. Kuflik, T. Volansky and J.G. Wacker, *Mechanism for Thermal Relic Dark Matter of Strongly Interacting Massive Particles*, *Phys. Rev. Lett.* **113** (2014) 171301 [1402.5143].

[241] R.T. D'Agnolo and J.T. Ruderman, *Light Dark Matter from Forbidden Channels*, *Phys. Rev. Lett.* **115** (2015) 061301 [1505.07107].

[242] J.A. Dror, E. Kuflik and W.H. Ng, *Codecaying Dark Matter*, *Phys. Rev. Lett.* **117** (2016) 211801 [1607.03110].

[243] E. Kuflik, M. Perelstein, N.R.-L. Lorier and Y.-D. Tsai, *Elastically Decoupling Dark Matter*, *Phys. Rev. Lett.* **116** (2016) 221302 [1512.04545].

[244] J.M. Cline, H. Liu, T. Slatyer and W. Xue, *Enabling Forbidden Dark Matter*, *Phys. Rev. D* **96** (2017) 083521 [1702.07716].

[245] R.T. D'Agnolo, D. Pappadopulo and J.T. Ruderman, *Fourth Exception in the Calculation of Relic Abundances*, *Phys. Rev. Lett.* **119** (2017) 061102 [1705.08450].

[246] M. Garny, J. Heisig, B. Lülf and S. Vogl, *Coannihilation without chemical equilibrium*, *Phys. Rev. D* **96** (2017) 103521 [1705.09292].

[247] J. Smirnov and J.F. Beacom, *New Freezeout Mechanism for Strongly Interacting Dark Matter*, *Phys. Rev. Lett.* **125** (2020) 131301 [2002.04038].

[248] P.J. Fitzpatrick, H. Liu, T.R. Slatyer and Y.-D. Tsai, *New pathways to the relic abundance of vector-portal dark matter*, *Phys. Rev. D* **106** (2022) 083517 [2011.01240].

[249] R. Frumkin, Y. Hochberg, E. Kuflik and H. Murayama, *Thermal Dark Matter from Freeze-Out of Inverse Decays*, *Phys. Rev. Lett.* **130** (2023) 121001 [2111.14857].

[250] K. Griest and M. Kamionkowski, *Unitarity Limits on the Mass and Radius of Dark Matter Particles*, *Phys. Rev. Lett.* **64** (1990) 615.

[251] D. Carney et al., *Snowmass2021 Cosmic Frontier White Paper: Ultraheavy particle dark matter*, 2203.06508.

[252] A. Berlin, D. Hooper and G. Krnjaic, *Thermal Dark Matter From A Highly Decoupled Sector*, *Phys. Rev. D* **94** (2016) 095019 [1609.02555].

[253] J. Hisano, S. Matsumoto, M. Nagai, O. Saito and M. Senami, *Non-perturbative effect on thermal relic abundance of dark matter*, *Phys. Lett. B* **646** (2007) 34 [hep-ph/0610249].

[254] H. Kim and E. Kuflik, *Superheavy Thermal Dark Matter*, *Phys. Rev. Lett.* **123** (2019) 191801 [1906.00981].

[255] A. Berlin, *WIMPs with GUTs: Dark Matter Coannihilation with a Lighter Species*, *Phys. Rev. Lett.* **119** (2017) 121801 [1704.08256].

[256] E.D. Kramer, E. Kuflik, N. Levi, N.J. Outmezguine and J.T. Ruderman, *Heavy Thermal Dark Matter from a New Collision Mechanism*, *Phys. Rev. Lett.* **126** (2021) 081802 [2003.04900].

[257] R. Frumkin, E. Kuflik, I. Lavie and T. Silverwater, *Roadmap to Thermal Dark Matter beyond the Weakly Interacting Dark Matter Unitarity Bound*, *Phys. Rev. Lett.* **130** (2023) 171001 [2207.01635].

[258] D.J.H. Chung, E.W. Kolb and A. Riotto, *Nonthermal supermassive dark matter*, *Phys. Rev. Lett.* **81** (1998) 4048 [hep-ph/9805473].

[259] D. Chway, T.H. Jung and C.S. Shin, *Dark matter filtering-out effect during a first-order phase transition*, *Phys. Rev. D* **101** (2020) 095019 [1912.04238].

[260] M.J. Baker, J. Kopp and A.J. Long, *Filtered Dark Matter at a First Order Phase Transition*, *Phys. Rev. Lett.* **125** (2020) 151102 [1912.02830].

[261] P. Asadi, E.D. Kramer, E. Kuflik, G.W. Ridgway, T.R. Slatyer and J. Smirnov, *Accidentally Asymmetric Dark Matter*, *Phys. Rev. Lett.* **127** (2021) 211101 [2103.09822].

[262] Y. Bai, A.J. Long and S. Lu, *Dark Quark Nuggets*, *Phys. Rev. D* **99** (2019) 055047 [1810.04360].

[263] J.-P. Hong, S. Jung and K.-P. Xie, *Fermi-ball dark matter from a first-order phase transition*, *Phys. Rev. D* **102** (2020) 075028 [2008.04430].

[264] K. Kawana, P. Lu and K.-P. Xie, *First-order phase transition and fate of false vacuum remnants*, *JCAP* **10** (2022) 030 [2206.09923].

[265] A. Azatov, M. Vanvlasselaer and W. Yin, *Dark Matter production from relativistic bubble walls*, *JHEP* **03** (2021) 288 [2101.05721].

[266] A. Falkowski and J.M. No, *Non-thermal Dark Matter Production from the Electroweak Phase Transition: Multi-TeV WIMPs and 'Baby-Zillas'*, *JHEP* **02** (2013) 034 [1211.5615].

[267] D.E. Kaplan, M.A. Luty and K.M. Zurek, *Asymmetric Dark Matter*, *Phys. Rev. D* **79** (2009) 115016 [0901.4117].

[268] P. Asadi, E.D. Kramer, E. Kuflik, G.W. Ridgway, T.R. Slatyer and J. Smirnov, *Thermal squeezeout of dark matter*, *Phys. Rev. D* **104** (2021) 095013 [2103.09827].

[269] T.C. Gehrman, B. Shams Es Haghi, K. Sinha and T. Xu, *The primordial black holes that disappeared: connections to dark matter and MHz-GHz gravitational Waves*, *JCAP* **10** (2023) 001 [2304.09194].

[270] T. Kim, P. Lu, D. Marfatia and V. Takhistov, *Regurgitated Dark Matter*, 2309.05703.

[271] F. LeBlanc, *An Introduction to Stellar Astrophysics* (2010).

[272] B. Paxton, L. Bildsten, A. Dotter, F. Herwig, P. Lesaffre and F. Timmes, *Modules for experiments in stellar astrophysics (mesa)*, *The Astrophysical Journal Supplement Series* **192** (2010) 3.

[273] B. Paxton, L. Bildsten, A. Dotter, F. Herwig, P. Lesaffre and F. Timmes, *Modules for Experiments in Stellar Astrophysics (MESA)*, ApJS **192** (2011) 3 [1009.1622].

[274] B. Paxton, M. Cantiello, P. Arras, L. Bildsten, E.F. Brown, A. Dotter et al., *Modules for experiments in stellar astrophysics (mesa): Planets, oscillations, rotation, and massive stars*, *The Astrophysical Journal Supplement Series* **208** (2013) 4.

[275] B. Paxton, P. Marchant, J. Schwab, E.B. Bauer, L. Bildsten, M. Cantiello et al., *Modules for experiments in stellar astrophysics (mesa): Binaries, pulsations, and explosions*, *The Astrophysical Journal Supplement Series* **220** (2015) 15.

[276] B. Paxton, J. Schwab, E.B. Bauer, L. Bildsten, S. Blinnikov, P. Duffell et al., *Modules for experiments in stellar astrophysics (*`mesa`*): Convective boundaries, element diffusion, and massive star explosions*, *The Astrophysical Journal Supplement Series* **234** (2018) 34.

[277] B. Paxton, R. Smolec, J. Schwab, A. Gautschy, L. Bildsten, M. Cantiello et al., *Modules for experiments in stellar astrophysics (mesa): Pulsating variable stars, rotation, convective boundaries, and energy conservation*, *The Astrophysical Journal Supplement Series* **243** (2019) 10.

[278] C. Angulo, M. Arnould, M. Rayet, P. Descouvemont, D. Baye, C. Leclercq-Willain et al., *A compilation of charged-particle induced thermonuclear reaction rates*, Nucl. Phys. A **656** (1999) 3.

[279] N. Grevesse and A.J. Sauval, *Standard Solar Composition*, Space Sci. Rev. **85** (1998) 161.

[280] S. Cassisi, A.Y. Potekhin, A. Pietrinferni, M. Catelan and M. Salaris, *Updated Electron-Conduction Opacities: The Impact on Low-Mass Stellar Models*, ApJ **661** (2007) 1094 [`astro-ph/0703011`].

[281] F.J. Rogers and A. Nayfonov, *Updated and Expanded OPAL Equation-of-State Tables: Implications for Helioseismology*, ApJ **576** (2002) 1064.

[282] D. Saumon, G. Chabrier and H.M. van Horn, *An Equation of State for Low-Mass Stars and Giant Planets*, ApJS **99** (1995) 713.

[283] F.X. Timmes and F.D. Swesty, *The Accuracy, Consistency, and Speed of an Electron-Positron Equation of State Based on Table Interpolation of the Helmholtz Free Energy*, ApJS **126** (2000) 501.

[284] P. Ledoux, *Stellar Models with Convection and with Discontinuity of the Mean Molecular Weight*, ApJ **105** (1947) 305.

[285] N. Langer, K.J. Fricke and D. Sugimoto, *Semiconvective diffusion and energy transport*, A&A **126** (1983) 207.

[286] S. Ekström, C. Georgy, P. Eggenberger, G. Meynet, N. Mowlavi, A. Wyttenbach et al., *Grids of stellar models with rotation. I. Models from 0.8 to 120 $M_\odot$ at solar metallicity ($Z = 0.014$)*, A&A **537** (2012) A146 [`1110.5049`].

[287] R. Kuhfuss, *A model for time-dependent turbulent convection*, A&A **160** (1986) 116.

[288] J.P. Cox and R.T. Giuli, *Principles of stellar structure* (1968).

[289] G. Meynet and A. Maeder, *Stellar evolution with rotation. I. The computational method and the inhibiting effect of the μ-gradient.*, A&A **321** (1997) 465.

[290] G.G. Raffelt, *Stars as laboratories for fundamental physics: The astrophysics of neutrinos, axions, and other weakly interacting particles* (5, 1996).

[291] G.G. Raffelt, *Astrophysical methods to constrain axions and other novel particle phenomena*, *Phys. Rept.* **198** (1990) 1.

[292] C.B. Adams et al., *Axion Dark Matter*, in *Snowmass 2021*, 3, 2022 [2203.14923].

[293] R. Essig et al., *Working Group Report: New Light Weakly Coupled Particles*, in *Snowmass 2013: Snowmass on the Mississippi*, 10, 2013 [1311.0029].

[294] A. Ayala, I. Domínguez, M. Giannotti, A. Mirizzi and O. Straniero, *Revisiting the bound on axion-photon coupling from Globular Clusters*, *Phys. Rev. Lett.* **113** (2014) 191302 [1406.6053].

[295] M.J. Dolan, F.J. Hiskens and R.R. Volkas, *Advancing globular cluster constraints on the axion-photon coupling*, *JCAP* **10** (2022) 096 [2207.03102].

[296] R. Kippenhahn, A. Weigert and A. Weiss, *Stellar structure and evolution*, Astronomy and Astrophysics Library, Springer (8, 2012), 10.1007/978-3-642-30304-3.

[297] D. Lauterborn, S. Refsdal and A. Weigert, *Stars with Central Helium Burning and the Occurrence of Loops in the H-R Diagram*, A&A **10** (1971) 97.

[298] J.W. Robertson, *Envelope Opacities and the Cepheid Loops at 5 $M_\odot$*, ApJ **173** (1972) 631.

[299] M. Alongi, G. Bertelli, A. Bressan and C. Chiosi, *Effects of envelope overshoot on stellar models.*, A&A **244** (1991) 95.

[300] A.S. Jermyn, E.B. Bauer, J. Schwab, R. Farmer, W.H. Ball, E.P. Bellinger et al., *Modules for Experiments in Stellar Astrophysics (MESA): Time-dependent Convection, Energy Conservation, Automatic Differentiation, and Infrastructure*, ApJS **265** (2023) 15 [2208.03651].

[301] N. Remage Evans, D. Massa, A. Fullerton, G. Sonneborn and R. Iping, *Cepheid Masses: FUSE Observations of S Mus*, *Astrophys. J.* **647** (2006) 1387 [astro-ph/0607489].

[302] M. Marconi, G. De Somma, V. Ripepi, R. Molinaro, I. Musella, S. Leccia et al., *Predicted Masses of Galactic Cepheids in the Gaia Data Release 2*, ApJ **898** (2020) L7 [2006.16610].

[303] P. Kervella, A. Gallenne, N.R. Evans, L. Szabados, F. Arenou, A. Mérand et al., *Multiplicity of Galactic Cepheids and RR Lyrae stars from Gaia DR2. II. Resolved common proper motion pairs*, A&A **623** (2019) A117 [1908.00545].

[304] I. Soszyński, D.M. Skowron, A. Udalski, P. Pietrukowicz, M. Gromadzki, M.K. Szymański et al., *Discovery of the Longest-period Classical Cepheid in the Milky Way*, ApJ **965** (2024) L17 [2404.00151].

[305] V. Ripepi, G. Clementini, R. Molinaro, S. Leccia, E. Plachy, L. Molnár et al., *Gaia Data Release 3. Specific processing and validation of all sky RR Lyrae and Cepheid stars: The Cepheid sample*, A&A **674** (2023) A17 [2206.06212].

[306] J.A. Guzik, J. Jackiewicz and N.R. Evans, *Challenges in Cepheid Evolution and Pulsation Modeling*, *arXiv e-prints* (2023) arXiv:2307.12386 [2307.12386].

[307] H.R. Neilson, M. Cantiello and N. Langer, *The Cepheid mass discrepancy and pulsation-driven mass loss*, A&A **529** (2011) L9 [1104.1638].

[308] A. Friedland, M. Giannotti and M. Wise, *Constraining the Axion-Photon Coupling with Massive Stars*, *Phys. Rev. Lett.* **110** (2013) 061101 [1210.1271].

[309] E. Glebbeek, E. Gaburov, S.E. de Mink, O.R. Pols and S.F. Portegies Zwart, *The evolution of runaway stellar collision products*, A&A **497** (2009) 255 [0902.1753].

[310] J.S. Vink, A. de Koter and H.J.G.L.M. Lamers, *Mass-loss predictions for o and b stars as a function of metallicity*, A&A **369** (2001) 574–588.

[311] T. Nugis and H.J.G.L.M. Lamers, *Mass-loss rates of Wolf-Rayet stars as a function of stellar parameters*, A&A **360** (2000) 227.

[312] G. De Somma, M. Marconi, R. Molinaro, M. Cignoni, I. Musella and V. Ripepi, *An Extended Theoretical Scenario for Classical Cepheids. I. Modeling Galactic Cepheids in the Gaia Photometric System*, ApJS **247** (2020) 30 [2001.11065].

[313] G. Bono, W.P. Gieren, M. Marconi, P. Fouqué and F. Caputo, *Improving the Mass Determination of Galactic Cepheids*, ApJ **563** (2001) 319 [astro-ph/0108271].

[314] N. Langer, K.J. Fricke and D. Sugimoto, *Semiconvective diffusion and energy transport*, A&A **126** (1983) 207.

[315] M. Asplund, N. Grevesse and A.J. Sauval, *The Solar Chemical Composition*, in *Cosmic Abundances as Records of Stellar Evolution and Nucleosynthesis*, I. Barnes, Thomas G. and F.N. Bash, eds., vol. 336 of *Astronomical Society of the Pacific Conference Series*, p. 25, Sept., 2005.

[316] K. Lodders, *Solar System Abundances and Condensation Temperatures of the Elements*, ApJ **591** (2003) 1220.

[317] R.I. Anderson, S. Ekström, C. Georgy, G. Meynet, N. Mowlavi and L. Eyer, *On the effect of rotation on populations of classical cepheids: I. predictions at solar metallicity*, A&A **564** (2014) A100.

[318] R.I. Anderson, H. Saio, S. Ekström, C. Georgy and G. Meynet, *On the effect of rotation on populations of classical cepheids: Ii. pulsation analysis for metallicities 0.014, 0.006, and 0.002*, A&A **591** (2016) A8.

[319] G.A. Tammann, A. Sandage and B. Reindl, *New period-luminosity and period-color relations of classical cepheids: I. cepheids in the galaxy*, A&A **404** (2003) 423–448.

[320] G.G. Raffelt and D.S.P. Dearborn, *Bounds on Hadronic Axions From Stellar Evolution*, *Phys. Rev. D* **36** (1987) 2211.

[321] I. Iben, *Age and Initial Helium Abundance of Stars in the Globular Cluster M15*, Nature **220** (1968) 143.

[322] F. Caputo, V. Castellani, A. Chieffi, L. Pulone and J. Tornambe, A., *The "Red Giant Clock" as an Indicator for the Efficiency of Central Mixing in Horizontal-Branch Stars*, ApJ **340** (1989) 241.

[323] J.J. Walmswell, C.A. Tout and J.J. Eldridge, *On the blue loops of intermediate-mass stars*, *Monthly Notices of the Royal Astronomical Society* **447** (2015) 2951 [https://academic.oup.com/mnras/article-pdf/447/3/2951/9388791/stu2666.pdf].

[324] G. Pietrzyński, I.B. Thompson, W. Gieren, D. Graczyk, G. Bono, A. Udalski et al., *The dynamical mass of a classical Cepheid variable star in an eclipsing binary system*, Nature **468** (2010) 542 [1012.0231].

[325] N. Remage Evans and C.T. Bolton, *The Mass of the Classical Cepheid Su-Cygni*, in *New Insights in Astrophysics. Eight Years of UV Astronomy with IUE*, E.J. Rolfe and R. Wilson, eds., vol. 263 of *ESA Special Publication*, p. 405, Sept., 1986.

[326] N.R. Evans, C. Proffitt, K.G. Carpenter, E.M. Winston, G.V. Kober, H.M. Günther et al., *The mass of the cepheid v350 sgr**, *The Astrophysical Journal* **866** (2018) 30.

[327] N.R. Evans, G.H. Schaefer, H.E. Bond, G. Bono, M. Karovska, E. Nelan et al., *Direct Detection of the Close Companion of Polaris with the Hubble Space Telescope*, *Astron. J.* **136** (2008) 1137 [0806.4904].

[328] A. Gallenne, P. Kervella, N.R. Evans, C.R. Proffitt, J.D. Monnier, A. Mérand et al., *A Geometrical 1% Distance to the Short-period Binary Cepheid V1334 Cygni*, ApJ **867** (2018) 121 [1809.07486].

[329] M. Wenger et al., *The simbad astronomical database*, *Astron. Astrophys. Suppl. Ser.* **143** (2000) 9 [astro-ph/0002110].

[330] K. Anderson, T.C. Gehrman, P. Sandick, K. Sinha, E. Walsh and T. Xu, *The effect of axions on period-luminosity relations of cepheid variables, in preparation* .

[331] N.E. Evans, H.E. Bond, G.H. Schaefer, B.D. Mason, M. Karovska and E. Tingle, *Binary Cepheids: Separations and Mass Ratios in 5 $M_\odot$ Binaries*, AJ **146** (2013) 93 [1307.7123].

[332] E. Böhm-Vitense, N. Remage Evans, K. Carpenter, B. Beck-Winchatz and R. Robinson, *The Mass of the Classical Cepheid S Muscae*, ApJ **477** (1997) 916.

[333] R. Janish and E. Pinetti, *Hunting Dark Matter Lines in the Infrared Background with the James Webb Space Telescope*, 2310.15395.

[334] W. Yin et al., *First Result for Dark Matter Search by WINERED*, 2402.07976.

[335] E. Todarello, M. Regis, J. Reynoso-Cordova, M. Taoso, D. Vaz, J. Brinchmann et al., *Robust bounds on ALP dark matter from dwarf spheroidal galaxies in the optical MUSE-Faint survey*, *JCAP* **05** (2024) 043 [2307.07403].

[336] D. Grin, G. Covone, J.-P. Kneib, M. Kamionkowski, A. Blain and E. Jullo, *A Telescope Search for Decaying Relic Axions*, *Phys. Rev. D* **75** (2007) 105018 [astro-ph/0611502].

[337] K. Nakayama and W. Yin, *Anisotropic cosmic optical background bound for decaying dark matter in light of the LORRI anomaly*, *Phys. Rev. D* **106** (2022) 103505 [2205.01079].

[338] P. Carenza, G. Lucente and E. Vitagliano, *Probing the blue axion with cosmic optical background anisotropies*, *Phys. Rev. D* **107** (2023) 083032 [2301.06560].

[339] S. Porras-Bedmar, M. Meyer and D. Horns, *Novel bounds on decaying axionlike particle dark matter from the cosmic background*, *Phys. Rev. D* **110** (2024) 103501 [2407.10618].

[340] K.J. Fricke and P.A. Strittmatter, *Evolutionary Aspects of the Cepheid Stage*, *Monthly Notices of the Royal Astronomical Society* **156** (1972) 129 [https://academic.oup.com/mnras/article-pdf/156/2/129/9360863/mnras156-0129.pdf].

[341] G.A. Wagle, A. Ray, A. Dev and A. Raghu, *Type IIP Supernova Progenitors and Their Explodability. I. Convective Overshoot, Blue Loops, and Surface Composition*, ApJ **886** (2019) 27 [1910.01679].

[342] G.A. Wagle, A. Ray and A. Raghu, *Type IIP Supernova Progenitors. III. Blue to Red Supergiant Ratio in Low-metallicity Models with Convective Overshoot*, ApJ **894** (2020) 118 [2004.14419].

[343] M. Godart, A. Noels, M.A. Dupret and Y. Lebreton, *Can mass loss and overshooting prevent the excitation of g-modes in blue supergiants?*, MNRAS **396** (2009) 1833 [0904.4641].

[344] A. Maeder and G. Meynet, *Tables of isochrones computed from stellar models with mass loss and overshooting.*, A&AS **89** (1991) 451.

[345] K.-P. Schroder, O.R. Pols and P.P. Eggleton, *A critical test of stellar evolution and convective core 'overshooting' by means of zeta Aurigae systems*, MNRAS **285** (1997) 696.

[346] M. Briquet, T. Morel, A. Thoul, R. Scuflaire, A. Miglio, J. Montalbán et al., *An asteroseismic study of the β Cephei star θ Ophiuchi: constraints on global stellar parameters and core overshooting*, MNRAS **381** (2007) 1482 [0706.3274].

[347] J.C. Mermilliod and A. Maeder, *Evolution of massive stars : comparison of cluster sequences and models with mass loss.*, A&A **158** (1986) 45.

[348] I. Brott, S.E. de Mink, M. Cantiello, N. Langer, A. de Koter, C.J. Evans et al., *Rotating massive main-sequence stars-i. grids of evolutionary models and isochrones*, *Astronomy & Astrophysics* **530** (2011) A115.

[349] S. Ekström, C. Georgy, P. Eggenberger, G. Meynet, N. Mowlavi, A. Wyttenbach et al., *Grids of stellar models with rotation. I. Models from 0.8 to 120 $M_\odot$ at solar metallicity ($Z = 0.014$)*, A&A **537** (2012) A146 [1110.5049].

[350] L. Di Luzio, M. Fedele, M. Giannotti, F. Mescia and E. Nardi, *Stellar evolution confronts axion models*, *JCAP* **02** (2022) 035 [2109.10368].

[351] K. Anderson, T.C. Gehrman, P. Sandick, K. Sinha, E. Walsh and T. Xu, *Blue loops, Cepheids, and forays into axions*, *JCAP* **04** (2025) 083 [2412.03652].

[352] G. Pietrzyński, I.B. Thompson, W. Gieren, D. Graczyk, G. Bono, A. Udalski et al., *The dynamical mass of a classical cepheid variable star in an eclipsing binary system*, *Nature* **468** (2010) 542–544.

[353] H.R. Neilson, M. Cantiello and N. Langer, *The cepheid mass discrepancy and pulsation-driven mass loss*, A&A **529** (2011) L9.

[354] A. Maeder, *Stellar evolution with rotation IV: von Zeipel's theorem and anisotropic losses of mass and angular momentum*, A&A **347** (1999) 185.

[355] G. Meynet and A. Maeder, *Stellar evolution with rotation. I. The computational method and the inhibiting effect of the μ-gradient.*, A&A **321** (1997) 465.

[356] A. Maeder and G. Meynet, *The evolution of rotating stars*, *Annual Review of Astronomy and Astrophysics* **38** (2000) 143–190.

[357] A. Maeder and J.-P. Zahn, *Stellar evolution with rotation. III. Meridional circulation with MU -gradients and non-stationarity*, A&A **334** (1998) 1000.

[358] J. Redondo and G. Raffelt, *Solar constraints on hidden photons re-visited*, *Journal of Cosmology and Astroparticle Physics* **2013** (2013) 034 [1305.2920].

[359] M. Giannotti, I. Irastorza, J. Redondo, A. Ringwald and K. Saikawa, *Stellar recipes for axion hunters*, *Journal of Cosmology and Astroparticle Physics* **2017** (2017) 010 [1708.02111].

[360] L. Henyey, M.S. Vardya and P. Bodenheimer, *Studies in Stellar Evolution. III. The Calculation of Model Envelopes.*, ApJ **142** (1965) 841.

[361] A. Heger and N. Langer, *Presupernova evolution of rotating massive stars. 2. - evolution of the surface properties*, *Astrophys. J.* **544** (2000) 1016 [astro-ph/0005110].

[362] G. Meynet and A. Maeder, *Stellar evolution with rotation. 5. Changes in all the outputs of massive star models*, *Astron. Astrophys.* **361** (2000) 101 [astro-ph/0006404].

[363] A. Palacios, S. Talon, C. Charbonnel and M. Forestini, *Rotational mixing in low - mass stars. 1. Effect of the mu - gradients in main sequence and subgiant Pop I stars*, *Astron. Astrophys.* **399** (2003) 603 [astro-ph/0210516].

[364] S. Talon and C. Charbonnel, *Hydrodynamical stellar models including rotation, internal gravity waves and atomic diffusion. 1. Formalism and tests on Pop I dwarfs*, *Astron. Astrophys.* **440** (2005) 981 [astro-ph/0505229].

[365] P.A. Denissenkov and M. Pinsonneault, *A Revised Prescription for the Tayler-Spruit Dynamo: Magnetic Angular Momentum Transport in Stars*, *Astrophys. J.* **655** (2007) 1157 [astro-ph/0604045].

[366] R.I. Anderson, S. Ekström, C. Georgy, G. Meynet, N. Mowlavi and L. Eyer, *On the effect of rotation on populations of classical Cepheids I. Predictions at solar metallicity*, *Astron. Astrophys.* **564** (2014) A100 [1403.0809].

[367] S. Ekstrom et al., *Grids of stellar models with rotation - I. Models from 0.8 to 120 Msun at solar metallicity (Z = 0.014)*, *Astron. Astrophys.* **537** (2012) A146 [1110.5049].

[368] S. Ekström, C. Georgy, P. Eggenberger, G. Meynet, N. Mowlavi, A. Wyttenbach et al., *Grids of stellar models with rotation. I. Models from 0.8 to 120 $M_\odot$ at solar metallicity (Z = 0.014)*, A&A **537** (2012) A146 [1110.5049].

[369] C. Georgy, S. Ekström, A. Granada, G. Meynet, N. Mowlavi, P. Eggenberger et al., *Populations of rotating stars. I. Models from 1.7 to 15 $M_\odot$ at $Z = 0.014$, 0.006, and 0.002 with Ω/Ω_{crit} between 0 and 1*, A&A **553** (2013) A24 [1303.2321].

[370] S. Ekström, C. Georgy, G. Meynet, P. Eggenberger, A. Maeder, S. Mowlavi et al., *Grids of stellar models with rotation. i. models from 0.8 to 120 $m_\odot$ at solar metallicity ($z = 0.014$)*, *Astronomy & Astrophysics* **537** (2012) A146.

[371] A. Maeder and G. Meynet, *Stellar evolution with rotation*, *Annual Review of Astronomy and Astrophysics* **38** (2000) 143.

[372] R.I. Anderson, H. Saio, S. Ekström, C. Georgy and G. Meynet, *On the effect of rotation on populations of classical cepheids: Ii. pulsation analysis for metallicities 0.014, 0.006, and 0.002*, A&A **591** (2016) A8.

[373] W. Huang, D.R. Gies and M.V. McSwain, *A stellar rotation census of b stars: From zams to tams*, *The Astrophysical Journal* **722** (2010) 605.

[374] C. Georgy, S. Ekström, A. Granada, G. Meynet, N. Mowlavi, P. Eggenberger et al., *Populations of rotating stars. i. models from 1.7 to 15 $m_\odot$ at $z = 0.014$, 0.006, and 0.002 with $\omega/\omega_{\rm crit}$ between 0 and 1*, *Astronomy & Astrophysics* **553** (2013) A24 [1303.2321].

[375] A. Heger, N. Langer and S.E. Woosley, *Presupernova Evolution of Rotating Massive Stars. I. Numerical Method and Evolution of the Internal Stellar Structure*, ApJ **528** (2000) 368 [astro-ph/9904132].

[376] H.C. Spruit, *Dynamo action by differential rotation in a stably stratified stellar interior*, *Astronomy & Astrophysics* **381** (2002) 923 [astro-ph/0108207].

[377] R.I. Anderson, S. Ekström, C. Georgy, G. Meynet, N. Mowlavi and L. Eyer, *On the effect of rotation on populations of classical cepheids. ii. the period-luminosity and period-age relations at solar metallicity*, *Astronomy & Astrophysics* **564** (2014) A100.

[378] N.R. Evans, G.H. Schaefer, H.E. Bond, G. Bono, M. Karovska, E. Nelan et al., *Direct Detection of the Close Companion of Polaris with the Hubble Space Telescope*, AJ **136** (2008) 1137 [0806.4904].

[379] N.R. Evans, D. Massa, E.D. Horch and K.W. Stassun, *Dynamical masses for cepheids: A 10 $m_\odot$ binary in the large magellanic cloud*, *The Astronomical Journal* **146** (2013) 93.

[380] A. Gallenne, P. Kervella, N.R. Evans, C.R. Proffitt, J.D. Monnier, A. Mérand et al., *A Geometrical 1% Distance to the Short-period Binary Cepheid V1334 Cygni*, ApJ **867** (2018) 121 [1809.07486].

[381] F. Caputo, G. Bono, S. Cassisi, V. Castellani, M. Marconi, M. Stornelli et al., *On the mass-luminosity relation of classical cepheids: Effects of chemical composition*, *The Astrophysical Journal* **629** (2005) 1021.

[382] P.J. Flower, *Transformations from theoretical hertzsprung–russell diagrams to color–magnitude diagrams: Effective temperatures, bv colors, and bolometric corrections*, *The Astrophysical Journal* **469** (1996) 355.

[383] D. Reimers, *Circumstellar absorption lines and mass loss from red giants*, *Memoires of the Societe Royale des Sciences de Liege* **8** (1975) 369.

[384] T. Blöcker, *Stellar evolution of low- and intermediate-mass stars. ii. post-agb evolution*, *Astronomy & Astrophysics* **297** (1995) 727.

[385] N. Langer, *Presupernova evolution of massive single and binary stars*, *Astronomy & Astrophysics* **329** (1998) 551.

[386] I. Brott, I. Hunter, P. Langer, A. de Koter, N. Langer, C. Trundle et al., *Rotating massive main-sequence stars. i. grids of evolutionary models and isochrones*, *Astronomy & Astrophysics* **530** (2011) A115.

[387] B. Holdom, *Two u(1)'s and epsilon charge shifts*, *Physics Letters B* **166** (1986) 196.

[388] R. Foot and X.G. He, *Comment on z-z' mixing in extended gauge theories*, *Physics Letters B* **267** (1991) 509.

[389] S. Davidson, S. Hannestad and G. Raffelt, *Updated bounds on milli-charged particles*, *Journal of High Energy Physics* **2000** (2000) 003 [hep-ph/0001179].

[390] E.R. Williams, J.E. Faller and H.A. Hill, *New experimental test of coulomb's law: A laboratory upper limit on the photon rest mass*, *Physical Review Letters* **26** (1971) 721.

[391] A.A. Prinz, R. Baggs, J. Ballam, S. Ecklund, C. Field, E.C. Friedlander et al., *Search for millicharged particles at slac*, *Physical Review Letters* **81** (1998) 1175 [hep-ex/9804008].

[392] H. Vogel and J. Redondo, *Dark radiation constraints on minicharged particles in models with a hidden photon*, *Journal of Cosmology and Astroparticle Physics* **2014** (2014) 029 [1311.2600].

[393] H. An, K.M. Zurek and Y. Zhao, *Revisiting constraints on millicharged particles from the sun and beyond*, *Journal of High Energy Physics* **2023** (2023) 126 [2308.07951].

[394] J. Redondo and G. Raffelt, *Solar constraints on hidden photons re-visited*, *Journal of Cosmology and Astroparticle Physics* **2013** (2013) 034 [1305.2920].

[395] A. Berlin, N. Blinov and S. Verner, *New constraints on millicharged particles from cosmology*, *Physical Review Letters* **129** (2022) 251103 [2209.06296].

[396] H. Vogel and J. Redondo, *Dark Radiation constraints on minicharged particles in models with a hidden photon*, *JCAP* **02** (2014) 029 [1311.2600].

[397] N. Vinyoles and H. Vogel, *Minicharged Particles from the Sun: A Cutting-Edge Bound*, *JCAP* **03** (2016) 002 [1511.01122].

[398] A. Fung, S. Heeba, Q. Liu, V. Muralidharan, K. Schutz and A.C. Vincent, *New bounds on light millicharged particles from the tip of the red-giant branch*, *Phys. Rev. D* **109** (2024) 083011 [2309.06465].

[399] E. Braaten and D. Segel, *Neutrino energy loss from the plasma process at all temperatures and densities*, *Phys. Rev. D* **48** (1993) 1478 [hep-ph/9302213].

[400] H.A. Weldon, *Simple Rules for Discontinuities in Finite Temperature Field Theory*, *Phys. Rev. D* **28** (1983) 2007.

[401] U.H. Danielsson, *A Note on inflation and transPlanckian physics*, *Phys. Rev. D* **66** (2002) 023511 [hep-th/0203198].

[402] C.T. Byrnes, P.S. Cole and S.P. Patil, *Steepest growth of the power spectrum and primordial black holes*, *JCAP* **06** (2019) 028 [1811.11158].

[403] J.L. Barrow et al., *Theories and Experiments for Testable Baryogenesis Mechanisms: A Snowmass White Paper*, 2203.07059.

[404] M.J. Dolan, F.J. Hiskens and R.R. Volkas, *Advancing globular cluster constraints on the axion-photon coupling*, J. Cosmology Astropart. Phys. **2022** (2022) 096 [2207.03102].